

5 July 2013 | \$10

Science



AAAS

EDITORIAL

- 10 Building Better Institutions
Paul Nurse et al.

NEWS OF THE WEEK

- 14 A roundup of the week's top stories

NEWS & ANALYSIS

- 17 NIH to Phase Out Most Chimp Research
18 New Law Would Dilute and Diminish Russian Science Academy
19 Budget Malaise May Hit DOE's One Big Growth Area
20 China's Exquisite Look at Earth's Rocky Husk Wins Raves
21 At Long Last, Europe's Mega R&D Program Comes Into Focus

NEWS FOCUS

- 22 Into the Minds of Birds
>> Science Podcast
26 Solution to Vaccine Mystery Starts to Crystallize

LETTERS

- 28 NextGenVOICES

BOOKS ET AL.

- 31 We Modern People
A. Banerjee, reviewed by A. Siddiqi
32 The Golden Ticket
L. Fortnow, reviewed by V. Elser

POLICY FORUM

- 33 Sustainable Intensification in Agriculture: Premises and Policies
T. Garnett et al.

PERSPECTIVES

- 35 Seabirds—Individuals in Colonies
H. Weimerskirch
>> Report p. 68
36 Spectroscopy Beyond the Single-Particle Limit
G. V. Hartland and S. S. Lo
>> Report p. 56
37 Fueling Function Over Expansion in T Cells
J. P. Argus and S. J. Bensinger
39 The Roots of Cultivation in Southwestern Asia
G. Willcox
>> Report p. 65
40 Radio Bursts, Origin Unknown
J. M. Cordes
>> Report p. 53
41 Making Macrophages Eat Cancer
M. H. Kershaw and M. J. Smyth
>> Report p. 88

REVIEW

- 43 Somatic Mutation, Genomic Variation, and Neurological Disease
A. Poduri et al.
Review Summary; for full text:
<http://dx.doi.org/10.1126/science.1237758>

RESEARCH ARTICLES

- 44 The Long-Term Stability of the Human Gut Microbiota
J. J. Faith et al.
Low-error sequencing data suggest that initial microbial colonizers of infant guts could persist over the life span of an individual.
Research Article Summary; for full text:
<http://dx.doi.org/10.1126/science.1237439>
45 Bringing Ecosystem Services into Economic Decision-Making: Land Use in the United Kingdom
I. J. Bateman et al.
The value of using land for recreation and wildlife, not just for agriculture, can usefully factor into planning decisions.

CONTENTS continued >>



page 22



page 31

ON THE WEB THIS WEEK

>> Science Podcast

Listen to stories on ultrahigh magnetoresistance at room temperature, tracing the roots of plant domestication, bird brains in the PET scanner, and more.

>> Find More Online

Check out *Science Express*, our podcast, videos, daily news, our research journals, and *Science Careers* at www.sciencemag.org.



COVER

Aerial view of farmland, Epping Forest, and the city of London. Landscapes such as this one produce important ecosystem services, but minor increases in marketed goods often cause major losses in the value of those services. This situation can be reversed by combining science and economics in a comprehensive approach to target improvements in the natural environment. See page 45.

Photo: Andrew Holt/Alamy

DEPARTMENTS

- 9 This Week in *Science*
11 Editors' Choice
12 *Science Staff*
92 New Products
93 *Science Careers*

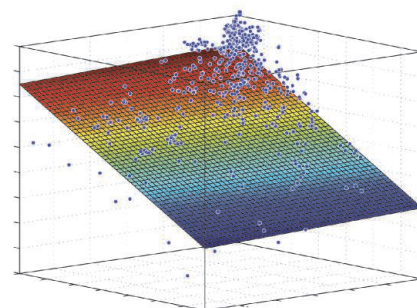
REPORTS

- 50** Signatures of Cool Gas Fueling a Star-Forming Galaxy at Redshift 2.3
N. Bouché et al.
Observations of gas near a star-forming galaxy reveal kinematic signatures expected from gas inflowing onto the galaxy.
- 53** A Population of Fast Radio Bursts at Cosmological Distances
D. Thornton et al.
Radio telescope data revealed four short, extragalactic, nonrepeating bursts of radio emission whose source is unknown.
>> *Perspective p. 40*
- 56** Ultrafast Three-Dimensional Imaging of Lattice Dynamics in Individual Gold Nanocrystals
J. N. Clark et al.
An x-ray free-electron laser is used to probe the elastic modes of a gold nanocrystal.
>> *Perspective p. 36*
- 59** Chiral Symmetry Breaking in Superfluid $^3\text{He-A}$
H. Ikegami et al.
The asymmetric deflection of impurities beneath the surface of helium-3 reveals the handedness of the superfluid A phase.
- 62** Crystal Structure Determination of the Nonclassical 2-Norbornyl Cation
F. Scholz et al.
A long-standing debate about the structural symmetry of a positively charged hydrocarbon is settled by x-ray diffraction.
- 65** Emergence of Agriculture in the Foothills of the Zagros Mountains of Iran
S. Riehl et al.
An archaeobotanical assemblage spans the transition period from foraging to farming in the Near East.
>> *Perspective p. 39; Science Podcast*
- 68** Space Partitioning Without Territoriality in Gannets
E. D. Wakefield et al.
Gannets establish foraging territory boundaries in colonies through local competition and information exchange.
>> *Perspective p. 35*

- 71** MiR-200b and miR-429 Function in Mouse Ovulation and Are Essential for Female Fertility
H. Hasuwa et al.
MicroRNAs regulate hormone synthesis in the pituitary and the production of oocytes.
- 74** A Secreted Disulfide Catalyst Controls Extracellular Matrix Composition and Function
T. Ilani et al.
Laminin incorporation is promoted by a secreted enzyme, which is important for cell adhesion and migration.
- 77** Structure of the Repulsive Guidance Molecule (RGM)—Neogenin Signaling Hub
C. H. Bell et al.
A complex of a guidance molecule and its receptor reveals how signals cross the membrane.
- 80** Inhibition of RNA Helicase Brr2 by the C-Terminal Tail of the Spliceosomal Protein Prp8
S. Mozaffari-Jovin et al.
Regulating an RNA helicase in the eukaryotic splicing reaction involves intermittent blockade of the catalytic tunnel.
- 84** Monitoring Drug Target Engagement in Cells and Tissues Using the Cellular Thermal Shift Assay
D. Martinez Molina et al.
A method to monitor drug binding to proteins in cells may help in target validation and drug optimization.
- 88** Engineered SIRP α Variants as Immunotherapeutic Adjuvants to Anticancer Antibodies
K. Weiskopf et al.
CD47 antagonists augment the effectiveness of antibody-mediated tumor immunotherapy in mice.
>> *Perspective p. 41*



pages 40 & 53



page 44

SCIENCE (ISSN 0036-8075) is published weekly on Friday, except the last week in December, by the American Association for the Advancement of Science, 1200 New York Avenue, NW, Washington, DC 20005. Periodicals Mail postage (publication No. 484460) paid at Washington, DC, and additional mailing offices. Copyright © 2013 by the American Association for the Advancement of Science. The title SCIENCE is a registered trademark of the AAAS. Domestic individual membership and subscription (51 issues): \$149 (\$74 allocated to subscription). Domestic institutional subscription (51 issues): \$990; Foreign postage extra: Mexico, Caribbean (surface mail) \$55; other countries (air assist delivery) \$85. First class, airmail, student, and emeritus rates on request. Canadian rates with GST available upon request, GST #1254 88122. Publications Mail Agreement Number 1069624. Printed in the U.S.A.

Change of address: Allow 4 weeks, giving old and new addresses and 8-digit account number. Postmaster: Send change of address to AAAS, P.O. Box 96178, Washington, DC 20090-6178. Single-copy sales: \$10.00 current issue, \$15.00 back issue prepaid includes surface postage; bulk rates on request. Authorization to photocopy material for internal or personal use under circumstances not falling within the fair use provisions of the Copyright Act is granted by AAAS to libraries and other users registered with the Copyright Clearance Center (CCC) Transactional Reporting Service, provided that \$30.00 per article is paid directly to CCC, 222 Rosewood Drive, Danvers, MA 01923. The identification code for Science is 0036-8075. Science is indexed in the Reader's Guide to Periodical Literature and in several specialized indexes.

Genetic Mosaicism in Brain Development

With the increased power now available in sequencing and genomic technologies has come the realization that within an organism, individual cellular genomes can diverge from one another. **Poduri et al.** (p. 43) review how de novo mutations, which arise in the parental germ line, or during development of the child, are the cause of a variety of neurodevelopmental disorders.

Cool Accretion

Numerical models predict that in order to keep forming stars, galaxies should be continuously replenished with gas from the intergalactic medium. Using data from the Very Large Telescope in Chile, **Bouché et al.** (p. 50) report observations that are consistent with accretion of cold, chemically pristine gas onto a star-forming galaxy at a time when the cosmic star-formation activity was at its peak.

Distorted Nanoparticle

Nanoparticles have found many applications in modern technology; however, the full characterization of individual particles is challenging. One of the most interesting mechanical properties is the particle's response to lattice distortion.

This property has been probed for ensembles of nanoparticles, but the required averaging may distort the results. **Clark et al.** (p. 56, published online 23 May; see the Perspective by **Hartland and Lo**) were able to image the generation and subsequent evolution of coherent acoustic phonons from an individual perturbed gold nanocrystal on the picosecond time scale.

Quantum Handedness

When a rotating object is placed in circulating fluid, an imbalance of pressures on either side of it causes a deflecting force called the Magnus force. The quantum analog of this effect has been predicted to appear in the low-temperature A phase of ^3He , where the Cooper pairs forming the superfluid have a specific handedness. An impurity traveling through such a superfluid would experience a deflecting force in the

direction determined by the chirality of the pairs. **Ikegami et al.** (p. 59) trapped impurities beneath the free surface of ^3He , set them in motion, and demonstrated the existence of this deflecting force by measuring the differential transverse current. The sign of the deflection varied over different cooling runs, indicating that the system was choosing one or the other chirality upon entering the superfluid phase—a signature of spontaneous symmetry breaking.

A Nonclassical Conclusion

The concept of valence, which underlies the Periodic Table, originated in studies of reactivity rather than structure. Nonetheless, when studies in the mid-20th century suggested that the transient norbornyl cation ($\text{C}_7\text{H}_{11}^+$) reacted as though a carbon center had adopted a formally pentacoordinate motif, this nonclassical structural hypothesis engendered tremendous controversy. **Scholz et al.** (p. 62) have now succeeded in characterizing the norbornyl cation by x-ray crystallography and confirm the symmetrical fivefold motif.

Inheritance Guts

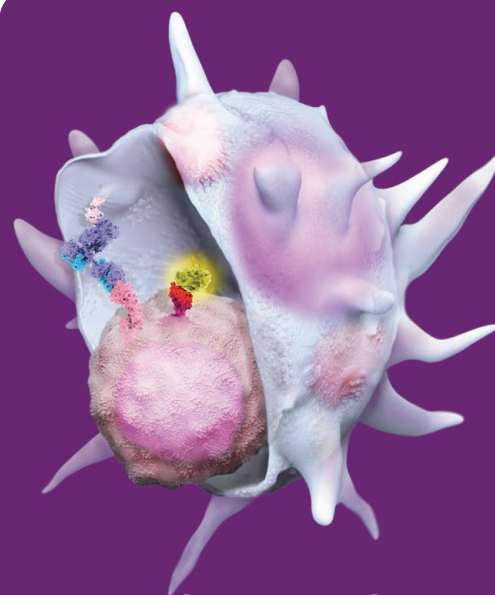
We know little about the stability of the constituent microbiota in the human gut or the extent to which the gut microbiota are a potential target for long-term health interventions. **Faith et al.** (p. 44) analyzed the fecal microbiota of 37 individuals and found that, on average, 60% of bacterial strains remained stable for up to 5 years and many were estimated to remain stable for decades.

Female Infertility

Anovulation, the failure of a woman's ovary to release an oocyte, is a major cause of female infertility. The mechanisms of ovulation have been studied extensively, with the hypothalamic-pituitary axis serving as a key player in its regulation. **Hasuwa et al.** (p. 71, published online 13 June) describe a mechanism by which anovulation can be caused by the disruption of two microRNAs that are expressed in the pituitary gland.

This Is the Place

Bats, bees, seals, and many seabirds practice central-place foraging, leaving a central home site, such as a hive or a rookery, to forage in a specific territory. Such species also share the



Immunotherapy Packs a One-Two Punch

Despite the immune system's best efforts, cancer always seems to be one step ahead. One example of this is that tumor cells express CD47 on their cell surface. CD47 acts as a "don't eat me" signal to phagocytic macrophages. A potential therapeutic strategy could thus be to block this signal. **Weiskopf et al.** (p. 88, published online 30 May; see the Perspective by **Kershaw and Smyth**) created variants of the CD47 receptor, SIRP α , that could act as high-affinity antagonists of CD47. Although the antagonists blocked CD47 effectively in tumor-bearing mice, on their own they did not induce macrophages to phagocytose the tumor cells. When paired with a variety of therapeutic antitumor antibodies, however, the CD47 antagonists were very effective in treating several mouse tumor models.

challenge of competing for local resources with individuals from separate colonies. Using satellite tags, **Wakefield et al.** (p. 68, published online 6 June; see the Perspective by **Weimerskirch**) followed over 180 northern gannets to determine potential drivers of foraging territory division. Boundaries among colonial territories arose as a result of competition with individuals from other territories. Individuals from the same colony appeared to share information about foraging sites, presumably contributing to the establishment and maintenance of specific, long-term colonial territories.

Additional summaries

Monitoring Land Use

Land-use decisions are based largely on agricultural market values. However, such decisions can lead to losses of ecosystem services, such as the provision of wildlife habitat or recreational space, the magnitude of which may overwhelm any market agricultural benefits. In a research project forming part of the UK National Ecosystem Assessment, **Bateman *et al.*** (p. 45) estimate the value of these net losses. Policies that recognize the diversity and complexity of the natural environment can target changes to different areas so as to radically improve land use in terms of agriculture and greenhouse gas emissions, recreation, and wild species habitat and diversity.

Mysterious Radio Bursts

It has been uncertain whether single, short, and bright bursts of radio emission that have been observed are celestial or terrestrial in origin. **Thornton *et al.*** (p. 53; see the Perspective by **Cordes**) report the detection of four nonrepeating radio transient events with millisecond duration in data from the 64-meter Parkes radio telescope in Australia. The properties of these radio bursts indicate that they had their origin outside our galaxy, but it is not possible to tell what caused them. Because the intergalactic medium affects the characteristics of the bursts, it will be possible to use them to study its properties.

Early Farmers?

What was the role of the eastern Fertile Crescent (which includes southeastern Turkey, northeastern Iraq, and western Iran) in the transition from foraging to farming? **Riehl *et al.*** (p. 65; see the Perspective by **Willcox**) investigated an archaeobotanical assemblage from Chogha Golan, in modern Iran over an apparently continuous occupation of the site over 2000 years, which captures the transition from foraging to farming. The rich archaeobotanical remains suggest

the use of a wide array of plant species, including the progenitors of key crop plants (wheat, barley, and large-seeded legumes). Residents of the eastern Fertile Crescent thus appear to have been involved in plant management and possibly in the domestication of wild crop plants.

RGM Proteins

Members of the repulsive guidance molecule (RGM) family of proteins can be secreted or reside on the surface of cells where they bind to the cell surface receptor, neogenin. The RGM proteins are named for their role in axon

guidance for developing neurons, but their function is also linked to a range of human diseases, including inflammation, multiple sclerosis, and cancer. **Bell *et al.*** (p. 77) solved the crystal structures of the external portions of the RGMB protein with

portions of neogenin. The structures revealed interactions of dimers of RGMB with neogenin in which ligand binding induced conformational changes that may initiate intracellular signaling from the receptor. RGM proteins contain a site of autocatalytic cleavage that affects secretion of the proteins, and some disease-associated mutations in RGM proteins were clustered at this site.

Form and Function

The contribution of disulfide bonding to oxidative protein folding and assembly, quality control, and stress responses in the endoplasmic reticulum (ER) are widely recognized. In contrast, catalysis of disulfide bond formation downstream of the ER is uncharted territory. QSOX, a Golgi-localized or

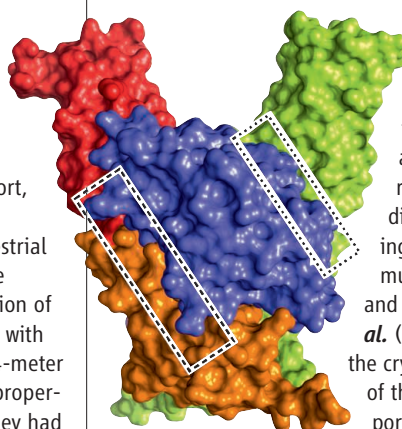
secreted disulfide catalyst, was identified in the 1970s and was more recently shown to be up-regulated in many cancers. However, the physiological importance of QSOX catalytic activity has been unclear. **Ilani *et al.*** (p. 74, published online 23 May) found that human QSOX1 is essential for incorporation of laminin into the extracellular matrix, with profound effects on the capability of the matrix to support integrin-mediated cell adhesion and migration.

Spliceosome Helicase

Introns are removed from eukaryotic pre-messenger RNA by the spliceosome. The spliceosome is assembled and disassembled during the course of each splicing reaction, and the RNA-protein remodeling involved is carried out by RNA helicases, whose activities must be closely regulated. **Mozaffari-Jovin *et al.*** (p. 80, published online 23 May) determined the crystal structure of the human Brr helicase in complex with the Jab1 domain of the Prp1 spliceosomal protein. The C-terminal tail of the Prp8 Jab1 domain inserts into the RNA-binding tunnel of Brr2, disrupting interaction of the RNA with the conserved helicase motifs inside tunnel. The temporal regulation of Brr2 RNA-binding and adenosine triphosphatase activity likely avoids premature disassembly of structures required during the splicing reaction.

Drug Targeting

Drug efficacy depends on the extent of binding to a cellular target (often a protein) with adverse effects caused by excessive target binding or by off-target binding. Engagement of a target protein inside cells is influenced by the effective drug concentration and by factors that regulate the protein conformation, making it difficult to predict efficacy based on in vitro affinity studies. **Martinez Molina *et al.*** (p. 84) took advantage of the shift in protein thermal stability caused by drug binding to directly monitor target protein-drug interactions in cells. The method was used to monitor drug target engagement in cancer cells and in mouse livers and kidneys.



Building Better Institutions

WHAT IS THE BEST WAY TO PROMOTE INNOVATIVE RESEARCH? HOW CAN WE BUILD RESEARCH institutions of the future that will promote cross-disciplinary interactions among young creative minds? Despite the recent growth in scientific knowledge, conventional discipline-based methods have not been sufficiently effective at developing new understanding and treatments. Researchers need to be encouraged to identify important questions and tackle them with multidisciplinary approaches. Contemporary biomedical research has to integrate biological, nonbiological, and clinical disciplines, and its application requires interactions with hospital and commercial partners. This can be facilitated by research institutions with an environment that supports strong interdisciplinary interactions between scientists: a place where laboratory biologists are encouraged to collaborate with clinical researchers to understand the medical implications of their work, with pharmaceutical companies for the translation of discoveries into treatments, and with physical scientists to expand their thinking and repertoire of experimental approaches. Such an institution must be continually open to new ideas and permeable to interactions with outside researchers and organizations.

Another imperative is to support early career scientists in setting up their own independent research programs. This initial period, when young investigators are often at their most creative, frequently sees them rein in their ambition and originality, given the pressures of securing grant funding and establishing a laboratory group. Too often this results in derivative research goals and aspirations driven by incremental objectives. New principal investigators need a supportive research environment, secure research funding, and time to make important discoveries.

New institutions have adopted different approaches to promote innovative and collaborative atmospheres, including the Janelia Farm Research Campus and more recently the Francis Crick Institute, opening in London in 2015. The Crick will be a large institute (120 groups) with a broad and diverse research agenda. Cross-disciplinary and clinical interactions will be forged with researchers from three university partners (University College London, Imperial College London, and King's College London) and the Wellcome Trust Sanger Institute, through the reciprocal interchange of small satellite groups of one to three researchers. And the institute will encourage exchanges and visits from other research institutions, including the for-profit sector and health care delivery organizations. Architecturally, the institute has been designed to resemble a chromosome, with the four arms meeting at a "centromere" that facilitates informal encounters and exchanges. The largely open-plan laboratories will juxtapose groups with different interests and encourage their mixing.

Rather than traditional departments, Crick investigators will self-organize into interest groups focused around research questions or technical approaches. Researchers will be free to join as many or as few of these as they wish, and the groups will come and go as science develops. Moreover, around two-thirds of the Crick's research group leaders will be in the initial phase of their independent careers, with a smaller number of more senior investigators to mentor younger colleagues and help identify the best new recruits. These appointments will be of up to 12 years, supported by the Crick's funding partners (the Medical Research Council, Cancer Research UK, and the Wellcome Trust). Group leaders will then leave the institute to establish a research group elsewhere; the aim is to give researchers who are effective and remain in the United Kingdom a transition package to support their moves, creating a thriving network of highly trained researchers.

Francis Crick commented that "by the time most scientists have reached age thirty they are trapped by their own expertise." It is fitting that Crick's eponymous institute aims to develop a culture that escapes this constraint.

— Paul Nurse, Richard Treisman, Jim Smith

10.1126/science.1242307

Paul Nurse is president of the Royal Society and director of the Francis Crick Institute, London, UK.

Richard Treisman is director of the Cancer Research UK London Research Institute and research director at the Francis Crick Institute, London, UK.

Jim Smith is director of the Medical Research Council–National Institute for Medical Research and research director at the Francis Crick Institute, London, UK.





ENVIRONMENTAL SCIENCE

Governance by the People

Real-world challenges in how to manage public resources have frequently been met by bottom-up collective action. One area in which researchers have yet to reach consensus is the relation of group size to collective action and resource outcomes. Yang *et al.* use data gathered over many years from the Wolong Nature Reserve in Sichuan Province, China. Within the reserve, the administrative bureau of the National Forest Conservation Program had assigned forest parcels to groups composed of 1 to 16 households. Each group decided on a strategy for monitoring illegal activity, such as logging, and the bureau conducted assessments of how much activity had occurred. Group size had a U-shaped relation to the monitoring efforts per household and on increasing forest cover. Intermediate group sizes of 8 or 9 households were optimal in balancing between two opposing factors: free-riding (the tendency to let others in the group do the work) and within-group enforcement. These findings, as well as the demonstration that stronger social relationships within the groups and with local leaders promoted collective action, suggest strategies for effective governance. — BJ

Proc. Natl. Acad. Sci. U.S.A. **110**, 10.1073/pnas.1301733110 (2013).

VIROLOGY

Location, Location, Location

The ability of HIV to reside in a latent form in T cells is a major hurdle to finding a cure. With no widely protective vaccine on the horizon, there is growing interest in understanding how to convert latent HIV into a replication active state, which would allow therapies that target infected cells to eliminate them. Mechanisms that contribute to HIV latency, however, are poorly understood. Using a combination of immuno-3D fluorescent in situ hybridization and chromatin immunoprecipitation, Lusic *et al.* find that location matters for latency. In T cell lines and in a model of primary T cells chronically infected with HIV, silenced but not active provirus was located close to nuclear bodies, as measured by their association with promyelocytic leukemia

protein (PML), a marker of these structures. The blockade or silencing of PML led to the activation of viral transcription. This was associated with a loss of binding to the methyltransferase G9a and a loss of epigenetic silencing marks from the proviral DNA. Actin-mediated movement away from nuclear bodies was required for transcriptional activation of the virus. Whether modulation of these pathways may be used therapeutically to reactivate and eradicate infected cells remains to be determined. — KLM

Cell Host Microbe **13**, 665 (2013).

EDUCATION

Interdisciplinary Check

Interdisciplinarity has been increasingly called for in U.S. science education, but it is not always

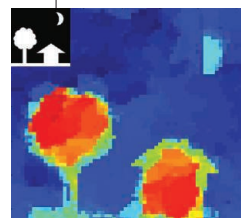
clear how to best integrate it into the curricula. Gouvea *et al.* considered the learning objectives of interdisciplinary science courses and created a framework intended to aid in redesigning tasks to better align with these learning objectives. They tested the framework in an introductory physics course that connected with both biology and chemistry. Tasks were divided into those with an imbalance in the interaction between the disciplines, those applying a reasoning strategy or technique from one discipline to another, and those bringing ideas from two separate disciplines together. Using a theoretical analysis of interaction between disciplines, the authors asked a series of questions about the degree to which each of the disciplines was represented in the tasks included in their curriculum, in addition to examining students' written performance on homework and exams and analyzing videos and transcripts of students' reasoning in group problem-solving settings. The results showed that the value of the framework lay not in its ability to characterize tasks in an interdisciplinary context, but rather in its being a tool that can help guide interdisciplinary task creation and revision. — MM

CBE Life Sci. Educ. **12**, 187 (2013).

APPLIED PHYSICS

Compressively Sensing Ghosts

The storing and processing of images can place large overheads on the hardware and software required to identify targets within each frame. Compressive sensing exploits the fact that much of an image is redundant, or sparse, in terms of the information it contains. Specially designed lenses and filters can sift through the large pile of data and automatically pick out the targets of interest, thereby reducing the computational overheads. Magaña-Loaiza *et al.* combined compressive sensing with ideas in ghost imaging, a technique in which the correlations between quantum-mechanically entangled

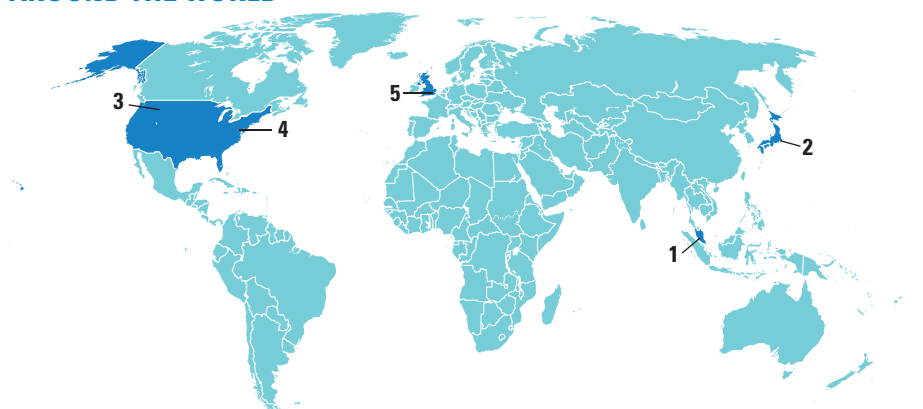


photons can be used to build up an image of an object with photons that have not interacted with the object directly. The authors demonstrate that such a combination of advanced imaging techniques can be used

to track a moving target, requiring many fewer measurements to do so, and describe how such a resource-efficient strategy is applicable to real-world applications of stealth imaging of moving targets. — ISO

Appl. Phys. Lett. **102**, 231104 (2013).

AROUND THE WORLD



Kuala Lumpur 1

WHO Calls for Starting HIV Treatment Earlier

The World Health Organization (WHO) has issued new treatment guidelines that promise to make antiretroviral drugs more accessible to more of the 34 million people in the world who are infected with HIV.

Antiretroviral drugs extend the lives of HIV-infected people and make them less infectious. But many poor- and middle-income countries can't afford to treat



Bigger tent. Guidelines make more patients eligible for drugs.

everyone, so they reserve the drugs for people who need them most. HIV targets and destroys CD4 white blood cells, and since 2010, WHO has recommended that resource-limited countries treat those with a CD4 count below 350 cells per microliter of blood (normal ranges between 600 to 1200).

WHO's new recommendations, presented on 30 June at an international AIDS conference here, change the eligibility to a CD4 count of 500. The guidelines further suggest that all children under 5, HIV-infected pregnant or breastfeeding women, and uninfected people in a relationship with

a known infected partner receive antiretroviral drugs, regardless of their CD4 count. The new guidelines would make an additional 9 million people eligible for the antiretroviral drugs, but it's unclear who will pay for the expansion.

Tokyo 2

Approval Nears for Trial With Induced Pluripotent Stem Cells

A Japan Ministry of Health, Labour and Welfare panel last week accepted a plan to carry out what would be the world's first clinical trials involving induced pluripotent stem (iPS) cells. The acceptance paves the way for an official green light from the ministry.

Researchers at the RIKEN Center for Developmental Biology in Kobe plan to generate replacement retinal pigment epithelial cells from iPS cells generated from patients suffering age-related macular degeneration. Safety concerns led the panel to delay a decision in late May, but RIKEN submitted additional data. If given approval, RIKEN could start recruiting patients sometime this year. <http://scim.ag/iPStrial>

Bozeman, Montana 3

***T. rex* Goes to Washington**

"It's kind of like seeing your beloved kid go off to college and into the real world."

Sheldon McKamey, executive director of the Museum of the Rockies (MOR) here, is talking about the nearly complete *Tyrannosaurus rex* fossil that is headed to the Smithsonian Institution's National Museum of Natural History, where it will anchor a new \$48 million dinosaur hall to open in 2019. The Wankel *T. rex*, named after the local rancher who discovered the bones in 1988, was displayed for 10 years in what

Greetings. Bronze *T. rex* cast to remain outside Montana museum.



McKamey calls "its death pose" before its owners, the U.S. Army Corps of Engineers, struck a deal with the Smithsonian for a 50-year loan. McKamey, who helped excavate the 85% complete fossil, says that MOR wanted its display to show visitors "how we find bones" rather than the dinosaur's more regal pose of stalking prey. The bronze cast outside the museum serves that purpose, she adds. MOR actually replaced the Wankel *T. rex* last year with an even rarer exhibit of a baby and young adult *Triceratops*.

Bethesda, Maryland 4

U.S. Cancer Institute to Target RAS Protein

The U.S. National Cancer Institute last week outlined a 5-year plan to find ways to block a mutated protein that drives growth in one-third of all cancers but was thought impossible to "drug" until now. The project will bring together the agency's contract lab in Frederick, Maryland, and outside researchers. NCI's Frederick National Laboratory for Cancer Research will serve as the "hub" for the \$10-million-a-year project, providing tools and services to "spokes" comprised of extramural research labs and companies.

NOTED

>The British Medical Association (BMA) decided last week that "**selective non-publication of unflattering trial data is research misconduct.**" The resolution, adopted at BMA's annual meeting, states that any one of its 152,000 members suspected of deliberately keeping data unpublished should have his or her fitness to practice assessed by the General Medical Council. The motion was prompted by AllTrials, a movement pushing for full publication of all clinical trial data.

RAS, for rat sarcoma, is a family of genes whose proteins transmit signals that allow cells to grow and survive. Scientists hope to determine structures of various forms of RAS, build on new strategies for blocking the protein, and map the surface of cells with RAS mutations. The project will be led by Frank McCormick, who is stepping down as director of the cancer center at University of California, San Francisco. <http://scim.ag/RASproject>

London 5

U.K. Wants to Allow Mitochondrial Replacement

The U.K. government is moving toward approving a new type of in vitro fertilization that could enable patients with mitochondrial diseases to avoid passing the condition to their children. The technique is controversial, because it involves introducing new DNA into a human embryo. But the Department of Health announced on 28 June that it would draw up draft guidelines to permit the procedure. The proposal would be released for public comment later this year, and Parliament could vote on a final version next year. The procedure is not ready for human trials.



Mitochondria, the cell's power generators, carry their own DNA, called mtDNA. Mutations in those genes cause mitochondrial diseases, and the diseases are passed from mother to child because the egg provides most of an embryo's mtDNA. The new technique transfers the nuclear DNA from the sperm and egg of the potential parents into a second egg from a donor with healthy mitochondria. <http://scim.ag/UKmito>

NEWSMAKERS

Stapel Agrees to Community Service

Diederik Stapel, the former Tilburg University professor who fabricated dozens of research studies, has reached a settlement with Dutch prosecutors to do 120 hours of community service. He also will forgo benefits from his former employer that would have been equivalent to 18 months' salary.

Stapel was a high-profile social psychologist whose career unraveled in 2011 when it was discovered that he had been fabricating data for more than a decade. Dutch prosecutors



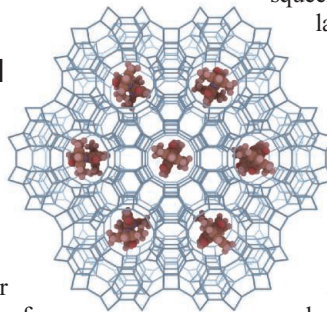
concluded that Stapel hadn't defrauded the taxpayer, however, because he had used the grants he received for research, even though he manufactured the data. Much of the money from the grants was spent on salaries, the prosecutors' statement says. Officials also took into consideration that Stapel had voluntarily returned his doctorate degree.

"I very much regret the mistakes I have made," Stapel tells *Science*. "I am happy for my colleagues as well as for my family that, with this settlement, a court case has been avoided." <http://scim.ag/StapelCommSer>

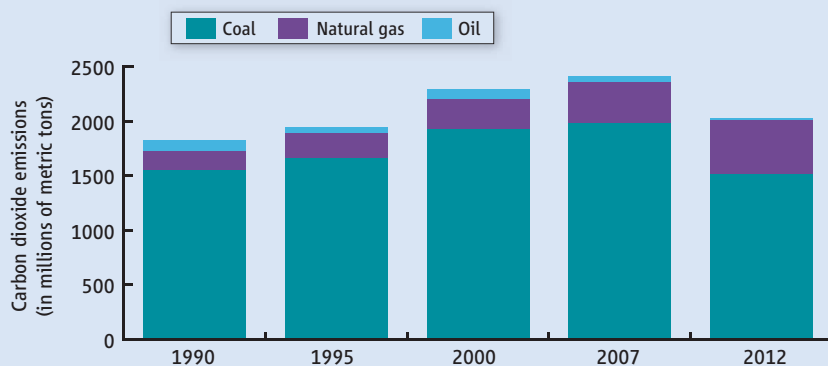
FINDINGS

Molecular Wires Show Strong Magnetic Potential

The capacity of computer hard drives has been skyrocketing for decades, thanks partly to improvements in the magnetic sensors used to read them. Published in *Science* this week, researchers led by Wilfred van der Wiel, a physicist at the University of Twente in the Netherlands, describe a new room-temperature magnetic sensor three times as sensitive as the previous champ.



The new material is made of dye molecules called DXP. Normally DXP is nonmagnetic. But when the researchers squeezed it into the pores of latticelike minerals called zeolites, DXP formed molecular wires in which a quantum effect called Pauli exclusion came into play. As a result, any electrons moving through the wire stopped in their tracks when the wire encountered a magnetic field. That electron-blocking property, called magnetoresistance, is the key to reading magnetic bits. >>



On the Way to Cleaner Power

The big news in President Barack Obama's climate change speech last week at Georgetown University in Washington, D.C., was his promise that the Environmental Protection Agency would draw up regulations next year for limiting carbon emissions from existing power plants. The country is already headed down that road: Last year, the country's total emissions from generating electricity dropped to their lowest level in 2 decades, thanks in large part to the switch from burning coal to natural gas. The global recession also helped in that regard: Emissions have dropped 24% since peaking in 2007.

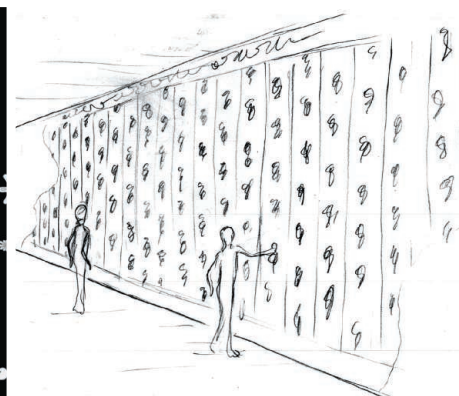
CREDITS (TOP TO BOTTOM): TILBURG UNIVERSITY; W. G. VAN DER WIEL ET AL.; COURTESY: RWJMS; IVE LABORATORY/WIKIMEDIA COMMONS; (SOURCE) U.S. ENERGY INFORMATION ADMINISTRATION

Random Sample

Wallpaper as Art and Science

The studio of Pittsburgh artist Natalie Settles is located in the lab of evolutionary geneticist Stephen Tonsor at the University of Pittsburgh in Pennsylvania. Her art—painting Victorian era wallpaper—has also taken an unusual turn since she and Tonsor received \$35,000 last year from the Heinz Endowments and Pittsburgh Foundation. The grant is spawning an interactive exhibit with a computer program that carries out digital evolution experiments.

Settles has modified her wallpaper approach to include motifs that, like organisms, evolve by changing in space and over time. The motifs have 80 genes that build upon simple geometric designs to create thousands of unique designs. If a viewer touches a motif, that motif's "fitness" will increase; when it comes time to reproduce, the fitter motifs will



generate more offspring. Over time, the wallpaper will take on ever more inviting motifs. In addition, Tonsor hopes that other researchers will use the program to explore additional parameters of evolution.

Settles discussed the project last week at Evolution 2013 in Snowbird, Utah, and art museum directors and potential funders will get a glimpse of it this fall. Tonsor and Settles hope to have the work on display by early 2014.

>>FINDINGS

The wires are still too small to be used in computers. But the scientists say that they may be useful for touch screens and novel magnetic sensing devices.

Monarchs Medicate Their Young

For the monarch butterfly, milkweeds are a multipurpose plant. When ingested, their toxins not only make the insect unpalatable to birds and other predators, but they also fight infection, says Jacobus de Roode, an evolutionary biologist from



Overloaded.
An overly infected monarch can't emerge from its cocoon.

Emory University in Atlanta.

De Roode discovered that different milkweed species reduce protozoan growth in caterpillars to varying degrees in proportion to the amount of toxin they produce. Caterpillars don't seem to know this, but the adults do, De Roode reported last week at Evolution 2013 in Snowbird, Utah. By a 2-to-1 margin, infected adult butterflies choose to lay eggs on the milkweed that will most retard protozoan growth, thus medicating their young. "Just the idea that they are selecting plants to fight the parasites of their offspring is really cool," says evolutionary biologist Curtis Lively of Indiana University, Bloomington.

Map Offers Millennium Of Earthquake Records

Researchers meeting last week in Pavia, Italy, were presented with a new worldwide seismic database based on tens of thousands of earthquake records stretching back more than 1000 years. The Global Earthquake Model (GEM) Foundation, which supported the research largely with contributions from insurance companies, says that the database is part of a push to make the long-fragmented field of earthquake forecasting more open and systematic.

"Everyone knew we needed to do this," says GEM's co-founder, Ross Stein, a seismologist with the U.S. Geological Survey. "No one was willing to put the money up.

BY THE NUMBERS

32% Fraction of global biodiversity in the 40 countries with the greatest shortfall in conservation funding, according to an analysis in the *Proceedings of the National Academy of Sciences* online this week that estimates the world spent about \$21.5 billion a year on global biodiversity last decade.

\$977 billion The economic burden of childhood lead exposure in low- and middle-income countries. The toll represents 4% of the gross domestic product for African countries and nearly 2% for Asian nations, according to a paper by New York University researchers in *Environmental Health Perspectives*.

GEM did." Other GEM projects include a global map of tectonic strain and socioeconomic studies aimed at estimating potential casualties and damage from future quakes.

While geoscientists welcomed the effort, some cautioned that no amount of data can overcome the deep uncertainties inherent in Earth faulting processes. <http://scim.ag/GEMseismic>



Greener pastures.
All but 50 of NIH's 360 research chimpanzees will be retired in the next few years.

BIOMEDICAL RESEARCH

NIH to Phase Out Most Chimp Research

Marking what he described as a new era in biomedical research, National Institutes of Health (NIH) Director Francis Collins announced last week that his agency plans to retire most of the 360 chimpanzees that it has available for research and phase out half of the studies that it supports on “our closest relatives.” Few, if any, invasive experiments will remain, effectively ending a half-century of such U.S.-sponsored biomedical research on chimpanzees. Eight noninvasive behavioral and genomics studies can continue, NIH said, but only if they meet strict new criteria for animal living conditions.

Collins described the decision, which follows more than 2 years of public and internal discussion, as “a major milestone.” Chimpanzees share 98% of our DNA, he said, and “they deserve special respect.” Recent scientific advances have obviated the need to use chimpanzees in most research, and reducing their use is “scientifically sound and the right thing to do.”

As intense as the debate has been, the potential community of researchers affected by NIH's decision has continued to decline. For various reasons, the number of NIH-funded chimpanzee projects has been dwindling, from 53 in 2011 to 30 last year, some of which have since expired.

NIH has declined to make public which ongoing chimp studies will be shut down, but one field where some think chimps still have a place is hepatitis C vaccine research. Michael Houghton of the University of Alberta in Edmonton, Canada, a co-discoverer of hepa-

titis C virus, does not use chimpanzees, but he believes that clinical trials of candidate vaccines are less likely to succeed “in the absence of chimpanzee data.”

Yet, that opinion isn't universal even in that small arena. Hepatitis C vaccine researcher Paul Klenerman of the University of Oxford in the United Kingdom suggests that animal studies have already provided sufficient “proof of concept” for several vaccine candidates, and “the really important issue now is to do the best possible human studies.”

NIH's formal involvement with chimp research began in 1960 when Congress established a network of NIH-funded primate research centers. The animals were pivotal for developing a hepatitis B vaccine and were also used to study malaria, respiratory syncytial virus, and immunology. In 1986, after the AIDS epidemic hit, NIH began breeding chimpanzees to ensure a supply to study HIV. But it turned out that the virus doesn't usually cause disease in chimps, and rhesus macaques were a better model. With little demand for the chimps, in 1995 NIH imposed a moratorium on breeding that was extended several times (*Science*, 26 January 2007, p. 450).

Few other countries ever allowed biomedical research on chimpanzees, and they had all banned the practice by 2007. In 2009, the Humane Society of the United States ramped up its campaign to stop invasive research on great apes, leading Congress to propose a bill to that effect. In 2010, under pressure from lawmakers, NIH asked the Institute of Medicine (IOM) to review the

need for chimpanzees in research.

The IOM report, issued in December 2011 by a panel of bioethicists and scientists, found that most research on chimps is unnecessary. It laid out three criteria for determining which projects should continue: The work must advance public health; it cannot be done in humans or another animal model; and the chimpanzees must be kept in an ethologically appropriate environment. Collins immediately accepted the guidelines in principle, putting a hold on new chimpanzee research grants and asking a working group of his Council of Councils to advise him on how to specifically carry out IOM's recommendations.

In January, the working group concluded that many of NIH's 30 ongoing projects involving chimpanzee research or care should end. That includes six of nine invasive biomedical research projects, leaving only three studies that the working group said involve immunology and infectious agents such as hepatitis C. These, along with eight comparative genomics and behavioral projects that got the nod, can continue only if the chimpanzees are kept in appropriate conditions, such as in groups of at least seven animals, in large outdoor spaces, and with room to climb.

The agency received more than 12,500 comments on the working group's 28 recommendations. NIH plans to follow nearly all of them except the stipulation that the animals have at least 93 m² of primary living space per chimpanzee. (Current guidelines require a minimum cage size of about 2 m².) “There's not enough data” supporting that recommendation, which could be costly, Collins said. NIH plans to continue reviewing the scientific evidence for how much space chimpanzees need. Meanwhile, NIH is working with Congress to lift a \$30 million spending cap imposed in 2000 on the National Chimpanzee Sanctuary; the agency will reach that limit in the next few months.

NIH officials said last week that 310 of its 360 research chimpanzees, which are now in three locations, will move to the national sanctuary at Chimp Haven, in Keithville, Louisiana, or other sanctuaries over the next few years. (About 100 retired animals have recently moved or are slated to be transferred later this year from New Iberia Research Center in Louisiana.)

NIH will likely support a single colony of 50 animals for future research, officials said. In accordance with the working group's recommendation, NIH will not breed the animals but will revisit that policy in 5 years.

NIH has begun notifying principal inves-

tigators about how their projects will be affected. Projects that don't meet the IOM criteria will "wind down in a way that preserves the research," Collins said. Approved projects could be renewed if, after peer review, a new subcommittee of the NIH Council of Councils decides that they comply with the IOM recommendations.

NIH's decision does not affect privately funded research involving 300 or so chimpanzees, but any U.S. researcher wishing to study the animals will also likely soon need a permit because of a new rule the U.S. Fish and Wildlife Service proposed on 11 June that would change the status of captive chimpanzees from "threatened" to "endangered." NIH officials said they think that this will still allow for biomedical research.

The eight comparative genomics and behavioral projects approved by the working group involve 290 animals (many not owned

by NIH). Lisa Newbern, a spokesperson for the Yerkes National Primate Research Center in Atlanta, says that her center has not yet learned how its five NIH-funded behavioral research projects, some set to end in 2016 and two recently expired, will be affected. Although her center is worried that the new housing standards could cost tens of millions of dollars, NIH's decision to hold off on the 93 m² requirement "eases one of our concerns."

At least two of the three approved biomedical projects, which use 12 animals, are thought to involve research on developing vaccines for hepatitis C, which kills 350,000 people a year worldwide. Opinions vary on whether chimpanzees are essential to this work. The IOM panel, for instance, was unable to reach consensus on whether hepatitis C vaccine studies should continue. At any rate, scientists familiar with this area tell *Science* that such chimpanzee work seems to be ending anyway.

One academic researcher says that his group has completed its work with chimpanzees since the IOM report came out, but analysis of archived samples will continue. NIH intramural research on a hepatitis C vaccine that used chimpanzees has been phased out, in part because one researcher retired.

NIH has made its decision, but public debate is likely to continue. The Texas Biomedical Research Institute, which now uses about 115 chimpanzees owned or supported by NIH, decried NIH's decision. In a statement, the institute said it is "disappointed in most of [NIH's] responses." The institute calls the 50-animal colony an "arbitrarily chosen number" that will limit the pace of research on hepatitis, immunotherapies, and diseases affecting chimpanzees in the wild. But the Humane Society of the United States is delighted, calling the decision a "historic moment."

—JOCELYN KAISER

RUSSIA

New Law Would Dilute and Diminish Science Academy

MOSCOW—When some of the biggest names in Russia's scientific community elected Vladimir Fortov to lead the Russian Academy of Sciences (RAS) this spring, they had great expectations that the physicist would infuse the august institution with fresh blood and undertake long overdue reforms. Now it seems that Fortov may not get that chance. At a press conference here last week, Russia's science minister, Dmitry Livanov, who for months has derided RAS as ineffective, unveiled a draft law that would merge it with two other science academies, strip it of control of its extensive real estate holdings, and abolish any distinction between full-fledged academicians and scientists of a lower rank, called corresponding members.

The radical transformation of the 289-year-old RAS is on hold for the moment however. The science ministry had initially asked Russia's lower house of parliament to fast-track debate on the law, but later agreed to have the Duma take a final vote on the matter after its summer break. To the chagrin of scientists who may have hoped to see the law derailed, it has backing from the country's top leaders. Speaking to RIA Novosti news agency last week, Russian Prime Minister Dmitry Medvedev explained that the law is meant to help scientists concentrate. "It's important to allow the scholars to focus on science and research and spare them the irrelevant function of managing real estate," he said.



Merge and acquire. Science minister Dmitry Livanov has not hidden his low regard for RAS.

Many scientists are now too blinded by rage over the draft law to focus on their work. The legislation is a "national tragedy," fumes Alexandr Spirin, an academician and former director of the Institute of Protein Research in Pushchino. "The academy will lose the independence it has enjoyed since the time of Peter the Great," the czar who created RAS in 1724, he says.

Under the draft law, RAS would merge with two more-specialized bodies, the Russian Academy of Agricultural Sciences and the Russian Academy of Medical Sciences. The law would also establish an Agency for RAS Scientific Institutions that will manage the academy's real estate holdings and property, leasing of which has often brought it much-needed funds. And it would pro-

mote all corresponding members to full academicians—"eliminating the scientific elite," Spirin says—and impose a 3-year moratorium on election of new academicians.

The law would increase the stipend paid to academy members significantly, but that hasn't mollified some researchers who bristle at the way that the law was drawn up. "They didn't even consult with us," says physicist Alexei Khokhlov, vice-rector of Lomonosov Moscow State University and head of the science ministry's Council on Science. Such stealth and unveiling of the law by press conference are "disgusting," says Mikhail Gelfand, a bioinformatics professor and a member of the Ministry of Education and Science's Public Council. "Many rights were declared for researchers, but in reality everything was decided without their consent."

Fortov told *Science* that the draft law must be postponed and discussed by the scientific community, but declined further comment. Livanov could not be reached for comment before *Science* went to press. Rumors are rampant about the motives that may be driving a law that many scientists feel would neuter the academy. The stark bottom line, says Mikhail Ugryumov, an academician at the Koltzov Institute of Developmental Biology here, may be apathy of Russia's leadership toward science. "It just looks like science is not among the priorities in Russia," he says.

—VLADIMIR POKROVSKY

Vladimir Pokrovsky is a writer in Moscow.

ENERGY RESEARCH

Budget Malaise May Hit DOE's One Big Growth Area

It's been a lean decade for the Department of Energy's (DOE's) Office of Science, the largest funder of the physical sciences in the United States. But through it all, one DOE research program has prospered. The Basic Energy Sciences (BES) program, which funds the bread-and-butter research with the closest ties to energy and which runs DOE's big user facilities, has seen its budget nearly triple in the past 15 years. Last week, however, a spending panel of the U.S. House of Representatives signaled that such growth may be over. Legislators voted to clip the BES program's budget for next year and warned that new projects must fit into a flat budget scenario.

The budget process for 2014 has a long way to run. But in years past, the House has generally been supportive of BES. So this year's spending bill has scientists wondering whether the program will be able to continue building the facilities needed to keep the United States on top in broad swathes of research.

"If you're looking at a billion-dollar project, that's pretty tough to do with a flat budget," says James Decker, a consultant in Washington, D.C., who served as principal deputy director of the Office of Science from 1985 to 2006. John Hemminger, a chemical physicist at the University of California, Irvine, and chair of DOE's Basic Energy Science's Advisory Committee (BESAC), notes that BES already faces stiff competition from abroad. "Given what's already been started in Europe and Asia, the number of high-quality facilities outside the United States is going to be larger than the number inside," he says. "That's already happening."

BES funds research in condensed matter physics, chemistry, materials science, and related fields. It also runs DOE's x-ray synchrotrons, neutron sources, and other user facilities that serve tens of thousands of researchers in fields such as structural biology. Within the science office, BES' budget has grown to dwarf those for programs in high-energy physics, nuclear physics, fusion, biological and environmental research, and

advanced scientific computing (see chart).

BES is also machine-builder to the broader science community. It has built a string of major facilities, including the \$812 million Advanced Photon Source at Argonne National Laboratory in Illinois, completed in 1996; the \$1.4 billion Spallation Neutron Source (SNS) at Oak Ridge National Laboratory in Tennessee, finished in 2006; the \$420 million Linac Coherent Light Source at SLAC National Accelerator Laboratory in Menlo Park, California, finished in 2009; and the \$912 million National Synchrotron Light Source II (NSLS-II) at Brookhaven National Laboratory in Upton, New York, which should be completed this year. The last comparable machine built by another DOE pro-

double the capacity of the SNS.

Sequestration would make a flat budget more challenging. BES has built facilities in series, applying money "saved" as construction on one project winds down to begin work on the next one. Lab directors call that tranche of money roll-off, and this time the roll-off from NSLS-II has been consumed by sequestration, says Thom Mason, director of Oak Ridge. "When you've cashed in all the roll-off, then when you try to build the next thing, there's no established funding stream to tap into," he says.

Thanks to sequestration, BES' existing facilities are already running on reduced schedules. But researchers say that BES must continue to build better ones to main-

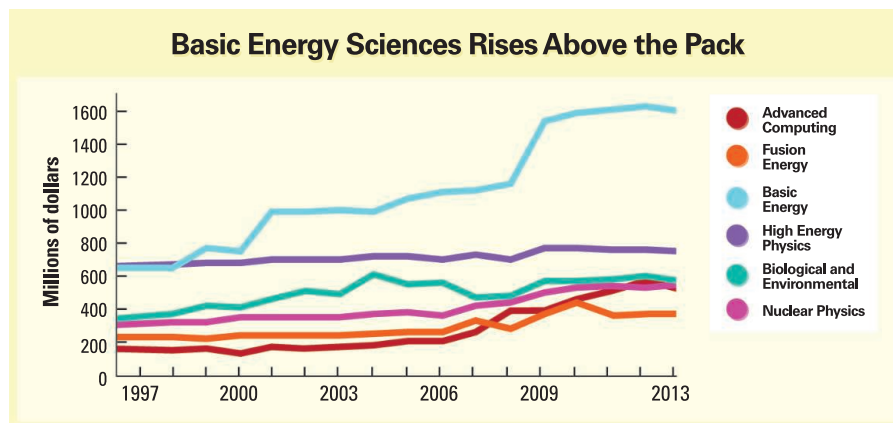
tain U.S. leadership. Hemminger fears that under a flat budget, DOE will try to obtain money for construction by squeezing research grants, which make up roughly half of the BES budget. William Madia, vice president for SLAC at Stanford University in Palo Alto, California, which manages the lab, suspects that BES officials may have to sacrifice one or more of the 16 existing user facilities. "My read-

ing is that [the House budget] is a signal," he says. "Show us what you're *not* going to do. Show us your hard choices."

Congress is not close to resolving DOE's budget for next year, much less deciding how much to allocate across the entire federal government. Last week, the Senate counterpart to the House panel approved the full \$5.153 billion that the Obama administration requested for the Office of Science and all but \$57 million of the president's \$1.862 billion request for BES. That boost was possible because the Senate, controlled by Democrats, has given itself \$92 billion more to spend than the House, which is controlled by Republicans.

It's too early to say whose vision for BES will prevail, Decker says. But Madia suspects that the final numbers may be closer to those adopted by the House and that lean times have arrived: "I think they're there."

—ADRIAN CHO



Dominant. The growing popularity of user facilities in fields such as materials science and structural biology has driven expansion of Basic Energy Sciences' budget, now twice as large as any other DOE science program.

gram was nuclear physics' \$1.1 billion Relativistic Heavy Ion Collider at Brookhaven, which turned on in 1999.

But BES' major projects were built in a time of growth. The House bill would slam that to a halt, shrinking BES' budget next year by 1%, to \$1.583 billion, while giving the Office of Science a 0.2% haircut, to \$4.653 billion. The cuts would come on the heels of sequestration, the automatic budget cuts that kicked in on 1 March as required by the 2011 deficit-reduction agreement between the White House and Congress.

The House bill asks DOE to figure out how it would build a proposed x-ray laser facility without more money. That request refers to the billion-dollar Next Generation Light Source proposed for Lawrence Berkeley National Laboratory in California. The implied spending cap would presumably also apply to a planned \$1 billion "end station" to

GEOLOGY

China's Exquisite Look at Earth's Rocky Husk Wins Raves

CHENGDU, CHINA—Dong Shuwen likens his homeland's ambitions to study deep Earth to exploring deep space or the deep sea. For geologists, "it's the final frontier," says Dong, a vice president of the Chinese Academy of Geological Sciences (CAGS) in Beijing. And much as exploring the depths of space and oceans is expensive, peering beneath Earth's skin will require deep pockets. China's Cabinet is now weighing plans for a 15-year, \$6.5 billion effort to peel away the secrets of our planet's crust and uppermost mantle, together known as the lithosphere.

As a prelude to the megaproject, Dong and colleagues, at a joint meeting of the Geological Society of China and Geological Society of America here last month, unveiled early findings from SinoProbe, a \$200 million effort that Dong leads. In the 5-year program, which is just now wrapping up, Chinese scientists have imaged the lithosphere by exploding dynamite and recording seismic waves from the detonations reflected back to the surface.

The campaign hasn't failed to impress. "It's a remarkable achievement," says Suzanne Mahlburg Kay of Cornell University, the president of the Geological Society of America. SinoProbe, she says, "has significantly advanced our understanding of many aspects of the lithosphere." At the same time, some scientists worry that SinoProbe's coupling to mineral exploration may impede access to project data.

SinoProbe echoes the pioneering U.S. EarthScope program (*Science*, 14 June, p. 1283). But whereas EarthScope uses broadband seismometers to detect earthquake-generated seismic waves and thus probe our planet's interior, from crust to core, SinoProbe heavily relies on explosive charges and images only the lithosphere, at high resolution.

SinoProbe has a much more applied bent as well. In 2006, driven by a hunger for resources and the need to better understand earthquakes, China's Cabinet backed SinoProbe as an exploration program with an eye on future mineral extraction. "The use of mineral resources [in China] has been increasing exponentially in the past few decades," Dong says. "Known domestic reserves are running out fast, and we are increasingly dependent on imports." To date, mineral excavation in China is mostly limited to reserves within 500 meters of the surface; in other countries, mines go as deep as 5 kilometers. "There is

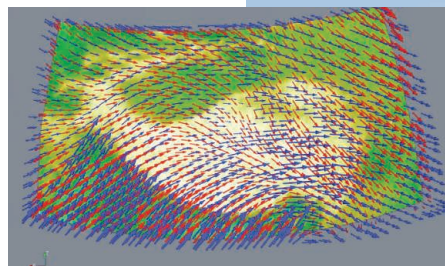
an untapped wealth down there waiting to be explored," Dong says.

Since SinoProbe kicked off, Chinese geoscientists have set off dynamite along nearly 6000 kilometers of transects across the country. With resolutions of up to 250 meters, their images are much sharper than those gleaned from similar campaigns in North America in the 1980s. "The quality of the reflection data is outstanding," says G. Randy Keller, a geologist at the University of Oklahoma in Norman. SinoProbe has profited from advances in seismometer sensitivity and computational power. "It's like having a better telescope," says An Yin, a geologist at the University of California, Los Angeles (UCLA). "Things that looked fuzzy before come into sharp focus. Then we realize they might not be what we thought they are."

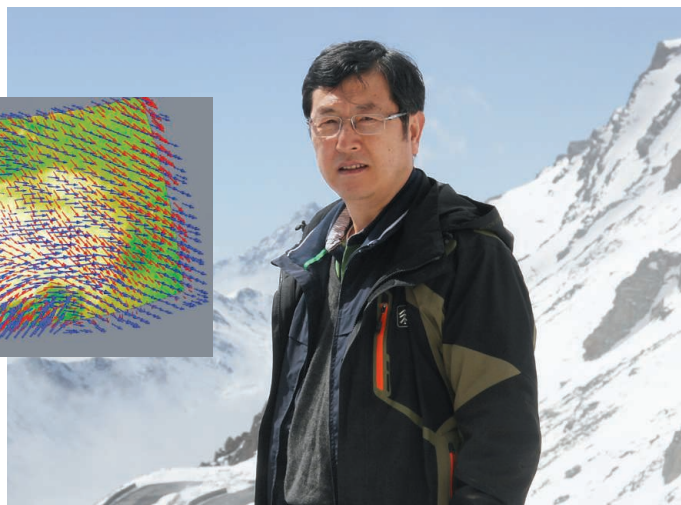
For instance, many researchers have long believed that the lower crust under Tibet is weak and soft, like a block of butter taken out of the refrigerator, because of the weight of the high plateau above. Some softened crust, propo-

middle crust. The "intriguing" results "challenge the channel flow theory," says Eric Kirby, a geologist at Pennsylvania State University, University Park. Others caution that reflection seismology requires a lot of interpretation. "There is a danger that comes with having a tool that only sees a small part of what's out there," says Mark Harrison, a geologist at UCLA.

SinoProbe has already pinpointed new reserves of rare earth metals, nickel, chromite, and tungsten, Dong says. The commercial potential of such discoveries has outsiders worrying about SinoProbe's openness. For now, its data are available only to scientists directly involved in the program and their collaborators. "It's very difficult to cross check or verify the results," says Jérôme van der Woerd, a geologist at the Institut de Physique du Globe in Strasbourg, France. Openness, he argues, "is the only way to make the most out of the project." In another 2 years or so, Dong says, some data will be available



Under the hood. Dong Shuwen's SinoProbe has shed light on mantle flow in Tibet (inset).



nents say, flows west to east, where it encounters the rigid Sichuan Basin. In a phenomenon that has puzzled geologists for decades, the flow creates the elevation of Eastern Tibet without deforming the surface very much. Tibet "is the Rosetta stone for what happens when continents collide," says Cornell geologist Larry Brown.

The seismic reflection data tell a different tale, says Gao Rui, a geologist at CAGS' Institute of Geology in Beijing. If the channel flow model were correct, the boundary between the lower crust and the mantle should be smooth. Instead, SinoProbe revealed faults along the boundary, some extending to the

to scientists worldwide and other data will be shared according to bilateral agreements.

In the meantime, Dong and others are making a play for a far grander project: SinoProbe phase II. They have proposed 20,000 kilometers of seismic reflection transects that will feature 3D imaging of the lithosphere, as well as magnetotelluric studies of subsurface conductivity and geochemical surveys. If Cabinet support for phase II comes through—no one knows when the decision will come—"the sky's the limit" for Chinese geologists, Dong says.

—JANE QIU

Jane Qiu is a writer in Beijing.

SCIENCE FUNDING

At Long Last, Europe's Mega R&D Program Comes Into Focus

BRUSSELS—European scientists breathed a sigh of relief last week when leaders of the European Union (E.U.) agreed on a budget and rules for the next continent-wide R&D program, Horizon 2020. A full 19 months after the European Commission unveiled its proposal (*Science*, 9 December 2011, p. 1331), the twin deals should enable the timely rollout of the program, slated to get €70.2 billion from 2014 to 2020. This would be a 23.4% boost compared to the previous incarnation, Framework Programme 7 (FP7), which began in 2007 and ends this year.

In the bigger picture, science fared well: Overall spending will decline 3.4% from the current period, with areas such as agriculture and regional development absorbing heavy hits. Still, research organizations had lobbied hard for an even heftier increase for Horizon 2020, arguing that Europe needs much bigger doses of research and innovation to cure its economic malaise (*Science*, 16 November 2012, p. 872). And in the short-term, scientists from the Cliffs of Mohar to the Carpathian Mountains will feel some pain: FP7 spending peaked this year at nearly €11 billion, while Horizon 2020 next year will spend roughly €8.8 billion as it ramps up to full-speed (see graph).

“Money’s a bit tight, but that’s a sign of the times,” says Chris Hull, former secretary-general of the European Association of Research and Technology Organizations. This budget remains significant enough, he says, to help steer R&D across the continent.

The long and winding path for Horizon 2020 started with the commission’s proposed €80 million budget, wound through the European Parliament, where some members tried to inflate the program to €100 billion, and was downsized by the E.U.’s cost-conscious 27 member states, which have to sign off on the budget details. Last week, lead negotiators reached two agreements: one on the E.U.’s budget caps for 2014–20, including research spending, and one on Horizon 2020’s structure and content. Parliament and

the member states are expected to formally accept both deals in the coming months.

The program will consist of three main parts, or pillars. The first, “excellent science,” will fund basic research and receive about 32% of Horizon 2020’s budget. This includes a beefed-up European Research Council (ERC), which will snare 17% of the budget, about €12 billion, for its elite research grants, up from 15% (€7.5 billion) in FP7.

The second pillar is a 22% share of the budget to boost European industry; one mechanism will be public-private partnerships in areas such as pharmaceuticals and aeronautics. The third component will fund R&D in seven “societal challenges,” includ-

societal impact of their work when applying for Horizon 2020 funding.

The commission and its agencies are now fine-tuning implementation plans. Last week’s agreements are “not the end of the process,” says Amanda Crowfoot, director of Science Europe, an association of European funding agencies. One danger for Horizon 2020, she says, is the possibility of a flood of applications next year. The program is eagerly anticipated, even more so now that national science budgets have tightened in many E.U. member states. “Researchers will try harder to get money from Horizon 2020” than they did from past programs, says Marja Makarow, vice-president for research at the Academy of Finland and former head of the European Science Foundation. “We already have pressure from our ministry, saying that researchers have to go for E.U. funding.”

The commission welcomes an onslaught of funding applications, a spokesman says.

“A higher number of applications would mean that the program is attractive,” he says, adding that heavier competition will raise the bar on research quality. But E.U. funding is only a small percentage of the total money spent on R&D in Europe, and cannot make up for national budget cuts, the spokesman adds.

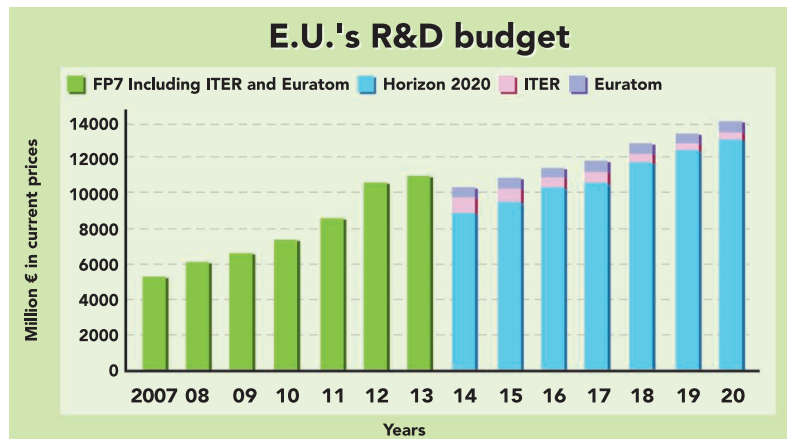
The dip in Europe’s 2014 R&D budget will also make competition keener. ERC President Helga Nowotny says that her agency will issue fewer calls for proposals next

year. And youth will be served first. ERC will delay a call for grants for established researchers until the end of the year, giving priority to grants for young scientists, Nowotny says.

The deals don’t mean that scientists should sit back and wait for money to start flowing. “It’s important that the research community is involved in the discussion ... to influence and shape the programs” as the commission works out how to translate the “societal challenges” into concrete grant calls that scientists can respond to, Crowfoot says. So far, adds Nowotny, “everything was focused on getting the structure right. Now comes the hard part: How are we going to implement it?”

—TANIA RABESANDRATANA AND
GRETCHEN VOGEL

Tania Rabesandratana is a writer in Brussels.



What goes down must come up. It won’t be until 2016 that planned Horizon 2020 funding (blue) exceeds FP7’s (green) peak in 2013.

ing climate change and food security. Aside from the three pillars, the young (and controversial) European Institute of Innovation and Technology will see its budget shoot up to €2.5 billion, from €309 million in 2008–13 (*Science*, 26 August 2011, p. 1090).

The European Commission casts Horizon 2020 as a break with the past, in that it will emphasize innovation and a “market-driven approach.” The commission seems to have hit upon a reasonable formula, Hull says. “Money is not infinite. You need a balance between long-term, speculative research that seeks to roll back the frontiers of knowledge, [and] research where there’s a short-term demand or potential to produce stuff that will have an impact on Alzheimer’s or climate change,” he says. Hull hopes that researchers will be increasingly required to demonstrate the relevance and



Into the Minds of Birds

A new brain-scanning method offers a window into the brains of birds, which have emerged as the surprising stars of many animal cognition studies

BIRD 7, AN AMERICAN CROW BLACK OF feather, beak, and eye, stood unmoving behind the bars of the cage, his right eye fixed on me. Outside the bars, with a mask covering my face, I sat unmoving, looking back at him. In my outstretched hands lay the corpse of a dead crow. For a full minute, Bird 7 stared at me and the cadaver. In the wild with his fellows, he likely would have also cawed, scolded, and mobbed me, perceiving me as a threat because of my association with a dead crow. As a lone captive, he merely studied my masked face. “Focus on one of his eyes and count the number of times he blinks,” John Marzluff, the wildlife biologist behind this experiment at the University of Washington, Seattle, had instructed me. Blinks are a simple measure of a bird’s nervousness, and in that minute, I counted 29. Relaxed birds average 36 blinks per minute, a statistically significant difference. Looking at me made Bird 7 nervous.

When the minute was up, Marzluff and graduate student Kaeli Swift moved in. They slipped a hood over the crow’s head while an anesthesiologist stepped forward to sedate him. Marzluff then gently strapped Bird 7 onto the examining tray of a positron emission tomography (PET) scanner. For the next 15 minutes, a radiologist captured images of the crow’s brain—specifically, those areas that had been activated when Bird 7 stared at me. Before the test, the scientists had injected the crow with a radioactive tracer

that metabolizes so slowly that it would highlight the brain’s synaptic activity in the past 15 minutes. Thus, the scan would reveal what scientists had seldom witnessed: the brain of a wild bird in the act of thinking about—or processing—a real-life, threatening event.

“We’re seeing that the crows’ brains are cognitively flexible,” Marzluff explained later as we looked at Bird 7’s scan and those of 23 other crows, all wild-caught. Different types of threats—a predator like a red-tailed hawk, or my masked

face—elicit the same staring behavior but involve different kinds of processing in the brain, Marzluff, lead author Donna J. Cross, and colleagues report

in this week’s issue of the *Proceedings of the Royal Society B*. When looking at me holding a dead crow—but not when looking at a hawk—Bird 7 activated its hippocampus and cerebellum, regions involved in learning and memory. “Even though their outward reaction appears to be the same, their mental processing of these threats is very different,” Marzluff said. “The crow wasn’t just responding to a danger when he was watching you. He was learning the features of your masked face. That’s why we think his hippocampus was activated.”

While Marzluff emphasizes that the PET scanning is a “first try” at glimpsing bird

Danger! Danger! American crows chase a bald eagle, which is an innate behavior.

brains in the act of working, it is already being hailed as a powerful new tool for studying avian cognition. “This is pioneering avian cognition neuroscience,” says Russell Gray, an evolutionary biologist at the University of Auckland in New Zealand. “They’re showing us what’s going on inside the crows’ heads. There’s a lot more cognitive processing that’s much more finely tuned than we would think by observing the birds’ outward behavior. It means that if you only judge animals by the way they behave, you could be mistaken.”

Gray and others hope that the scans will spur an already-booming field. Being able to tell what parts of the brain are active in an animal’s response might offer clues to when—or if—it is “thinking,” rather than simply responding to a stimulus. Thus, the scans have the potential to illuminate a long-term debate over animal capabilities. On one side are researchers who consider animals’ stereotypical behaviors as evidence of mental inflexibility. On the other are those who suspect that animals have more complex thought processes, but who struggle to prove it. The scans “may help close the divide,” says Corina Logan, a comparative cognition scientist at the University of California, Santa Barbara.

But not everyone is persuaded that brain scans will change views. “This kind of comparative behavioral neuroscience is definitely worthwhile,” says Sara J. Shettleworth, a professor emerita of psychology at the University of Toronto in Canada and self-described “killjoy” when it comes to animal smarts. But “it is not a substitute for behavioral tests” of mental abilities.

Feathered apes?

A decade ago, researchers might have been surprised that scientists would bother studying the minds of birds so intensely. Members of the avian family were once dismissed as “bird brains” and regarded as mentally simple. They were thought to lack a cerebral cortex, the area in the mammalian brain where higher cognitive functioning takes place.

Online sciencemag.org

S Podcast interview with author Virginia Morell (http://scim.ag/pod_6141).



Then, in 2004, an international team of neurobiologists and ornithologists reported that the brains of birds have structures, including an advanced forebrain, that are analogous with those of mammals. Even before that study, some comparative cognition researchers had demonstrated that some birds—especially parrots, crows, and jays—behaved in ways that suggested sophisticated cognitive skills (*Science*, 23 June 2006, p. 1734; 23 February 2007, p. 1074). The 2004 report “provided the neural evidence. It showed that there was real brain power behind what these labs were revealing, and helped convince skeptical people,” says Logan, who entered the field partly because of that paper. “Now bird cognition is hot.”

Indeed, over the past decade, the field has gathered momentum, producing a stream of papers. Researchers have detailed sophis-

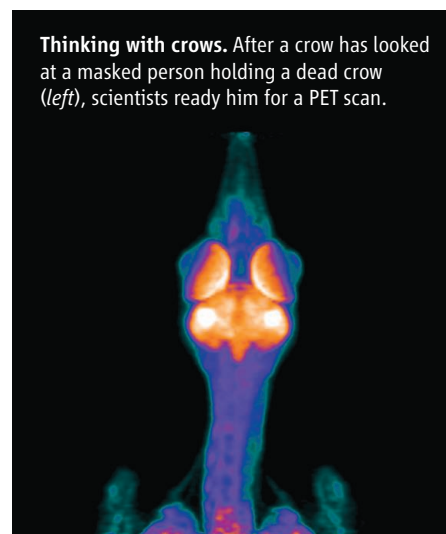
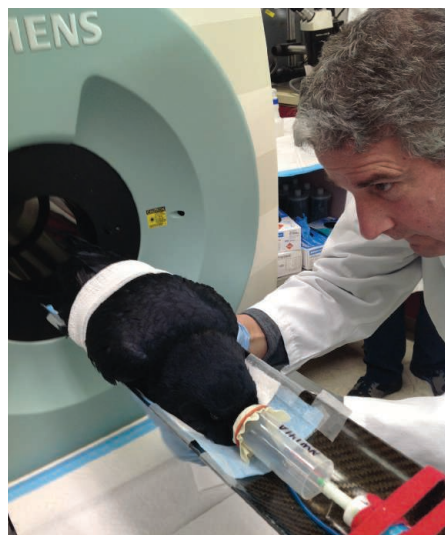
Some researchers argued that those behaviors could be explained by simpler cognitive processes such as associative learning. The same arguments seem to play out over study after study (*Science*, 2 March 2012, p. 1036). “The two sides keep doing what they’ve always been doing,” says Elske van der Vaart, a postdoctoral theoretical biologist at the University of Groningen in the Netherlands. “One side says it’s found some new mental ability in an animal, and the other says that’s still not enough proof.”

Why might birds have evolved a rich repertoire of mental abilities? Thomas Bugnyar, a cognitive psychologist at the University of Vienna, suggests that it may be a result of living complex social lives—the same theory proposed as the driving force behind the evolution of primate cognition. “We’re trying to see how well the social intelligence hypothe-

ing work that he reported in *Current Biology* in 2007. Clayton agrees that despite the similarities between some of our skills and those of birds, they don’t experience the world as we do. That’s why they’re so useful to study—if one can figure out how.

Bird “folk physics”

Behavioral experiments that try to explore just what’s behind a bird’s actions are often tortuously complex, as researchers try to come up with protocols to test how birds process their world. Many experiments examine tool use and manufacture and the manipulation of objects to get a treat. Researchers say that such experiments offer clues to the “folk physics” of animals—how they perceive the mechanical world. “Physical tasks are appealing because they are more likely to reveal the precise cognitive operations an



Thinking with crows. After a crow has looked at a masked person holding a dead crow (left), scientists ready him for a PET scan.

ticated memories in ravens and jays; tool-manufacturing and reasoning abilities in crows; and complex social skills in many species, especially corvids and parrots. Corvids are the most studied. “The range of behaviors—from counting to caching—that corvids do and are surprisingly good at, just shows how flexible and diverse they are,” says Nicola Clayton, a comparative psychologist at the University of Cambridge in the United Kingdom. She and Nathan Emery of Queen Mary, University of London termed corvids “feathered apes” because they have many of the talents celebrated in the great apes, from toolmaking to social networking (*Science*, 10 December 2004, p. 1903). Some corvids even surpassed apes on tests designed to reveal things such as the ability to recognize that others have intentions.

But not everyone is convinced by these claims of advanced cognition in birds.

sis fits with nonmammalian species, and corvids in particular,” explains Bugnyar, who recently published a summary of his team’s studies in *Comparative Cognition & Behavior Reviews*. American crows, for instance, have complex social lives that might shape their evolution: They mate for life; have extended families; communicate in complex vocalizations; and travel, forage, and roost in large social groups. If similar social pressures drove both avian and primate intelligence, it would be a stunning example of convergent evolution.

But there are key differences between the evolutionary pressures that likely led to the social smarts of ravens and mammals, Bugnyar notes, beginning with their most basic social bond. “In mammals, it is the mother-infant bond, but in birds it is the partner relationship, the pair-bond. It is a bond that develops through learning,” he said, cit-

animal makes to solve a problem,” says Alex Kacelnik, a behavioral ecologist at the University of Oxford in the United Kingdom.

His group, led by Alice Auersperg at the University of Vienna, last year reported that a captive Goffin’s cockatoo, Figaro, can spontaneously invent, make, and modify tools. The bird picked up a twig from the floor of the aviary, snapped off the side branches, and cut it to the right length to rake a nut into his cage.

That sounds like a dramatic, spontaneous invention out of whole cloth. But did Figaro have a mental image of a finished rake and take all these steps toward that image?

If so, no one has proved it yet. It may be that the bird learned through a series of intermediate, exploratory steps.

Just this week, the same team reported in *PLOS ONE* that other captive cockatoos were able to learn to unlock a series of



five locks to get a treat, suggesting that the birds can learn sequential steps without extra rewards. The birds also succeeded when the locks were presented in a different sequence, showing that they could consider each step independently. “It’s a kind of ratchet mechanism—little steps—that leads them toward a solution,” Kacelnik says.

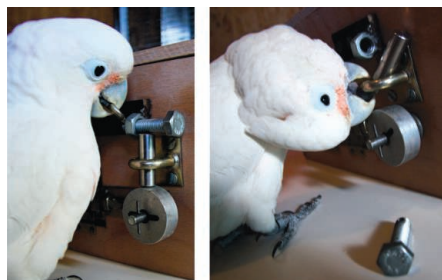
The lockbox experiment shows stepwise progress, but the mechanism behind the birds’ abilities to create tools and manipulate objects remains a mystery, says Alex Taylor, an evolutionary biologist at the University of Auckland. “These are impressive performances, but it is difficult to know exactly what cognition is being used; what is going on in the bird’s mind.”

Indeed, the same question—whether the birds imagined a full-blown solution or proceeded in small steps—inspired Taylor and Gray to further explore New Caledonian crows’ ability to use “insight” to solve a problem. Although not well-defined, insight is considered a kind of instantaneous problem-solving skill—the aha! moment.

New Caledonian crows are one of a few species of birds, including ravens, African gray parrots, and keas, that can get a treat dangling out of reach from a vertical string that’s suspended from a perch. The birds all use the same stepwise method: They pull up the string with their beak, then step on that segment with their feet, freeing their beak to pull up more string, and so on, until they reach the treat. But what goes on in their minds when they do this?

Some have argued that the birds mentally imagine the result of repeatedly pulling on the string—that the food will be within reach—and so are working toward that final goal. But others suggest that the birds may simply be responding to a feedback loop, and that the rising food acts as a reinforcement that keeps them pulling and stepping.

Taylor tested the two hypotheses by slightly changing the setup for 11 wild New Caledonian crows, in work reported in the *Proceedings of the Royal Society B* in 2012. Instead of dropping the string from a perch, he arranged it in two separate coils on a table. Both ropes had meat at their ends; but one rope was broken into two pieces, so if a bird pulled, the meat on the end would not move. Most of the birds pulled the continuous rope rather than the broken one, but only one did so enough times to get the food. The others stopped after a couple tugs, or didn’t bother to pull at all, Taylor reported. He suggests that—at least in this case—the birds are indeed responding to the results of each step, rather than imagining the end result.



But what are they thinking? To get a treat, crows can pull strings (top), and cockatoos can craft tools and open five locks (middle and bottom), but just how they solve these problems is a mystery.

Marzluff points out that the birds had enough understanding of the test to pull the connected string, not the broken one. “I think they just didn’t get the experiment; it doesn’t mean that they don’t have insight.”

Inside a crow’s head

These differences of interpretation are why researchers are so excited about the idea of viewing the brain at work. Marzluff already knew, for example, that crows are extremely attentive and have excellent memories. They pay attention to the dead body of another crow, cawing and mobbing when they see one, and they don’t forget the faces of people who threaten them, Marzluff reported in 2010 in *Animal Behaviour*. In 2006, wearing identical Halloween cavemen masks, he and his students captured seven crows on campus, tagged, and released them. Later, when the researchers donned their masks again and walked around campus, the banded crows scolded them; they ignored people wearing a Dick Cheney mask. To this day, campus crows (even those that the cavemen never handled) harass Marzluff if he wears the

caveman mask. That’s why lab workers wear masks when working with crows—so they won’t be mobbed later.

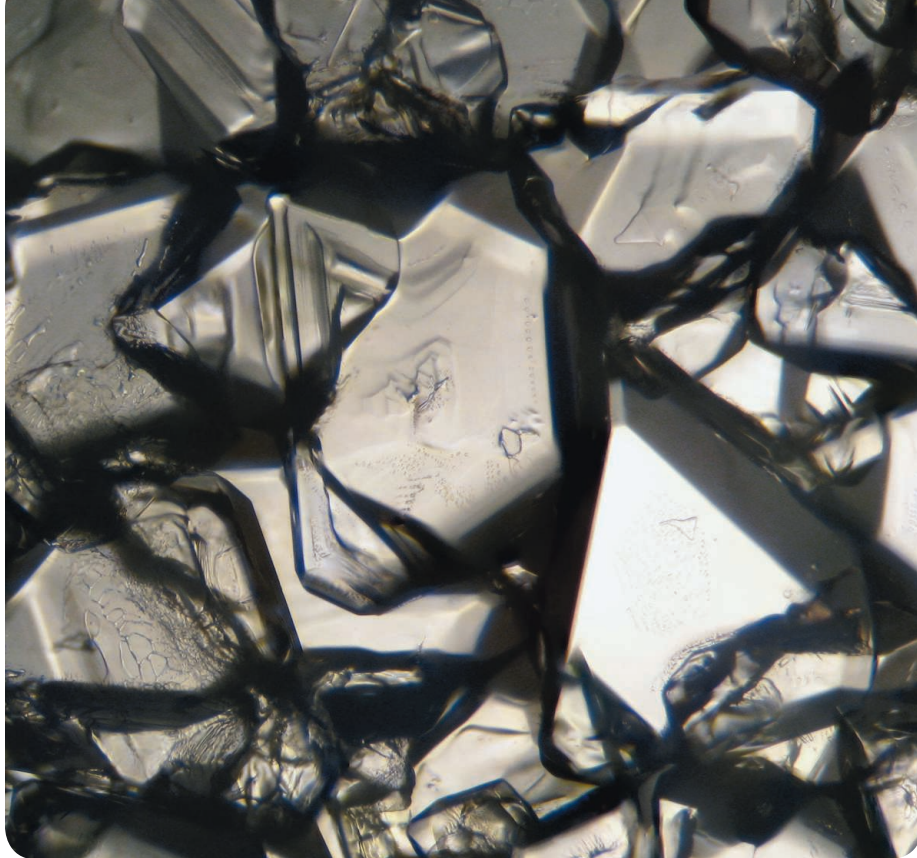
Last year in a study in the *Proceedings of the National Academy of Sciences*, using his brain-scanning technique for the first time, Marzluff examined the neural circuitry active when crows scan and remember masked faces. Now, the new study shows that the parts of the brain active when viewing a predator that crows innately fear (a hawk) is different from those that are active when a crow learns and memorizes the face of a threatening person they’ve not seen before. This method “should vastly improve our understanding of how animals interface, interpret, and internalize information,” says Teresa Iglesias, a behavioral ecologist at the Australian National University in Canberra, who has studied mobbing in Western scrub jays.

“It’s a technical and conceptual breakthrough,” agrees Erich Jarvis, a neural anatomist at Duke University in Durham, North Carolina, “the first study that I am aware of that asks cognitive questions about fear and memory in the avian brain using in vivo imaging.” But he cautions that Marzluff’s team may be “too quickly explaining the results in purely cognitive terms.” More basic brain functions—sensory processing and activation of nerves that move muscles—might also explain some of the differences in the scans.

Even if the first run of the method isn’t foolproof, Gray, Logan, and others are excited about combining it with their behavioral experiments for clues on just what is going on in a bird’s mind—the brass ring for cognition researchers. Taylor and Gray would like to try the string-pulling tests with Marzluff’s scanning technique, to see what areas of the brain are involved. Because some crows are better than others at solving the vertical string-pulling test—and certain songbird species can do it only after being trained—the researchers hypothesize that there may be key differences in the birds’ brains, both within and between species.

Of course, there are some things we’ll never know, such as just what the crows thought about their 2-week visit to Marzluff’s lab. Earlier this month, however, Marzluff spotted Bird 7, identified by his band. He’s back in the area where he’d been trapped, “is doing fine, is territorial, and is the king of the valley,” Marzluff reports. Maybe the crow had learned something, too, because this time, he was smart enough to evade the scientists’ trap while making off with the bait—a dozen hard boiled eggs.

—VIRGINIA MORELL



Key addition. Crystals of the first form of “alum” in vaccines, aluminum potassium sulfate.

Solution to Vaccine Mystery Starts to Crystallize

For 80 years, people have received injections of alum as part of vaccines, but only recently have researchers begun to explain how the compound helps stimulate immunity

These days, only collectors drive Model T Fords or listen to music on a hand-cranked Victrola. You don't balance your checkbook using a calculator that's heavy enough to be part of your weight-lifting regimen, and you can cross the Atlantic Ocean in a few hours instead of a few days. Technology has raced ahead since the 1920s, but one hold-over from the decade remains in a surprising place—our vaccines.

More than 80 years ago, manufacturers started spiking vaccines with alum, an additive, termed an adjuvant, that spurs a stronger reaction from the immune system. Today, almost everyone on the planet has received immunizations containing alum, a catchall term for several types of aluminum-containing adjuvants. “It's one of the most used compounds in modern medicine,” says immunologist Bart Lambrecht of Ghent University in Belgium. It's also an intriguing puzzle. “Considering how long this stuff has been used in human beings, ... it's amazing

how little we know about it,” says immunologist Philippa Marrack of National Jewish Health in Denver.

But scientists say that they are at last zeroing in on an explanation for how alum prods the immune system to induce protection against a pathogen. Researchers have recently floated at least three possible mechanisms, including one that involves DNA spilled from dying cells. The reason alum works so well, several studies suggest, is that it trips an alarm that alerts the immune system when cells are in trouble.

By mixing alum with other adjuvants, scientists have already shown that they can improve vaccines. Insights into how alum works might allow researchers to design replacements that retain alum's advantages but lose some of its shortcomings, such as its limited ability to muster certain antipathogen immune cells. “The alum field used to be really dead,” Lambrecht says. “That's no longer the case.”

Vaccines' little helpers

A typical vaccine primes our defenses against infections by delivering antigens, pathogen molecules—or pieces of them—that the immune system recognizes. But many immunizations wouldn't work without adjuvants, which rev up the immune response. In recent years, adjuvants have become even more important for providing disease protection, says immunologist Ennio De Gregorio of Novartis Vaccines and Diagnostics in Siena, Italy. Vaccinemakers are increasingly refining the antigen-containing portions of their products to quell side effects—for example, by replacing disabled viruses with fragments of viral molecules. “The more you purify, the less they are immunogenic,” De Gregorio says. So adjuvants have to pick up the slack.

Not every vaccine incorporates adjuvants. In the United States, for instance, the shots for measles, mumps, and influenza don't contain them. But these immune assistants are integral to vaccines against hepatitis A and the human papillomavirus, and they are critical to the diphtheria-tetanus-pertussis combo. The U.S. Food and Drug Administration doesn't approve adjuvants per se; it evaluates the whole vaccine. But of the adjuvant-containing vaccines the agency has licensed, all include alum. Elsewhere in the world, other adjuvants have gotten formally evaluated and approved by regulators. Some vaccines in Europe, for instance, include the oil-in-water mixtures MF59 or AS03. Yet alum remains a vaccine staple around the globe. “It's really the only adjuvant that has been used extensively,” says immunologist Fabio Re of the Rosalind Franklin University of Medicine and Science in Chicago, Illinois.

Researchers have discovered that alum helps induce our bodies to manufacture antibodies, defensive proteins that are crucial for defeating some kinds of pathogens. It's attractive as an adjuvant because it stimulates the immune system without causing a dangerous overreaction. “The beautiful thing about alum is that it's effective without being too effective,” says immunologist Stephanie Eisenbarth of Yale University School of Medicine.

Alum first proved its mettle in studies by the British immunologist Alexander Glenny and colleagues in the mid-1920s. They were hunting for compounds that would make antigens insoluble, a step they thought would improve a vaccine's immune-stimulating ability. The researchers vetted an assortment of compounds. Glenny and colleagues

revealed in 1926 that aluminum potassium sulfate was good at precipitating an antigen—the toxin from the bacterium that causes diphtheria—and increased guinea pigs' production of antibodies against the poison. Alum debuted in human vaccines not long afterward, and it's been there ever since. Most modern vaccines now use aluminum hydroxide and aluminum phosphate as their alum.

Working in mysterious ways

Glenny also bequeathed us the explanation for alum's action that prevailed for decades. According to his depot hypothesis, alum lingers at the injection site and gradually parcels out the antigen, thus provoking a longer, stronger immune response. However, this rationale doesn't jibe with more recent data. In a 2012 study for example, immunologist James Brewer of the University of Glasgow in the United Kingdom and colleagues injected mice with alum and an antigen and then removed the surrounding tissue as little as 2 hours later. "We cut the injection site out, and it had no effect" on the animals' ability to make antibodies, he says.

Discoveries about how alum interacts with the body's innate immune system, generic defenses that include macrophages and dendritic cells (DCs), have lately steered researchers in new directions. In 2007, teams led by Re and by Harm Hogen-Esch, an immunologist at Purdue University's College of Veterinary Medicine in West Lafayette, Indiana, found in cell studies that alum can trigger DCs and other immune cells to emit interleukin-1 β (IL-1 β), an immune signal that promotes antibody production. Researchers suspected that the link between alum and antibody output involved innate cells, but the mechanism wasn't obvious, says Eisenbarth, who was then a postdoc in the lab of immunologist Richard Flavell of the Yale University School of Medicine. "These two papers came out, and it was very clear."

The findings pointed to the inflammasome, a protein congregation inside cells that detects pathogens and danger signals, such as uric acid, leaking from wounded and dying cells. The inflammasome responds by spurring immune cells to release, among other molecules, IL-1 β .

Researchers pounced on the inflammasome connection, but Eisenbarth, Flavell, and colleagues got into print first, in *Nature* in 2008. They revealed that mice lacking a key

inflammasome protein, Nalp3, manufactured few antibodies after injections that included alum and an antigen. But the rodents made ample amounts after immunizations that included a different adjuvant. "Lo and behold, you needed Nalp3" to see a response to alum, Eisenbarth says. A team led by Re and another that included Lambrecht reported similar results later that year.

Other researchers didn't buy this explanation. In a 2009 study in *The Journal of Immunology*, Marrack and colleagues revealed that mice injected with alum and an antigen made plenty of antibodies even if they lacked the same inflammasome protein. Papers discounting an essential role for the inflammasome in alum's immune-stimulating ability now outnumber those supporting a link. "We see that the inflammasome is triggered [by alum], but nobody has been able to show that it's critical" for a vaccine response, Lambrecht concedes.

Other researchers have homed in on the

ensnare pathogens. Immunologist Christophe Desmet of the University of Liège in Belgium and colleagues reported in the August 2011 issue of *Nature Medicine* that the jettisoned DNA serves as an immune alarm, sparking antibody production in mice. Earlier this year in the *Proceedings of the National Academy of Sciences*, Marrack and colleagues delved deeper into this mechanism. Their results suggest that the DNA from dying cells galvanizes DCs, causing them to adhere more tightly to helper T cells. This lingering embrace, the findings indicate, ultimately leads to an increased release of antibodies by B cells.

The multiple hypotheses for alum's effects may appear at odds with each other, but De Gregorio and other researchers say the apparent disparities likely reflect how alum actually works. "It's really going to be down to multiple mechanisms," Lambrecht says. If the adjuvant triggers several kinds of responses, that would explain why it's such a good immune stimulant, Eisenbarth says.

**"The alum field used to be really dead.
That's no longer the case."**

**—Bart Lambrecht,
Ghent University in Belgium**

Ready for retirement?

For all its virtues, alum isn't the perfect adjuvant. It does a poor job of enlisting the cytotoxic T cells that are necessary for fighting diseases such as malaria and tuberculosis. For that reason, vaccinemakers around the globe are testing potential replacements.

Instead of ditching alum, other researchers are looking to soup it up. Already, vaccine manufacturers have introduced several composite adjuvants that include alum and a second compound. In the United States, a vaccine against human papillomavirus, Cervarix, pairs alum with MPL, a modified bacterial coat molecule. MPL prods Toll-like receptors, pathogen sensors on many types of body cells, that alum doesn't target, and it spurs production of cytotoxic T cells as well as antibodies.

If they understand alum better, researchers might be able to tweak it in other ways, for example by developing new adjuvant mixtures or by modifying its chemistry. But this tinkering has its risks. "We might be able to make it better—but not too much better," Marrack says. "You don't want the vaccine to kill the child" who receives it.

Even without an upgrade, alum's immune-activating prowess and safety record are hard to beat. Most researchers agree that this biomedical throwback has a future. "It's not going to go away soon," Marrack says.

—MITCH LESLIE



LETTERS

edited by Jennifer Sills

NextGenVOICES

Results: Science Time Travel

If you could go back in time and share one piece of scientific knowledge from today, what time period would you choose, what would you share, and how might that information change the course of history? In April, we asked young scientists to hop in their time machines and report back.

We heard from almost 200 readers, with tales of travel ranging from the dawn of man, to ancient Greece and Rome, to the Industrial Revolution, to the World Wars and recent decades. They imagined the effects of sharing knowledge about climate change, disease prevention, and seminal works in a wide variety of fields. A sample of the best responses can be found below. To allow for as many voices as possible, in some cases we have printed excerpts of longer submissions (indicated by ellipses) and lightly copyedited original text for clarity. To read the complete versions, as well as many more, go to <http://scim.ag/NextGen7Results>.

Submit Now: Work-Life Balance

Add your voice to *Science*! Our new NextGen VOICES survey is now open:

What one change would most improve work-life balance for scientists?

To submit, go to http://scim.ag/NextGen_8

Deadline for submissions is 16 August. A selection of the best responses will be published in the 4 October issue of *Science*. Submissions should be 250 words or less. Anonymous submissions will not be considered. Please submit only once.

earlier than it was, the impact on humankind would be immeasurably large.

JUGAL K. SHAH

School of Medicine, University of California, San Francisco, San Francisco, CA 94143, USA. E-mail: jugal.shah@ucsf.edu

221 B.C.E., XIANYANG, CHINA. THE MAJESTIC Emperor Qin, who has conquered all opposing states and unified China, is declaring to the whole world that the great and the first feudal dynasty has been established. Fortunately, I travel back in time just to be here and see the unrivalled state celebration.

As the future scientific envoy, I have an audience with Emperor Qin and present my gift: Women are capable of doing the same thing as men; they even can do better. Certainly, with adequate data, glorious accomplishment stories, and plenty of examples, such as Madame Curie, Mrs. Thatcher, Deng Yaping, and Oprah Winfrey, I can convince Emperor Qin to give women more chances to receive education and give full play to their talent in science and technology, culture, politics, and the military. In that way, more than 2000 years later, China would surely be a super power stronger than today....

JIAN ZHANG

School of Mechanical and Automotive Engineering, South China University of Technology, Guangzhou, Guangdong, 510641, China. E-mail: zhangjian3954@126.com

I WOULD GO BACK TO ANCIENT ROME ON the morning of 15 March, 44 B.C.E., to the steps of the Roman Senate, and share Bayes' Theorem with Julius Caesar. In the days leading up to his assassination, Rome was awash with rumors of an assassination plot. According to legend,

an old soothsayer had forewarned Caesar himself of a great danger that threatened him on the Ides of March, and Caesar's own wife Calpurnia had a premo-

NextGen Speaks



...I WOULD TRAVEL BACK TO THE years around 600 to 400 B.C.E., when there were heated debates in ancient Greece about the origin of life. I would tell the philosophers and lecturers of that time what we now know about life on a molecular level... I would like to see the impact this would have on art, industry, science, and religion throughout the centuries to come. This might even accelerate the onset of the scientific and industrial era by reducing the impact of religion in everyday life and perhaps even allow different cultures to understand each other better, once they realize that our nature is essentially the same.

MARTIN PAČESA

National Centre for Biomolecular Research, Faculty of Science, Masaryk University, Brno, 62500, Czech Republic. E-mail: martin.pacesa@kcdesign.com

...IF I COULD TRAVEL BACK IN TIME, I WOULD transport to Syracuse, Sicily, in 222 B.C.E. to introduce the fundamental theorem of calculus to Archimedes 10 years before his death. As the great mathematical genius of his era, he would have been most poised to understand and disseminate the knowledge of linking the concept of a derivative of a function with the concept of the integral.... So much technology of today, from the internal combustion engine to the principles of economics, has been made possible due to calculus. Perhaps in the present era we would be traveling in flying cars, or we would have colonized Mars. Or, more grimly, we would have achieved nuclear apocalypse. Undoubtedly, however, had calculus been introduced to the world 1900 years





How seabirds forage

35



A burst of distant radio waves

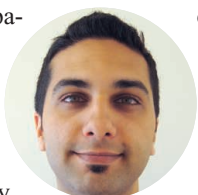
40

nition of her husband's murder and tried to warn him of the danger. But were these dark forebodings and dire prophecies just idle gossip (noise) or a credible forecast of the future (signal)? Given this uncertainty, I would advise Caesar to guess the prior probability of an assassination plot and then update his prior based on the sundry rumors swirling around Rome. Had Caesar applied Bayesian reasoning, it is likely he would have followed his wife's advice and stayed home on that fateful day. Had he done so, Bayes' Rule might have changed the course of history, for the Roman Republic might have yet been saved, and perhaps we would all still be speaking Latin.

ENRIQUE GUERRA-PUJOL

Dwayne O. Andreas School of Law, Barry University, Orlando, FL 32807, USA. E-mail: eguerra@barry.edu

I WOULD TRAVEL TO CHINA IN THE YEAR 1070 with the knowledge of bacteria and fungi that produce substances capable of fighting infection. In 1070, Su Song compiled the *Bencao Tujing*, a revolutionary treatise on pharmaceutical botany, zoology, and mineralogy. By



providing Su Song this knowledge, it would be in the hands of an individual capable of understanding, utilizing, and preserving this knowledge. Su's treatise survived until the 16th century, when it was incorporated into the *Bencao Gangmu* by Li Shizhen, demonstrating the lasting impact of his work. After Su demonstrated the efficacy of fungi, such as penicillium, during the Song Dynasty, which oversaw some of the most significant scientific advances in Chinese history, antibiotic pharmaceutical preparations would likely be developed. It would be over 250 years before arguably the most devastating pandemic in recorded history, the Black Death (caused by *Yersinia Pestis*), would arise in China, spreading west as far as Europe. The Black Death was responsible for over 100 million deaths.... In addition to the tragic death toll it exerted, the Black Death led to massive social unrest, including economic decline and widespread persecution of

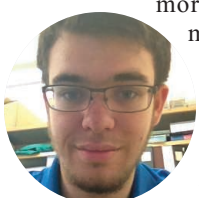


those thought responsible. Providing Su Song with antibiotic knowledge in 1070 would allow ample time for development of appropriate therapies to combat the Black Death at its source, averting one of the greatest tragedies in the history of mankind.

ZESHAAN N. MAAN

Department of Surgery, Stanford University, Stanford, CA 94305, USA. E-mail: zmaan@stanford.edu

IN 1687, SIR ISAAC NEWTON PUBLISHED HIS *Principia* outlining the fundamentals of what quickly became called Newtonian mechanics. I would travel back to Cambridge, England, 5 years before this date and teach Einstein's, theory of relativity to Isaac Newton. The obvious change in history resulting from this action would of course be a massive head start for the field of modern physics.... However, I would argue that a less obvious but possibly more important consequence of this historical change would be its effect on how we teach science. Currently, high school students and first year undergraduates are taught the limited version of physics discovered by Newton. Only students who choose to continue in the discipline learn Einstein's



more generalized form of mechanics and how classical mechanics is encompassed in this modern understanding. If Newton had discovered both his and Einstein's contribu-

tions at the same time, the result would be an educational system that introduces a more complete view of physics to a wider audience of people from an earlier age....

MATTHEW HAMMOND

Department of Biochemistry, University of Pennsylvania, Philadelphia, PA 19104, USA. E-mail: mhamm@sas.upenn.edu

...INSTEAD OF A PIECE OF TECHNICAL KNOWL-

edge, I would share something that would provide perspective: the photo of Earth taken by the Apollo 17 astronauts in 1972. "The Blue Marble," as it is often called, shows both the unity and finitude of the planet and its resources. The photo is emblematic of the modern environmental movement's birth in the 1970s. I would bring this photo to early 19th-century Britain, during the Industrial Revolution, when consumption of Earth's resources began to increase dramatically. Providing this information 150 years earlier would

be an opportunity for the soon-to-be industrialized culture of western Europe to reconsider its relationship with the planet.... For a little extra perspective, I would share the photo with its original orientation, Southern Hemisphere on top!

STEVEN M. ROELS

Department of Zoology, Michigan State University, East Lansing, MI 48824, USA. E-mail: roelsste@msu.edu

I WOULD TRAVEL BACK TO 1847 TO JOIN Hungarian physician Ignaz Semmelweis at the Vienna General Hospital in his hand-washing crusade. At that time puerperal fever was epidemic, but its etiology unknown. After observing mortality from the disease to be three-fold higher in doctors wards compared to the wards run by mid-



wives, Semmelweis drew up his novel intervention: hand-washing by physicians using a chlorinated lime solution. However, the medical fraternity vehemently rejected his proposed intervention, and ostracized him for it.... In hindsight, while we marvel at the brilliance and simplicity of Semmelweis's work, we have done little to celebrate a practice of accepting simple and unconventional work, even when backed by solid thorough science. Traveling back to the time of Semmelweis,

I would share the importance of embracing such unconventional work when supported by sound evidence and stringent scientific process.... Laying the foundation with Semmelweis, one can hope to cultivate a scientific culture founded in discussion and driven by radical innovation; encouraging the willingness and openness needed to accept alternative ideas—even those which may conflict with one's own beliefs....

SAMUEL D. RUTLEDGE

Department of Biological Sciences, Virginia Polytechnic Institute and State University, Blacksburg, VA 24060, USA. E-mail: srut07@vt.edu

...NOWADAYS IT IS EASY TO FORGET THAT COMMUNICATION among scientists once was difficult, due to geographic and linguistic boundaries. A striking example is that of Charles

Darwin and Gregor Mendel. Their

written legacy allowed for the advance in genetics, yet they never met in life. If I could travel back in time, I would go to Downe, England, in 1866 and inform Charles Darwin of Gregor Mendel's results.

Realizing that Mendel's work provided the proof for evolution by natural selection, this would result in a modern synthesis 50 years ahead of time and advance medical genetics by 50 years. Accordingly, we would be much further in our understanding of human genetic diseases and closer to their treatments.

ANTOINE DE MORRÉE

Paul F. Glenn Laboratories for the Biology of Aging and Department of Neurology and Neurological Sciences, Stanford University School of Medicine, Stanford, CA 94305, USA. E-mail: demorree@stanford.edu

I MET ALFRED NOBEL IN SWEDEN IN 1895, A few days before he died.... He had just finished writing his last will, leaving much of his wealth to honor outstanding achievements in physics, chemistry, medicine, literature, and peace.... While drinking coffee together...I told him that in

the future, scientists are communicators, writers needing to share ideas with clarity to different audiences. I described the new and diverse ways of communicating science in the time to come.

He smiled, enjoying looking into the future through my eyes. We both agreed that better science communicators are, ultimately, better scientists and that science is not just for scientists. When he fell asleep, I returned to the future. Although he thought my visit was part of his nap's dreams, minutes before dying

he included an award for science communication in the Nobel list. Ever since, writing and communication have become part of the syllabus in undergraduate and graduate programs, together with physics and chemistry. More efficient scientific communication has accelerated the pace of discoveries; created greater public scientific awareness, literacy, and crowdfunding; and inspired young generations to pursue careers in science. More than 108 academics have already been honored with the Nobel Prize in Science Communication. I hope one day I will win this award!

PAULA DE TEZANOS PINTO

IEGEB, Laboratorio de Limnología, Departamento de Ecología, Genética y Evolución, Universidad de Buenos Aires, C1428EHA, Buenos Aires, Argentina. E-mail: paulatezanos@ege.fcen.uba.ar

IT WAS A WINTER NIGHT IN 1896. TWO SWEDISH scientists, Svante Arrhenius and Arvid Högbom, were chatting in Arrhenius's office room. "I believe a doubling of atmospheric CO₂ would give a total warming of 5°C to 6°C," said Arrhenius. Högbom

agreed, but they both thought the warming would take thousands of years. At this point, I decided to show up. Rather than falling from the chimney like Santa Claus, I chose to knock on their door.

They were really shocked when they found a Chinese girl standing in front of them. "Hello, Professors, I travel back in time from 2013 to tell you that...since the early 20th century, Earth's mean surface temperature has increased by about 0.8°C. The primary cause is greenhouse gases produced by human activities. The Intergovernmental Panel on Climate Change indicated that during the 21st century the global surface temperature is likely to rise another 1.1°C to 2.9°C, even for their lowest emissions scenario. Global warming isn't just about things getting hotter; other changes include stormier, drier, and even colder conditions." The next day, they wrote to the government and the scientific associations to call people's attention to global warming and adaptations to eliminate it. Actions like reducing fossil fuel use, planting trees, and conserving water were known by people all over the world. Instead of destroying the planet, every single man on Earth began to protect and sustain it in their daily life.

QIFEI HAN

State Key Laboratory of Desert and Oasis Ecology, Xinjiang Institute of Ecology and Geography, Chinese Academy of Sciences, Urumqi, Xinjiang 830011, China. E-mail: hanqifei08@mails.ucas.ac.cn

I WOULD CHOOSE THOMAS EDISON IN THE beginning of the year 1900 in New York City. I would describe the events of the future and how he and I could help keep our environment cleaner.

I would give him designs to solar panels and hope that the future of solar technology would make America and other countries independent of oil production. Thomas Edison's name alone could create Edison Panels that would be on every Victorian home in the world, especially in hard-to-reach locations.... Fewer trees would be cut, and the world would remain more rural and yet prosper from a new power source.

DAN FERRELL

Alexandria, VA 22305, USA. E-mail: dannielferrell@yahoo.com

IT'S 24 JULY 1948, AND I'M AT THE PALAIS des Nations, Geneva, Switzerland. I walk into the resting room of Dr. George Brock Chisholm, who is about to be appointed the first Director-General of the World Health Organization. I tell him that I come from

the 21st century, and that people in my time are suffering from the increasing prevalence of antimicrobial-resistant bacterial infections, mainly as a result of the misuse of antibiotics. I urge him, in a time penicillin is just being mass-produced, to emphasize the importance of appropriate antibiotic use to the world, and to develop and promote policies of proper use of antibiotics. He believes in me, and delivers the message in his acceptance speech. During his 5 years in office, he is actively involved in the development and promotion of national medicines policies and guidelines on proper antibiotic use....

MAN KIT CHEUNG

School of Life Sciences, The Chinese University of Hong Kong, Shatin, NT, Hong Kong SAR, China. E-mail: mkcheung@cuhk.edu.hk

Letters to the Editor

Letters (~300 words) discuss material published in *Science* in the past 3 months or matters of general interest. Letters are not acknowledged upon receipt. Whether published in full or in part, Letters are subject to editing for clarity and space. Letters submitted, published, or posted elsewhere, in print or online, will be disqualified. To submit a Letter, go to www.submit2science.org.

SCIENCE AND CULTURE

Being Modern in Revolutionary Russia

Asif Siddiqi

In seeking to remake backward and agrarian Russia into a modern state, the architects of the Russian Revolution consistently extolled the fundamentally transformative powers of modern science and technology. Their infatuation with the manifestations of modern science—railroads, radio, electricity, the telegraph, airplanes, and so forth—was potentially expressed in language that often bordered on the mystical and magical. Consider Lenin's oft-quoted phrase that "communism is equal to Soviet power plus the electrification of the entire country." In *We Modern People*, an erudite and thoughtful study of Soviet science fiction, Anindita Banerjee uncovers the literary responses and manifestations of Russia's struggle to come to terms with modern science and technology. She seeks to show, in particular, how during a roughly 30-year period from the 1890s to the 1920s, "science fiction became a way of not just telling but also of making modernity in Russia."

Banerjee (who teaches comparative literature at Cornell University) frames her narrative along four thematic axes that cluster the principal concerns of Russian and Soviet science fiction: space, time, power, and the human body. For each of these narratives through which science fiction "etched out new locations and histories for Russia," two things are clear. First, many of the discourses about "alternative modernities" given voice in science fiction were not simply a product of the millenarianism of 1917 but rather part of a longer and continuous debate about the meaning of "modern" in Russia that preceded the revolution. Second, these messages embedded in literary texts

transcended easy dichotomies (such as utopian-dystopian, rational-spiritual, and individualistic-collectivist) in favor of a more complex epistemology. Drawing from the French thinker Michel Foucault, Banerjee calls this "heterochronotopia," which suggests a kind of perception of the modern world that accommodates hybrid and contradictory modes of temporality. If most of our attention has been paid to the first kind of "modern" where science and technology are unquestioned forces for progress, Banerjee argues that the second kind—with all its doubts, uncertainties, and anxieties about science, technology, and biology—was as much an expression of modernity, one that Russian science fiction anticipated long before the debates over Soviet industrialization in the 1920s.

Beyond her obvious mastery of a vast corpus of Russian literary and intellectual output at the turn of the 20th century, Banerjee shows an uncanny ability to make connections between works, idioms, and ideas separated by time and space. In the chapter on science-fictional meditations on Russian "space"—defined broadly as the hinterlands to the east, the open skies of aviation, and the cosmos itself—she seamlessly pulls together insights from a panoply of philoso-

phers, writers, playwrights, poets, and artists. The value of her analysis is furthered by her recovery of the enormous subtlety of this vibrant discourse. One might expect that Russian intellectuals of the time were unequivocally enamored of the power of modern science and technology to produce new understandings of the Russian landscape, but as Banerjee demonstrates, much of this writing was deeply ambivalent, equal parts enthusiasm and fear. In the section on perceptions of time, for example, she shows how Russian writers sought to resist powerful narratives about the scientific management of time through carefully conceived stories about the conflicts between private time (still premodern) and on the onslaught of mechanical time (of industrialization).

There are two lacunae worth noting. Her bold claims about the importance of science fiction in fundamentally complicating Russians' sense of themselves in the modern world rests on shaky ground when one has no idea how many people actually read any of this. Consider the most often-invoked Soviet-era work of science fiction, Yevgeny Zamyatin's infamous and dystopian *We* (1), which gives Banerjee's book its name [although that also curiously echoes Bruno Latour's equally famous *We Have Never Been Modern* (2)]. Despite being written in the early 1920s, *We* was not published in the Soviet Union until the late 1980s. The average educated Soviet citizen of the 1920s would most likely have never even heard of it. Second and more important, as one gets deeper into the narrative, one begins to notice that many if not the majority of the works that Banerjee invokes are not fiction but instead popular science.

She skirts the issue, but as a number of other historians have shown, the genre of popular science was a massive enterprise in the Russian context, with literally scores of journals and hundreds of books published since the late 19th century. Fictional meditations—as aesthetically rich as they were—were only a minority of this deluge of thoughtful commentary on science.

Despite these minor concerns, *We Modern People* successfully underscores how, already by the 1920s, Russian writers and artists of all ilk—not just a hand-

We Modern People
Science Fiction and
the Making of Russian
Modernity

by **Anindita Banerjee**
Wesleyan University
Press, Middletown,
CT, 2012. 218 pp. \$75.
ISBN 9780819573339.
Paper, \$24.95. ISBN
9780819573346.



An alternative environment. Poster for Yakov Protazanov's film *Aelita* (1924), adapted from Alexei Tolstoy's 1922 novel, in which the protagonists stage a socialist revolution on Mars.

The reviewer, the author of *The Rocket's Red Glare: Spaceflight and the Russian Imagination, 1857–1957*, is at the Department of History, Fordham University, 441 East Fordham Road, Bronx, NY 10458, USA. E-mail: siddiqi@fordham.edu

CREDIT: WWW.ALLOCINE.FR

ful of science fiction writers—were deeply engaged in critiques of positivist notions of modernity. Banerjee's deeply insightful recovery of this discourse adds much fodder for thought for those who confine their studies on the history of modernity and its relationship to science and technology to Western Europe and the United States. There is much to learn from her book.

References

1. Y. I. Zamyatin, *We*, G. Zilboorg, Transl. (Dutton, New York, 1924).
2. B. Latour, *We Have Never Been Modern*, C. Porter, Transl. (Harvard Univ. Press, Cambridge, MA, 1993).

10.1126/science.1238707

MATHEMATICS

Can Oompa-Loompas Save Us from Perebor?

Veit Elser

Princeton University is home to the Center for Computational Intractability (PCCI), a National Science Foundation-funded operation that so far has dodged the attentions of Senator Tom Coburn and others critical of “wasteful” science spending. And while the researchers at PCCI do not study shrimp on treadmills or engage in jello-wrestling, there is something unsettling in the thought of mathematicians high-fiving one another after a tough day of successfully not solving any problems. Fortunately for the public, Lance Fortnow's *The Golden Ticket* may convince even senators that NSF support of the PCCI is money well spent.

Both the Intractability Center's website and the title of Fortnow's book feature a curious epigraph comprising the symbols P and NP. The mathematical question $P \stackrel{?}{=} NP$, or the phrase P versus NP, have become icons of what may be the profoundest problem in computer science, if not all of mathematics. Each symbol represents a broad classification of difficulty or “complexity,” and the distinction between the two classes may not seem all that profound at first.

Consider a sudoku puzzle. After it has been solved, the task of checking the solution's validity is squarely in class P. Although it may be tedious, checking to make sure that all the rows, columns, and blocks contain each

of the symbols 1 through 9 is easy to carry out by a systematic procedure, or algorithm. The P is shorthand for “polynomial,” a characterization of how the time required to do the checking scales up when the puzzle size is increased to 16 by 16, 25 by 25, and so on. Polynomial growth just means that the time grows as some algebraic power of the puzzle size; the precise power is not at issue (and so it doesn't actually matter if standard sudoku has size 9 or 81). But contrast solution checking with the task of finding the solution itself. Fans of the more difficult puzzles know that the chains of deduction can be quite long and the possibilities multiply. Is solving sudoku also in class P?

Most computer scientists believe solving sudoku belongs not in P but in a higher complexity class, NP. The running times for the most powerful known algorithms grow exponentially, that is, faster than any polynomial function of the puzzle size. More generally, problems in class NP have solutions that can easily be checked but, as far as we know, cannot easily be found. Fortnow (a computer scientist at the Georgia Institute of Technology) considers two scenarios. If class NP really is distinct from P—as is widely believed, although we lack a mathematical proof—then our current approach to “intractable” problems will continue to develop along several productive lines that the author discusses in the book. Besides learning to live with approximate solutions, we can exploit intractability to make cryptography secure or develop new types of algorithms designed for a fundamentally different kind of quantum hardware. But there is also the other, “golden ticket,” scenario in which P and NP turn out to be the same.

Fortnow uses the plot element of Roald Dahl's *Charlie and the Chocolate Factory* (1) to convey the long odds of finding something of such life-changing consequences as the $P = NP$ scenario would hold. He devotes a chapter to the “beautiful world” a universal algorithm capable of quickly solving NP problems would make possible: Cancer is cured by personalized gene therapy derived by the algorithm from a patient's DNA. The workings of the universe are laid bare when the algorithm is operated as the ultimate Occam's razor. And perfect weather prediction makes possible a perfectly scheduled season of Major League Baseball. Remarkably, watching games would still be fun because, unlike the weather, the algorithm is still flummoxed by the physics of bats and balls.

The Golden Ticket P, NP, and the Search for the Impossible

by Lance Fortnow
Princeton University
Press, Princeton, NJ, 2013.
188 pp. \$26.95, £18.95.
ISBN 9780691156491.

On the serious side of P versus NP is the problem of finding a proof that the two classes of problems are truly different. The odds of that happening in our lifetimes, Fortnow would have us believe, are about as long as finding a golden ticket. He would know: as a leading complexity theorist and coauthor of the Computational Complexity Blog (2), he has followed the fortunes of numerous proof strategies. What's interesting is that whole general lines of attack are known to be dead ends. Perhaps

that is not all too surprising, since proof-discovery is much like an NP problem.

A fair amount of historical research has gone into the writing of the book, from the Stouffer's Somerset Inn where Stephen Cook first articulated P versus NP to Donald Knuth's offer of a live turkey for the first proof. One of the most interesting stories is the parallel line of P-NP research carried out behind the Iron Curtain, where the specter of “brute force” search, the only option for hard problems, went by the ominous sounding name “Perebor.” I know what I will be muttering under my breath the next time a student tells me his computations are taking forever.

A slim volume, *The Golden Ticket* could have been expanded in two ways. The first would have been to acknowledge that very often the real-world instances of NP problems turn out to be easy. Sudoku puzzles designed for human consumption yield to relatively simple logic, and proteins designed by nature seem to quickly find their folded forms without having to try myriad combinations. Whereas in both cases the worst-case instances are NP problems, only the subclass with the P designation arises in practice. In the other direction is the sad truth that there are problem classes beyond NP, in which even solution checking is not easy. Is there a first move in checkers (and its generalization to larger boards) that guarantees a win? If it were possible to easily check the (polynomially growing) options for the first move, then checkers would be trivial and uninteresting. But on the whole, Fortnow's book is just the ticket for bringing one of the major theoretical problems of our time to the level of the average citizen—and yes, that includes elected officials.

References

1. R. Dahl, *Charlie and the Chocolate Factory* (Knopf, New York, 1964).
2. <http://blog.computationalcomplexity.org>.

10.1126/science.1240634

The reviewer is at the Cornell Center for Computational Tractability and Department of Physics, Cornell University, Ithaca, NY 14853, USA. E-mail: ve10@cornell.edu

AGRICULTURE

Sustainable Intensification in Agriculture: Premises and Policies

T. Garnett,¹ M. C. Appleby,² A. Balmford,³ I. J. Bateman,⁴ T. G. Benton,⁵ P. Bloomer,⁶ B. Burlingame,⁷ M. Dawkins,¹ L. Dolan,¹ D. Fraser,⁸ M. Herrero,⁹ I. Hoffmann,⁷ P. Smith,¹⁰ P. K. Thornton,¹¹ C. Toulmin,¹² S. J. Vermeulen,¹¹ H. C. J. Godfray^{1*}

Food security is high on the global policy agenda. Demand for food is increasing as populations grow and gain wealth to purchase more varied and resource-intensive diets. There is increased competition for land, water, energy, and other inputs into food production. Climate change poses challenges to agriculture, particularly in developing countries (1), and many current farming practices damage the environment and are a major source of greenhouse gases (GHG). In an increasingly globalized world, food insecurity in one region can have widespread political and economic ramifications (2).

These challenges require action throughout the food system. One response has been a call to increase food production from existing farmland in ways that place far less pressure on the environment and that do not undermine our capacity to continue producing food in the future. This “sustainable intensification” (SI) approach is a policy goal for a number of national and international institutions (3–5) but also attracts criticism as being too narrowly focused on production or representing a contradiction in terms (6).

The origins of SI lie in discussions about increasing yields, chiefly of arable crops, in the face of resource scarcity and environmental challenges (see the photo). Our goal here is to articulate a more sophisticated definition of SI, one that clarifies the logic on which it rests and the context and conditions within which it should be implemented. We define four underpinning premises of SI, situating it within a broader framework of priority actions for the food system. We then explore

how SI interfaces with other major food-system goals and show how they may guide SI implementation. We argue that this broad perspective is essential if SI is to fulfill its goal of helping foster global food security.

Four Premises Underlying SI

(i) The need to increase production. The challenge of achieving sustainable food security for all is only in part a supply-side problem (2, 7, 8). Urgent action is also needed on moderating demand for resource-intensive foods (such as meat and dairy products), reducing food waste, and developing systems of governance that improve the efficiency and resilience of the food system, as well as making food accessible and affordable to all.

Nevertheless, overall increases in production are essential because no one approach to address food insecurity will be fully effective, given the inevitability of policy failures, as well as the time lags in the demand and supply dynamics of the food system. It is too risky to assume otherwise. Yield increases in many low-income countries are required today; elsewhere, the goal may not necessarily be to increase yields immediately but to develop the potential to respond to future increases in demand. Critically, all responses must be environmentally sustainable. SI should be seen as part of a multipronged strategy to achieving sustainable food security rather than an all-encompassing solution.

(ii) Increased production must be met through higher yields because increasing the area of land in agriculture carries major environmental costs. Although land usable for agriculture exists, it consists mainly of forests, wetlands, or grasslands, whose conversion would greatly increase GHG emissions (9) and the loss of biodiversity and important ecosystem services (10). Although less intensive, generally lower-yielding production may generate local environmental benefits, it is critical to consider potential indirect consequences, in particular the risk that land is cleared for agricultural production elsewhere to compensate for locally lower yields (5).

(iii) Food security requires as much attention to increasing environmental sustainabil-

Clearer understanding is needed of the premises underlying SI and how it relates to food-system priorities.

ity as to raising productivity. SI does not mean business-as-usual food production moderated by marginal improvements in sustainability. As we envisage it, SI demands radical rethinking of food production to achieve major reductions in environmental impact. In some areas, increases in yield will be compatible with environmental improvements. In others, yield reductions or land reallocation will be needed to ensure sustainability and deliver benefits such as wildlife conservation, carbon storage, flood protection, and recreation. An overall increase in production does not mean yields should increase everywhere or at any cost: The challenge is context- and location-specific.

(iv) SI denotes a goal but does not specify a priori how it should be attained or which agricultural techniques to deploy. The merits of diverse approaches—conventional, “high-tech,” agro-ecological, or organic—should be rigorously tested and assessed, taking biophysical and social contexts into account. Building the social and natural science evidence base to allow formulation of context-dependent SI strategies is a research priority.

Other Policy Goals Interfacing with SI

Policy-makers need to consider multiple goals for the food system in multifunctional landscapes (11). Although there will often be synergies, tensions among competing priorities also arise. Here, we highlight five areas that interface with SI and explore ways in which shared agendas might best be pursued.

(i) Biodiversity and land use. By using and contaminating land and water, agriculture is a greater threat to biodiversity than any other human activity (4). One response is to integrate agriculture and conservation goals through wildlife-friendly “land-sharing” practices. However, because yields are typically lower, more land is needed for a given output. This suggests an alternative approach: land sparing, in which yields are increased on farmed land, freeing up land elsewhere for conservation (12). SI could involve either approach, but understanding which is more beneficial, and in what context, is hampered by the shortage of relevant

¹University of Oxford, Oxford OX1 3QY, UK. ²World Society for the Protection of Animals, London WC1 X8HB, UK. ³University of Cambridge, Cambridge CB2 3EJ, UK. ⁴University of East Anglia, Norwich NR4 7TJ, UK. ⁵University of Leeds, Leeds LS29JT, UK. ⁶Oxfam, Oxford OX4 2JY, UK. ⁷Food and Agriculture Organization of the United Nations, Rome 00153, Italy. ⁸University of British Columbia, Vancouver V6T 1Z4, Canada. ⁹Commonwealth Scientific and Industrial Research Organisation, Brisbane, Australia. ¹⁰University of Aberdeen, Aberdeen AB24 3UU, UK. ¹¹CGIAR, Frederiksberg DK-1958, Denmark. ¹²International Institute for Environment and Development, London WC1X 8NH, UK.

*Corresponding author. E-mail: charles.godfray@zoo.ox.ac.uk

quantitative data. The practical effectiveness of both approaches hinges on real-world constraints—coupling on-farm yield increases to safeguards for conservation elsewhere (in the case of land-sparing), and design and widespread adoption of low-impact farming approaches (for land-sharing). Successful SI will require (a) establishing how land-sharing can deliver sufficiently high yields and multiple ecosystem services, (b) quantifying trade-offs between yields and different environmental benefits and assessing how best to resolve them across different circumstances and spatial scales, and (c) exploring policy and market mechanisms that enhance implementation of sharing or sparing initiatives.

(ii) Animal welfare. The word “intensification” is particularly problematic for those concerned with animal welfare. It is often associated with forms of production that have demonstrably negative effects on animal health and welfare. Although attention to many aspects of welfare can increase productivity (particularly where low productivity is caused by disease, insufficient feed, and other causes of ill health), some strategies, such as highly selective breeding for extreme levels of production, can produce congenitally harmed animals and undermine well-being in other ways (13, 14). For us, SI goals are contingent upon acceptable standards of welfare. In applying SI to the livestock sector, we need to (a) place SI within a wider ethical framework that may disbar some potential options, (b) identify areas with the greatest potential for joint SI and welfare gains, and (c) recognize that there are limits on our ability to meet projected future livestock product demand while also achieving animal welfare and environmental goals, limits that signal the need for urgent action to reduce overconsumption and escalating demands.

(iii) Human nutrition. Food security incorporates the need for micronutrient, as well as energy and protein, adequacy (15). Progress on the former has lagged behind efforts to end hunger. Good human nutrition requires a diverse diet. It is important that SI does not result in narrowed dietary options, especially for poor consumers. This might occur through excessive dependence on a few high-yielding commodity crops bred for productivity rather than for micronutrient quality. Post-harvest fortification as well as breeding strategies (including biofortification) that improve crops’ nutritional content can help mitigate these problems but may be counterproductive if they exacerbate reduced dietary diversity. SI farming strategies thus need to take nutrition into account. This requires us to (a) assess impacts of current production approaches on



Increase in rice yields. Rice yields increased greatly during the “Green Revolution” of the 1970s and 1980s. The challenge now is to make equivalent progress on sustainability.

the spectrum and adequacy of food available to local communities, (b) better understand the dietary importance for many poor people of wild foods and often-neglected indigenous crops and livestock and take this into account in land-use policy, and (c) apply traditional and modern breeding techniques to improve yields of neglected crop and livestock species.

(iv) Rural economies. In many countries, agricultural policy is inextricably linked with economic support for rural economies. The design and operation of agricultural support could be radically improved, and SI goals need to be developed within this broader policy context. We should (a) identify where current support mechanisms can be reoriented to incentivize SI, (b) revitalize and reinvent extension services to provide the support required for SI implementation, and (c) use modern information and communications technology and appropriate financial instruments to enable food producers applying SI practices to be more resilient to shocks and responsive to market signals.

(v) Sustainable development. In least-developed countries and for low-income producers, improving yields and farmer incomes are priorities but are frequently hampered by insufficient economic, physical, and human capital, themselves held back by institutional failure. Targeting investment in agriculture as an engine of economic growth is receiving new attention, as is the possibility that low-income countries can orient production along more sustainable pathways (16). SI needs to engage with the sustainable development agenda to (a) identify SI agricultural practices that strengthen rural communities, improve smallholder livelihoods and employment, and

avoid negative social and cultural impacts, including loss of land tenure and forced migration; (b) invest in the social, financial, natural, and physical capital needed to facilitate SI’s implementation; and (c) where sustainability objectives (e.g., GHG mitigation or biodiversity protection) require actions that may carry economic costs, develop mechanisms to pay poor farmers for undertaking such measures.

Conclusion

SI is a new, evolving concept, its meaning and objectives subject to debate and contest. But SI is only part of what is needed to improve food system sustainability and is by no means synonymous with food security. Both sustainability and food security have multiple social and ethical (17), as well as environmental, dimensions. Achieving a sustainable, health-enhancing food system for all will require more than just changes in agricultural production, essential though these are. Equally radical agendas will need to be pursued to reduce resource-intensive consumption and waste and to improve governance, efficiency, and resilience.

References and Notes

1. M. Parry *et al.*, *Climate Change and Hunger, Responding to the Challenge* (World Food Programme, Rome, 2009).
2. H. C. J. Godfray *et al.*, *Science* **327**, 812 (2010).
3. Royal Society, *Reaping the Benefits: Science and the Sustainable Intensification of Global Agriculture* (Royal Society, London, UK, 2009).
4. *Foresight: The Future of Food and Farming* (Government Office of Science, London, 2011).
5. D. Tilman, C. Balzer, J. Hill, B. L. Befort, *Proc. Natl. Acad. Sci. U.S.A.* **108**, 20260 (2011).
6. E. D. Collins, K. Chandrasekaran, *A Wolf in Sheep’s Clothing? An Analysis of the ‘Sustainable Intensification’ of Agriculture* (Friends of the Earth International, Amsterdam, 2012).
7. J. A. Foley *et al.*, *Nature* **478**, 337 (2011).
8. A. Sen, *Poverty and Famines* (Oxford Univ. Press, Oxford, 1981).
9. N. Stern, *The Economics of Climate Change* (Cambridge Univ. Press, Cambridge, 2007).
10. United Nations, *The Millennium Development Goals Report* (United Nations, New York, 2009).
11. International Assessment of Agricultural Knowledge, Science and Technology for Development (IAASTD), *Agriculture at the Crossroads* (Island Press, Washington DC, 2009).
12. B. Phalan, M. Onial, A. Balmford, R. E. Green, *Science* **333**, 1289 (2011).
13. M. S. Dawkins, *Why Animals Matter* (Oxford Univ. Press, Oxford, 2011).
14. D. Fraser, *Understanding Animal Welfare: The Science in its Cultural Context* (Wiley-Blackwell, Oxford, 2008).
15. Food and Agriculture Association of the United Nations (FAO), *An Introduction to the Basic Concepts of Food Security* (FAO, Rome, 2008).
16. FAO, *Save and Grow: A Policymaker’s Guide to the Sustainable Intensification of Smallholder Crop Production* (FAO, Rome, 2011).
17. P. B. Thompson, Ed., *The Ethics of Intensification* (Springer, Heidelberg, Germany, 2008).

Acknowledgments: T.G. and H.C.J.G. acknowledge support from the Oxford Martin School. T.G.B. acknowledges support from the UK Global Food Security Programme. S.J.V. acknowledges support from the Canadian International Development Agency, the Danish International Development Agency, the European Union, and the International Fund for Agricultural Development.

10.1126/science.1234485

CREDIT: ADINA TOVY/GETTY IMAGES

ECOLOGY

Seabirds—Individuals in Colonies

Henri Weimerskirch

In a large seabird colony, hundreds of thousands of individual birds rear their young (see the figure). Such colonies require abundant food resources within the foraging range of individuals. But what happens when two or more colonies occur in close vicinity? On page 68 of this issue, Wakefield *et al.* (1) provide strong evidence that seabirds in neighboring colonies do not directly compete for food but rather segregate to search for food in different areas. They propose modeling hypotheses on how such separation might have evolved over time.

In extremely rich marine ecosystems—such as off the coasts of Peru, where nutrient-rich water upwelling from the deep ocean allows the development of immense quantities of anchovies—millions of guano-producing seabirds breed in spectacular colonies (see the figure). Fifty years ago, Ashmole argued that if food is limited, competition between individuals from the same species occurs, and resources are likely to become depleted around the colony, forcing individuals to forage farther (2). Foraging range is restricted to a maximum range set by the movement abilities of parents and the need of offspring to be fed frequently, and each colony has therefore been assumed to have its own foraging zone in the neighborhood (3). But when two colonies are located nearby, maximum ranges overlap, causing competition between individuals of the two colonies unless some form of segregation between colonies exists.

Development of satellite telemetry in the early 1990s allowed seabirds to be tracked from their colonies, allowing these hypotheses to be tested. Several studies have provided evidence that colony size and foraging range are influenced by food availability and that overlap between foraging zones of colonies may be limited. Wakefield *et al.* now report the foraging movements of gannets tracked simultaneously from 12 colonies around the United Kingdom. They show that overlap between birds from the different colonies is surprisingly limited, especially between nearby colonies, where one would expect the highest overlap, and that larger colonies use longer foraging ranges. Using a model simulating the movements of gannets, they can

Seabirds from nearby colonies forage in different locations rather than directly competing for food.



Divide and conquer. When food is abundant, seabird colonies can concentrate hundreds of thousands of individuals on a single island, such as here off the coast of Peru, where guano-producing boobies, cormorants, and pelicans pack. Wakefield *et al.* show that if such colonies are located near each other, they do not compete for food but rather segregate such that birds from each colony search for food in different locations.

only reproduce the segregation at sea between colonies if they introduce rules imposing density-dependence and neighborhood effect. Thus, by mixing two long-standing hypotheses—the Ashmole and Neighborhood models—their model can reproduce compellingly how segregation occurs.

If individuals from two neighboring colonies do not overlap at sea, this means that they do not forage randomly in all directions but fly in particular directions from the colonies. How did such segregation arise over time? Wakefield *et al.* tackle this question by modeling individual movements. They show that to obtain segregation between colonies, individuals must remember previous foraging trips and use information from other birds of the same species.

Seabirds forage from colonies in zones of high food abundance, where food availability is predictable at large scale over time. However, the exact locations of prey aggregation are generally less predictable, and to locate them, predators use specific foraging strategies (4). Given that seabirds are

long-lived, they probably use their memory not only to return to a successful prey patch from one trip to the next but also to identify larger-scale features from one season to the next and probably over their lifetime. Because prey location may change at small scale from one foraging trip to the next, having the most recent information on prey location could be important for a rapid provisioning. Colonial animals may also use information on food location from other birds of the same species, with colonies acting as an information center (5). Such information transfer has long been known for social insects such as bees but has been controversial for colonial vertebrates because of a lack of empirical evidence due to the difficulty of studying social interactions, particularly in the case of marine animals (6). Yet, information transfer between foragers may be the key process that allows active segregation between two neighboring colonies.

Although Wakefield *et al.* show through modeling that such information transfer may help to explain the evolution of segregation

Centre d'Etudes Biologiques de Chizé, CNRS, 79360 Villiers-en-Bois, France. E-mail: henriw@cebc.cnrs.fr

over time, it is still necessary to understand how individuals convey information on food location (7). They may do so passively, with birds first dispersing homogeneously and then joining other birds of the same species that have located a food patch (8). Alternatively, they may convey the information actively, similar to the way in which bees transfer information on food location in the hive by their dance (5). No study has so far been able to demonstrate this latter hypothesis, but some recent studies have suggested that the information may be passed not in the colony but through aggregations away from the colony that signal the direction of food resources (9).

To date, studies on seabird foraging have mostly remained descriptive, focusing on the patterns of distribution and their rela-

tion with the environment. Wakefield *et al.* go beyond this to not only show clear segregation patterns, but also examine the underlying processes through modeling. The next step will be to use empirical or experimental research to explore how these behaviors may have evolved through culture and social behaviors. These investigations will be facilitated by further technological developments that allow us to determine not only an animal's location but also its precise behavior, activity, energy expenditure, and prey capture. Studying interactions between individuals in the colony and at sea is also technically feasible but requires large numbers of individuals to be tracked (10). These future data on animal foraging and social interactions will open new perspectives in our understanding and ability to make more

robust predictions on many aspects, such as colony dynamics and the future impact of climate change or of fisheries (11).

References

1. E. D. Wakefield *et al.*, *Science* **341**, 68 (2013).
2. N. P. Ashmole, *Ibis* **103**, 458 (1963).
3. D. K. Cairns, *Am. Nat.* **134**, 141 (1989).
4. H. Weimerskirch, *Deep Sea Res. Part II Top. Stud. Oceanogr.* **54**, 211 (2007).
5. P. Ward, A. Zahavi, *Ibis* **115**, 517 (1973).
6. H. Richner, P. Heeb, *Adv. Stud. Behav.* **24**, 1 (1995).
7. S. R. Dall *et al.*, *Trends Ecol. Evol.* **20**, 187 (2005).
8. J. F. Wittenberger, G. L. Hunt Jr., *Avian Biology* **8**, 1 (1985).
9. H. Weimerskirch *et al.*, *PLoS ONE* **5**, e9928 (2010).
10. C. Rutz *et al.*, *Curr. Biol.* **22**, R669 (2012).
11. P. M. Cury *et al.*, J. F. Piatt, J. P. Roux, L. Shannon, W. J. Sydeman, *Science* **334**, 1703 (2011).

10.1126/science.1240316

PHYSICS

Spectroscopy Beyond the Single-Particle Limit

Gregory V. Hartland and Shun Shang Lo

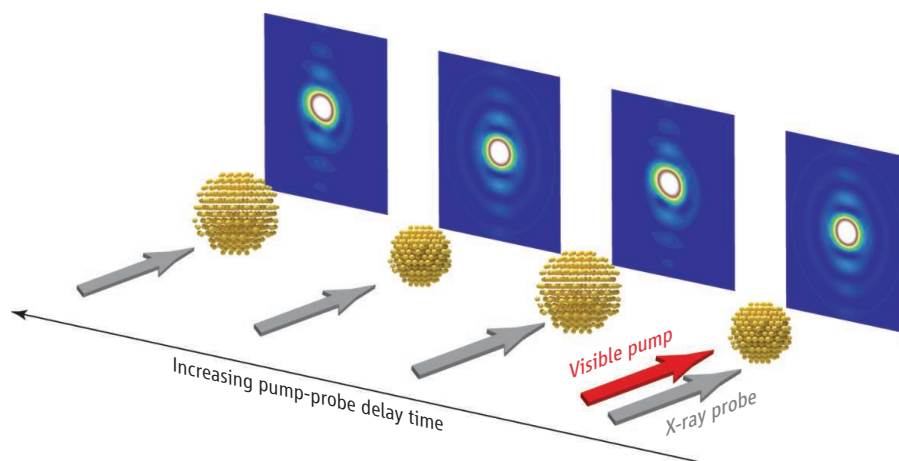
Scientists can now routinely detect and study single molecules and nanoparticles (1). However, direct observation of chemical processes and/or atomic motions in real time remains a challenge, primarily because ultrafast (subpicosecond) time resolution is needed. Optical techniques have recently been developed to study the dynamics of individual molecules or nanoparticles where two laser beams (a pump and a probe) are focused onto a single nano-object under a microscope (2, 3). The spatial resolution of these measurements is limited by the diffraction of light, so that the movements of the individual atoms can only be inferred. On page 56 of this issue, Clark *et al.* (4) present a study of the lattice motions of individual gold nanoparticles recorded using ultrafast coherent x-ray pulses as a probe. These measurements yield three-dimensional images of the atomic displacements in the particles as a function of time, with a spatial resolution that is orders of magnitude better than what can be achieved with optical microscopes.

The usual way of studying single molecules or particles, by selecting isolated objects with a high-magnification micro-

scope, is not currently possible for x-ray sources. To overcome this limitation, Clark *et al.* used a fundamentally different approach to single-particle spectroscopy. Particles with different orientations have spatially separated Bragg diffraction patterns at the image plane of the detector (5). By analyzing the position and phase of the diffraction patterns, the authors could reconstruct the time-dependent lattice distortions of selected particles. These data experimentally determine the form of the

vibrational normal modes that are excited by the pump laser in the experiments, as well as their frequencies (see the figure).

This type of information is not accessible in conventional optical transient absorption measurements, where the assignment of the observed modes (that is, a picture of what the vibrational motion looks like) relies on comparing the measured oscillation periods to continuum mechanics calculations (6, 7). For particles with simple shapes (spheres and wires), these calculations can



Particularly revealing. Time-resolved x-ray measurements by Clark *et al.* reveal the lattice motions of single nanoparticles with subnanometer spatial resolution.

Department of Chemistry and Biochemistry, University of Notre Dame, Notre Dame, IN 46557-5670, USA.
E-mail: ghartlan@nd.edu; shunshang.lo@nd.edu

be done analytically, whereas for complex-shaped particles, numerical approaches are needed. However, in both cases, fairly precise knowledge of the size and shape of the nanoparticle is required in order to assign the vibrational modes.

The analysis of Clark *et al.* does not rely on a priori knowledge of the particle's size and shape: Both the size and shape and the form of the vibrational modes come directly from the experiments. The combination of single-particle sensitivity, atomic-scale information, and ultrafast time resolution represents a tour de force in nanoscience. In addition to providing detailed information about lattice motions, x-ray measurements can be used to study any crystalline material, and are sensitive to all the vibrational motions of the object, not just ones that are strongly coupled to optical transitions (2, 6, 7). These advantages are what we mean by spectroscopy beyond the single-molecule limit.

However, there are many challenges to overcome before this technique makes conventional transient absorption microscopy measurements performed with table-top visible and near-infrared laser sources obsolete. For example, in studies of the acoustic phonon modes of nanoparticles, an important question is the time scale for energy dissipation, in particular, the effect of liquids on the relaxation of the vibrational modes (8).

These questions can be studied in conventional single-particle transient absorption measurements by using optically trapped particles (9), or by examining nanowires suspended over trenches (10). These types of experiments will be difficult to do with x-ray pulses, although it may be possible to interrogate particles in thin liquid cells by borrowing methods developed for transmission electron microscopy measurements (11).

The particles interrogated by Clark *et al.* were also fairly large—more than several hundred nanometers, which is considerably bigger than the detection limits in optical transient absorption experiments. Substantial improvements in sensitivity will be needed before particles with sizes on the order of 10 nm can be studied, which is the size range where new effects in the properties of nanoparticles start to emerge.

Advances in science often come from advances in measurement technology. The technique described by Clark *et al.* represents a fundamentally new way of studying the dynamics of single nanoparticles. The use of x-ray diffraction as a probe circumvents several of the limitations of current single-particle experiments. These measurements give direct information about atomic motions and should work for all crystalline nanomaterials. By contrast, optical transient absorption measurements can only be

used to study samples that have resonances within the tuning range of the laser source. With the current time resolution available, time-resolved x-ray measurements are well suited to studying the acoustic modes of nanomaterials. The ability to image the form of the acoustic modes, as well as follow their evolution in time, can potentially provide information about how vibrational energy is redistributed in materials after ultrafast excitation. In particular, these measurements may allow researchers to watch energy transfer between internal modes of the nanoparticle, as well as between the particles and their surroundings.

References

1. W. E. Moerner, M. Orrit, *Science* **283**, 1670 (1999).
2. M. A. van Dijk, M. Lippitz, M. Orrit, *Phys. Rev. Lett.* **95**, 267406 (2005).
3. R. Hildner, D. Brinks, N. F. van Hulst, *Nat. Phys.* **7**, 172 (2011).
4. J. N. Clark *et al.*, *Science* **341**, 56 (2013); 10.1126/science.1236037.
5. M. J. Bogan *et al.*, *Nano Lett.* **8**, 310 (2008).
6. A. L. Tchegobotareva *et al.*, *ChemPhysChem* **10**, 111 (2009).
7. A. Crut, P. Maioli, N. D. Fatti, F. Vallée, *Phys. Chem. Chem. Phys.* **11**, 5882 (2009).
8. M. Pelton *et al.*, *Nat. Nanotechnol.* **4**, 492 (2009).
9. P. V. Ruijgrok, P. Zijlstra, A. L. Tchegobotareva, M. Orrit, *Nano Lett.* **12**, 1063 (2012).
10. T. A. Major *et al.*, *Phys. Chem. Chem. Phys.* **15**, 4169 (2013).
11. J. M. Yuk *et al.*, *Science* **336**, 61 (2012).

10.1126/science.1240500

IMMUNOLOGY

Fueling Function Over Expansion in T Cells

Joseph P. Argus^{1,2} and Steven J. Bensinger^{1,2,3,4}

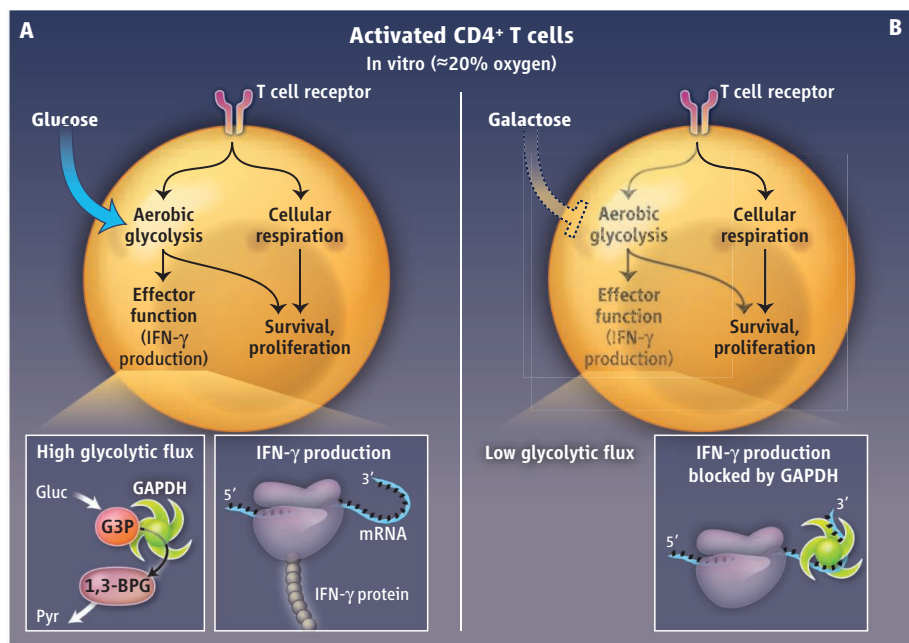
Vertebrates generate millions of unique T cell receptors during T cell development, ensuring that the immune system can recognize any number of potential pathogens. A compromise for this extraordinary molecular diversity is that the T cell population of a given individual contains only a handful of cells that can recognize any particular foreign invader.

To solve this problem, T cells can undergo extraordinary proliferation in response to infection (1). Upon activation, they adopt specialized metabolic programs, such as aerobic glycolysis [the Warburg effect (2–5)], which has long been thought to meet the biosynthetic and bioenergetic requirements associated with rapid expansion (2). But a recent study by Chang *et al.* (6) raises questions about this model and suggests instead that aerobic glycolysis is necessary for T cell effector function rather than proliferation.

Rapidly proliferating cells must accumulate biomass at a rate that keeps up with cell division. To support rapid growth, cells have evolved common metabolic themes including heightened energy production, increased protein, nucleic acid, and lipid

Cellular metabolism plays an active role in regulating immune cell function.

¹Institute for Molecular Medicine, David Geffen School of Medicine, University of California, Los Angeles, CA 90095, USA. ²Department of Molecular and Medical Pharmacology, David Geffen School of Medicine, University of California, Los Angeles, CA 90095, USA. ³Department of Pathology and Laboratory Medicine, David Geffen School of Medicine, University of California, Los Angeles, CA 90095, USA. ⁴Jonsson Comprehensive Cancer Center, University of California, Los Angeles, CA 90095, USA. E-mail: sbensinger@mednet.ucla.edu



T cell metabolism. In activated CD4⁺ T cells, T cell receptor signaling drives aerobic glycolysis and cellular respiration. When cultured in 20% O₂, T cell survival and proliferation can be supported by either metabolic process, whereas the production of effector cytokines such as IFN-γ requires aerobic glycolysis. (A) When cultured in glucose, glycolytic flux is high, GAPDH acts on the glycolytic substrate G3P, mRNA, and IFN-γ mRNA is translated. (B) When cultured in galactose, glycolytic flux is inhibited, and the lack of glycolytic intermediates causes GAPDH to bind to IFN-γ mRNA, repressing its translation. Gluc, glucose; Pyr, pyruvate; 1,3-BPG, 1,3-bisphosphoglycerate.

confer a proliferative or survival advantage. Furthermore, there are immune cells, such as macrophages and dendritic cells, that engage aerobic glycolysis during their activation but have little or no accompanying proliferation (7, 8). Thus, it is possible that the acquisition of specific metabolic programs, such as aerobic glycolysis, could be required for immune cell function but not necessary for cell division.

Chang *et al.* asked whether aerobic glycolysis or cellular respiration is an absolute requirement for T cell activation and proliferation in response to mitogenic signals. Quite strikingly, the authors found that inhibiting aerobic glycolysis through the use of a glucose analog (galactose) had only a marginal effect on the activation of CD4⁺ T cells in vitro. By contrast, inhibition of cellular respiration using an ATP synthase inhibitor (oligomycin) abolished T cell activation. In activated CD4⁺ T cells, inhibition of either aerobic glycolysis or cellular respiration did not substantially impair proliferative capacity or survival, indicating that these T cells can readily use either pathway to meet the biosynthetic and energetic requirements of clonal expansion and have considerable metabolic plasticity once they enter the replicative cycle.

Chang *et al.* further show that aerobic glycolysis is required for key features of effector T cell function. Inhibition of glycolytic flux attenuated production of the proinflammatory cytokine interferon-γ (IFN-γ) by CD4⁺ T cells. This occurred through the binding of the glycolytic enzyme glyceraldehyde-3-phosphate dehydrogenase (GAPDH) to the 3' untranslated region (3'UTR) of messenger RNA (mRNA) encoding IFN-γ, thereby blocking efficient mRNA translation. This occurred most efficiently under conditions where glycolytic flux was reduced, presumably decreasing the cellular concentration of GAPDH glycolytic substrates and allowing more GAPDH to bind to IFN-γ mRNA. Indeed, addition of the GAPDH substrate glyceraldehyde-3-phosphate (G3P) to cultures partially restored IFN-γ production, likely by outcompeting the IFN-γ mRNA for GAPDH. In this way, aerobic glycolysis becomes necessary for proinflammatory responses in CD4⁺ T cells, and GAPDH serves as the molecular sensor that coordinates glycolytic metabolism with effector T cell function (see the figure).

The full implications of the study by Chang *et al.* have yet to be understood, and a thorough series of mechanistic studies is clearly warranted. In one potential appli-

cation, the pharmacologic manipulation of GAPDH may provide a new therapeutic approach to controlling unwanted inflammation. Conversely, sequestering GAPDH away from IFN-γ mRNA may restore effector function to T cells that have reengaged cellular respiration or are “exhausted” from chronic activation. The authors did correlate the expression of a marker of T cell exhaustion, programmed death 1 (PD-1) (9), with a decline in IFN-γ production and decreased aerobic glycolysis. This suggests that chronic exhaustion could have its roots in altered metabolism. However, it remains unclear whether GAPDH directly regulates IFN-γ expression in vivo in a physiologic context. Much of the work identifying this mechanism was performed under nonphysiologic culture conditions (e.g., 20% oxygen and 100% galactose instead of glucose). Thus, it may be that under conditions that better recapitulate physiology, such as lower oxygen tension and physiologic amounts of glucose (which can reinforce aerobic glycolysis), this model of metabolic plasticity in proliferation may have limitations.

Likewise, it remains unclear whether there will ever be insufficient glycolytic flux to free up enough GAPDH protein to attenuate IFN-γ mRNA translation in vivo. One could imagine that the availability of small amounts of its preferred substrate G3P would be sufficient to keep GAPDH engaged in the glycolytic pathway rather than binding to IFN-γ mRNA. It also will be important to define the mRNAs influenced by GAPDH. Is there a wide range of mRNAs subject to this mechanism of translational control, or is it limited to the inflammatory response? Nevertheless, the study of Chang *et al.* adds to the growing body of evidence that cellular metabolism plays an active role in the regulation of immune cells' fate and function.

References

1. K. P. Murphy, P. Travers, M. Walport, C. Janeway, *Jane-way's Immunobiology* (Garland Science, New York, ed. 7, 2008).
2. C. J. Fox, P. S. Hammerman, C. B. Thompson, *Nat. Rev. Immunol.* **5**, 844 (2005).
3. M. G. Vander Heiden, L. C. Cantley, C. B. Thompson, *Science* **324**, 1029 (2009).
4. V. A. Gerriets, J. C. Rathmell, *Trends Immunol.* **33**, 168 (2012).
5. K. A. Frauwirth *et al.*, *Immunity* **16**, 769 (2002).
6. C. H. Chang *et al.*, *Cell* **153**, 1239 (2013).
7. J. C. Rodríguez-Prados *et al.*, *J. Immunol.* **185**, 605 (2010).
8. C. M. Krawczyk *et al.*, *Blood* **115**, 4742 (2010).
9. D. L. Barber *et al.*, *Nature* **439**, 682 (2006).

ANTHROPOLOGY

The Roots of Cultivation in Southwestern Asia

George Willcox

The origins of agriculture have been the source of much speculation, but recent discoveries are enabling archaeologists to piece together a more accurate picture. Fifty years ago, the earliest known farming village was Jericho in the southern Levant, dated to about 11,000 years ago (1). Since then, a series of sites dated hundreds of years earlier has been found in an arc extending to northern Iraq. Discoveries in Iran at Chogha Golan and Sheikh-e Abad (2), dated to 11,700 years ago, extend the arc to Iran, allowing five clusters of sites to be defined (see the figure, panel A). Archaeological excavations in the foothills of the Zagros Mountains of Iran reported by Riehl *et al.* on page 65 of this issue (3) provide evidence that wild cereal cultivation in the eastern cluster occurred almost as early as in the clusters farther west.

The emerging evidence shows that cultivation began at more or less the same time in all five clusters, but that the crops were different from one cluster to another. This pattern has been established at 11 sites dated to between 11,500 and 11,000 years ago, including Chogha Golan in the Zagros Mountains, where charred cereals were recovered in association with arable weeds (4). At this time, the inhabitants of these sites were not yet herders but continued to hunt large game, aurochs, gazelle, sheep, goat, and equids.

At some sites, cultivation of wild cereals occurred on a large scale, as demonstrated by discoveries of storage structures (5), installations with multiple querns (see the figure, panels C and D), and massive quantities of cereal chaff used to temper daub for construction (6). Imposing architecture has been unearthed, sometimes consisting of spectacular communal buildings, but with different styles in each cluster (7). The earliest known rectangular buildings were constructed during the early Holocene, all previous buildings being circular. Long-distance transportation of rare raw materials took place; obsidian, marine shells, bitumen, ochre, and chlorite (a stone used for carving) have been found on sites far from their sources, indicating contact between clusters.

Archeorient, CNRS–Université Lumière Lyon 2, 1 Rue Raoul-Lin, Lyon F-69365, France. E-mail: willcox.george@neuf.fr

Evidence of early cultivation of crops in the Zagros Mountains of Iran helps to elucidate where and when humans first started to cultivate wild cereals.



Early cultivation. (A) Archaeological finds from Iran reported by Riehl *et al.* allow definition of an eastern cluster of sites in the Zagros foothills where wild cereals were cultivated almost as early as in clusters farther west. Dates in blue denote early cultivation of wild cereals; dates in green are for earlier finds of cereals without evidence for cultivation. These dates may be revised as new sites are discovered. Ongoing excavations in central Anatolia and Cyprus are pushing dates back in these areas. Isolated sites without cereals are not included. (B) Mortar and pestle from Wadi Hammeh in the southern Levant, dated to 14,000 years ago (14). (C) Bases of three aligned querns in a room at Jerf el Ahmar, northern Syria (7). (D) Large quern from Tell 'Abr, northern Syria. The finds in (C) and (D) have been dated to 11,300 years ago.

Cultural and agricultural developments during the early Holocene differed strongly from one cluster to another, as recent finds from the Zagros Mountains, Cyprus (8, 9), central Anatolia, and the southern Levant (10) demonstrate. At Chogha Golan, wild cereals began to lose the ability to disperse their seeds after 9800 years ago. This evolutionary adaptation, called morphological domestication, occurred earlier in western clusters, between 10,500 and 10,000 years ago. Goat herding in the Zagros Mountains

is also dated to around 9800 years ago (11), again later than in the west. Genetic studies point to independent local domestication of barley in the Zagros cluster (12). However, more data are required to distinguish and date local domestications, as opposed to introductions between clusters.

How did cultivation originate in the Zagros foothills? Late Pleistocene sites in the Zagros Mountains have querns, but no cereal remains have been found. Cereals were in use nearly 12,000 years ago in

northern Iraq and 13,000 years ago in northern Syria. In the southern Levant they are attested at 23,000 years ago, but by 14,000 years ago, houses comparable to those of the early Holocene contained mortars and pestles that were probably used for cereal processing (see the figure, panel B). These Late Pleistocene remains do not allow differentiation between gathering and cultivation (13), but it is probable that these societies had knowledge of cultivation.

Ethnographic literature shows that hunter-gatherer groups in many parts of the world propagated plants, although they had little or no contact with farmers. The discovery

of early cultivation in the Zagros Mountains by Riehl *et al.* and the series of dates pointing back to the Late Pleistocene in the southern Levant suggest, but do not prove, that the roots of cultivation may lie there. It remains to be seen, however, whether ideas, crops, or migration were responsible for disseminating cultivation as far as the Zagros Mountains.

References and Notes

1. This and all other dates are calibrated ^{14}C dates before the present.
2. R. Matthews, W. Matthews, Y. Mohammadifar, *Central Zagros Archaeological Project: The Earliest Neolithic of Iran: 2008 Excavations at Sheikh-E Abad and Jani* (Oxbow, Oxford, 2013).
3. S. Riehl, M. Zeidi, N. J. Conard, *Science* **341**, 65 (2013).
4. G. Willcox, *Veg. Hist. Archaeobot.* **21**, 163 (2012).
5. I. Kuijt, B. Finlayson, *Proc. Natl. Acad. Sci. U.S.A.* **106**, 10966 (2009).
6. G. Willcox, D. Stordeur, *Antiquity* **86**, 99 (2012).
7. T. Watkins, *Antiquity* **84**, 621 (2010).
8. J.-D. Vigne *et al.*, *Proc. Natl. Acad. Sci. U.S.A.* **109**, 8445 (2012).
9. S. W. Manning, C. McCartney, B. Kromer, S. T. Stewart, *Antiquity* **84**, 693 (2010).
10. S. Mithen *et al.*, *Antiquity* **85**, 350 (2011).
11. M. Zeder, *Curr. Anthropol.* **52**, 5221 (2011).
12. P. L. Morrell, M. T. Clegg, *Proc. Natl. Acad. Sci. U.S.A.* **104**, 3289 (2007).
13. S. Colledge, J. Conolly, *Env. Archaeol.* **15**, 13 (2010).
14. P. C. Edwards, Ed., *Wadi Hammeh 27: An Early Natufian Settlement at Pella in Jordan* (Brill, Leiden, Netherlands, 2013), pp. 95–120.

10.1126/science.1240496

ASTRONOMY

Radio Bursts, Origin Unknown

James M. Cordes

Analyzing the transient electromagnetic signals pervading the cosmos has led to the identification of a plethora of exotic astrophysical objects. On page 53 of this issue, Thornton *et al.* (1) report on the discovery of several short radio bursts, only a few milliseconds in duration, from four widely spaced directions during a survey of the sky using the Parkes radio telescope in Australia. The bursts are not unlike individual pulses seen from pulsars, neutron stars whose spins regularly sweep a lighthouse-like beam into Earth's direction. Because of their weak emission, the majority of known pulsars reside within the Milky Way or in one of its satellite dwarf galaxies, the Large and Small Magellanic Clouds. By contrast, the new bursts appear to originate from large distances, outside the Milky Way. Truly remarkable is that a burst rate of about 10^4 bursts per day over the entire sky has been deduced. It is still early days for identifying the astrophysical origins of such common but (so far) rarely detected events.

The sources of the bursts are undoubtedly exotic by normal standards. The usual suspects include emissions from evaporating black holes (2) or from gamma-ray burst (GRB) sources that include supernovae, mergers of neutron stars, and magnetars (neutron stars with hyperstrong magnetic fields). They could originate in the centers of galaxies where compact stars interact with and plunge into supermassive black holes.

Or they could represent an entirely new class of source. Another possibility is that they are bursts much brighter than the giant pulses seen from some pulsars (3).

The measured properties of the new bursts allow the range of possible explanations to be narrowed. The pulses are distinguished from terrestrial interference by the characteristic plasma dispersion effect that causes

Observations of radio bursts that appear to originate from outside the Milky Way may suggest the existence of a large and exotic source population.

radio waves to travel more slowly at lower radio frequencies. The pulse shape encodes the amount of plasma that the pulse propagates through. The measured plasma dispersion is too high to be explained by interstellar gas in the Milky Way for the particular source directions. Where does the “extra” plasma come from? One possibility is the intergalactic medium. That would require



Remote sensing. The observed radio bursts sample ionized gas along the entire path length and therefore provide the means for sampling any host galaxy, intervening galaxies, and the intergalactic medium.

Department of Astronomy, Cornell University, Ithaca, NY 14853, USA. E-mail: jmc33@cornell.edu

the burst sources to be at large, cosmological distances. But this scenario is complicated by the possible residence of the sources within host galaxies that could contribute appreciably to the plasma budget. The source itself or its local environment may also be relevant.

Any of these complications would mandate a closer distance than if the intergalactic medium were solely responsible. The most extreme near-sited explanation would invoke a source whose emission process itself involves or mimics the plasma dispersion effect. Although contrived, this possibility cannot be excluded at present.

The observations by Thornton *et al.* provide an additional clue that favors a far-sited picture. The asymmetry of one of the pulses is easiest to explain if the scattering plasma is neither unduly close to the source nor close to Earth, which argues against the extreme near-sited explanation (see the figure). An extragalactic interpretation seems secure, but exact source distances are not known. Redshifts of 0.5 to 1 are indicated if the intergalactic medium dominates dispersion, but sources residing in galactic centers could be much closer. Determining distances is important for analyzing source energetics and estimating event rates. Translating the deduced daily rate of 10^4 radio bursts to a per-galaxy rate scales as the inverse cube of the distance, which makes any comparison highly uncertain.

The method used for identifying transient sources when sources are not well localized is to find counterparts at other wavelengths. The story of GRBs provides some lessons. Initial localizations were very poor, there was no distance information, and bursts did not repeat. Not until more than 20 years after their discovery were GRBs known to have originated from cosmological sources. Until GRB afterglows were localized in the x-ray, optical, and radio bands, speculation ranged all the way from the solar system (Oort cloud comets) to cosmological supernovae. Although the plasma dispersion of the radio bursts indicates an extragalactic origin, localization on the sky remains problematic. The single-dish telescope used for their discovery localizes to about 0.25° , far too large to find a smoking gun in, say, a particular galaxy among the large number contained in the field of view.

The future is extremely promising for time-domain astronomy. Extragalactic radio bursts are a disruptive discovery that will alter the usage and construction of radio telescopes for surveying the cosmos. Few radio bursts have been seen so far because radio observations have lacked either the necessary time resolution or the large field of view needed to sample large fractions of the sky.

Increasing the detection rate requires telescopes with much larger fields of view, such as those now being deployed and planned at low frequencies (4–7). New technologies for

multiple-pixel systems on reflector antennas will make the Square Kilometre Array and its precursors important time-domain telescopes (8–10). Currently, any repeating bursts could be localized with the Jansky Very Large Array or the Very Long Baseline Array. Arc-second positioning will result from these interferometric arrays combined with high-bandwidth digital processing to apply detection algorithms. This big-data aspect of blind radio transient surveys is a necessary part of operations for both existing and future telescopes, especially the latter. The mystery of the radio bursts will be solved and, with a sufficiently large sample, these bursts will provide an important tool for probing ionized gas, including magnetic fields, in host galaxies, the intergalactic medium, and the cosmic web.

References and Notes

1. D. Thornton *et al.*, *Science* **341**, 53 (2013).
2. M. Rees, *Nature* **266**, 333 (1977).
3. T. H. Hankins, J. A. Eilek, *Astrophys. J.* **670**, 693 (2007).
4. Long Wavelength Array; www.phys.unm.edu/~lwa.
5. Low Frequency Array (LOFAR); www.lofar.org/.
6. M. P. van Haarlem *et al.*; <http://arxiv.org/abs/1305.3550> (2013).
7. Murchison Widefield Array; www.haystack.mit.edu/mwa/.
8. Square Kilometre Array; www.skatelescope.org/.
9. MeerKAT is an antenna array under construction in South Africa; www.ska.ac.za/meerkat/.
10. ASKAP is an antenna array under construction in Western Australia; www.atnf.csiro.au/projects/mira/.

10.1126/science.1240618

IMMUNOLOGY

Making Macrophages Eat Cancer

Michael H. Kershaw¹ and Mark J. Smyth^{2,3}

A growing number of approaches to treating cancer, including antibodies, vaccines, and cell therapy, harness the immune system to seek and destroy cancer cells (1–3). Antibody-mediated immunotherapies have the potential to treat a large proportion of cancers. For decades, monoclonal antibodies have been used to directly target tumors (4, 5). However, cancer cells can develop resistance to antibodies and tumor regression may not persist in some patients. On page 88 of this issue,

Weiskopf *et al.* (6) describe an antibody-mediated tumor immunotherapy in mice that overcomes the resistance of cancer cells to antibodies.

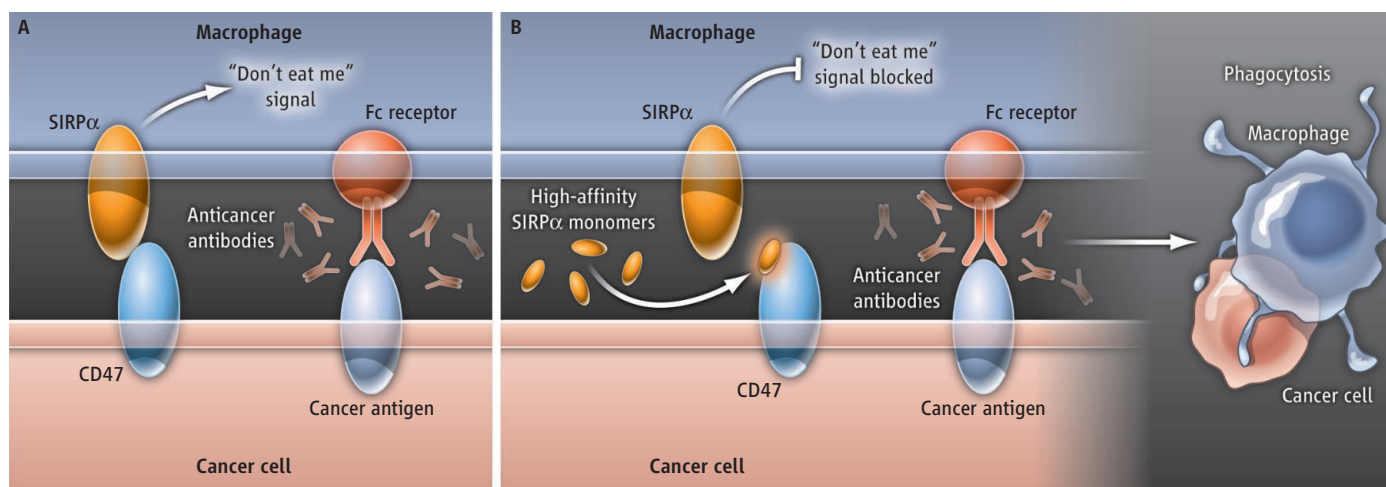
Antibodies can combat disease by aiding the action of macrophages. These immune cells engulf or “eat” diseased cells in a process called phagocytosis, which is mediated by engagement of the constant fragment (Fc) of antibodies with Fc receptors on the surface of macrophages (see the figure). However, tumors subvert normal immune control mechanisms to escape the attention of immune cells (7), including macrophages. One such mechanism involves CD47, a protein expressed by normal cells. CD47 interacts with a receptor on macrophages called signal-regulatory protein α (SIRP α). This leads to the transmission of a “don’t

Antibody-based therapies to treat cancer may get a boost from an adjuvant that prevents cancer cells from escaping engulfment by macrophages.

eat me” signal to macrophages, which then leave normal cells alone (8). Expression of CD47 by cancer cells renders them resistant to macrophages, even when the cancer cells are coated with an antibody. Because macrophages often occur in large numbers in tumors, they are ideally placed to act against cancer cells if the “don’t eat me” signal is switched off.

One therapeutic strategy is to block the “don’t eat me” signal with a monoclonal antibody against CD47 (9). However, binding of anti-CD47 antibodies to normal cells can produce adverse side effects, and their large size can impede their penetrance of tumors. To overcome these limitations, Weiskopf *et al.* synthesized a soluble form of SIRP α monomers that block the interaction of CD47 with SIRP α expressed by mac-

¹Cancer Immunology Program, Sir Peter MacCallum Department of Oncology, University of Melbourne, Parkville, 3010 Victoria, Australia. ²Immunology in Cancer and Infection Laboratory, Queensland Institute of Medical Research, Herston, 4006 Queensland, Australia. ³School of Medicine, University of Queensland, Herston, 4006 Queensland, Australia. E-mail: mark.smyth@qimr.edu.au



Macrophages, unleashed. (A) Cancer cells can be eliminated either directly by immune cells (not shown) or indirectly by antibodies that bind to antigens expressed by cancer cells, but many tumor cells escape destruction and continue to proliferate. Binding of CD47 on cancer cells to SIRP α on macrophages

transmits a “don’t eat me” signal to the macrophage, and the cancer cell evades destruction. (B) High-affinity soluble SIRP α monomers, when administered with antibodies, block CD47–SIRP α interaction, thereby preventing the “don’t eat me” signal and allowing the macrophage to engulf the cancer cell.

rophages. This soluble SIRP α (~14 kD) is much smaller than anti-CD47 antibodies. By screening a library of mutant forms of SIRP α , the authors identified variants (FD6 and CV1) with affinities 50,000-fold greater than that of natural SIRP α .

The crystal structure of FD6 bound to CD47 revealed that the interaction would likely block the “don’t eat me” signal. Indeed, Weiskopf *et al.* showed that monomeric high-affinity SIRP α increased the engulfment of antibody-coated cancer cells by macrophages in vitro. Remarkably, when CV1 was given to mice in combination with the monoclonal antibodies rituximab or trastuzumab (used to treat lymphoma and breast cancer, respectively), tumor growth was reduced or eliminated entirely.

The immunodeficient mice used by Weiskopf *et al.* express a SIRP α allele that binds to human CD47, which enables in vivo evaluation of human CD47 blockade by high-affinity SIRP α . The high-affinity soluble SIRP α can bind to mouse CD47 and thus the animal model allows not only the engraftment of human tumors, but also the evaluation of efficacy and toxicity due to CD47 expression on normal mouse cells. Interestingly, chronic anemia was noted in both mice and cynomolgus macaques (which express a CD47 ortholog that is nearly identical to human CD47), but only when the SIRP α variant (CV1) contained a region that could bind to the Fc receptor. Thus, separating CD47 blockade from Fc receptor engagement appears to be a safer anticancer strategy. One important limitation of the animal model is that the immunodeficient mice lack many types of immune cells, including regulatory and effector T cells, B

cells, and natural killer cells; and it is unclear whether this approach to therapy will succeed in immune-competent mice or patients. Further, the immunodeficient mice used by Weiskopf *et al.* lack endogenous antibodies, and it is unknown how safe or immunogenic this approach would be in humans, particularly those possessing autoimmune antibodies.

Weiskopf *et al.* did observe a marked increase in macrophage-mediated phagocytosis of cancer cells and/or inhibition of tumor growth in the mouse model, irrespective of the type of cancer or therapeutic monoclonal antibody used. Therefore, the high-affinity SIRP α molecules may be useful to treat many types of cancer for which therapeutic antibodies currently have limited effects.

Antibodies can act on tumors in a number of ways, from blocking growth factors to recruiting immune cells that attack cancer cells (10). Although macrophages have some anticancer activity, the study by Weiskopf *et al.* suggests that their potential has been underestimated and that harnessing their phagocytic capabilities with antibodies and monomeric SIRP α is a substantial improvement.

Advances in generating antibodies for treating malignant disease include the humanization of antibodies and optimization of their binding to Fc receptors (11, 12). Weiskopf *et al.* build on these improvements to realize a much greater potential of antibodies. Direct coupling of drugs and toxins to antibodies has also provided better targeting of cytotoxic agents against cancer (13), although some side effects still occur. Perhaps the SIRP α strategy described by Weiskopf *et al.* will enable macrophages to destroy cancer without the use of toxins.

This approach could also be used in combination with immunotherapies that boost the activity of immune cells other than macrophages. One method is to also block the so-called checkpoint molecules—cytotoxic T lymphocyte–associated antigen 4 (CTLA-4) and programmed death 1 (PD-1)—that inhibit T cells of the immune system (3). Combining SIRP α and antitumor antibodies with checkpoint blockade may liberate multiple components of immunity, including macrophages and T cells, in a united assault on cancer. More than 100 antibodies are in current clinical use against cancer. It is likely that a combination of tumor immunology, structural chemistry, and genetic engineering will dramatically revolutionize cancer treatment.

References and Notes

1. D. L. Porter, B. L. Levine, M. Kalos, C. H. June, *N. Engl. J. Med.* **365**, 725 (2011).
2. S. L. Topalian *et al.*, *N. Engl. J. Med.* **366**, 2443 (2012).
3. J. D. Wolchok *et al.*, *N. Engl. J. Med.* 10.1056/NEJMoa1302369 (2013).
4. G. Salles *et al.*, *Lancet* **377**, 42 (2011).
5. D. J. Slamon *et al.*, *N. Engl. J. Med.* **344**, 783 (2001).
6. K. Weiskopf *et al.*, *Science* **341**, 88 (2013); 10.1126/science.1238856.
7. R. D. Schreiber, L. J. Old, M. J. Smyth, *Science* **331**, 1565 (2011).
8. S. B. Willingham *et al.*, *Proc. Natl. Acad. Sci. U.S.A.* **109**, 6662 (2012).
9. D. Tseng *et al.*, *Proc. Natl. Acad. Sci. U.S.A.* 10.1073/pnas.1305569110 (2013).
10. M. J. Glennie, R. R. French, M. S. Cragg, R. P. Taylor, *Mol. Immunol.* **44**, 3823 (2007).
11. M. S. Co, C. Queen, *Nature* **351**, 501 (1991).
12. F. Li, J. V. Ravetch, *Science* **333**, 1030 (2011).
13. M. Mathew, R. S. Verma, *Cancer Sci.* **100**, 1359 (2009).

Acknowledgments: M.H.K. and M.J.S. are supported by the National Health and Medical Research Council of Australia.

10.1126/science.1241716

Somatic Mutation, Genomic Variation, and Neurological Disease

Annapurna Poduri, Gilad D. Evrony, Xuyu Cai, Christopher A. Walsh*

READ THE FULL ARTICLE ONLINE
<http://dx.doi.org/10.1126/science.1237758>

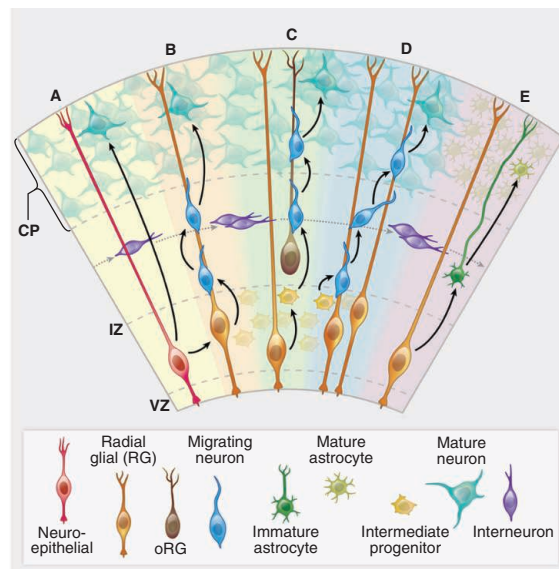
Cite this article as A. Poduri *et al.*, *Science* **341**, 1237758 (2013). DOI: 10.1126/science.1237758

Background: Genetic mutations that cause human disease are conventionally considered to be inherited from one's parents and present in all somatic (body) cells. We do know, however, that most mutations that cause cancer arise somatically, and we are becoming increasingly aware of mutations that cause other diseases and that arise *de novo*, meaning they are undetectable in the parents. Some such *de novo* mutations arise in the gamete of a parent, but some arise after fertilization during embryonic development, generating somatic mutations. Somatic mutations occur in several neurodevelopmental diseases associated with epilepsy, autism spectrum disorders, and intellectual disability, although their broader relevance for neurological disease is unknown.

Advances: A key recent advance has been the increasing identification of somatic mutations in affected tissues. For example, somatic mutations in several genes (*PIK3CA*, *AKT3*, and *mTOR*) cause enlargement of just one hemisphere of the brain, a malformation called hemimegalencephaly that is highly associated with epilepsy. These mutations may or may not be found in the blood, the convenient source tissue for DNA analysis, thus presenting a challenge to disease gene identification. Remarkably, patients can show dysfunction of essentially an entire half of their cerebral cortex when only 8 to 35% of the brain cells carry the mutation, suggesting that a minority of cells with a somatic mutation can disrupt the function of widespread cortical circuits. These discoveries suggest that somatic, perhaps brain-only, mosaic mutations may be important for other neurodevelopmental diseases. However, finding the mutations and the affected cells may require special study designs and technology.

In parallel with the discovery of somatic mutations responsible for neurological disease has been a continuing interest in the possibility that somatic mutations may occur in brain cells during normal development. New technologies, such as the study of the genomes of single neurons, promise to address some of these questions by allowing the systematic analysis of all types of somatic mutations in normal and diseased tissue.

Outlook: The role of somatic mutation in neurological disease is only beginning to be explored and may have relevance to many types of conditions from brain malformations to epilepsy, intellectual disability, and autism. Novel, highly sensitive technologies will allow more accurate evaluation of somatic mutations in neurodevelopmental disorders and during normal brain development.



Cortical development—origins of pyramidal neurons and astrocytes in the cerebral cortex. (A) A neuroepithelial cell (red) at the ventricular zone serves as progenitor for both a pyramidal neuron (green-blue) as well as a radial glial cell (gold). (B) A newly differentiated neuron (blue) migrates along a radial glial process. (C) Neurons (blue) continue to migrate as intermediate progenitor cells (small yellow) form. (D) Intermediate progenitor cells begin to generate neurons (blue). (E) The progenitor cells in the ventricular zone begin to give rise to astrocytes (dark green). Interneurons (purple) generated elsewhere migrate tangentially. CP, cortical plate; IZ, intermediate zone; VZ, ventricular zone. The VZ early in development has a thickness of ~10 cell bodies (50 to 100 μ m). The CP ranges in thickness from two to three cell bodies at the earliest stages of development, eventually forming a mature cerebral cortex that is 2 to 4 mm thick.

ARTICLE OUTLINE

"Obligatory" Somatic Mosaic Disorders?

How Do Somatic Mutations Manifest as Neurological Disease?

"Second Hit" Mutations Produce Mosaicism

Neurodevelopmental Disorders Caused by Somatic Mutations

"Brain-Only" Somatic Mutations

Neurodegenerative Diseases Caused or Modulated by Somatic Mutation

How Does Cortical Clonal Architecture Influence Mosaic Mutations?

Other Neurological Diseases Attributable to Somatic Mutation?

Contribution to Functional Cellular Diversity in the Brain?

Techniques for Further Study of Somatic Variation in the Brain

Conclusions

BACKGROUND READING

Somatic mutations that activate the signaling kinase AKT3 and related genes suggest mechanisms for the neurodevelopmental malformation hemimegalencephaly. Sequencing of individual cells from a patient with a mutation has shown that an early progenitor in the developing brain was the site of mutation.

A. Poduri *et al.*, Somatic activation of AKT3 causes hemispheric developmental brain malformations. *Neuron* **74**, 41–48 (2012). doi:10.1016/j.neuron.2012.03.010

J. B. Rivière *et al.*, *De novo* germline and postzygotic mutations in AKT3, PIK3R2 and PIK3CA cause a spectrum of related megalencephaly syndromes. *Nat. Genet.* **44**, 934–940 (2012). doi:10.1038/ng.2331

J. H. Lee *et al.*, *De novo* somatic mutations in components of the PI3K-AKT3-mTOR pathway cause hemimegalencephaly. *Nat. Genet.* **44**, 941–945 (2012). doi:10.1038/ng.2329

Neurodevelopment
 Part of an occasional series
www.sciencemag.org/extra/neurodev

The list of author affiliations is available in the full article online.

*Corresponding author. E-mail: christopher.walsh@childrens.harvard.edu

Somatic Mutation, Genomic Variation, and Neurological Disease

Annapurna Poduri,^{1,2} Gilad D. Evrony,^{3,4} Xuyu Cai,^{3,4} Christopher A. Walsh^{2,3,4*}

Genetic mutations causing human disease are conventionally thought to be inherited through the germ line from one's parents and present in all somatic (body) cells, except for most cancer mutations, which arise somatically. Increasingly, somatic mutations are being identified in diseases other than cancer, including neurodevelopmental diseases. Somatic mutations can arise during the course of prenatal brain development and cause neurological disease—even when present at low levels of mosaicism, for example—resulting in brain malformations associated with epilepsy and intellectual disability. Novel, highly sensitive technologies will allow more accurate evaluation of somatic mutations in neurodevelopmental disorders and during normal brain development.

With the exception of cancer, human genetic diseases have been until relatively recently thought to reflect inherited DNA variation. Inherited mutations are present in the parent (or parents) and in all tissues of the affected individual (Fig. 1, A and B). Hence, they can be conveniently assayed in any tissue of the body, including readily available peripheral blood. Even though inherited mutations are present in essentially all cells, they may affect some tissues more than others, depending upon where and when the gene involved has its essential roles.

Increasing evidence shows the importance of “de novo” mutations—those present in affected offspring but not detected in the parents—in neuropsychiatric and pediatric disorders (1–8). These de novo mutations are typically present in the sperm or egg of one parent and yet are not detectable in blood taken from the parents; once transmitted to the embryo, they are present in all tissues of the offspring (Fig. 1, C and D). Whole-exome sequencing studies have shown that most individuals have one or two spontaneous mutations in the exome (the part of the genome encoding proteins) that are not present in their parents, but in individuals with neurodevelopmental and neuropsychiatric conditions [such as autism spectrum disorders (ASDs)] these de novo mutations are more likely to be damaging, suggesting that some of these de novo mutations cause disease (1, 4, 5, 8). In fact, mutations that greatly increase the risk of neurodevelopmental or neuropsychiatric disease—even when only one of the two alleles of a gene is affected (heterozygous mutations)—appear to arise de novo most of the time and are inherited relatively rarely. This is not unexpected because individuals with

these disorders are less likely to bear offspring, placing the disease-causing mutations under strong negative selection. Because affected people thus rarely transmit the mutation to children, the presence of the disease reflects the ongoing appearance of new mutations.

Disease-causing mutations can also occur during the mitotic cell divisions that generate the embryo after fertilization and zygote formation. These mutations lead to individuals who are mosaic, with only a subset of their cells harboring the mutation (Fig. 1, E and F). These mutations are de novo in the sense that they are not detectable in the parents of the affected individuals but are more specifically termed somatic mutations. Somatic mutations can give rise to cancer (9), as well as noncancerous diseases. Noncancerous somatic mutations that occur during development may affect cell proliferation, as would be the case in cancer, or they may simply alter cellular function without causing a proliferative effect. There are estimates that the mutation burden in somatic cells is quite high, and estimates based on known mutation rates suggest that every cell division creates some form of genetic variation, which may or may not have an effect on cellular function (10, 11). Several recent studies have even suggested that the brain may harbor widespread somatic mutations, in the form of aneuploidy or retrotransposon insertions, perhaps as part of its “normal” development (12–14). If somatic mutations, especially in brain cells, do play a role in “complex” diseases (that is, diseases with genetic influences that are non-Mendelian), detecting them represents a substantial challenge with current sequencing strategies that mainly analyze blood DNA.

Here, we will review the present state of data about somatic mutations in human neurological disease. We highlight the recent identification of disease-associated somatic mutations present in the brain but undetectable in the blood of the same patient (Fig. 1, G and H) and discuss the challenges of identifying such rare mosaic mutations. We further discuss how emerging techniques will allow more refined study of the types

and rates of somatic mutation and genomic variation in the brain.

“Obligatory” Somatic Mosaic Disorders?

Severe genetic diseases that are not compatible with survival or fertility would be expected to be preferentially or exclusively caused by either recessive mutations or dominant de novo (detectable in the affected child but not the parents) mutations. This is because recessive mutations that affect survival or fertility in the homozygous state can persist in the population in a heterozygous state, whereas severe dominant mutations cannot be passed to offspring when present in enough cells to cause severe disease in a parent. From this, we would predict that for any disease caused by a dominant mutation the ratio of sporadic cases caused by de novo mutations to cases caused by inherited mutations as seen in recurrent familial cases should correlate with the severity of the disease's effect on survival and fertility. The most deleterious mutations that are not compatible with embryonic development might even be found only as somatic mosaic and not as inherited mutations.

Indeed, there are numerous examples of diseases spanning the spectrum of severity that follow these predictions. Proteus syndrome is a severe syndrome characterized by multiple overgrowths of the skin, bone, connective tissue, and other tissues caused by a dominant somatic mutation in the gene encoding serine-threonine protein kinase B α (PKB α), *AKT1* (15). It has never been reported to be recurrent in a family or to be heritable across generations, which is consistent with its severity in the mosaic state and likely incompatibility with survival if it were inherited and present at the zygote stage. The multiple lesions of Proteus syndrome contain between 1 and 50% mutant cells, suggesting that a small fraction of abnormal cells can induce a lesion (15). McCune-Albright syndrome is often cited as an example of a severe disease caused by somatic mutation (in the gene encoding the guanine nucleotide binding protein, alpha stimulating, *GNAS1*) but not seen as familial inherited cases, which is likely due to the incompatibility of inherited mutations with embryonic development (16). Maffucci syndrome is another example of a severe overgrowth syndrome, characterized by multiple cartilaginous tumors, seen only as sporadic cases caused by somatic mutation in the gene encoding isocitrate dehydrogenase 1, *IDH1* (17). Somatic activating mutations in the gene encoding phosphatidylinositol-4,5-bisphosphate 3-kinase, catalytic subunit alpha, *PIK3CA*, are the cause of congenital lipomatous overgrowth with vascular, epidermal, and skeletal anomalies (CLOVES) syndrome (18, 19). Similarly, somatic activating mutations in the gene encoding guanine nucleotide binding protein q polypeptide, *GNAQ*, are associated with the lesions seen in the neurocutaneous disease Sturge Weber syndrome (20). As with the previous examples, these latter examples

¹Department of Neurology, Boston Children's Hospital, Boston, MA 02115, USA. ²Department of Neurology, Harvard Medical School, Boston, MA 02115, USA. ³Division of Genetics, Manton Center for Orphan Disease Research, and Howard Hughes Medical Institute, Department of Medicine, Boston Children's Hospital, Boston, MA 02115, USA. ⁴Program in Biological and Biomedical Sciences, Harvard Medical School, Boston, MA 02115, USA.

*Corresponding author. E-mail: christopher.walsh@childrens.harvard.edu

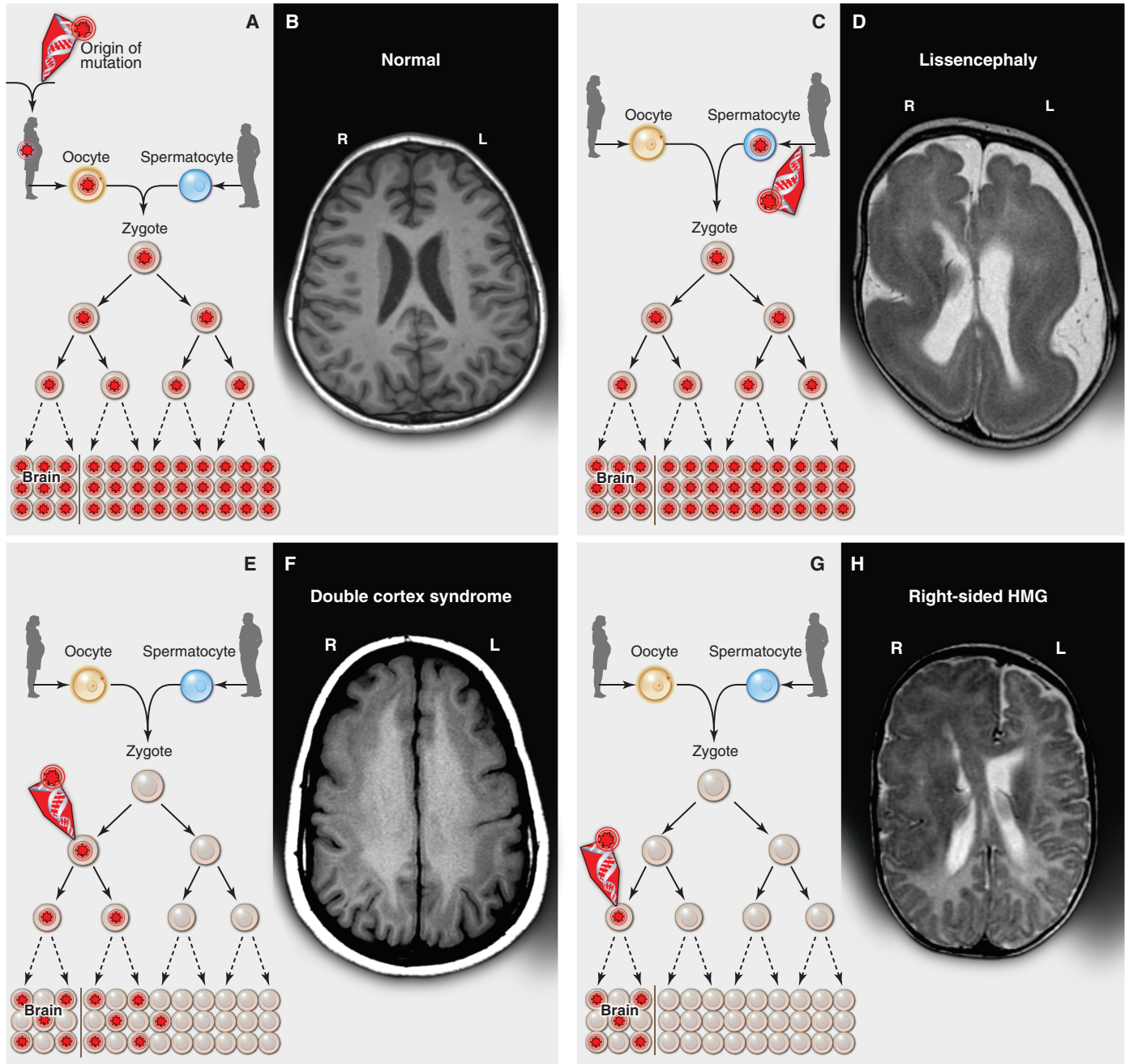


Fig. 1. Inherited, de novo, and somatic mutations causing neurological disease. (A) A heterozygous mutation is inherited from one parent. This mechanism is typical of autosomal dominant epilepsy. In this example, the mutation originally presented in the mother, whose oocytes in turn carry the mutation. (The mutation arose during gametogenesis in one of the parents of the mother, top left.) It is present in the zygote and thus all cells of the affected child. (B) This axial T1-weighted image from a MRI study of a patient with inherited epilepsy appears normal. Individuals with dominantly inherited epilepsies caused by mutations in genes encoding ion channels, for example, have normal neuroimaging studies despite every cell carrying a mutation. (C) A de novo mutation may arise sporadically during gametogenesis, in this case spermatogenesis. This mechanism of mutation would be typical of a de novo mutation in the gene *SCN1A* associated with severe myoclonic epilepsy of infancy or *LIS1* associated with lissencephaly. Even though every cell in the individual carries the mutation, the predominant effects of the mutation depend on the distribution of gene expression; in these examples, the brain is primarily affected. (D) An axial T2-weighted MRI image shows the severe gyral simplification—more pronounced posteriorly (the bottom of the figure)—that

is associated with mutations in the gene *LIS1*. (E) An early post-zygotic mutation results in a mutation present in most or all tissues of the organism (including the leukocytes, which are generally assayed for clinical genetic testing) but in a mosaic fashion, with only a portion of all cells in each tissue harboring the mutation. This pattern, illustrated by the axial T1-weighted image in (F), has been observed in mosaic cases of double cortex syndrome involving the gene *DCX*. Visible is the extra band of gray matter underlying the normal-appearing outer aspect of the cerebral cortex. Because *DCX* is required for normal migration of neurons from the ventricular region deep in the brain to the superficial cortex, the cells carrying the *DCX* mutation only migrate about halfway to the cortex and then arrest their migration. (G) A late post-zygotic mutation will be present in only certain tissues in a mosaic fashion, in this case apparently in half of the brain. This is the pattern observed in some cases of HMG with somatic mosaic point mutations in *AKT3* and other related genes and somatic mosaic increase of copy number of chromosome 1q. (H) This axial T2-weighted MRI image shows right-sided HMG, characterized here by enlargement of the right hemisphere, abnormally thick and dark-appearing gray matter anteriorly, heterotopic periventricular gray matter, and abnormal white matter signal in the right hemisphere. (R, right; L, left).

do not recur in families and present as sporadic somatic disorders. Somatic mutations affecting the brain are discussed below.

The above examples resemble chromosomal aneuploidies in that many aneuploidies that cause severe disease are tolerated only as somatic mosaic mutations. Aneuploidy of chromosomes 13, 18, 21, and the sex chromosomes accounts for nearly all aneuploidy live births, in which all cells in the body carry the extra chromosome. On the other hand, aneuploidies of other chromosomes are only tolerated during development as somatic mosaics (21, 22). Down syndrome (trisomy of chromosome 21) and other chromosomal trisomies, such as trisomy 13 or 18, are associated with intellectual disability and other features of brain dysfunction caused by the abnormal chromosome number. Mosaic forms of trisomy 21 occur in a certain proportion of cases of Down syndrome in which the extra chromosome is present in some but not all cells of the body (23). Mosaic trisomies have also been observed for many other chromosomes (such as chromosomes 1, 8, 9, 16, 17, and 22) that are rarely observed constitutionally (present in all cells) because these trisomies, if present in all cells of the body, would be lethal before or soon after birth (24–30). In each of these conditions, the severity of the disorder is determined by the particular chromosome duplicated, as well as by the proportion of cells in the body carrying the abnormality.

How Do Somatic Mutations Manifest as Neurological Disease?

"Second Hit" Mutations Produce Mosaicism

The importance of somatic mutations has long been understood in the context of several dominant conditions in which patients inherit a heterozygous mutation, present in all cells, with somatic second mutations leading to overgrowth of specific tissues because of inactivation of a second allele, according to the "two-hit" model of Knudson (31). For example, neurofibromatosis type 1 (NF1)—which is associated with focal lesions of the skin, optic gliomas, and peripheral nervous system tumors called neurofibromas—is characterized by germline mutations in the gene *NF1*, with second mutations in the other *NF1* allele causing the neurofibromas (32). A similar phenomenon occurs in the multisystem disorder tuberous sclerosis complex (TSC), a condition caused by mutations in the genes *TSC1* and *TSC2* (33, 34), whose gene products form a protein-protein complex together and regulate the mammalian target of rapamycin (mTOR) pathway; somatic second mutations have been shown in non-nervous system tumors of TSC (35), and "second hits" in the form of posttranslational inactivation of *TSC2* have been shown in subependymal giant cell astrocytomas, as well as in the noncancerous cortical tubers in patients with TSC (36). Mutation of the second *TSC* allele in cortical tubers has been hypothesized to occur as well but has so far been demonstrated for only

a single TSC lesion (37). These neurocutaneous syndromes give us a sense of how common somatic mutations really are because the somatic mutations are revealed in the presence of hamartomatous lesions. Remarkably, typical patients with these conditions have dozens of lesions of various tissues, suggesting that deleterious somatic mutations at any single gene occur many times during normal development.

Neurodevelopmental Disorders Caused by Somatic Mutations

The role of somatic mutations has been known for many years in genetic conditions that can be diagnosed by means such as physical examination or magnetic resonance imaging (MRI). In two examples, genetic disorders of neuronal migration in the brain have been associated with somatic mutations in 5 to 10% of patients. Mutations in the gene *lissencephaly-1* (*LIS1*) are typically associated with a "smooth brain" phenotype of lissencephaly (an example of which is shown in Fig. 1D) because of grossly abnormal neuronal migration, whereas mutations in *doublecortin* (*DCX*), located on the X chromosome, are associated with lissencephaly in males and a subcortical band heterotopia pattern (or "double cortex") in females (an example of which is shown in Fig. 1F) (38, 39) because chromosome X-inactivation creates mosaic populations of cells in the female that have either normal or abnormal *DCX* function. Somatic mutations in *LIS1* affecting only a portion of migrating neurons can result in the "double cortex" pattern (40), and similarly, males with somatic mutations in *DCX* can exhibit a "double cortex" because only some neurons carry the mutation (41). In both of these cases, mutations were detectable in mosaic form in leukocytes, suggesting that a relatively early postzygotic, somatic mutation occurred.

Somatic mutation has also been described in cases without visible focal lesions, including in epilepsy. For example, severe myoclonic epilepsy of infancy (Dravet syndrome), typically caused by de novo mutations in the gene encoding the sodium channel alpha-1 subunit, *SCN1A*, has recently been described as occurring not only at the gamete stage but also in the form of a somatic mutation at the postzygotic stage, including in monozygotic twins discordant for the mutation (42, 43).

"Brain-Only" Somatic Mutations

Many focal malformations of cerebral cortical development, such as focal cortical dysplasia, have been hypothesized to occur via somatic mutation in the developing brain (44), but testing this hypothesis required the availability of brain tissue that was resected from affected individuals for control of intractable epilepsy. We and others recently reported a somatic genetic explanation for a condition called hemimegalencephaly (HMG), which is characterized by enlargement and extensive malformation of an entire cerebral hemisphere (Fig. 1H) (45–47). Previously, no spe-

cific genes had been identified for isolated HMG, although there had been rare reports of HMG associated with the overgrowth syndromes TSC (48) and Proteus syndrome (49). Direct study of HMG brain tissue surgically resected in the course of treatment of the severe epilepsy led to the identification of somatic activating mutations in the gene *AKT3*, encoding PKBy a serine-threonine kinase upstream from mTOR that is highly expressed in the developing brain during corticogenesis. In at least some cases, the mutation was shown to be absent from leukocytes of the affected child (46). HMG can also result from somatic mutations in other genes of the phosphoinositide 3-kinase (PI3K)–AKT3–mTOR pathway, including *PIK3CA* and *mTOR* itself (45, 47). Additional cases carry mosaic gain of copy number of chromosome 1q (the locus of *AKT3*) in HMG brain tissue, demonstrating a different mechanism of mutation that can occur somatically during brain development and one that would not be tolerated if it were present in the germline because of severe developmental defects in multiple organ systems (24, 46). The most common HMG-associated *AKT3* mutation, Glu¹⁷Lys, is precisely paralogous to the *AKT1* mutation that causes Proteus syndrome, whereas the paralogous mutation in *AKT2* causes a predominantly non-neurological disorder, hypoglycemia-hemihypertrophy syndrome (15, 50). The different phenotypes presumably arise because of differences in the timing and location of expression of the three *AKT* genes.

In addition to some cases being caused by mutations apparently limited to brain, megalencephaly (large brain size, affecting one or both hemispheres) can also occur in the setting of somatic de novo mutations, which are detectable at low levels in leukocytes, and in *AKT3* and *PIK3CA* as part of the megalencephaly-capillary malformation and megalencephaly-polydactyly-polymicrogyria-hydrocephalus syndromes (45). Taken together, these studies suggest that brain overgrowth syndromes can be caused by mutations in brain progenitor cells, but that some of these mutations occur early enough in development to be present in many tissues, affecting cells outside the brain as well. In contrast, other mutations might be limited to the brain because they occur after the embryonic separation of brain from nonbrain tissue.

Neurodegenerative Diseases Caused or Modulated by Somatic Mutation

Some cases of neurodegenerative diseases have been associated with somatic mutations or can be modified by somatic mutations. A fascinating case of sporadic, early-onset Alzheimer's disease has been attributed to a somatic mosaic presenilin-1 mutation present in the brain (51). A case of sporadic Creutzfeldt-Jakob disease was caused by an early embryonic somatic mutation identified by the presence of three alleles for the gene encoding the major prion protein PrP (*PRNP*) in the individual (52). Incontinentia pigmenti can

lead to atrophy of the cortex and cerebellum, with some cases due to somatic mutation in the gene encoding the inhibitor of kappa light polypeptide gene enhancer in β cells, kinase gamma (IKBKG, also known as *NEMO*) (53). Some neurodegenerative diseases—such as Friedrich's ataxia, dentatorubral-pallidoluysian atrophy, and Huntington's disease—are caused by inheritance of expanded microsatellite repeats that are highly mutable; these loci can exhibit marked somatic heterogeneity in repeat lengths across brain regions and tissues of affected individuals (54–60). Age-related (postdevelopmental) somatic mutation, known to play a role in cancer, has also been widely postulated as playing a role in normal aging processes as well as in neurodegeneration (61, 62), but a full consideration of such age-related somatic mutation is beyond the scope of this Review.

How Does Cortical Clonal Architecture Influence Mosaic Mutations?

A specific progenitor cell in which a somatic mutation occurs transmits the mutation to its daughter cells, the extent and effects of which will depend on which cells of the developing cortex are involved. Understanding the clonal architecture of the developing human brain can therefore help us understand how somatic mutations cause neurogenetic disease. Cortical development, showing various neuronal and glial cells and their origins, is outlined in Fig. 2. Direct information about cell lineage patterns in the human brain is not available, but studies in animal models suggest substantial complexity in the brain's clonal structure. The principal (excitatory) neurons of the cerebral cortex and hippocampus are derived from an embryonic neuroepithelium, with progenitor cells lining the ventricular surfaces, deep in the brain (63). However, unlike most embryonic epithelia, which typically produce patches of clonal cells that adjoin or remain near one another, cerebral cortical progenitors produce postmitotic neurons that migrate radially from the deep ventricle to the superficial, outer layers of the brain. This long-distance, radial migration has been shown in a number of animal models to be associated with substantial dispersion between neurons with common clonal origins (64).

Clones of related pyramidal neurons generally maintain a funnel shape but are typically highly interspersed with neurons of diverse clonal origins, so that neurons carrying a mosaic mutation would be expected to be somewhat clustered but intermingled with neurons from distinct origins (65–68). More limited studies in animals with large, gyrated brains (for example, ferret and macaque) suggest similar patterns of clustering of sibling cells, but with extensive intermingling of clones (illustrated in Fig. 3, A and B) (65, 66, 68, 69). Thus, somatic mutations could produce clones of mutant cells that might mainly concentrate in functional regions of cortex (70) but may also involve only a small proportion of the cells harboring the mutation, making

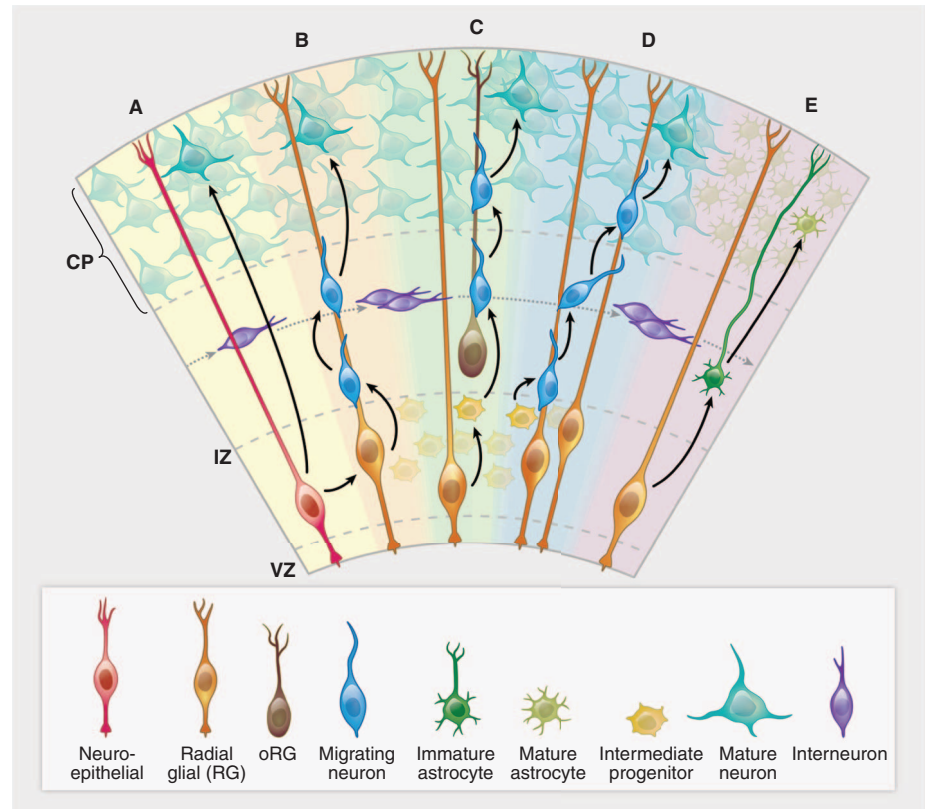


Fig. 2. Cortical development—origins of pyramidal neurons and astrocytes in the cerebral cortex. (A) A neuroepithelial cell (red) at the ventricular zone serves as progenitor for both a pyramidal neuron (green-blue) as well as a radial glial cell (gold). (B) A newly differentiated neuron (blue) migrates along a radial glial process. (C) Neurons (blue) continue to migrate as intermediate progenitor cells (small yellow) form. (D) Intermediate progenitor cells begin to generate neurons (blue). (E) The progenitor cells in the ventricular zone begin to give rise to astrocytes (dark green). Interneurons (purple) generated elsewhere migrate tangentially. CP, cortical plate; IZ, intermediate zone; VZ, ventricular zone. The VZ early in development has a thickness of ~10 cell bodies (50 to 100 μ m). The CP ranges in thickness from two to three cell bodies at the earliest stages of development, eventually forming a mature cerebral cortex that is 2 to 4 mm thick.

such mutations difficult to detect by standard sequencing techniques. Human lesions with a funnel-shaped appearance on neuroimaging exist in the form of focal cortical dysplasias (Fig. 3, C and D). The appearance of these focal cortical dysplasias, their frequent continuity into the ventricular region of the brain even in adulthood, and their similarity to the focal cortical lesions (“tubers”) in TSC all have suggested that focal cortical dysplasias may represent mosaic mutations of these deep pyramidal-neuron progenitors, but this remains incompletely worked out. In addition to the determination of the extent of dispersion of neurons derived from progenitors at the ventricular zone, neurons undergo layer specification through a series of fate restriction and specification processes during or after mitosis (64). Any disruption in the normal sequence of layer determination and subsequent functional specification—for example, by mutations occurring during progenitor mitoses—might place an individual at risk for localized, cell type-specific or even layer-specific functional abnormalities, such as those that occur in conditions such as epilepsy.

In contrast to pyramidal neurons, other cell types of the brain show even less evidence of clonal clustering, so that sibling cells sharing a mosaic mutation would be expected to be quite widely scattered. For example, in animal models the inhibitory interneurons that populate the cerebral cortex are formed outside the cortex altogether in a second proliferative zone in the basal forebrain called the ganglionic eminence, which generates the basal ganglia. These inhibitory interneurons migrate large distances in a nonradial (tangential) direction before turning radially to enter the cortex (71). Direct lineage studies in mouse and in ferret suggest that deep progenitors of inhibitory interneurons generate clones of neurons covering broad regions of the cerebral cortex (66, 68) at very low levels of mosaicism. Astrocytic glial cells arise from several sources, including progenitors that also generate principal neurons (66, 72), whereas oligodendrocytes arise from yet a fourth source in the basal forebrain that generates cells for essentially the entire forebrain (73). Hence, cells carrying common somatic mutations would be expected to be quite dispersed,

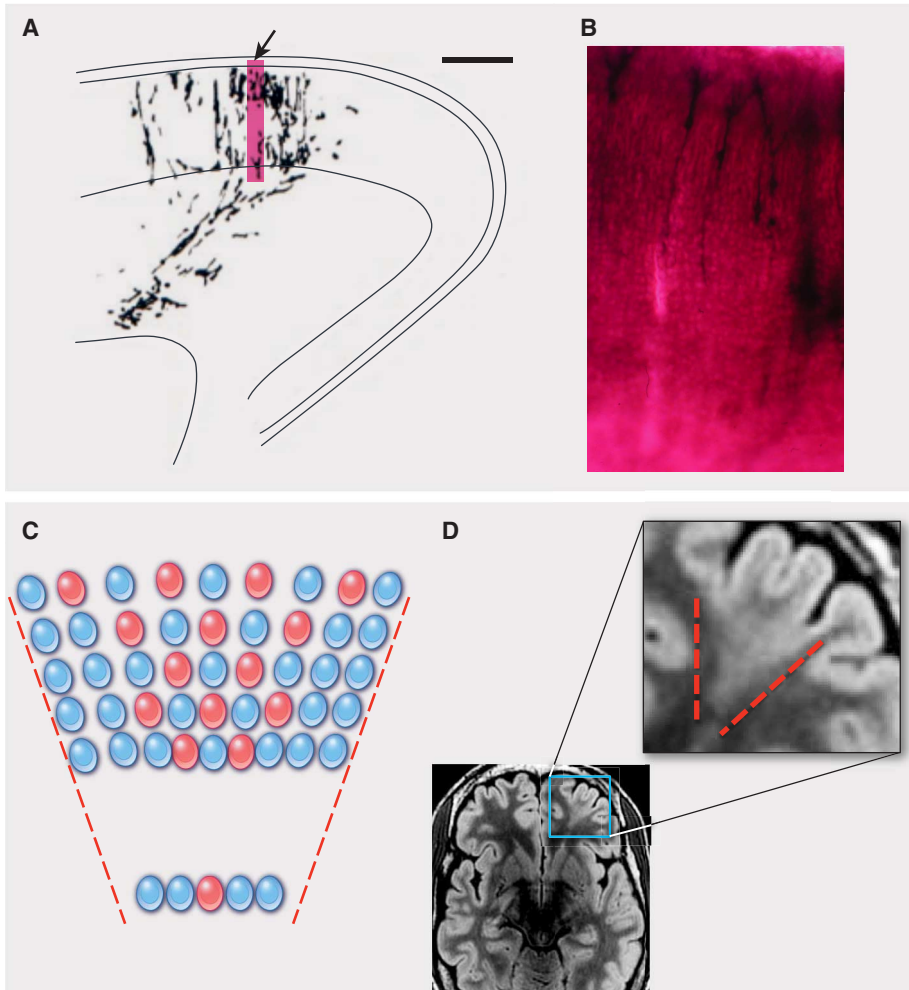


Fig. 3. Focal cortical dysplasia: a clonal-appearing brain lesion suspected to be caused by somatic mutation in a progenitor cell. (A) A camera lucida drawing shows a radial cluster from the developing ferret brain, labeled at E29 and studied at P8 (scale bar, 500 μ m) [from (68)]. The arrow indicates the region enlarged in (B). The accompanying photograph (B) shows an enlarged view of retrovirally labeled migrating pyramidal neurons at the same stage. (C) A schematic depicts the predicted effects of a somatic mutation affecting a progenitor cell in the VZ, producing a funnel-shaped lesion emanating from the ventricle. Shown are offspring (red) of the progenitor that experienced a mutation and are partially interspersed with normal cells (blue). (D) This axial T2-weighted MRI of the brain of a patient with focal epilepsy shows a focal cortical dysplasia in the left frontal region. In this image, normal gray matter appears gray, and normal white matter appears black. In the expanded view of the lesion, outlined in the smaller region by the blue box, the MRI shows a wedge-shaped abnormality roughly bounded by red dashed lines. The lesion consists of abnormal white matter signal (normally black, but in the lesion light gray in the region between the dashed lines) and thickened gray matter. The boundary between the gray matter and the white matter is blurred in this focal region as compared with the rest of the brain. In contrast, the normal regions surrounding the focal cortical dysplasia show gray matter of appropriate thickness, a sharp distinction between the gray matter and the white matter, and appropriate (black) signal in the white matter. [The MRI image is courtesy of Dr. A. James Barkovich, Department of Radiology, University of California, San Francisco]

and neighboring cells in the cortex have diverse clonal origins. This complex architecture with dispersed and intermingled clones makes it difficult to detect somatic mutations through genotyping or sequencing of bulk brain tissue because of the inherent difficulty in detecting the signal of low-level mosaic mutations.

Studies in the human brain suggest the potential of somatic mutations in the cerebral cortex to create dysfunction surprisingly out of proportion to their level of mosaicism. For example, in

HMG, which morphologically on MRI appears as a malformation affecting the entire affected hemisphere, as few as 8% and generally less than 35% of cells (neurons and glia) carry the disease-causing mutation yet are distributed over an entire hemisphere (46, 47, 74), which is consistent with the diverse clonal origins suggested by cell lineage studies in animal models. Even levels of mosaicism as low as 8% are sufficient to disrupt the normal architecture and function of essentially the entire hemisphere, causing motor weak-

ness, intractable epilepsy, and cognitive dysfunction that often improves dramatically with removal or disconnection of the abnormal cerebral hemisphere. Somatic mosaic mutations in *LIS1* or *DCX* can also cause marked cognitive dysfunction and epilepsy with levels of mosaicism detected in blood as low as 10 to 40% (40, 41); although we presume the brain is likewise mosaic, the precise level of mosaicism is such that cases can only be determined by studying cells from the brain directly, which has yet to be done. Given that complex neural circuits underlying human cognitive function are highly interconnected throughout the cortex, localized disruptions caused by somatic mutations may affect widespread networks, leading to substantial disease.

Other Neurological Diseases Attributable to Somatic Mutation?

De novo mutation has been implicated in almost all neurodevelopmental and neuropsychiatric disease, most notably intellectual disability and ASDs (2, 3, 5–8), suggesting that some disease-associated neuropsychiatric mutations may occasionally occur somatically as well—not only chromosome rearrangements, but also de novo copy number variants. Furthermore, de novo point mutations appear to be common collectively as a cause of ASD, although any given gene appears to be implicated infrequently. The example of *SCN1A* above demonstrates that de novo mutations may be present in some cells of a parent of an affected individual (yet not detected in parental blood) or may arise post-zygotically during development of the affected individual (somatic mutation). Similarly, de novo mutations in the X-linked *methyl CpG binding protein 2* (*MECP2*) gene cause Rett syndrome, an ASD that is dominant in females and typically prenatally lethal in males (75); mosaic mutations have been reported in males with both classic and atypical forms of Rett syndrome (76, 77).

Our ability to detect a pathogenic somatic mutation by using current clinical methods depends on how abundant it is in the leukocytes. The examples above suggest that at least some cases of autism, epilepsy, and perhaps other neuropsychiatric conditions such as schizophrenia may show roles for somatic mutations that have been overlooked by the usual paradigm of leukocyte DNA sequencing. Some cases of epilepsy, for example, may be due to somatic mutations affecting a specific cell lineage, such as γ -aminobutyric acid-secreting interneurons. Autism and other disorders that predominantly affect language function may be due to somatic mutations in populations of cells critical for language function in specific regions of the developing cortex. These may have been systematically missed by previous research designs that rarely sequence affected brain tissue and often do not account for the possibility of somatic mutations present at low levels in a mosaic pattern. The possibility of somatic mosaic mutations in some patients with high-functioning ASD is intriguing because it

could provide a mechanism for the remarkable preservation of some abilities (“splinter or savant skills”) in some rare autistic patients: Mosaic mutations could result in a brain that is normal in some regions yet abnormal in other regions, which is analogous to HMG, in which gain-of-function mutations in the mTOR pathway result in one hemisphere that is impaired whereas the other hemisphere may function normally. Nevertheless, studies relying on direct analysis of brain tissue are limited to autopsy studies for patients with autism or epilepsy and studies of human brain tissue removed in epilepsy surgery for patients with medically uncontrollable epilepsy. Such ongoing studies will continue to be informative, but they may or may not be generalizable to the broader group of patients with neurodevelopmental disease. Thus, it is difficult to predict to what extent somatic mutation may account for conditions such as autism and epilepsy.

Contribution to Functional Cellular Diversity in the Brain?

Against the backdrop of an increasing recognition of the pathological role of somatic mutations in brain disease is an open question of whether genetic variation may generate functional diversity among cells in the brain, and if so, how this may affect brain function. In addition to single-nucleotide variation, somatic deletions and duplications have been reported in the brains of individuals without disease (12, 78). Retrotransposition of long interspersed nuclear elements (LINE-1, or L1) is a special subset of somatic mutation that has been of particular interest recently in terms of nervous system development. Retrotransposon insertion can cause gene mutation by inactivating genes by inserting into them or by changing patterns of gene expression. A number of studies made the observation that somatic L1 retrotransposition can occur during normal brain development (79, 80), and initial estimates of these events suggested that dozens of somatic L1 insertions may be present in each neuronal genome (80). Recent quantitative analysis of the rate of somatic L1 insertions in human neurons by a single-cell sequencing approach confirmed that L1 retrotransposition occurs during neurogenesis in the human brain but suggested a rate of less than one unique insertion per cell (74), which is much lower than previous estimates. This work highlights the potential of single-cell sequencing to quantify somatic mutation rates in humans. Further work remains to determine L1 retrotransposition rates across different regions of the human brain and to assess the potential role of these and other types of somatic mutations in neurological disease.

Techniques for Further Study of Somatic Variation in the Brain

As next-generation sequencing techniques become more efficient and affordable, we will be able to push the limits of detection of all types of somatic mosaic mutations and quantify somatic

mutation rates across all regions, cell types, and time points of brain development. Studies of brain-only somatic mutations will still be limited by access to brain tissue. Nonetheless, the optimization of new techniques, such as single-cell sequencing and high depth sequencing, along with improved bioinformatic analyses, will allow us to address the role of somatic mosaicism in conditions such as focal epilepsy without malformations, autism, and intellectual disability in patients with mosaic mutations detectable in a small proportion of accessible cells such as leukocytes, or perhaps skin fibroblasts.

An exciting extension of the discovery of brain-only somatic mutations is the recent ability not only to characterize somatic mutations in a more refined manner but also to study the mutations as a means of understanding the lineage in which the mutation occurred. In the case of the somatic mutation of *AKT3* in HMG, single-cell sorting and sequencing of neurons and glia from the surgically resected brain tissue specimen provided corroboration that the mutation was present in both neurons and glia in a mosaic fashion, in approximately one third of each cell population, indicating that the mutation occurred in a neuronal-glia progenitor (74). The detailed techniques to accurately study somatic mutation at the single-cell level are beyond the scope of this Review; we highlight some recent examples of single-cell approaches applied to tumors to evaluate their clonal evolution (81–83) and applied to gametes to evaluate spontaneous mutation rates (84, 85).

Conclusions

Ultimately, single-cell and ultra-deep genome sequencing will allow systematic measurement of somatic mutation rates in different cell types and lineages during development of the normal human brain. Deeper sequencing will enable a better understanding of (i) the prevalence of somatic mutations as an occasional cause of otherwise unexplained “complex” neuropsychiatric diseases, (ii) the extent to which somatic mutation in the brain may modify the pathogenesis of neurological diseases more broadly, and (iii) whether there are possible roles for genomic variability in normal developmental processes. Because the key to treating disease lies in understanding its underlying molecular causes, determining whether somatic mutation in the brain is responsible for relatively common conditions such as epilepsy, autism, and schizophrenia is one of the next major challenges in the field of somatic mutation. Somatic mutation sequencing also affords the exciting opportunity to perform lineage tracing that will add to our understanding of the diverse cell types and developmental processes that build the human brain.

References and Notes

1. S. J. Sanders *et al.*, De novo mutations revealed by whole-exome sequencing are strongly associated with autism. *Nature* **485**, 237 (2012). doi: [10.1038/nature10945](#); pmid: [22495306](#)

2. J. J. Michaelson *et al.*, Whole-genome sequencing in autism identifies hot spots for de novo germline mutation. *Cell* **151**, 1431 (2012). doi: [10.1016/j.cell.2012.11.019](#); pmid: [23260136](#)
3. J. A. Veltman, H. G. Brunner, De novo mutations in human genetic disease. *Nat. Rev. Genet.* **13**, 565 (2012). doi: [10.1038/nrg3241](#); pmid: [22805709](#)
4. P. Awadalla *et al.*, Direct measure of the de novo mutation rate in autism and schizophrenia cohorts. *Am. J. Hum. Genet.* **87**, 316 (2010). doi: [10.1016/j.ajhg.2010.07.019](#); pmid: [20797689](#)
5. B. J. O’Roak *et al.*, Exome sequencing in sporadic autism spectrum disorders identifies severe de novo mutations. *Nat. Genet.* **43**, 585 (2011). doi: [10.1038/ng.835](#); pmid: [21572417](#)
6. B. J. O’Roak *et al.*, Multiplex targeted sequencing identifies recurrently mutated genes in autism spectrum disorders. *Science* **338**, 1619 (2012). doi: [10.1126/science.1227764](#); pmid: [23160955](#)
7. B. J. O’Roak *et al.*, Sporadic autism exomes reveal a highly interconnected protein network of de novo mutations. *Nature* **485**, 246 (2012). doi: [10.1038/nature10989](#); pmid: [22495309](#)
8. B. M. Neale *et al.*, Patterns and rates of exonic de novo mutations in autism spectrum disorders. *Nature* **485**, 242 (2012). doi: [10.1038/nature11011](#); pmid: [22495311](#)
9. S. Bamford *et al.*, The COSMIC (Catalogue of Somatic Mutations in Cancer) database and website. *Br. J. Cancer* **91**, 355 (2004). pmid: [15188009](#)
10. M. Lynch, Evolution of the mutation rate. *Trends Genet.* **26**, 345 (2010). doi: [10.1016/j.tig.2010.05.003](#); pmid: [20594608](#)
11. D. Frumkin, A. Wasserstrom, S. Kaplan, U. Feige, E. Shapiro, Genomic variability within an organism exposes its cell lineage tree. *PLoS Comput. Biol.* **1**, e50 (2005). doi: [10.1371/journal.pcbi.0010050](#); pmid: [16261192](#)
12. S. K. Rehen *et al.*, Constitutional aneuploidy in the normal human brain. *J. Neurosci.* **25**, 2176 (2005). doi: [10.1523/JNEUROSCI.4560-04.2005](#); pmid: [15745943](#)
13. A. R. Muotri, F. H. Gage, Generation of neuronal variability and complexity. *Nature* **441**, 1087 (2006). doi: [10.1038/nature04959](#); pmid: [16810244](#)
14. J. K. Baillie *et al.*, Somatic retrotransposition alters the genetic landscape of the human brain. *Nature* **479**, 534 (2011). doi: [10.1038/nature10531](#); pmid: [22037309](#)
15. M. J. Lindhurst *et al.*, A mosaic activating mutation in *AKT1* associated with the Proteus syndrome. *N. Engl. J. Med.* **365**, 611 (2011). doi: [10.1056/NEJMoa1104017](#); pmid: [21793738](#)
16. M. A. Aldred, R. C. Trembath, Activating and inactivating mutations in the human *GNAI1* gene. *Hum. Mutat.* **16**, 183 (2000). doi: [10.1002/1098-1004\(200009\)16:3<183::AID-HUMU1>3.0.CO;2-L](#); pmid: [10980525](#)
17. T. C. Pansuriya *et al.*, Somatic mosaic *IDH1* and *IDH2* mutations are associated with enchondroma and spindle cell hemangioma in Ollier disease and Maffucci syndrome. *Nat. Genet.* **43**, 1256 (2011). doi: [10.1038/ng.1004](#); pmid: [22057234](#)
18. K. C. Kurek *et al.*, Somatic mosaic activating mutations in *PIK3CA* cause CLOVES syndrome. *Am. J. Hum. Genet.* **90**, 1108 (2012). doi: [10.1016/j.ajhg.2012.05.006](#); pmid: [22658544](#)
19. M. J. Lindhurst *et al.*, Mosaic overgrowth with fibroadipose hyperplasia is caused by somatic activating mutations in *PIK3CA*. *Nat. Genet.* **44**, 928 (2012). doi: [10.1038/ng.2332](#); pmid: [22729222](#)
20. M. D. Shirley *et al.*, Sturge-Weber syndrome and port-wine stains caused by somatic mutation in *GNAQ*. *N. Engl. J. Med.* **368**, 1971 (2013). doi: [10.1056/NEJMoa1213507](#); pmid: [23656586](#)
21. R. P. Erickson, Somatic gene mutation and human disease other than cancer: an update. *Mutat. Res.* **705**, 96 (2010). doi: [10.1016/j.mrrev.2010.04.002](#); pmid: [20399892](#)
22. R. P. Erickson, Somatic gene mutation and human disease other than cancer. *Mutat. Res.* **543**, 125 (2003). doi: [10.1016/S1383-5742\(03\)00010-3](#); pmid: [12644182](#)

23. C. Pangalos *et al.*, Understanding the mechanism(s) of mosaic trisomy 21 by using DNA polymorphism analysis. *Am. J. Hum. Genet.* **54**, 473 (1994). PMID: [8116616](#)
24. C. Patel *et al.*, Mosaic trisomy 1q: The longest surviving case. *Am. J. Med. Genet. A* **149A**, 1795 (2009). doi: [10.1002/ajmg.a.32959](#); PMID: [19610079](#)
25. A. Kleczkowska, J. P. Fryns, H. Van den Bergh, On the variable effect of mosaic normal/balanced chromosomal rearrangements in man. *J. Med. Genet.* **27**, 505 (1990). doi: [10.1136/jmg.27.8.505](#); PMID: [2213843](#)
26. C. T. Schrander-Stumpel *et al.*, Mosaic tetrasomy 8p in two patients: Clinical data and review of the literature. *Am. J. Med. Genet.* **50**, 377 (1994). doi: [10.1002/ajmg.1320500416](#); PMID: [7516121](#)
27. M. Gérard-Blanluet *et al.*, Mosaic trisomy 9 and lobar holoprosencephaly. *Am. J. Med. Genet.* **111**, 295 (2002). doi: [10.1002/ajmg.10481](#); PMID: [12210326](#)
28. A. C. Laus *et al.*, Karyotype/phenotype correlation in partial trisomies of the long arm of chromosome 16: case report and review of literature. *Am. J. Med. Genet. A* **158A**, 821 (2012). doi: [10.1002/ajmg.a.32988](#); PMID: [22354628](#)
29. R. Daber *et al.*, Mosaic trisomy 17: Variable clinical and cytogenetic presentation. *Am. J. Med. Genet. A* **155**, 2489 (2011). doi: [10.1002/ajmg.a.34172](#); PMID: [21998853](#)
30. C. A. Crowe, S. Schwartz, C. J. Black, V. Jaswaney, Mosaic trisomy 22: A case presentation and literature review of trisomy 22 phenotypes. *Am. J. Med. Genet.* **71**, 406 (1997). doi: [10.1002/\(SICI\)1096-8628\(19970905\)71:4<406::AID-AJMG7>3.0.CO;2-R](#); PMID: [9286446](#)
31. A. G. Knudson Jr., Mutation and cancer: Statistical study of retinoblastoma. *Proc. Natl. Acad. Sci. U.S.A.* **68**, 820 (1971). doi: [10.1073/pnas.68.4.820](#); PMID: [5279523](#)
32. C. García-Linares *et al.*, Dissecting loss of heterozygosity (LOH) in neurofibromatosis type 1-associated neurofibromas: Importance of copy neutral LOH. *Hum. Mutat.* **32**, 78 (2011). doi: [10.1002/humu.21387](#); PMID: [21031597](#)
33. European Chromosome 16 Tuberous Sclerosis Consortium, Identification and characterization of the tuberous sclerosis gene on chromosome 16. *Cell* **75**, 1305 (1993). doi: [10.1016/0092-8674\(93\)90618-Z](#); PMID: [8269512](#)
34. M. van Slegtenhorst *et al.*, Identification of the tuberous sclerosis gene TSC1 on chromosome 9q34. *Science* **277**, 805 (1997). doi: [10.1126/science.277.5327.805](#); PMID: [9242607](#)
35. Y. Niida *et al.*, Survey of somatic mutations in tuberous sclerosis complex (TSC) hamartomas suggests different genetic mechanisms for pathogenesis of TSC lesions. *Am. J. Hum. Genet.* **69**, 493 (2001). doi: [10.1086/321972](#); PMID: [11468687](#)
36. S. Han *et al.*, Phosphorylation of tuberin as a novel mechanism for somatic inactivation of the tuberous sclerosis complex proteins in brain lesions. *Cancer Res.* **64**, 812 (2004). doi: [10.1158/0008-5472.CAN-03-3277](#); PMID: [14871804](#)
37. W. Qin *et al.*, Analysis of TSC cortical tubers by deep sequencing of TSC1, TSC2 and KRAS demonstrates that small second-hit mutations in these genes are rare events. *Brain Pathol.* **20**, 1096 (2010). doi: [10.1111/j.1750-3639.2010.00416.x](#); PMID: [20633017](#)
38. J. G. Gleeson *et al.*, Doublecortin, a brain-specific gene mutated in human X-linked lissencephaly and double cortex syndrome, encodes a putative signaling protein. *Cell* **92**, 63 (1998). doi: [10.1016/S0092-8674\(00\)80899-5](#); PMID: [9489700](#)
39. N. Bahi-Buisson *et al.*, SBH-LIS European Consortium, New insights into genotype-phenotype correlations for the doublecortin-related lissencephaly spectrum. *Brain* **136**, 223 (2013). PMID: [23365099](#)
40. F. Sicca *et al.*, Mosaic mutations of the LIS1 gene cause subcortical band heterotopia. *Neurology* **61**, 1042 (2003). doi: [10.1212/WNL.61.8.1042](#); PMID: [14581661](#)
41. J. G. Gleeson *et al.*, Somatic and germline mosaic mutations in the doublecortin gene are associated with variable phenotypes. *Am. J. Hum. Genet.* **67**, 574 (2000). doi: [10.1086/303043](#); PMID: [10915612](#)
42. E. Gennaro *et al.*, Somatic and germline mosaicism in severe myoclonic epilepsy of infancy. *Biochem. Biophys. Res. Commun.* **341**, 489 (2006). doi: [10.1016/j.bbrc.2005.12.209](#); PMID: [16430863](#)
43. L. Vadlamudi *et al.*, Timing of de novo mutagenesis—A twin study of sodium-channel mutations. *N. Engl. J. Med.* **363**, 1335 (2010). doi: [10.1056/NEJMoa0910752](#); PMID: [20879882](#)
44. Y. Hua, P. B. Crino, Single cell lineage analysis in human focal cortical dysplasia. *Cereb. Cortex* **13**, 693 (2003). doi: [10.1093/cercor/13.6.693](#); PMID: [12764046](#)
45. J. B. Rivière *et al.*, Finding of Rare Disease Genes (FORGE) Canada Consortium, De novo germline and postzygotic mutations in AKT3, PIK3R2 and PIK3CA cause a spectrum of related megalencephaly syndromes. *Nat. Genet.* **44**, 934 (2012). doi: [10.1038/ng.2331](#); PMID: [22729224](#)
46. A. Poduri *et al.*, Somatic activation of AKT3 causes hemispheric developmental brain malformations. *Neuron* **74**, 41 (2012). doi: [10.1016/j.neuron.2012.03.010](#); PMID: [22500628](#)
47. J. H. Lee *et al.*, De novo somatic mutations in components of the PI3K-AKT3-mTOR pathway cause hemimegalencephaly. *Nat. Genet.* **44**, 941 (2012). doi: [10.1038/ng.2329](#); PMID: [22729223](#)
48. M. S. Cartwright, S. C. McCarthy, E. S. Roach, Hemimegalencephaly and tuberous sclerosis complex. *Neurology* **64**, 1634 (2005). doi: [10.1212/01.WNL.0000154465.87255.78](#); PMID: [15883333](#)
49. P. D. Griffiths, R. J. Welch, D. Gardner-Medwin, A. Gholkar, V. McAllister, The radiological features of hemimegalencephaly including three cases associated with proteus syndrome. *Neuropediatrics* **25**, 140 (1994). doi: [10.1055/s-2008-1073012](#); PMID: [7969796](#)
50. K. Hussain *et al.*, An activating mutation of AKT2 and human hypoglycemia. *Science* **334**, 474 (2011). doi: [10.1126/science.1210878](#); PMID: [21979934](#)
51. J. A. Beck *et al.*, Somatic and germline mosaicism in sporadic early-onset Alzheimer's disease. *Hum. Mol. Genet.* **13**, 1219 (2004). doi: [10.1093/hmg/ddh134](#); PMID: [15115757](#)
52. A. Alzualde *et al.*, Somatic mosaicism in a case of apparently sporadic Creutzfeldt-Jakob disease carrying a de novo D178N mutation in the PRNP gene. *Am. J. Med. Genet. B. Neuropsychiatr. Genet.* **153B**, 1283 (2010). doi: [10.1002/ajmg.b.31099](#); PMID: [20872767](#)
53. A. Smahi *et al.*, The International Incontinentia Pigmenti (IP) Consortium, Genomic rearrangement in NEMO impairs NF- κ B activation and is a cause of incontinentia pigmenti. *Nature* **405**, 466 (2000). doi: [10.1038/35013114](#); PMID: [10839543](#)
54. Y. Hellenbroich, E. Schwinger, C. Zühlke, Limited somatic mosaicism for Friedrich's ataxia GAA triplet repeat expansions identified by small pool PCR in blood leukocytes. *Acta Neurol. Scand.* **103**, 188 (2001). doi: [10.1034/j.1600-0404.2001.103003188.x](#); PMID: [11240567](#)
55. H. Hashida *et al.*, Single cell analysis of CAG repeat in brains of dentatorubral-pallidoluysian atrophy (DRPLA). *J. Neurol. Sci.* **190**, 87 (2001). doi: [10.1016/S0022-510X\(01\)00596-2](#); PMID: [11574112](#)
56. P. Kahlem, P. Djan, The expanded CAG repeat associated with juvenile Huntington disease shows a common origin of most or all neurons and glia in human cerebrum. *Neurosci. Lett.* **286**, 203 (2000). doi: [10.1016/S0304-3940\(00\)01029-6](#); PMID: [10832020](#)
57. L. Møllersen, A. D. Rowe, E. Larsen, T. Rognes, A. Klungland, Continuous and periodic expansion of CAG repeats in Huntington's disease R6/1 mice. *PLoS Genet.* **6**, e1001242 (2010). doi: [10.1371/journal.pgen.1001242](#); PMID: [21170307](#)
58. Y. Ito *et al.*, Somatic mosaicism of the expanded CAG trinucleotide repeat in mRNAs for the responsible gene of Machado-Joseph disease (MJD), dentatorubral-pallidoluysian atrophy (DRPLA), and spinal and bulbar muscular atrophy (SBMA). *Neurochem. Res.* **23**, 25 (1998). doi: [10.1023/A:1022441101801](#); PMID: [9482263](#)
59. S. Ueno *et al.*, Somatic mosaicism of CAG repeat in dentatorubral-pallidoluysian atrophy (DRPLA). *Hum. Mol. Genet.* **4**, 663 (1995). doi: [10.1093/hmg/4.4.663](#); PMID: [7633415](#)
60. L. Montermini, S. J. Kish, S. Jiralerspong, J. B. Lamarque, M. Pandolfo, Somatic mosaicism for Friedrich's ataxia GAA triplet repeat expansions in the central nervous system. *Neurology* **49**, 606 (1997). doi: [10.1212/WNL.49.2.606](#); PMID: [9270608](#)
61. K. B. Jacobs *et al.*, Detectable clonal mosaicism and its relationship to aging and cancer. *Nat. Genet.* **44**, 651 (2012). doi: [10.1038/ng.2270](#); PMID: [22561519](#)
62. S. R. Kennedy, L. A. Loeb, A. J. Herr, Somatic mutations in aging, cancer and neurodegeneration. *Mech. Ageing Dev.* **133**, 118 (2012). doi: [10.1016/j.mad.2011.10.009](#); PMID: [22079405](#)
63. A. Kriegstein, S. Noctor, V. Martínez-Cerdeño, Patterns of neural stem and progenitor cell division may underlie evolutionary cortical expansion. *Nat. Rev. Neurosci.* **7**, 883 (2006). doi: [10.1038/nrn2008](#); PMID: [17033683](#)
64. S. J. Franco, U. Müller, Shaping our minds: Stem and progenitor cell diversity in the mammalian neocortex. *Neuron* **77**, 19 (2013). doi: [10.1016/j.neuron.2012.12.022](#); PMID: [23312513](#)
65. I. Reillo, C. de Juan Romero, M. A. García-Cabezas, V. Borrell, A role for intermediate radial glia in the tangential expansion of the mammalian cerebral cortex. *Cereb. Cortex* **21**, 1674 (2011). doi: [10.1093/cercor/bhq238](#); PMID: [21127018](#)
66. C. B. Reid, S. F. Tavazoie, C. A. Walsh, Clonal dispersion and evidence for asymmetric cell division in ferret cortex. *Development* **124**, 2441 (1997). PMID: [9199370](#)
67. C. Walsh, C. L. Cepko, Widespread dispersion of neuronal clones across functional regions of the cerebral cortex. *Science* **255**, 434 (1992). doi: [10.1126/science.1734520](#); PMID: [1734520](#)
68. M. L. Ware, S. F. Tavazoie, C. B. Reid, C. A. Walsh, Coexistence of widespread clones and large radial clones in early embryonic ferret cortex. *Cereb. Cortex* **9**, 636 (1999). doi: [10.1093/cercor/9.6.636](#); PMID: [10498282](#)
69. D. R. Kornack, P. Rakic, Changes in cell-cycle kinetics during the development and evolution of primate neocortex. *Proc. Natl. Acad. Sci. U.S.A.* **95**, 1242 (1998). doi: [10.1073/pnas.95.3.1242](#); PMID: [9448316](#)
70. P. Rakic, Specification of cerebral cortical areas. *Science* **241**, 170 (1988). doi: [10.1126/science.3291116](#); PMID: [3291116](#)
71. S. J. Pleasure *et al.*, Cell migration from the ganglionic eminences is required for the development of hippocampal GABAergic interneurons. *Neuron* **28**, 727 (2000). doi: [10.1016/S0896-6273\(00\)00149-5](#); PMID: [11163262](#)
72. S. Magavi, D. Friedmann, G. Banks, A. Stolfi, C. Lois, Coincident generation of pyramidal neurons and protoplasmic astrocytes in neocortical columns. *J. Neurosci.* **32**, 4762 (2012). doi: [10.1523/JNEUROSCI.3560-11.2012](#); PMID: [22492032](#)
73. N. Kessaris *et al.*, Competing waves of oligodendrocytes in the forebrain and postnatal elimination of an embryonic lineage. *Nat. Neurosci.* **9**, 173 (2006). doi: [10.1038/nn1620](#); PMID: [16388308](#)
74. G. D. Evrony *et al.*, Single-neuron sequencing analysis of L1 retrotransposition and somatic mutation in the human brain. *Cell* **151**, 483 (2012). doi: [10.1016/j.cell.2012.09.035](#); PMID: [23101622](#)
75. R. E. Amir *et al.*, Rett syndrome is caused by mutations in X-linked MECP2, encoding methyl-CpG-binding protein 2. *Nat. Genet.* **23**, 185 (1999). doi: [10.1038/138110](#); PMID: [10508514](#)
76. J. I. Piasas *et al.*, Somatic mosaicism for Y120X mutation in the MECP2 gene causes atypical Rett syndrome in a male. *Brain Dev.* **33**, 608 (2011). doi: [10.1016/j.braindev.2010.09.012](#); PMID: [20970936](#)
77. M. Topçu *et al.*, Somatic mosaicism for a MECP2 mutation associated with classic Rett syndrome in a boy. *Eur. J. Hum. Genet.* **10**, 77 (2002). doi: [10.1038/sj.ejhg.5200745](#); PMID: [11896459](#)
78. M. O'Huallachain, K. J. Karczewski, S. M. Weissman, A. E. Urban, M. P. Snyder, Extensive genetic variation in somatic human tissues. *Proc. Natl. Acad. Sci. U.S.A.* **109**, 18018 (2012). doi: [10.1073/pnas.1213736109](#); PMID: [23043118](#)
79. A. R. Muotri *et al.*, Somatic mosaicism in neuronal precursor cells mediated by L1 retrotransposition.

- Nature* **435**, 903 (2005). doi: [10.1038/nature03663](https://doi.org/10.1038/nature03663); pmid: [15959507](https://pubmed.ncbi.nlm.nih.gov/15959507/)
80. N. G. Coufal *et al.*, L1 retrotransposition in human neural progenitor cells. *Nature* **460**, 1127 (2009). doi: [10.1038/nature08248](https://doi.org/10.1038/nature08248); pmid: [19657334](https://pubmed.ncbi.nlm.nih.gov/19657334/)
 81. N. Navin *et al.*, Tumour evolution inferred by single-cell sequencing. *Nature* **472**, 90 (2011). doi: [10.1038/nature09807](https://doi.org/10.1038/nature09807); pmid: [21399628](https://pubmed.ncbi.nlm.nih.gov/21399628/)
 82. X. Xu *et al.*, Single-cell exome sequencing reveals single-nucleotide mutation characteristics of a kidney tumor. *Cell* **148**, 886 (2012). doi: [10.1016/j.cell.2012.02.025](https://doi.org/10.1016/j.cell.2012.02.025); pmid: [22385958](https://pubmed.ncbi.nlm.nih.gov/22385958/)
 83. Y. Hou *et al.*, Single-cell exome sequencing and monoclonal evolution of a JAK2-negative myeloproliferative neoplasm. *Cell* **148**, 873 (2012). doi: [10.1016/j.cell.2012.02.028](https://doi.org/10.1016/j.cell.2012.02.028); pmid: [22385957](https://pubmed.ncbi.nlm.nih.gov/22385957/)
 84. J. Wang, H. C. Fan, B. Behr, S. R. Quake, Genome-wide single-cell analysis of recombination activity and de novo mutation rates in human sperm. *Cell* **150**, 402 (2012). doi: [10.1016/j.cell.2012.06.030](https://doi.org/10.1016/j.cell.2012.06.030); pmid: [22817899](https://pubmed.ncbi.nlm.nih.gov/22817899/)
 85. S. Lu *et al.*, Probing meiotic recombination and aneuploidy of single sperm cells by whole-genome sequencing. *Science* **338**, 1627 (2012). doi: [10.1126/science.1229112](https://doi.org/10.1126/science.1229112); pmid: [23258895](https://pubmed.ncbi.nlm.nih.gov/23258895/)

Acknowledgments: A.P. is supported by the National Institute of Neurological Disorders and Stroke (NINDS) (K23NS069784).

G.D.E. is supported in part by NIH Medical Science Training Program grant T32GM007753 and by the Louis Lange III Scholarship in Translational Research. X.C. was supported in part by NIH National Institute of General Medical Sciences grant T32GM007726-35. C.A.W. is supported by the Simons Foundation, the Manton Center for Orphan Disease Research, and grants from NINDS (R01 NS079277, R01 NS032457, and R01 NS035129) and the National Institute of Mental Health (R01 MH083565 and 1RC2MH089952). C.A.W. is an Investigator of the Howard Hughes Medical Institute.

[10.1126/science.1237758](https://doi.org/10.1126/science.1237758)

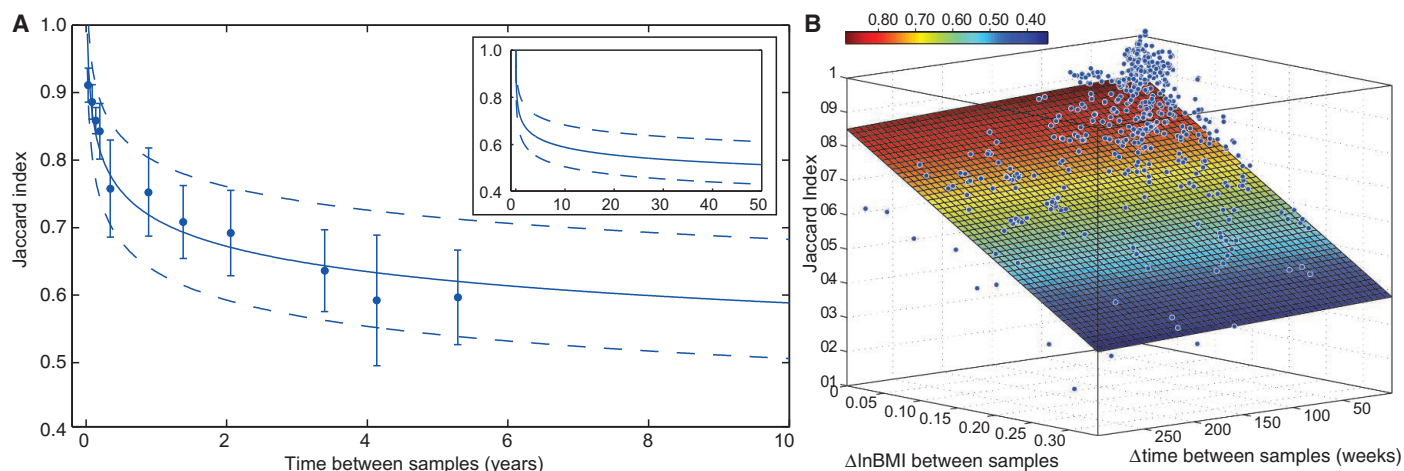
The Long-Term Stability of the Human Gut Microbiota

Jeremiah J. Faith, Janaki L. Guruge, Mark Charbonneau, Sathish Subramanian, Henning Seedorf, Andrew L. Goodman, Jose C. Clemente, Rob Knight, Andrew C. Heath, Rudolph L. Leibel, Michael Rosenbaum, Jeffrey I. Gordon*

Introduction: Understanding the dynamics and stability of the human gut microbiota is important if its characterization is to play a role in the diagnosis, treatment, and prevention of disease. To characterize stability in related and unrelated individuals and its responsiveness to physiologic change (weight loss), we developed a method for bacterial 16S rRNA amplicon sequencing at high depth with high precision. We also sequenced the genomes of anaerobic bacteria represented in culture collections prepared from fecal samples collected from individuals over time.

Methods: Low-error amplicon sequencing (LEA-Seq) is a quantitative method based on redundant sequencing of bacterial 16S rRNA genes. A dilute, barcoded, oligonucleotide primer solution is used to create ~150,000 linear PCR extensions of the template DNA. The labeled, bottlenecked linear PCR pool is amplified with exponential PCR, using primers that specifically amplify only the linear PCR molecules. The exponential PCR pool is sequenced at sufficient depth to obtain ~20× coverage. Multiple reads enable the generation of an error-corrected consensus sequence for each barcoded template molecule. LEA-Seq can be used for a variety of other applications.

Results and Discussion: LEA-Seq of fecal samples from 37 healthy U.S. adults sampled 2 to 13 times up to 296 weeks apart revealed that they harbored 195 ± 48 bacterial strains, representing 101 ± 27 species. On average, their individual microbiota was remarkably stable, with 60% of strains remaining over the course of 5 years. Stability followed a power law, which, when extrapolated, suggests that most strains in an individual's intestine are residents for decades (figure, panel A). Members of Bacteroidetes and Actinobacteria are significantly more stable components than the population average. LEA-Seq of four individuals sampled during an 8- to 32-week period during a calorie-restricted dietary study showed that weight stability is a significantly better predictor of microbiota stability than the time interval between samples (figure, panel B). After generating clonally arrayed collections of anaerobic bacteria from frozen fecal samples collected from six weight-stable individuals sampled 7 to 69 weeks apart, we produced draft genome sequences for 534 isolates representing 188 strains and 75 species. A targeted approach focused on *Methanobrevibacter smithii* isolates from two sets of twin pairs and their mothers and *Bacteroides thetaiotaomicron* strains from nine donors including sister-sister and mother-daughter pairs. Strains, defined as isolates sharing >96% of their genome content, were maintained over time within an individual and between family members but not between unrelated individuals. Thus, early gut colonizers, such as those acquired from our parents and siblings, have the potential to exert their physiologic, metabolic, and immunologic effects for most, and perhaps all, of our lives.



READ THE FULL ARTICLE ONLINE
<http://dx.doi.org/10.1126/science.1237439>

Cite this article as J. J. Faith *et al.*, *Science* **341**, 1237439 (2013). DOI: 10.1126/science.1237439

FIGURES AND TABLE IN THE FULL ARTICLE

Fig. 1. Multiplex bacterial 16S rRNA gene sequencing using LEA-Seq; comparison with previous methods using mock communities composed of sequenced gut bacterial species.

Fig. 2. Measuring the stability of an individual's fecal microbiota over time with LEA-Seq.

Fig. 3. Relationship among weight stability, time, and fecal microbiota stability.

Fig. 4. Comparison of genome stability in fecal bacterial isolates recovered from individuals over time.

Table 1. Species composition of the sequenced arrayed culture collections from six donors.

SUPPLEMENTARY MATERIALS

Materials and Methods

Fig. S1 to S8

Table S1 to S15

References

Relationship among time, physiology, and microbiota stability. (A) Stability of fecal microbiota follows a power-law function ($n = 37$ females sampled over time; <1 week to >5 years). Dashed lines show 95% confidence bounds over 10- and 50-year extrapolations (inset). (B) Microbiota stability is inversely related to the stability of each individual's body mass index.

The list of author affiliations is available in the full article online.

*Corresponding author. E-mail: jgordon@wustl.edu

The Long-Term Stability of the Human Gut Microbiota

Jeremiah J. Faith,^{1*} Janaki L. Guruge,¹ Mark Charbonneau,¹ Sathish Subramanian,¹ Henning Seedorf,¹ Andrew L. Goodman,^{1†} Jose C. Clemente,^{3*} Rob Knight,^{3,4,5} Andrew C. Heath,² Rudolph L. Leibel,⁶ Michael Rosenbaum,⁶ Jeffrey I. Gordon^{1‡}

A low-error 16S ribosomal RNA amplicon sequencing method, in combination with whole-genome sequencing of >500 cultured isolates, was used to characterize bacterial strain composition in the fecal microbiota of 37 U.S. adults sampled for up to 5 years. Microbiota stability followed a power-law function, which when extrapolated suggests that most strains in an individual are residents for decades. Shared strains were recovered from family members but not from unrelated individuals. Sampling of individuals who consumed a monotonous liquid diet for up to 32 weeks indicated that changes in strain composition were better predicted by changes in weight than by differences in sampling interval. This combination of stability and responsiveness to physiologic change confirms the potential of the gut microbiota as a diagnostic tool and therapeutic target.

Our growing understanding of the human gut microbiota as an indicator of and contributor to human health suggests that it will play important roles in the diagnosis, treatment, and ultimately prevention of human disease. These applications require an understanding of the dynamics and stability of the microbiota over the life span of an individual. Amplicon sequencing of the bacterial 16S rRNA gene from fecal microbial communities (microbiota) has revealed that each individual harbors a unique collection of species (1–3). Estimates of the number of species present in an individual's microbiota have varied greatly. Culture-based techniques (4) indicate ~100 such species, whereas culture-independent deep shotgun sequencing of fecal community DNA (5) indicates ~160 such species. Several times these numbers of species are suggested by the results of 16S rRNA amplicon sequencing, even after *in silico* attempts to remove chimeric molecules formed in the course of a polymerase chain reaction (PCR) and errors introduced during sequencing (2). These artifacts complicate tracking of individ-

ual bacterial taxa across time by inflating the set of strains in each sample with false positives. Shotgun sequencing of the community's microbiome is another approach for defining diversity (6), but it is difficult to associate gene sequences with their genome of origin.

With these limitations in mind, we have developed a method for amplicon sequencing to assay the bacterial composition of the gut microbiota of individuals at high depth with high precision over time. When combined with high-throughput methods for culturing and sequencing the genomes of anaerobic bacteria, these results reveal that the majority of the bacterial strains in an individual's microbiota persist for years, and suggest that our gut colonizers have the potential to shape many aspects of our biological features for most and in some cases all of our lives.

A Method for Low-Error Amplicon Sequencing (LEA-Seq) of Bacterial 16S rRNA genes

A 16S rRNA sequencing method for assaying the stability of an individual's microbiota over time would ideally retain high precision at high sequencing depth [precision = (true positives)/(true positives + false positives)]. Low-precision data complicate comparison of sequences between samples, as it becomes difficult to differentiate species (typically defined as isolates that share ≥97% sequence identity in their 16S rRNA genes) and strains (isolates of a given species with more minor variations in their 16S rRNA gene sequences) from sequencing errors. Standard amplicon sequencing is limited in its precision by the overall error rate of the sequencing method. If sequencing depth is low, it becomes impossible to determine whether a strain has dropped out of a given individual's microbiota or has fallen below the limits of detection at the sampling depth used.

In many applications it would be advantageous to exchange sequencing depth for improved sequence quality. Despite several optimizations we developed to increase the precision of standard amplicon sequencing at shallow depths, we found that sequencing a sample beyond 10,000 reads did not substantially increase the lower detection limit possible at high precision (7). Exchanging sequence quantity for sequence quality is inherent in shotgun genome sequencing, where redundant sequencing of genomes at 10× to 50× coverage enables a far lower error rate than is attainable from single reads alone. In general, to redundantly sequence DNA fragments, it is necessary to create a finite DNA pool that is smaller than the amount of sequencing available (i.e., create a bottleneck) and to have a method of labeling the molecules in the pool (8–10). To adapt these techniques to redundantly sequence PCR amplicons, the initial template DNA could be diluted to create a bottleneck. However, this dilution would likely need to be empirically determined for every input sample (e.g., using quantitative PCR), and one would still need to label each template molecule. As an alternative, we developed a method called low-error amplicon sequencing (LEA-Seq).

As outlined in Fig. 1A, LEA-Seq is based on redundant sequencing of a set of linear PCR template extensions of 16S rRNA genes to trade sequence quantity for quality. In this method, we create the bottleneck with a linear PCR extension of the template DNA with a dilute, barcoded, oligonucleotide primer solution. Each oligonucleotide is labeled with a random barcode positioned 5' to the universal 16S rRNA primer sequence (Fig. 1A and fig. S1). We then amplify the labeled, bottlenecked linear PCR pool with exponential PCR, using primers that specifically amplify only the linear PCR molecules. During the exponential PCR, an index primer is added to the amplicons with a third primer to allow pooling of multiple samples in the same sequencing run (fig. S1). This exponential PCR pool is then sequenced at sufficient depth to redundantly sequence (~20× coverage) the bottlenecked linear amplicons. The resulting sequences are separated by sample, using the index sequence, and the amplicon sequences within each sample are separated by the unique barcode; the multiple reads for each barcode allow the generation of an error-corrected consensus sequence for the initial template molecule. In LEA-Seq, the linear PCR primers are diluted to a concentration that generates ~150,000 amplicon reads at 20× coverage per amplicon on an Illumina HiSeq DNA sequencer.

To empirically test LEA-Seq against existing 16S rRNA amplicon sequencing methods, we first generated nine *in vitro* “mock” communities composed of different proportions of strains from a 48-member collection of phylogenetically diverse, cultured human gut bacteria whose genomes had been characterized (7) (table S1). To

¹Center for Genome Sciences and Systems Biology, Washington University School of Medicine, St. Louis, MO 63108, USA.

²Department of Psychiatry, Washington University School of Medicine, St. Louis, MO 63110, USA. ³Department of Chemistry and Biochemistry, University of Colorado, Boulder, CO 80309, USA. ⁴BioFrontiers Institute, University of Colorado, Boulder, CO 80309, USA. ⁵Howard Hughes Medical Institute, University of Colorado, Boulder, CO 80309, USA. ⁶Departments of Pediatrics and Medicine, Division of Molecular Genetics, Columbia University College of Physicians and Surgeons, New York, NY 10032, USA.

*Present address: Immunology Institute and Institute for Genomics and Multiscale Biology, Icahn School of Medicine at Mount Sinai, New York, NY 10029, USA.

†Present address: Department of Microbial Pathogenesis and Microbial Diversity Institute, Yale University School of Medicine, West Haven, CT 06516, USA.

‡Corresponding author. E-mail: jgordon@wustl.edu

calculate precision, we compared amplicons generated using two sequencing platforms (Illumina MiSeq and 454 FLX instruments), targeting different variable (V) regions of the 16S rRNA gene with different PCR primers. We defined a true positive sequence as 100% identical across 100% of its length to the 16S rRNA gene sequence(s) in the reference genome. We calculated precision at different abundance thresholds by including only those sequences representing at least a minimal portion of the total sequencing reads (0.5%, 0.1%, 0.05%, 0.01%, or 0.005%).

Relative to the existing standard approaches, LEA-Seq produced amplicon sequences with higher precision at lower abundance thresholds (Fig. 1B). For 16S rRNA sequences representing $\geq 0.01\%$ of the reads, LEA-Seq enabled a precision of 0.83 ± 0.02 (V4) and 0.63 ± 0.03 (V1V2) versus 0.08 ± 0.064 and 0.09 ± 0.005 , respectively, for the same regions with standard amplicon sequencing (table S2). These performance improvements are dependent on generating the consensus sequence from the redundant amplicon reads (table S2, method “LEA-Seq without consensus”). LEA-Seq also produced slower saturation in performance (precision of >0.7 for reads representing 0.001% of the total; fig. S2 and table S2). Similar results were obtained using the several different mock communities [see (7) for additional details of the analysis, including V1V2 versus V4 comparisons]. On the basis of this assessment of its attributes, we used LEA-Seq to quantify the stability of the gut microbiota within individuals as a function of time and change in body mass index

(BMI) while they consumed controlled monotonous or free diets.

Applying LEA-Seq to Define the Stability of the Fecal Microbiota of 37 Healthy Adults

Stability of a Microbiota Best Fits a Power-Law Function

We used LEA-Seq to characterize the microbiota in 175 fecal samples obtained from 37 healthy adults residing throughout the United States; 33 of these donors were sampled 2 to 13 times up to 296 weeks apart (1, 11) (table S3). The remaining four individuals were sampled on average every 16 days for up to 32 weeks while consuming a monotonous liquid diet as part of a controlled in-patient weight loss study (see methods) (12–14). None of the individuals took antibiotics for at least 2 months before sampling. All fecal samples were cooled to -20°C immediately after they were produced and then to -80°C within 24 hours. DNA was isolated from all samples by bead beating in phenol and chloroform.

Using an Illumina HiSeq 2000 instrument to sequence amplicons from the V1V2 region of bacterial 16S rRNA genes, we generated $108,677 \pm 60,212$ (mean \pm SD) LEA-Seq reads per fecal DNA sample. Reads were then filtered using a minimum sequence abundance threshold cutoff of eight reads (i.e., to detect strains present in the fecal microbiota at an average relative abundance of 0.007%). On the basis of our mock community data, the precision at this threshold for the V1V2 region is 0.63. We defined the

number of strains in a sample as the number of unique amplicon sequences, and the number of species-level operational taxonomic units (OTUs) in the sample as the number of clusters with 97% shared sequence identity. To correct for false positives, we multiplied the number of strains by the precision (i.e., if we detect 100 unique sequences, we expect 63 of them to be true). For individuals sampled over multiple time points, we calculated the number of species and strains for each sample individually and averaged them. The results indicated that individuals in this cohort harbored 195 ± 48 bacterial strains in their fecal gut microbiota, representing 101 ± 27 species.

To study each individual’s microbiota over time, we took all possible pairs of samples from the time series of each individual (table S3) and calculated the time in weeks between the sample dates as well as the fraction of shared strains between them, as measured by the binary Jaccard index (an unweighted metric of community overlap):

Jaccard index(sample A, sample B) =
$$\frac{\text{sample A} \cap \text{sample B}}{\text{sample A} \cup \text{sample B}} \tag{1}$$

Control experiments using mock communities (table S1) established that LEA-Seq of V1V2 16S rRNA amplicons produced highly accurate estimates of the Jaccard index [correlation between known and measured Jaccard index = 0.996; see (7)]. To characterize the stability of an individual’s microbiota, we binned fecal samples into intervals (<3 weeks, 3 to 6 weeks, 6 to

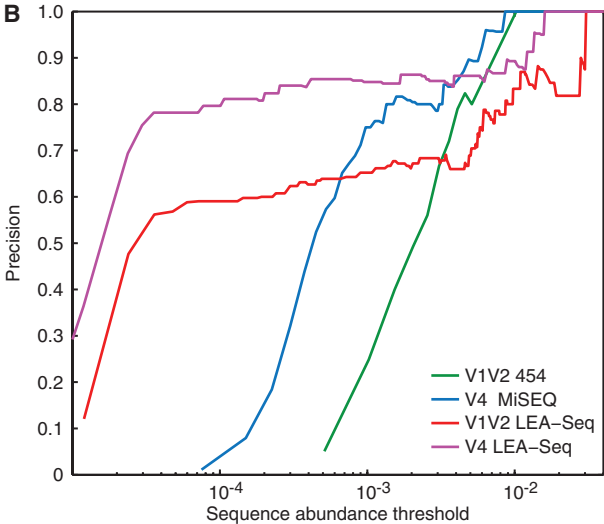
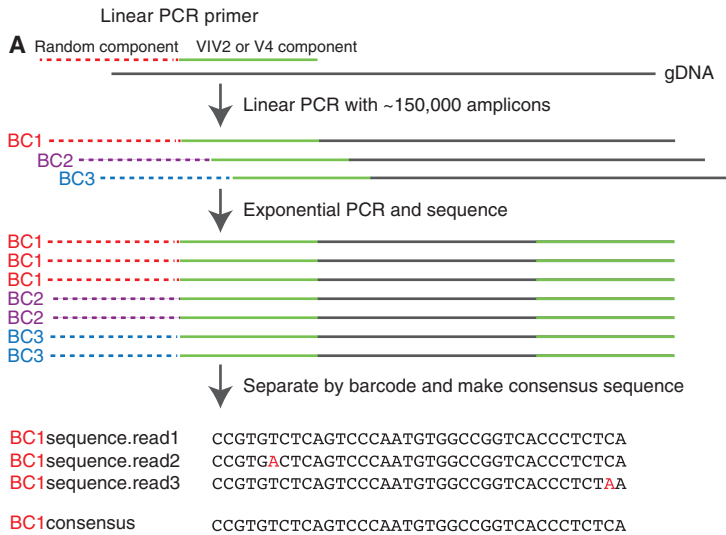


Fig. 1. Multiplex bacterial 16S rRNA gene sequencing using LEA-Seq; comparison with previous methods using mock communities composed of sequenced gut bacterial species. (A) Schematic of how the LEA-Seq method is used to redundantly sequence PCR amplicons from a set of linear PCR template extensions of bacterial 16S rDNA. This approach results in amplicon sequences with a higher precision than standard amplicon sequencing at lower abundance thresholds. **(B)** Performance of 16S rRNA amplicon sequencing methods assayed as the precision obtained for

different sequence abundance thresholds. Standard methods for amplicon sequencing using the 454 pyrosequencer and the Illumina MiSeq instrument exhibit increased precision as less abundant reads are filtered out. By redundantly sequencing each amplicon with LEA-Seq, the precision of amplicon sequencing is increased at lower abundance thresholds for both the V1V2 region of the bacterial 16S rRNA gene (compare red and green lines) and the V4 region (compare magenta and blue lines), thereby enabling detection of lower-abundance bacterial taxa at high precision.

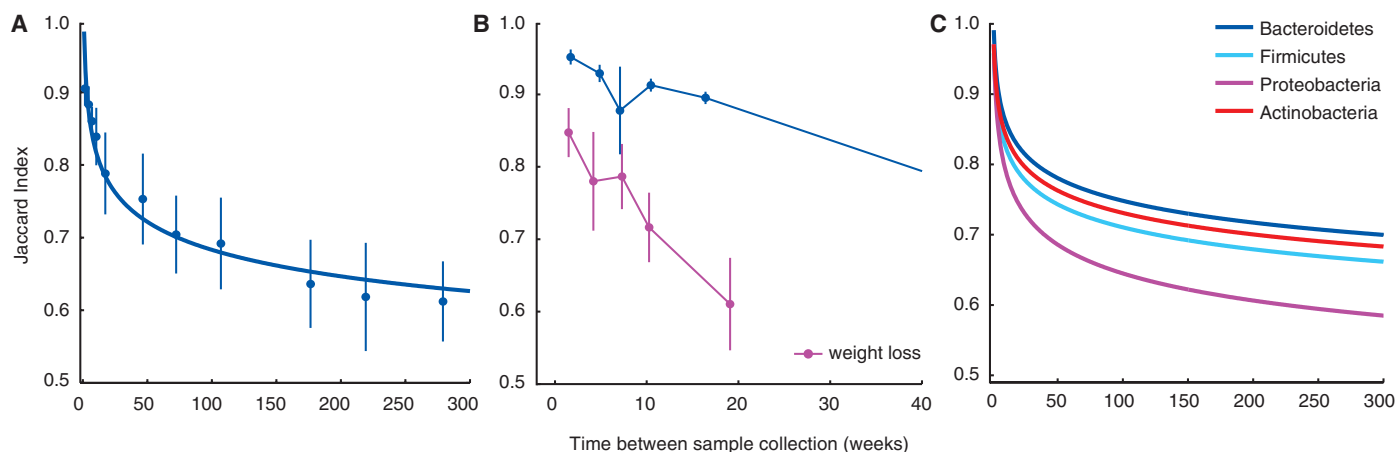


Fig. 2. Measuring the stability of an individual's fecal microbiota over time with LEA-Seq. (A) The Jaccard index (fraction of shared strains) was calculated between all possible pairwise combinations of fecal samples collected from each individual, where bacterial strains were considered shared if the nucleotide sequence was 100% identical across 100% of the length of the V1V2 region of their 16S rRNA genes. Jaccard indices were binned into intervals of <3 weeks, 3 to 6 weeks, 6 to 9 weeks, 9 to 12 weeks, 12 to 32 weeks, 32 to 52 weeks, 52 to 104 weeks, 104 to 156 weeks, 156 to 208 weeks, 208 to 260 weeks, and >260 weeks apart

(mean \pm SE for each bin is shown). The decay in the Jaccard index as a function of time between two samples best fits a power law (blue line). (B) Four individuals losing 10% of their body weight in the study involving consumption of a monotonous low-calorie liquid diet (magenta) had significantly less stable microbiota than the mean of the 33 remaining individuals (blue). Means \pm SE for the Jaccard index are plotted. (C) At the phylum level, Bacteroidetes (blue) and Actinobacteria (red) were more stable components of the microbiota than Proteobacteria and Firmicutes (hypergeometric distribution).

9 weeks, 9 to 12 weeks, 12 to 32 weeks, 32 to 52 weeks, 52 to 104 weeks, 104 to 156 weeks, 156 to 208 weeks, 208 to 260 weeks, and >260 weeks) and determined the average Jaccard index values for each bin. The results disclosed that the bacterial composition of each individual's fecal microbiota changed over time, with more strains shared between shorter sampling intervals relative to long intervals (Fig. 2A). Nonetheless, the set of microbial strains was remarkably stable overall, with more than 70% of the same strains remaining after 1 year and few additional changes occurring over the following 4 years. The stability of a microbiota best fits a power-law function ($R^2 = 0.96$; Fig. 2A, blue line, and table S4); large differences in community composition occur on shorter time scales, whereas a stable core set of strains persists at longer time scales.

To define the stability of a given strain as a function of its relative abundance in the microbiota, we used all pairwise combinations of fecal samples obtained from each individual to calculate (i) the mean abundance of the strains shared by two or more samples, and (ii) the mean abundance of strains that were not shared between any two samples. Strains that were shared across two time points were roughly 3 times as abundant as those that were not shared [0.030 ± 0.013 fraction of the community versus 0.011 ± 0.011 (mean \pm SD); $P = 2.2 \times 10^{-9}$ (t test); fig. S3A]. We also binned the strain abundances for each donor using five fractional abundance thresholds of 0.1, 0.01, 0.001, 0.0001, and <0.0001 (e.g., bin 0.01 contains all strains ≤ 0.1 and >0.01) and calculated the probability that strains in a given bin were shared between samples. We found that the higher the fractional

abundance of a strain, the more likely the strain was shared between samples ($r = 0.96$, $P < 0.0087$; fig. S3B). Together, these results suggest that the more stable components of the microbiota are also the most abundant members.

Effects of a Monotonous Low-Calorie Diet and Associated Weight Loss on Diversity

To explore the role of weight loss on the microbiota, we applied LEA-Seq to the fecal microbiota of four individuals sampled over the course of an 8- to 32-week period in a three-phase study that used different caloric intakes of a defined monotonous liquid diet to first stabilize initial weight, then decrease weight by 10%, and finally maintain weight at the 10% reduced level (Fig. 2B and table S3). Daily caloric intake was 2988 ± 290 kcal, 800 kcal, and 2313 ± 333 kcal for the three phases of the study, respectively (14, 15). While on this diet, these four individuals experienced significantly reduced stability of their microbiota, as measured by the Jaccard index (Fig. 2B). For each individual, we found no significant correlation between time and diversity/richness (i.e., number of strains in a sample; minimum $P = 0.17$). Additionally, we found no significant correlation between the change in composition of the microbiota (Jaccard index between two samples) and the change in diversity/richness (absolute difference in the number of species or strains between two samples) ($P = 0.09$ and 0.44 for strains and species, respectively). Considering family-level taxonomic bins, there were several groups whose abundance was strongly positively or negatively correlated with time during the weight loss period, including Clostridiaceae [average correlation (r) across donors during weight loss = 0.60], Coriobacte-

riaceae ($r = 0.53$), Bifidobacteriaceae ($r = 0.55$), Enterobacteriaceae ($r = 0.58$), Lachnospiraceae ($r = -0.65$), Oscillospiraceae ($r = -0.53$), and Oxalobacteraceae ($r = -0.74$).

Modeling the Relationship Among Time, Body Composition, and Microbiota Stability

Given the correlation between weight loss and changes in the microbiota of individuals consuming a monotonous 800 kcal/day diet, we took a broader view across all 37 individuals in our study to determine whether this correlation was due to the monotonous diet that the four individuals had consumed, or if there is a generalizable and quantifiable relationship between weight stability and microbiota stability. To explore this question, we not only calculated the time (Δ time) and Jaccard index between all pairs of fecal samples collected from an individual (Fig. 2), but also the absolute value of the change in natural logarithm of the BMI value (abbreviated $\Delta \ln \text{BMI}$) between all pairs. We found a significant negative correlation between $\Delta \ln \text{BMI}$ and Jaccard index (Fig. 3A; $r = -0.68$, $P = 2.98 \times 10^{-73}$) that was even greater than that between Δ time and Jaccard index (Fig. 3B; $r = -0.42$, $P = 1.45 \times 10^{-43}$). These relationships held when we removed the data generated from the four individuals on the monotonous diet ($\Delta \ln \text{BMI}$: $r = -0.69$, $P = 3.27 \times 10^{-54}$; Δ time: $r = -0.65$, $P = 9.05 \times 10^{-46}$).

To quantify the relationship among Δ time, $\Delta \ln \text{BMI}$, and the Jaccard index between pairs of samples (Fig. 3C), we fit the following model:

$$\text{Microbiota stability} = \beta_0 + \beta_{\ln \text{BMI}} X_{\ln \text{BMI}} + \beta_{\text{time}} X_{\text{time}} \quad (2)$$

where microbiota stability is the Jaccard index between samples, $X_{\ln\text{BMI}}$ is the change in $\ln\text{BMI}$ between any two samples collected from the individual ($\Delta\ln\text{BMI}$), X_{time} is the time between the two samples being compared (Δtime), β_0 is the estimated parameter for the intercept, and $\beta_{\ln\text{BMI}}$ and β_{time} are the linear regression estimated parameters for $\Delta\ln\text{BMI}$ and Δtime , respectively. Remarkably, this model explained 46% of the variance in the stability of the microbiota (Jaccard index) within the individuals over time ($R^2 = 0.46$, $P = 1.94 \times 10^{-72}$; when the monotonous dieters were excluded, $R^2 = 0.51$, $P = 1.40 \times 10^{-58}$). Once again, the weight stability of an individual [$\Delta\ln\text{BMI}$; analysis of variance (ANOVA), $P = 1.18 \times 10^{-51}$] was a better predictor of fecal microbiota stability than the time between samples (Δtime ; ANOVA, $P = 0.09$), with Δtime only being a significant predictor of

stability when the monotonous dieters were excluded (ANOVA, $P = 2.82 \times 10^{-7}$). Together, these relationships among time, BMI, and the stability of an individual's microbiota highlight the role that longitudinal surveys of a microbiota could play in health diagnostics.

Sequenced Collections of Fecal Bacteria Obtained from Individuals over Time

As in previous studies (1, 16–19), we found that each individual's microbiota at a given time point was most similar to their own at other time points (Jaccard index, 0.82 ± 0.022), followed by their family members (Jaccard index, 0.38 ± 0.020), and then unrelated individuals (Jaccard index, 0.30 ± 0.005). The Jaccard index estimates with LEA-Seq suggest that on average any two unrelated individuals share ~30% of the strains in their microbiota. However, it is possible that

unrelated individuals on average share no strains in their microbiota, and that this 30% represents the lower resolving limit of 16S rRNA amplicon sequencing of the targeted variable region (V1V2) and currently available maximum read lengths on the Illumina HiSeq 2000 instrument (paired-end, 101 base pairs).

Whole-genome alignments between bacteria isolated and sequenced from different samples provide many orders of magnitude of additional resolving power to determine which strains (now defined at the level of whole-genome sequence identity rather than 16S rRNA identity) remain in an individual's microbiota over time, or reside in two unrelated individuals. Isolation and sequencing of extensive collections of organisms from the human gut microbiota (20) can provide a practical method to look at the plasticity and evolution of the gene content of microbial

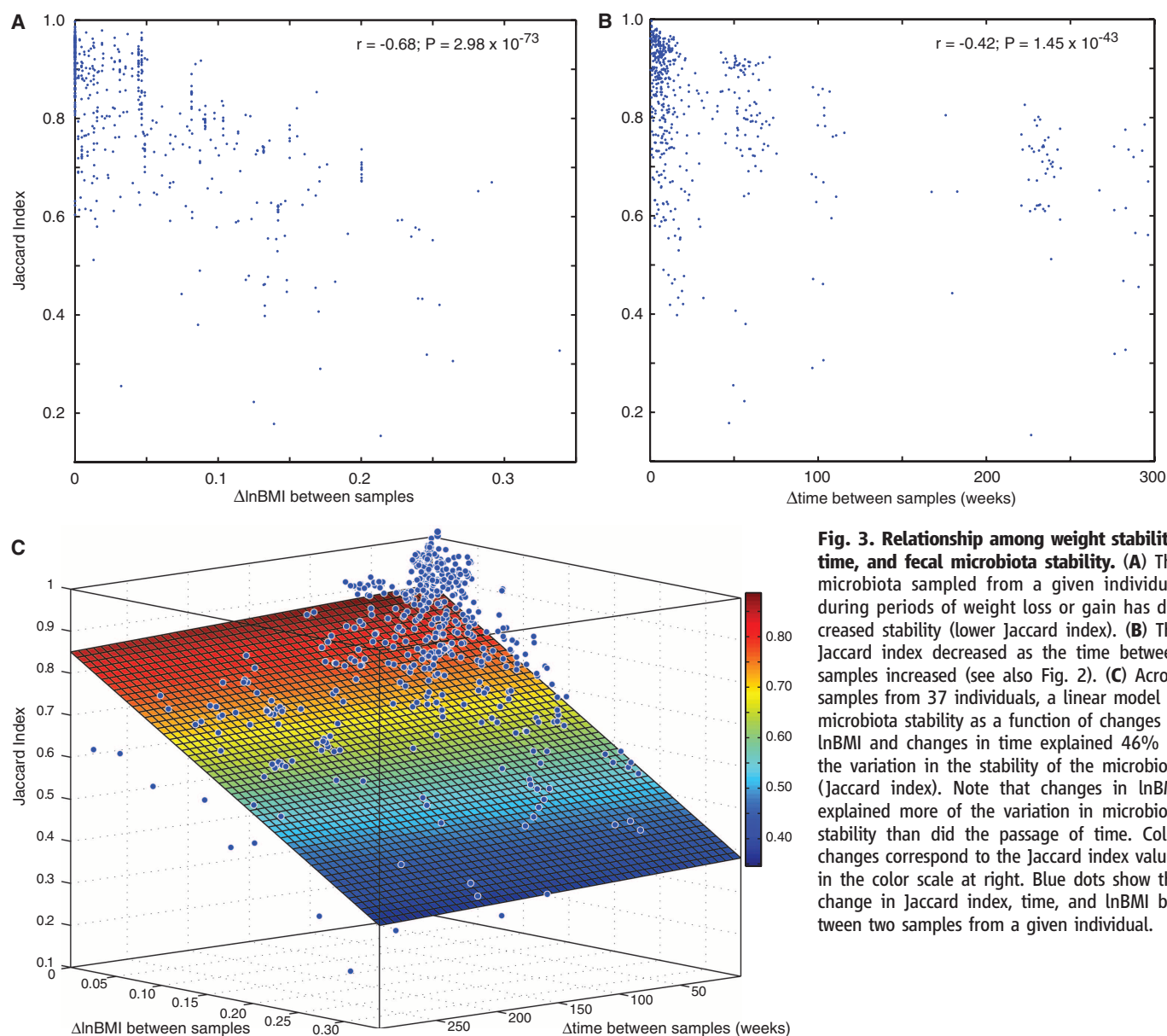


Fig. 3. Relationship among weight stability, time, and fecal microbiota stability. (A) The microbiota sampled from a given individual during periods of weight loss or gain has decreased stability (lower Jaccard index). (B) The Jaccard index decreased as the time between samples increased (see also Fig. 2). (C) Across samples from 37 individuals, a linear model of microbiota stability as a function of changes in $\ln\text{BMI}$ and changes in time explained 46% of the variation in the stability of the microbiota (Jaccard index). Note that changes in $\ln\text{BMI}$ explained more of the variation in microbiota stability than did the passage of time. Color changes correspond to the Jaccard index values in the color scale at right. Blue dots show the change in Jaccard index, time, and $\ln\text{BMI}$ between two samples from a given individual.

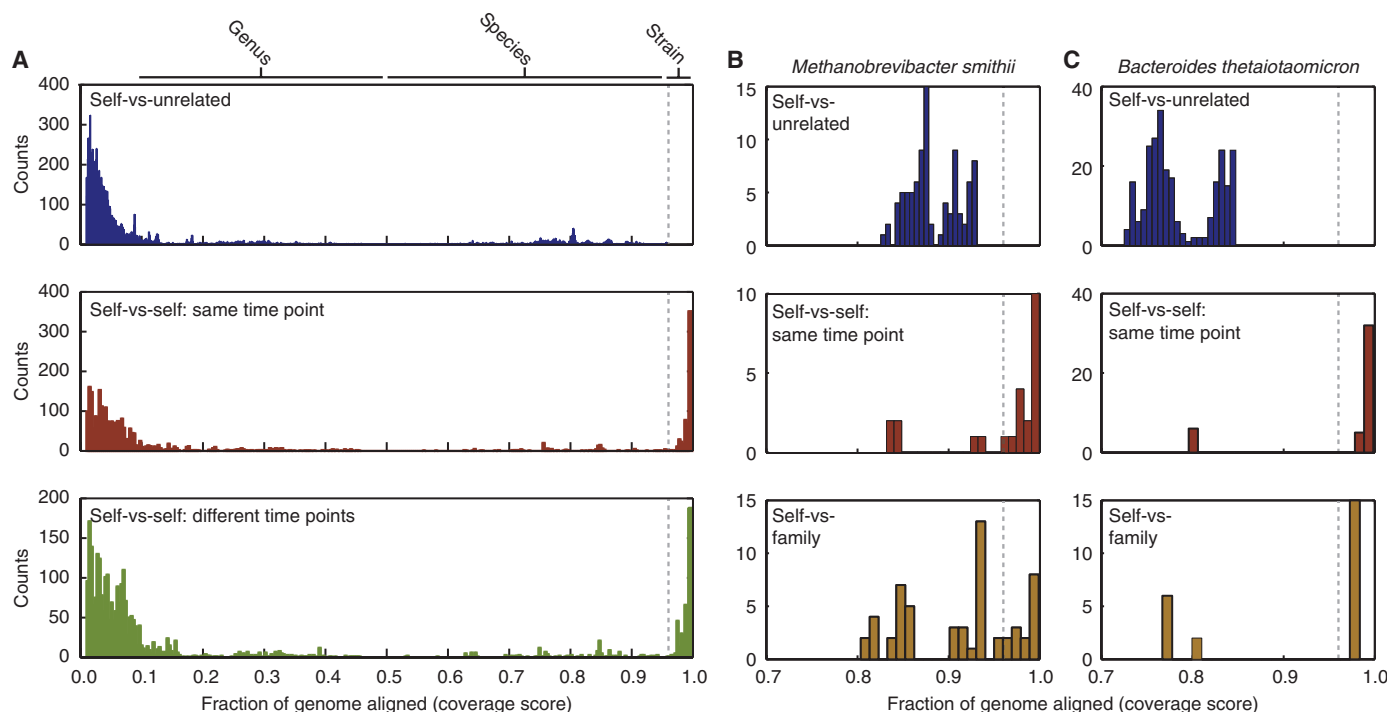


Fig. 4. Comparison of genome stability in fecal bacterial isolates recovered from individuals over time. The fraction of aligned nucleotides between any two microbial genomes was calculated using the coverage score (see text). (A) Histogram of the fraction of aligned genome content between all sequenced bacterial isolates from unrelated individuals (blue; only coverage scores ≥ 0.01 are shown) shows that the alignable genome content never exceeded 96% (dashed line). However, highly conserved strains with coverage scores exceeding this threshold were readily detected in the microbiota of individuals at a single time point

(red) or between samples from an individual taken up to 15 months apart (green). Counts denote the number of times a sample fell into each coverage score bin. (B and C) Sequencing the genomes of *M. smithii* strains (B) and *B. thetaiotaomicron* strains (C) revealed that no two isolates from unrelated individuals had more than 96% shared (alignable) gene content (blue), whereas highly conserved strains above this threshold were found between isolates obtained from a single individual's fecal microbiota at a single time point (red), as well as from isolates taken from different members of the same family (brown).

strains harbored in individuals' intestines over time. Therefore, adapting a high-throughput method we had developed for generating clonally arrayed collections of anaerobic bacteria in multiwell format from frozen fecal samples (20), we produced draft genome sequences for 444 bacterial isolates recovered from the frozen fecal microbiota of five donors who had been sampled across periods from 7 to 69 weeks apart ($n = 1$ to 4 time points per donor; 11 total samples; mean coverage per microbial genome = 118 \times ; see tables S5 and S6) (7). These genomes span a broad phylogenetic range within the four dominant bacterial phyla that constitute the human gut microbiota (Bacteroidetes, Firmicutes, Proteobacteria, and Actinobacteria; table S6).

To look for changes in bacterial genome content across time in each individual, we performed whole-genome alignment with nucmer (21) and calculated the fraction of DNA sequence aligned between each pair of genomes [coverage score = $(X_{\text{aln}} + Y_{\text{aln}})/(X + Y)$, where X and Y are the lengths of genome X and Y , respectively, and X_{aln} and Y_{aln} are the number of aligned bases of genomes X and Y , respectively] (7, 22). We found that the shared genome content between isolates from unrelated individuals was broadly distributed for taxa from the same genus (coverage score = 0.30 ± 0.20) or species (0.77 ± 0.12), with

a maximum of 0.956 (Fig. 4A, blue; fig. S4). We then compared the shared genome content between isolates within each fecal sample (i.e., self-versus-self at a single time point) and found isolates that shared a very high proportion of their content (0.965 to 0.999) (Fig. 4A, red). Remarkably, we found the same high proportion of shared genome content between isolates from a given donor between different time points (i.e., self-versus-self over time; Fig. 4A, green), which suggests that the same strains of bacteria persisted in these individuals over the course of the sampling period.

Defining replicate bacterial strains as those with a coverage score of >0.96 and species as those with a coverage score of >0.5 (fig. S4), we subsequently clustered the genome isolates by sample and by individual (table S5); this effort yielded a total of 165 strains and 69 species across the five donors (Table 1). Across the four donors with multiple time points, on average 36% of an individual's bacterial strains were isolated from multiple time points. This fraction of shared bacterial strains across time at the level of the genome is lower than that measured by LEA-Seq; however, this likely reflects the increased sampling depth and culture independence of LEA-Seq [detecting isolates at depths of 1:10,000 to 1:100,000 (0.01 to 0.001%) com-

pared with 0.14 to 0.06% for high-throughput culturing]. For the most deeply sampled individual (F3T1 in table S3), where isolates were sequenced from four samples taken over the course of ~ 16 months, more than 60% of the strains were isolated from multiple samples.

Stability Viewed from the Perspective of Phylum-Level Membership

When we assigned phylum-level taxonomy to all LEA-Seq 16S rRNA amplicons from each of the 37 individuals in our study (23), we found that members of the Bacteroidetes and Actinobacteria were significantly more stable components of the microbiota relative to the population average (hypergeometric distribution comparing the total number of shared/not shared strains within a given phylum for all samples versus the total number of shared/not shared strains across all phyla, except the phylum of interest; $P = 7.54 \times 10^{-28}$ and 0.0068, respectively), whereas the Firmicutes and Proteobacteria were significantly less stable (Fig. 2C; $P = 1.83 \times 10^{-11}$ and 0.0015, respectively). The cultured bacterial strains manifested similar trends for the Bacteroidetes and Firmicutes, where 52% and 21%, respectively, of the strains were isolated and sequenced across multiple time points (table S7), thus demonstrating at a whole-genome level the strain

stability initially identified when only the 16S rRNA gene was targeted for analysis.

Strains Shared Between Members of Human Families

The power-law response of the Jaccard index as a function of the sample collection interval makes it possible to extrapolate beyond the sampling time frame of the current study and suggests that the majority of strains in the microbiota represent a stable core that persists in an individual's intestine for his or her entire adult life, and could represent strains acquired during childhood from parents or siblings (fig. S5). Therefore, we used LEA-Seq to measure the fraction of shared strains between family members (sister-sister or mother-daughter). As in previous studies (1), we found the microbiota of related individuals was more similar than unrelated ones, with a significantly larger proportion of shared V1V2 16S rRNA sequences [Jaccard index = 0.38 ± 0.020 (related), 0.30 ± 0.005 (unrelated); *P* = 0.00053].

To determine whether this increased similarity between family members manifested itself at the level of their gut microbial genome sequences, we used a targeted approach to look at genome content differences in (i) two families using previously sequenced *Methanobrevibacter smithii* isolates (24) from two sets of twin pairs and their mothers (six total donors, 19 genomes; table S3), and (ii) five families where 26 *Bacteroides thetaiotaomicron* strains were isolated with a species-specific monoclonal antibody (7, 25) from nine donors including sister-sister and mother-daughter pairs (all isolates were from a single sample from each donor; table S3). *M. smithii*, a methanogen, is the dominant archaeon in the human gut microbiota and facilitates fermentation of polysaccharides by saccharolytic bacteria such as *B. thetaiotaomicron* by virtue of its ability to remove hydrogen (24). As with our untargeted large-scale genome sequencing of personal bacterial culture collections described above, we found that unrelated individuals had no pair of isolates of either species that shared >96% of their genome content. However, within an individual we once again found replicate isolates of the same strain (Fig. 4, B and C, blue and red). Strikingly, we also found replicate strains of *M. smithii* or *B. thetaiotaomicron* shared across family members (Fig. 4, B and C, brown; table S3).

In contrast with the results obtained using this taxon-targeted whole-genome sequencing approach, our untargeted sequencing of the clonally arrayed personal bacterial culture collections had only involved two related individuals (female dizygotic co-twins 1 and 2 from family 60; F60T1 and F60T2, table S3) and had revealed no strains with >96% of their genomes aligned. Therefore, we isolated and sequenced an additional 89 genomes from two time points of the dizygotic twin sister (F61T2) of subject F61T1 (yielding a total of 188 strains and 75 species across the six donors). As with the previous do-

Table 1. Species composition of the sequenced arrayed culture collections from six donors. Alternative names for species are in parentheses.

Species ID	Species	Donor					
		F3T1	F58T1	F60T1	F60T2	F61T1	F61T2
1	<i>Alistipes indistinctus</i>	+				+	
2	<i>Anaerococcus vaginalis</i> (<i>A. hydrogenalis</i>)		+	+	+		+
3	<i>Anaerofustis stercorihominis</i>		+				+
4	<i>Anaerofustis stercorihominis</i>					+	
5	<i>Bacteroides</i>					+	
6	<i>Bacteroides caccae</i>		+		+		+
7	<i>Bacteroides finegoldii</i>				+	+	
8	<i>Bacteroides fragilis</i>					+	+
9	<i>Bacteroides intestinalis</i> (<i>B. cellulosilyticus</i>)	+	+		+		+
10	<i>Bacteroides massiliensis</i>	+			+		
11	<i>Bacteroides ovatus</i>	+		+	+	+	
12	<i>Bacteroides salyersiae</i>	+					
13	<i>Bacteroides thetaiotaomicron</i> (<i>B. faecis</i>)	+			+	+	+
14	<i>Bacteroides uniformis</i> (<i>B. acidifaciens</i>)		+		+	+	+
15	<i>Bacteroides vulgatus</i> (<i>B. dorei</i>)	+	+	+	+	+	+
16	<i>Barnesiella intestinihominis</i>		+				
17	<i>Bifidobacterium adolescentis</i>				+	+	
18	<i>Bifidobacterium bifidum</i>					+	
19	<i>Bifidobacterium longum</i>	+			+		+
20	<i>Bifidobacterium pseudocatenulatum</i>				+	+	
21	<i>Blautia</i>		+				
22	<i>Blautia schinkii</i>				+	+	
23	<i>Butyrivibrio fibriosolvens</i>	+	+		+	+	
24	<i>Clostridiales</i>					+	
25	<i>Clostridiales</i>					+	
26	<i>Clostridiales</i>					+	
27	<i>Clostridiales</i>					+	
28	<i>Clostridiales</i>		+				
29	<i>Clostridiales</i>						+
30	<i>Clostridiales</i>					+	
31	<i>Clostridium</i>	+	+			+	
32	<i>Clostridium</i>					+	
33	<i>Clostridium bolteae</i>						+
34	<i>Clostridium hylemonae</i>						+
35	<i>Clostridium leptum</i>				+	+	
36	<i>Clostridium scindens</i>				+		+
37	<i>Clostridium scindens</i>			+			
38	<i>Collinsella</i>		+				
39	<i>Collinsella aerofaciens</i>	+			+	+	
40	<i>Coprococcus comes</i>	+	+		+		
41	<i>Dorea formicigenerans</i>	+	+		+	+	
42	<i>Dorea longicatena</i>	+	+		+		+
43	<i>Dorea longicatena</i>		+				
44	<i>Eggerthella lenta</i> (<i>Subdoligranulum variabile</i>)						+
45	<i>Escherichia coli</i>	+	+		+	+	+
46	<i>Eubacterium bifforme</i>		+				
47	<i>Eubacterium callanderi</i>				+		
48	<i>Eubacterium contortum</i>					+	
49	<i>Eubacterium eligens</i>		+				
50	<i>Finegoldia magna</i> (<i>Dialister invisus</i>)						+
51	<i>Lactobacillus</i>		+				
52	<i>Lactobacillus casei</i>		+				
53	<i>Megasphaera elsdenii</i>			+			
54	<i>Odoribacter splanchnicus</i>		+		+	+	
55	<i>Parabacteroides distasonis</i>	+	+	+	+	+	
56	<i>Parabacteroides goldsteinii</i>		+			+	
57	<i>Parabacteroides merdae</i>		+			+	
58	<i>Peptoniphilus harei</i>		+		+		
59	<i>Roseburia intestinalis</i>					+	

Table 1. (continued).

Species ID	Species	Donor					
		F3T1	F58T1	F60T1	F60T2	F61T1	F61T2
60	<i>Ruminococcaceae</i>					+	
61	<i>Ruminococcus</i> (<i>Lachnospiraceae</i>)			+		+	
62	<i>Ruminococcus albus</i>					+	
63	<i>Ruminococcus bromii</i>			+		+	
64	<i>Ruminococcus gauvreauii</i>	+					
65	<i>Ruminococcus gnavus</i>	+		+			+
66	<i>Ruminococcus obeum</i>	+					
67	<i>Ruminococcus</i> sp. CCUG 37327 A	+	+				
68	<i>Ruminococcus</i> sp. DJF VR70k1					+	
69	<i>Ruminococcus torques</i>	+				+	
70	<i>Streptococcus</i>			+			
71	<i>Streptococcus gordonii</i>					+	
72	<i>Streptococcus parasanguinis</i>					+	
73	<i>Streptococcus thermophilus</i>					+	
74	<i>Subdoligranulum variabile</i>	+	+	+	+		+
75	<i>Veillonella parvula</i>						+

nors, we were able to isolate numerous strains shared across the two time points (8 of 25 = 32%). In addition, we were able to isolate two strains (*B. thetaiotaomicron* and *Escherichia coli*) in both of the sisters, showing that even nontargeted genome isolation and sequencing can retrieve the same strain across family members. We did not explicitly sample members of our cohort of females during significant physiological transitions such as menarche and menopause. However, the presence of the same bacterial strain in mothers and their adult daughters who had progressed through one or both of these life-cycle milestones suggests that components of the microbiota are retained during these events.

Prospectus

The objects we touch and consume during the course of our lives are covered with diverse microbial life. Despite this, LEA-Seq revealed that on average 60% of the approximately 200 microbial strains harbored in each adult's intestine were retained in their host over the course of a 5-year sampling period. Our results are supported by a microarray-based profiling of fecal microbiota collected from three males and two females over ~8 years (19) but differ from those of a similar analysis using standard 16S rRNA amplicon sequencing, which found high variability in microbiota composition in two individuals sampled for up to 15 months (26). This difference likely reflects the fact that the sequencing depth and precision limitations of standard 16S rRNA amplicon sequencing are overcome to some extent with microarrays where amplicons are mapped and hybridized to a finite pool of target sequences (i.e., sacrificing resolution for precision). The differences could also be due to true differences in the stabilities in microbiota of the individuals, as both studies surveyed only a small number of individuals. Our findings are also supported by a recent report that mapped deep shotgun sequencing data sets of the fecal

microbiome to a set of reference bacterial genomes (6) and found that the gut communities of these individuals were more similar to each other at the microbiome level than to unrelated individuals (average maximum time between samples = 32 weeks with two individuals sampled over a period of >1 year). Applying LEA-Seq to longitudinal surveys of the fecal microbiota of 37 twins sampled for up to 5 years allowed us to show that the stability of an individual's microbiota follows a power-law function. Using this function, we could extrapolate the stability of the microbiota over decades. The resolution and accuracy of these predictions should improve as advances in sequencing chemistry enable longer regions of 16S rRNA genes to be characterized. LEA-Seq itself can be generalized to any application that requires deep amplicon sequencing with high precision (e.g., the VDJ regions of immunoglobulin and T cell receptor genes, or targeted searches for variants in candidate or known disease-producing genes).

Our study also illustrates how a highly personalized analysis of the gut community at strain-level microbial genome resolution can be conducted using collections of cultured bacteria (or archaea) generated from frozen fecal samples collected over time from a given subject. This strain-level analysis can be part of a broad phylogenetic survey, or it can target a particular species.

The stability of the microbiota that we document in healthy individuals has important implications for future use of the microbiota (and microbiome) as a diagnostic tool as well as a therapeutic target for individuals of various ages. Our findings suggest that obtaining a routine fecal sample as part of a yearly physical examination designed to promote disease prevention would be sufficient to monitor changes in the composition and stability of an individual's fecal microbiota. For example, in the case of inflammatory bowel diseases, the concordance for

Crohn's disease and ulcerative colitis among monozygotic twin pairs is only 38% and 15%, respectively (27). Our results suggest that these twins likely share identifiable unique subsets of their microbiota that represent long-term environmental exposures for their immune systems that should be considered when trying to predict disease risk, or infer which species or strains may have a causal role in disease initiation, progression, relapse, and treatment responses. Moreover, the effects of travel, changes in diet, weight gain and loss, diarrheal disease, antibiotics, immunosuppressive therapy, or clinical trials designed to deliberately manipulate the microbiota (e.g., through administration of existing or new prebiotics, probiotics, synbiotics, antibiotics, or transplantation of microbiota from healthy individuals to those with various diseases attributed to a dysfunctional microbiota) can be more accurately quantified by applying the methods we describe. Finally, the stability we document highlights the impact of early colonization events on our microbiota in later life; earlier colonizers, such as those acquired from our parents and siblings, have the potential to provide their metabolic products and exert their immunologic effects for our entire lives.

Methods

Diet Studies

Four obese (BMI > 30 kg/m²) female subjects with a mean (\pm SD) age of 26 \pm 3 years were admitted to the General Clinical Research Center at Columbia University Medical Center and remained as in-patients throughout the study. The protocol for recruitment and for the weight loss study was approved by the Institutional Review Board of New York Presbyterian Medical Center and is consistent with guiding principles for research involving humans. Written informed consent was obtained from all subjects. The diet protocol has been described in detail (12, 13). Briefly, subjects were fed a liquid-formula diet with 40% of energy as fat (corn oil), 45% as carbohydrate (glucose polymer), and 15% as protein (casein hydrolysate). Diet composition but not quantity was constant throughout the study. The diet had a caloric density of 1.25 digestible kcal of energy per gram and was supplemented with vitamins and minerals in quantities sufficient to maintain a stable weight, defined as an average daily weight variation of <10 g/day for \geq 2 weeks. This weight plateau is designated as Wt_{initial}. The four individuals in this study consumed 2600 to 3300 kcal/day of the diet to maintain Wt_{initial}. After a brief period at Wt_{initial}, subjects were provided 800 kcal/day of the same liquid-formula diet until they had lost ~10% of Wt_{initial}. The duration of the weight loss phase ranged from 36 to 62 days (table S3). Once 10% weight loss had been achieved, intake was adjusted upward until subjects were again weight-stable. Weight maintenance calories were disproportionately reduced (~22%) below those required to

maintain initial weight and ranged from 2050 to 2800 kcal/day for the four individuals. Subject F72 also received triiodothyronine (25 µg/day) during this second weight-stable period (table S3). Fecal samples were obtained throughout the study (table S3) and frozen at –80°C until processed for DNA extraction (*I*).

Twin Participants

Twins were selected from a general population cohort of female like-sex twin pairs, born in Missouri to Missouri-resident parents between 1 July 1975 and 30 June 1985, and first assessed at median age 15 with multiple waves of follow-up (*28, 29*). Selected twins were drawn from (i) a study, which included biological mothers where available, contrasting stably concordant lean twin pairs (both twins had BMIs in the range 18.5 to 24.9 by self-report at all completed assessments) and concordant obese twin pairs (both twins had BMIs ≥ 30 , but with pairs prioritized where at least one twin had BMI > 35 , to maximize separation from the concordant lean pairs) (*I*); (ii) a small-scale study of concordant lean monozygotic twin pairs contrasting free diet with free diet supplemented by twice-daily consumption of a fermented milk product (*II*); and (iii) an ongoing study of twin pairs selected for BMI discordance (either discordant lean/obese or quantitatively discordant).

Other Protocols

See (*7*) for procedures for (i) creating mock bacterial communities to benchmark standard methods for 16S rRNA sequencing and LEA-Seq, (ii) generating robotically arrayed personal bacterial culture collections from human fecal samples, (iii) isolating *B. thetaiotaomicron* strains from fecal samples collected over time from individuals and family members, and (iv) sequencing microbial genomes.

References and Notes

1. P. J. Turnbaugh *et al.*, A core gut microbiome in obese and lean twins. *Nature* **457**, 480 (2009). doi: [10.1038/nature07540](#); pmid: [19043404](#)
2. P. J. Turnbaugh *et al.*, Organismal, genetic, and transcriptional variation in the deeply sequenced gut microbiomes of identical twins. *Proc. Natl. Acad. Sci. U.S.A.* **107**, 7503 (2010). doi: [10.1073/pnas.1002355107](#); pmid: [20363958](#)
3. P. B. Eckburg *et al.*, Diversity of the human intestinal microbial flora. *Science* **308**, 1635 (2005). doi: [10.1126/science.1110591](#); pmid: [15831718](#)
4. T. Mitsuoka, Intestinal flora and aging. *Nutr. Rev.* **50**, 438 (1992). doi: [10.1111/j.1753-4887.1992.tb02499.x](#); pmid: [1488186](#)
5. J. Qin *et al.*, A human gut microbial gene catalogue established by metagenomic sequencing. *Nature* **464**, 59 (2010). doi: [10.1038/nature08821](#); pmid: [20203603](#)
6. S. Schlossnig *et al.*, Genomic variation landscape of the human gut microbiome. *Nature* **493**, 45 (2013). doi: [10.1038/nature11711](#); pmid: [23222524](#)
7. See supplementary materials on Science Online.
8. J. B. Hiatt, R. P. Patwardhan, E. H. Turner, C. Lee, J. Shendure, Parallel, tag-directed assembly of locally derived short sequence reads. *Nat. Methods* **7**, 119 (2010). doi: [10.1038/nmeth.1416](#); pmid: [20081835](#)
9. C. B. Jabara, C. D. Jones, J. Roach, J. A. Anderson, R. Swanstrom, Accurate sampling and deep sequencing of the HIV-1 protease gene using a Primer ID. *Proc. Natl. Acad. Sci. U.S.A.* **108**, 20166 (2011). doi: [10.1073/pnas.1110064108](#); pmid: [22135472](#)
10. T. Kivioja *et al.*, Counting absolute numbers of molecules using unique molecular identifiers. *Nat. Methods* **9**, 72 (2012). doi: [10.1038/nmeth.1778](#); pmid: [22101854](#)
11. N. P. McNulty *et al.*, The impact of a consortium of fermented milk strains on the gut microbiome of gnotobiotic mice and monozygotic twins. *Sci. Transl. Med.* **3**, 106ra106 (2011). doi: [10.1126/scitranslmed.3002701](#)
12. H. R. Kissileff *et al.*, Leptin reverses declines in satiation in weight-reduced obese humans. *Am. J. Clin. Nutr.* **95**, 309 (2012). doi: [10.3945/ajcn.111.012385](#); pmid: [22237063](#)
13. M. Rosenbaum *et al.*, A comparative study of different means of assessing long-term energy expenditure in humans. *Am. J. Physiol.* **270**, R496 (1996). pmid: [8780213](#)
14. M. Rosenbaum *et al.*, Effects of weight change on plasma leptin concentrations and energy expenditure. *J. Clin. Endocrinol. Metab.* **82**, 3647 (1997). doi: [10.1210/jc.82.11.3647](#); pmid: [9360521](#)
15. R. L. Leibel, M. Rosenbaum, J. Hirsch, Changes in energy expenditure resulting from altered body weight. *N. Engl. J. Med.* **332**, 621 (1995). doi: [10.1056/NEJM199503093321001](#); pmid: [7632212](#)
16. E. G. Zoetendal, A. D. Akkermans, W. M. De Vos, Temperature gradient gel electrophoresis analysis of 16S rRNA from human fecal samples reveals stable and host-specific communities of active bacteria. *Appl. Environ. Microbiol.* **64**, 3854 (1998). pmid: [9758810](#)
17. E. K. Costello *et al.*, Bacterial community variation in human body habitats across space and time. *Science* **326**, 1694 (2009). http://www.ncbi.nlm.nih.gov/entrez/query.fcgi?cmd=Retrieve&db=PubMed&list_uids=19892944&dopt=Abstract. doi: [10.1126/science.1177486](#); pmid: [19892944](#)
18. C. Huttenhower *et al.*, Structure, function and diversity of the healthy human microbiome. *Nature* **486**, 207 (2012). doi: [10.1038/nature11234](#); pmid: [22699609](#)
19. M. Rajilić-Stojanović, H. G. H. J. Heilig, S. Tims, E. G. Zoetendal, W. M. de Vos, Long-term monitoring of the human intestinal microbiota composition. *Environ. Microbiol.* (2012). doi: [10.1111/1462-2920.12023](#); pmid: [23286720](#)
20. A. L. Goodman *et al.*, Extensive personal human gut microbiota culture collections characterized and manipulated in gnotobiotic mice. *Proc. Natl. Acad. Sci. U.S.A.* **108**, 6252 (2011). doi: [10.1073/pnas.1102938108](#); pmid: [21436049](#)
21. S. Kurtz *et al.*, Versatile and open software for comparing large genomes. *Genome Biol.* **5**, R12 (2004). doi: [10.1186/gb-2004-5-2-r12](#); pmid: [14759262](#)
22. S. R. Henz, D. H. Huson, A. F. Auch, K. Nieselt-Struwe, S. C. Schuster, Whole-genome prokaryotic phylogeny. *Bioinformatics* **21**, 2329 (2005). doi: [10.1093/bioinformatics/bth324](#); pmid: [15166018](#)
23. Q. Wang, G. M. Garrity, J. M. Tiedje, J. R. Cole, Naive Bayesian classifier for rapid assignment of rRNA sequences into the new bacterial taxonomy. *Appl. Environ. Microbiol.* **73**, 5261 (2007). doi: [10.1128/AEM.00062-07](#); pmid: [17586664](#)
24. E. E. Hansen *et al.*, Pan-genome of the dominant human gut-associated archaeon, *Methanobrevibacter smithii*, studied in twins. *Proc. Natl. Acad. Sci. U.S.A.* **108** (suppl. 1), 4599 (2011). doi: [10.1073/pnas.1000071108](#); pmid: [21317366](#)
25. D. A. Peterson, N. P. McNulty, J. L. Guruge, J. I. Gordon, IgA response to symbiotic bacteria as a mediator of gut homeostasis. *Cell Host Microbe* **2**, 328 (2007). doi: [10.1016/j.chom.2007.09.013](#); pmid: [18005754](#)
26. J. G. Caporaso *et al.*, Moving pictures of the human microbiome. *Genome Biol.* **12**, R50 (2011). doi: [10.1186/gb-2011-12-5-r50](#); pmid: [21624126](#)
27. J. Halfvarson, Genetics in twins with Crohn's disease: Less pronounced than previously believed? *Inflamm. Bowel Dis.* **17**, 6 (2011). doi: [10.1002/ibd.21295](#); pmid: [20848478](#)
28. W. S. Slutske *et al.*, Do college students drink more than their non-college-attending peers? Evidence from a population-based longitudinal female twin study. *J. Abnorm. Psychol.* **113**, 530 (2004). doi: [10.1037/0021-843X.113.4.530](#); pmid: [15535786](#)
29. M. Waldron, K. K. Bucholz, M. T. Lynskey, P. A. Madden, A. C. Heath, Alcoholism and timing of separation in parents: Findings in a midwestern birth cohort. *J. Stud. Alcohol Drugs* **74**, 337 (2013). pmid: [23384382](#)

Acknowledgments: We thank D. Hopper and S. Marion for their contributions to the recruitment of twins from the MOAFTS cohort and for obtaining fecal samples for the present study; J. Hoisington-Lopez, M. Meier, and S. Deng for technical assistance; and members of the Gordon lab for their many helpful suggestions during the course of this study. Supported by NIH grants DK30292, DK078669, DK70977, DK64774, and UL1TR000040; the Crohn's and Colitis Foundation of America; Groupe Danone (through partial support of the postdoctoral stipend of J.J.F.); and the Howard Hughes Medical Institute. Draft genome assemblies are available from the European Bioinformatics Institute (EBI) under accession numbers PRJEB3419 to PRJEB3951. Raw and processed LEA-Seq data, as well as experimental protocols for LEA-Seq and phased 16S rRNA amplicon sequencing, can be found at http://gordonlab.wustl.edu/microbiota_stability/. The authors do not declare any conflicts of interest. Author contributions: J.J.F. and J.I.G. designed the experiments; A.C.H., R.L.L., and M.R. oversaw human studies; J.J.F., J.L.G., M.C., S.S., H.S., and A.L.G. generated the data; J.J.F., R.K., J.C.C., S.S., and J.I.G. analyzed data; J.J.F. and J.I.G. wrote the paper.

Supplementary Materials
www.sciencemag.org/content/341/6141/1237439/suppl/DC1
 Supplementary Methods
 Supplementary Text
 Figs. S1 to S8
 Tables S1 to S15
 References (30–41)

6 March 2013; accepted 30 May 2013
 10.1126/science.1237439

Bringing Ecosystem Services into Economic Decision-Making: Land Use in the United Kingdom

Ian J. Bateman,^{1*} Amii R. Harwood,¹ Georgina M. Mace,² Robert T. Watson,³ David J. Abson,^{4,5} Barnaby Andrews,¹ Amy Binner,¹ Andrew Crowe,⁶ Brett H. Day,¹ Steve Dugdale,¹ Carlo Fezzi,¹ Jo Foden,⁷ David Hadley,^{1,8} Roy Haines-Young,⁹ Mark Hulme,¹⁰ Andreas Kontoleon,¹¹ Andrew A. Lovett,¹ Paul Munday,¹ Unai Pascual,^{11,12} James Paterson,¹³ Grischa Perino,^{1,14} Antara Sen,¹ Gavin Siriwardena,¹⁰ Daan van Soest,¹⁵ Mette Termansen¹⁶

Landscapes generate a wide range of valuable ecosystem services, yet land-use decisions often ignore the value of these services. Using the example of the United Kingdom, we show the significance of land-use change not only for agricultural production but also for emissions and sequestration of greenhouse gases, open-access recreational visits, urban green space, and wild-species diversity. We use spatially explicit models in conjunction with valuation methods to estimate comparable economic values for these services, taking account of climate change impacts. We show that, although decisions that focus solely on agriculture reduce overall ecosystem service values, highly significant value increases can be obtained from targeted planning by incorporating all potential services and their values and that this approach also conserves wild-species diversity.

The Millennium Ecosystem Assessment (1) provided important evidence of the ongoing global degradation of ecosystem services and highlighted the need to incorporate their value into the economic analyses that underpin real-world decision-making. Previous studies have shown that the overall values of unconverted natural habitats can exceed the private benefits after conversion (2, 3); that knowledge of landscape heterogeneity and ecological processes can support cost-effective land planning (4–7); that

trade-offs in land-use decisions affect values from ecosystem services and biodiversity at the local level (8, 9); and that current land use is vulnerable to the impacts of global change (10, 11). In the UK National Ecosystem Assessment (NEA) (12), a comprehensive assessment of the United Kingdom's ecosystems was linked to a systematic environmental and economic analysis of the benefits they generate. Here, we show how taking account of multiple objectives in a changing environment (including, but not restricted to, climate

change) fundamentally alters decisions regarding optimal land use. The NEA analyses are based on highly detailed, spatially referenced environmental data covering all of Great Britain. These data supported the design and parameterization of models of both the drivers and consequences of land-use decisions, by incorporating the complexity of the natural environment and its variation across space and time (13). Model outputs provide inputs

¹Centre for Social and Economic Research on the Global Environment (CSERGE), School of Environmental Sciences, University of East Anglia (UEA), Norwich Research Park, Norwich, NR4 7TJ, UK. ²Department of Genetics, Ecology and Environment, University College London, London WC1E 6BT, UK. ³Tyndall Centre, Department of Environmental Sciences, University of East Anglia, Norwich Research Park, NR4 7TJ, UK and Monash Sustainability Institute, Monash University, Melbourne, Australia. ⁴FutureES Research Center, Leuphana Universität Lüneburg, 21335 Lüneburg, Germany. ⁵School of Earth and Environment, University of Leeds, Leeds LS2 9JT, UK. ⁶The Food and Environment Research Agency, Department for Environment, Food and Rural Affairs, H.M. Government, London SW1P 3JR, UK. ⁷Centre for Environment, Fisheries and Aquaculture Science (Cefas), Lowestoft, Suffolk NR33 0HT, UK. ⁸UNE Business School, University of New England, Armidale, New South Wales 2351, Australia. ⁹Centre for Environmental Management (CEM), School of Geography, University of Nottingham, Nottingham NG7 2RD, UK. ¹⁰British Trust for Ornithology, Thetford, Norfolk IP24 2PU, UK. ¹¹Department of Land Economy, University of Cambridge, Cambridge CB3 9EP, UK. ¹²Basque Centre for Climate Change (BC3) and IKERBASQUE, Basque Foundation for Science, 48011 Bilbao Bizkaia, Spain. ¹³School of Geosciences, University of Edinburgh, Edinburgh EH9 3JW, UK. ¹⁴School of Business, Economics and Social Sciences, University of Hamburg, Welckerstrasse 8, 20354 Hamburg, Germany. ¹⁵Department of Spatial Economics and Institute for Environmental Studies (IVM), VU University Amsterdam, 1081 HV Amsterdam, and Department of Economics, Tilburg University, 5037 AB Tilburg, Netherlands. ¹⁶Department of Environmental Science, Aarhus University, 8000 Aarhus, Denmark.

*Corresponding author. E-mail: i.bateman@uea.ac.uk

Table 1. Summary of the ecosystem service related goods considered in the analysis. [Metrics, data, modeling and valuation are fully documented in (13).]

Ecosystem service–related good	Metrics (in year specified)	Main data and sources	Model	Valuation
Agricultural production	Proportion and output of land use in each 2-km grid square	Land use, soils and physical environment, climate, digital mapping, etc. (31–33)	Environmental-econometric regression analysis of land-use decisions as a function of the local physical environment, prices, costs and policies, based on (34)	Market values (35)
Greenhouse gases	Net metric tons of CO ₂ , CH ₄ , and N ₂ O per 2-km grid square	Land-use predictions, GHG responses (36–38)	Process models for CO ₂ , CH ₄ , and N ₂ O; conversion to metric tons of CO ₂ equivalent (MTCO ₂ Eq) based on insulation factors	Official UK values per MTCO ₂ Eq (39)
Recreation	Visitors per 2-km grid square	National survey of >40,000 households, census (40, 41)	Regression model of visit count from outset to destination as a function of characteristics of both locations, population socioeconomics, etc.	Meta-analysis of 300 ecosystem-specific valuation estimates
Urban green-space amenity	Distance to green space from each 2-km grid square	Digital mapping census (32, 41)	Regression model linking distance from households to green-space sites, their size and quality	Meta-analysis of prior literature examining changes in value with respect to distance
Wild bird–species diversity	Wild bird diversity (20) per 2-km grid square	Breeding Bird Survey (42)	Regression model linking wild bird diversity to land use and location.	Not valued; analysis uses the opportunity cost of avoiding declines

to economic analyses that assess the value of both marketed and nonmarketed goods (Table 1).

The NEA specifically addressed the consequences of land-use change driven by either agricultural values only or a wider set of values, all within the context of ongoing climate change. To assess this, raw data on land use and its determinants were drawn from multiple sources to compile a 40-year data set, spatially disaggregated at a resolution of 2-km grid squares (400 ha) or finer across all of Great Britain, forming more than one-half million sets of spatially referenced, time-specific, land-use records. Data on the determinants of that land use were assembled from multiple sources and included the physical environment (both spatially variable factors, such as soil characteristics and slope, and spatio-temporal climate variables, such as growing season temperature and precipitation); policy (both agricultural and relevant environmental measures, including subsidies, taxes, and activity constraints); market forces (such as prices and costs); and technology (reflected as changes in costs).

Land-Use Change

Land use in the United Kingdom is dominated by agriculture, which accounts for some 18.3 million hectares or 74.8% of the total surface area (14) and includes not only cropland but also the majority of grassland, mountain, moor, and heathland habitats. Agricultural land use was analyzed by using integrated environmental-economic models developed to capture spatial and temporal variation in determinants (15). These models start from the premise that farmers seek to arrange land use so as to maximize long-run profit, subject to the physical-environmental, policy, and price conditions they face in a given location and time (13). Even within the relatively small area of Great Britain, variation in environmental conditions is sufficient to yield very substantial differences in agricultural productivity and, hence, land use. These differences are captured by the model along with the variation due to other drivers; the models are verified by using rigorous out-of-sample, actual-versus-predicted, testing (13).

The focus of the analysis concerned the consequences of alternative land-use futures up until 2060. To assess this, information was needed regarding how drivers of land-use change might alter over that period. Some physical environmental factors can be treated as fixed (for example, soil type) but others, most notably climate change, vary temporally and spatially. For these, modeled outputs of variables—such as growing season temperatures and precipitation (16)—were included in our land-use models. Certain market drivers were kept constant because of extreme uncertainties; for example, food prices may well rise because of increased demand from higher population and other pressures, but this may be mitigated by technological advance and behavioral change. Policy-induced changes—such as the consequences of stronger or weaker environmental regulation on both agricultural and other land—were addressed through an expert-based, deliberative process consistent with the Millennium Ecosystem Assessment (1). This process generated six plausible future scenarios, each described in terms of changes in regulations; these were either generally applied or spatially focused (Table 2). A rule-based approach was used to generate probabilities for each land-cover transition in each cell under each scenario [for example, transfers of land out of intensive agriculture to support the enhancement of areas of conservation importance, as per (17, 18)]. Resultant scenarios are summarized in Table 2 and discussed in detail in (13).

Response of Market-Priced Goods to Land-Use Change

An initial analysis demonstrates the outcome of conventional land-use decision-making, which emphasizes market values (for example, agricultural produce) and ignores nonmarket ecosystem services. Maps of the change in the market value of agricultural output from the present day (2010 baseline) to 2060 under alternative climate change and policy scenarios (ignoring any effects from inflation) are shown in Fig. 1. In the first scenario (Fig. 1A), low emissions from greenhouse gases

(GHGs) cause little climate change [taken from (16)] and have relatively little impact on farming during this period. However, relatively stronger environmental regulations are imposed (the NW scenario from Table 2) that restrict high-intensity farming in many areas, which results in declines in market agricultural values across much of the country. These relatively strong environmental regulations are maintained in the next scenario (Fig. 1B), but climate change now follows a high-emissions path. Although climate change is expected to have mixed consequences for agriculture at a global scale (18, 19), comparison of Fig. 1A and 1B shows that farming in the United Kingdom will largely benefit from warmer temperatures. When the high-emission assumption is maintained (Fig. 1C), it weakens environmental regulations (the WM scenario). This allows land-use changes such as the conversion of some currently protected conservation areas into higher-intensity farming, which results in substantial further increases in agricultural production and corresponding market values.

In these scenarios, irrespective of climate change projections, if land-use decisions are based on market-priced goods alone, then a reduction in environmental regulations must always appear justified. Land-use change, however, alters not only market-priced agricultural outputs but many other important (but typically nonmarket) ecosystem services as well.

Response of Nonmarket Ecosystem Services to Land-Use Change

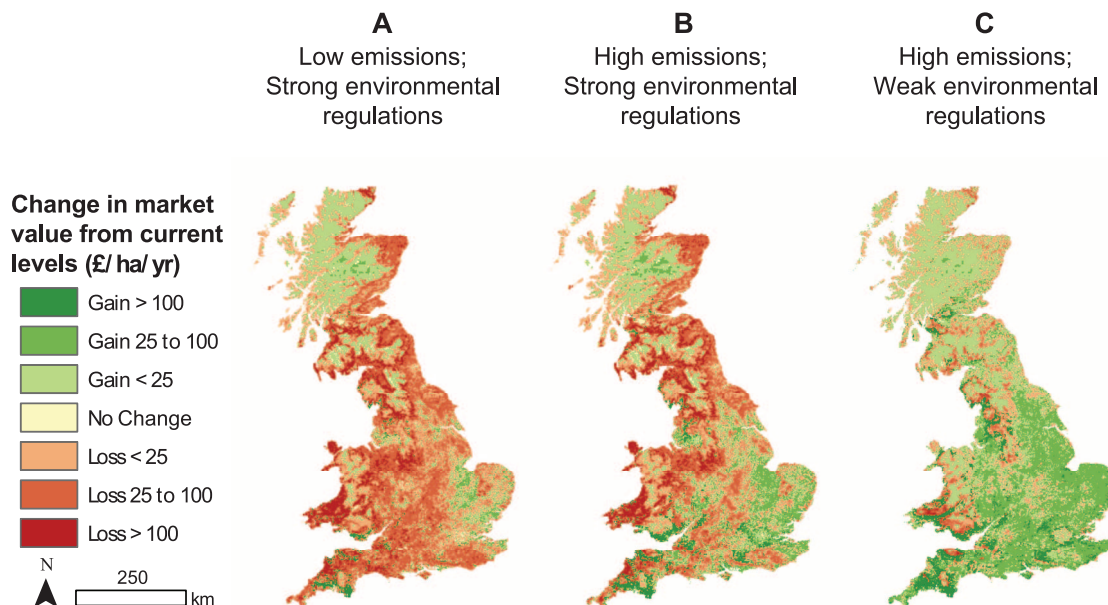
The analysis was extended to include the consequences of land-use change for GHG balance, open-access recreation, urban green space, and wild-species diversity [each modeled according to Table 1 and (13)]. Economic values were estimated for each of these additional impacts, with the exception of wild-species diversity, which is difficult to measure accurately using standard economic tools (15) and was accordingly assessed using a diversity index (13, 20).

Land-use change was then modeled for all scenarios, by embracing a variety of combinations of environmental regulation and climate change, with

Table 2. Summary of land-use change scenarios. [Details in (13).]

Scenario	Environmental regulation and planning policy relative to current	Spatial focusing of changes
Go with the flow (GF)	Similar: Policy and regulatory regime as today. Existing patterns of countryside protection relaxed only where economic priorities dominate.	Unfocused: Similar spatial constraints on land-use change as today. No expansion of the protected area network.
Nature at work (NW)	Stronger: Policy and planning emphasize multifunctional landscapes and the need to maintain ecosystem function.	Focused: Greening of urban and peri-urban areas to enhance recreation values.
Green and pleasant land (GPL)	Stronger: Agri-environmental schemes strengthened with expansion of stewardship and conservation areas.	Focused: Increased extent of existing conservation areas. Creation of functional ecological networks where possible.
Local stewardship (LS)	Stronger: Agri-environmental schemes strengthened with expansion of stewardship and conservation areas.	Unfocused: No strong spatial component to changes but protection of areas of national significance continues.
National security (NS)	Weaker: Emphasis on increasing UK agricultural production. Environmental regulation and policy is weakened.	Unfocused: Some land-use conversion into woodland occurs in areas of lower agricultural values
World markets (WM)	Weaker: Environmental regulation and policy are weakened unless they coincide with improved agricultural production.	Focused: Losses of greenbelt to urban development, which results in loss of recreational values. Weaker protection of designated sites and habitats.

Fig. 1. Change from 2010 to 2060 in the market value of United Kingdom agricultural production under various climate and policy scenarios. (A) Under low-emissions climate projections [from (16)] and strong environmental regulations (NW scenario further described in Table 1), environmentally important habitats are conserved and farm intensification is restricted. **(B)** Under high-emissions climate projections (16) with the policy scenario as in (A). **(C)** Emissions as in (B) but with weak environmental regulations (WM scenario see Table 1). All values are adjusted for inflation.



the consequences assessed for all market and non-market ecosystem services (including agricultural outputs) and their value or indices. Changes in value from the 2010 baseline are shown in Fig. 2 under either the weaker environmental regulations of the WM scenario (top row of Fig. 2) or the stronger regulations of the NW scenario (bottom row); high-emission climate change projections were assumed in both cases. Considering agricultural values alone, results are (as per Fig. 1, B and C) that the weaker environmental regulations of the WM scenario yield higher market values. However, the nonmarket impacts of land-use change illustrated in the rest of Fig. 2 show that, across much of the country, strong environmental policies yield gains in the value of ecosystem services resulting from reduced GHG emissions and enhanced recreation and urban green space, as well as improvements in species diversity. Temporarily setting aside the nonmonetary wild bird-diversity index and summing across all other values shows that weaker (or stronger) environmental regulations lead to net losses (or gains) nationally; a result that reverses the restricted, market value assessment of Fig. 1. It is clear that considering market prices alone can drive decisions for land use that would deprive society of many other benefits from the environment and would risk leaving the United Kingdom worse, rather than better, off.

Benefits of Spatially Targeted Land-Use Planning

Whereas the two alternative futures shown in Fig. 2 illustrate the importance of bringing ecosystem services into decision-making rather than simply relying on market values, these extremes ignore the potential gains from working with the spatial and temporal heterogeneity of the natural environment and the underpinning biophysical processes. This variation makes it unlikely that any single policy will be optimal everywhere (for example, in Fig. 2 the generally superior NW pol-

icy still yields higher GHG emissions in north-western Britain than the generally inferior WM scenario), which suggests, instead, that a move toward a spatially differentiated, targeted approach to decision-making will almost inevitably be better.

In order to examine the benefits of spatially explicit decision-making, the outcomes of each scenario were evaluated in each 2-km grid square across Great Britain, and the scenario that maximized a given objective in that cell was identified (Fig. 3). Results showed that, although a conventional, market-dominated approach to decision-making chooses options to maximize agricultural values (Fig. 3A), these policies will reduce overall values (including those from other ecosystem services) from the landscape in many parts of the country (Fig. 3B); notably in upland areas (where agricultural intensification results in substantial net emissions of GHG) and around major cities (where losses of greenbelt land lower recreation values). In comparison, an approach that considers all of those ecosystem services for which robust economic values can be estimated (Fig. 3C) yields net benefits in almost all areas, with the largest gains in areas of high population (Fig. 3D).

To provide an idea of the scale of potential gains, consider that our measure of agricultural profitability [technically, farm gross margins (21)] suggests returns to farming (including subsidies) ranging from £400/ha to in excess of £1000/ha, depending on location [see (22)]. Our analyses suggest that a targeted approach to land-use planning that recognizes both market goods and nonmarket ecosystem services would increase the net value of land to society by 20% on average, with considerably higher increases arising in certain locations.

Decisions based on all ecosystem services for which robust economic values can be derived (Fig. 3, C and D) are clearly better than those based only on a conventional pursuit of market priced goods (Fig. 3, A and B). However, this analysis

omits impacts that cannot be reliably monetized, for example, the effects on wild bird species diversity. We now incorporate our measures of change in wild bird species diversity through the application of a simple constraint requiring that, in each area, any policy that resulted in a reduction in the species-diversity index was ruled out for that area (Fig. 3, E and F). The similarity to Fig. 3, C and D, shows that, when applied in a targeted manner, this constraint has relatively little impact upon which scenario is best; that is, the “opportunity cost” (17) of imposing a species conservation constraint is relatively minor. Nevertheless, comparison of Fig. 3, C and E, shows that, in certain areas, the sustainability constraint causes a shift from scenario NW, which focuses on the enhancement of greenbelt areas for recreation, to scenario GPL, which focuses on extension of existing areas of conservation value.

National-Scale Implications

Monetary sums from the analyses of Fig. 3 are shown in Table 3. Even if we only consider agricultural market values, then a targeted approach to maximizing these values (first column of results) can yield a small gain in total values relative to the present situation (a result that is not feasible using single policies applied over all of the country, which highlights the inefficiency of current one-size-fits-all policies, even when they are only assessed in terms of market value). However, a targeted approach to optimizing both market and nonmarket values yields a major increase in gains (second column of results). Furthermore, placing a targeted biodiversity constraint on the latter approach only marginally reduces these gains (final column), which suggests both that such constraints are a highly effective and efficient solution to conserving wild-species diversity and that land-use policies that increase GHG storage and recreation values typically correlate with improvements in such diversity.

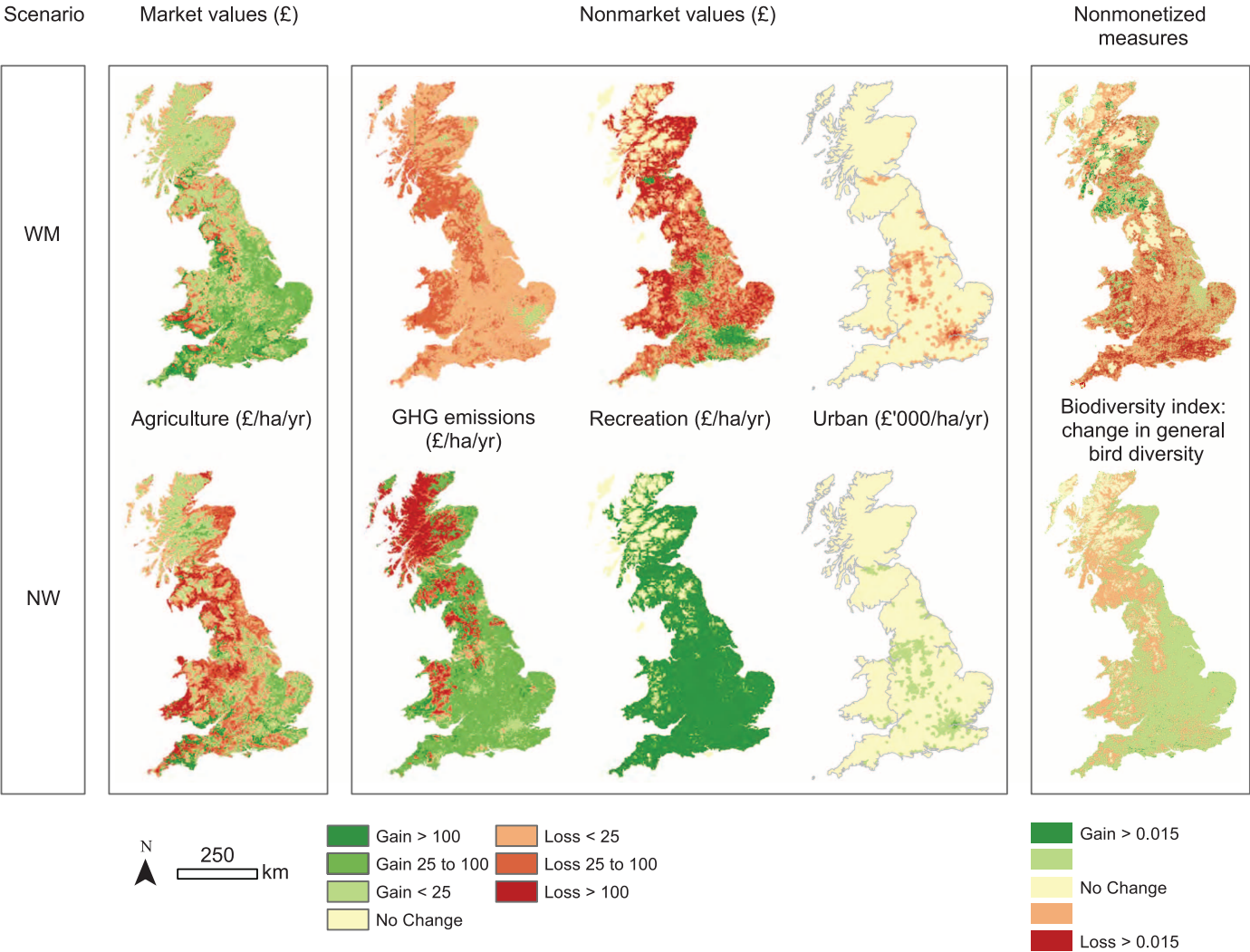


Fig. 2. Spatial distribution of the changes in market and nonmarket ecosystem service economic values and nonmonetary wild species-diversity assessments. These were measured as changes in Simpson's Diversity Index (13, 20) induced by moving from the year 2010 baseline to the WM and NW scenarios for 2060 [all analyses assume high GHG emission climate-change projections from (16)] (30).

Recreation values arising from these changes exceed those from agriculture (Table 3). This striking difference does not imply that the total value of recreation is greater than that of food. It comes about because economic analyses such as this evaluate alternatives by focusing not on total values but on the changes in value that these alternatives generate. In a highly developed country such as the United Kingdom, where food is plentiful and cheap but opportunities for recreational use of the natural environment are somewhat limited, it is not surprising that converting some comparatively small amount of land out of agriculture and into open-access recreation yields a relatively modest loss in farm produce value while at the same time generating a much bigger value from increased recreation. This positive disparity will be greater if (as in this analysis) such conversions are spatially targeted so as to maximize net benefits (here, by ensuring such land-use conversions occur near urban centers where resulting recreational gains can be huge).

However, as progressively more land is converted to recreation, the number of additional visits generated will fall, whereas the agricultural loss of each conversion steadily mounts (explaining why only a limited area, typically near to cities, is converted to recreation). Obviously, such results would vary substantially if analyses were conducted in very different contexts, such as in less developed countries where the value of changes in food may be much higher relative to those for recreation.

From Potential to Practice

Our analysis shows that land-use decisions based on market prices alone can reduce the overall value of the sum of agricultural and monetizable ecosystem services at the national scale. Although the economic values provided in Table 3 are subject to certain assumptions (13), further work to elaborate significant underpinning processes—such as the effects of ecological, biodiversity, and other global change factors (23–25)—and to better reflect links between economic valuation of eco-

system services and decisions seem unlikely to alter this general conclusion. Indeed, if other services such as water resources were added to the analysis, current national estimates of pollution costs (26) imply that the differences would be accentuated. Although potential improvements in land-use planning would generate social gains sufficient to more than compensate for any associated losses, a new direction for land-use decision-making does not come without implementation challenges. A first challenge concerns the mechanics of securing the participation of land managers in delivering land-use changes that are unlikely to be privately beneficial. In the United Kingdom, the obvious mechanism through which that goal could be achieved is reform of the European Union's (EU's) Common Agricultural Policy (CAP). Currently, CAP payments to UK farmers are in excess of £3 billion per annum (27) compared with a total value of UK agriculture of only £5 billion per annum (28) with the vast majority of those payments (70%) made without consideration of

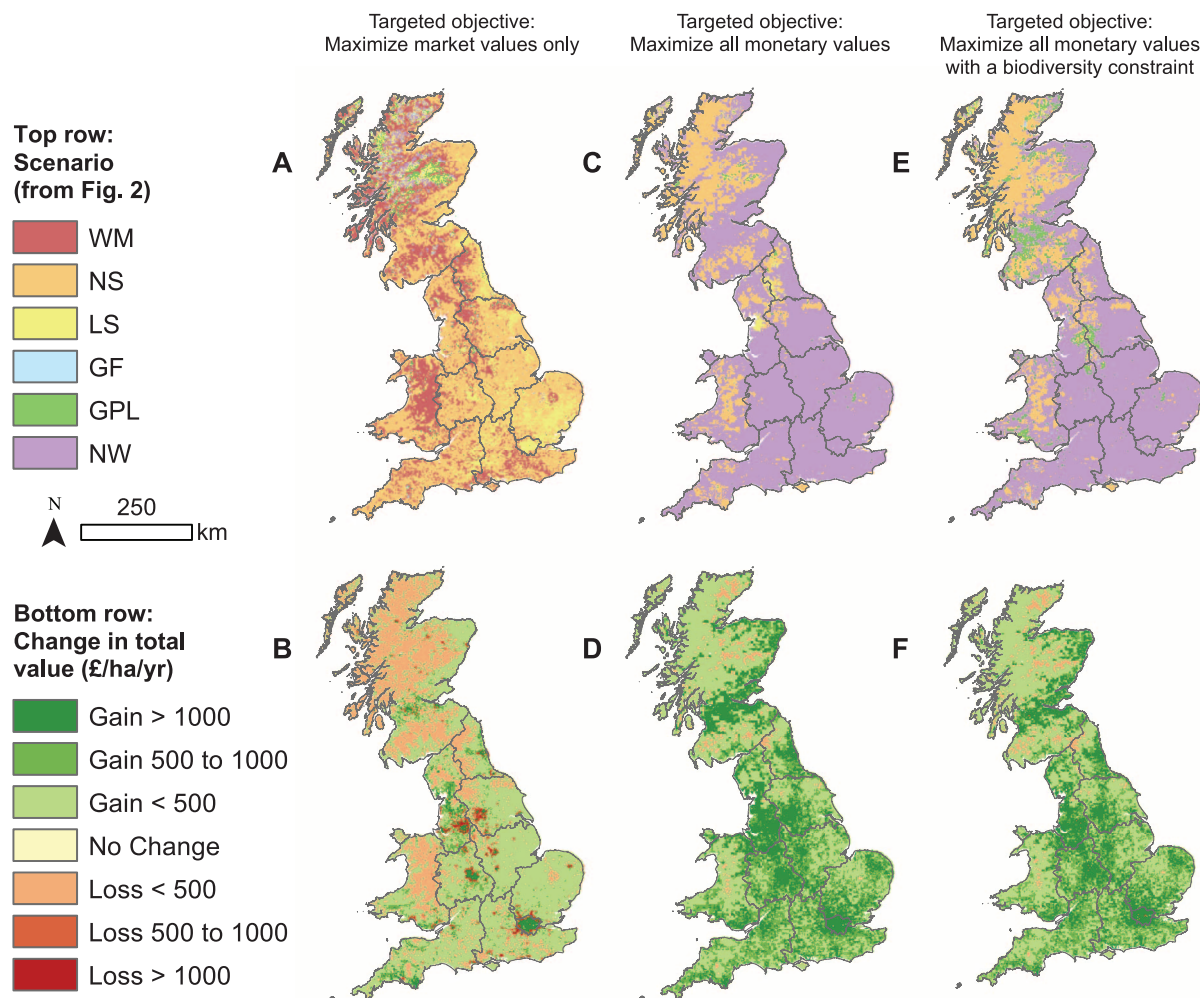


Fig. 3. Optimal scenarios and changes in value. Optimal scenarios (A, C, and E) for each 2-km grid square and corresponding changes in value from 2010 to 2060 (B, D, and F) in Great Britain under three alternative targeted objectives: (i) conventional approach maximizing market values only (A and B); (ii) maximizing the

value of all those ecosystem services that can be robustly monetized (C and D); (iii) maximizing all ecosystem service values but with a constraint so that no scenario that gives a net loss of wild bird diversity is permitted in the area affected (E and F) [all analyses assume low GHG emissions, climate change from (16)] (30).

Table 3. Change in values across Great Britain from the present day (2010) to 2060 achieved by the targeting of policy options under three decision rules. (Millions of £s per annum; real values in £2010; UK Climate Impacts Programme low-emission scenario throughout.)

Decision component	Maximize market (agricultural) values only (Fig. 3, A and B)	Maximize all monetary values (Fig. 3, C and D)	Maximize all monetary values with biodiversity constraint (Fig. 3, E and F)
Market agricultural value	971	−448	−455
Nonmarket GHG emissions	−109	1,517	1,510
Nonmarket recreation	2,550	13,854	12,685
Nonmarket urban green space	−2,520	4,683	4,352
All monetary values	892	19,606	18,092

environmental performance. Recasting the CAP as a Payment for Ecosystem Services (PES) mechanism, such that farmers are rewarded for the delivery of a broad spectrum of ecosystem services, would provide policy-makers with a very powerful tool through which to secure beneficial land-use change.

A second challenge arises from the need, clearly demonstrated in this research, for that mechanism to allow for spatial targeting, a prescription that stands in sharp contrast to the spatial insen-

sitivity of current CAP payment allocation. Spatial targeting, however, necessarily increases pressures upon decision-making and administrative institutions. The key challenge, therefore, is to realize the gains from spatial targeting without overly inflating the costs of policy implementation.

A final challenge concerns how to efficiently target payments when the costs of delivering ecosystem services differ across land managers but are unknown to the funding authority. To that end, recent developments in the design of PES

mechanisms suggest that competitive contracting may deliver considerable efficiency gains (29).

Principles for Future Land-Use Analysis and Planning

Our results allow us to refine the following principles for future analyses and decision-making: (i) The conventional focus upon market-priced goods alone can result in decisions that lower overall values; (ii) all the major ecosystem services generated by a change in resource use need

to be assessed; (iii) that assessment must recognize spatial and temporal variation in ecosystem services, as well as synergistic impacts such as those arising between climate and land-use change; (iv) changes in ecosystem service flows should be valued wherever robust economic values are available; (v) difficult-to-monetize impacts, such as those on wild species, should be incorporated through the imposition of sustainability constraints, which can then be satisfied in cost-effective ways; (vi) spatial targeting of policies can generate major gains; and, perhaps most important, (vii) a range of substantial benefits to society can be realized by bringing natural science and economic information together to inform environmental decision-making. Taken together, we hope that these principles and their demonstration through the case study illustrate the practical potential for national, yet spatially sensitive, application of an approach to decision-making that places ecosystem services on a level playing field with market-priced goods and, thereby, contributes to the sustainable use of Earth's limited resources.

References and Notes

1. Millennium Ecosystem Assessment, *Ecosystems and Human Well-Being: Synthesis* (Island Press, Washington, DC, 2005).
2. A. Balmford *et al.*, *Science* **297**, 950–953 (2002).
3. H. Tallis, A. Guerry, G. C. Daily, in *Encyclopedia of Biodiversity*, S. A. Levin, Ed. (Academic Press, Waltham, ed. 2, 2013), pp. 96–104.
4. E. B. Barbier *et al.*, *Science* **319**, 321–323 (2008).
5. J. A. Foley *et al.*, *Nature* **478**, 337–342 (2011).
6. R. Naidoo, T. H. Ricketts, *PLoS Biol.* **4**, e360 (2006).
7. E. Nelson *et al.*, *Front. Ecol. Environ.* **7**, 4–11 (2009).
8. J. H. Goldstein *et al.*, *Proc. Natl. Acad. Sci. U.S.A.* **109**, 7565–7570 (2012).
9. S. Polasky, E. Nelson, D. Pennington, K. A. Johnson, *Environ. Resour. Econ.* **48**, 219–242 (2011).
10. J. A. Foley *et al.*, *Science* **309**, 570–574 (2005).
11. D. Schröter *et al.*, *Science* **310**, 1333–1337 (2005).
12. NEA, *UK National Ecosystem Assessment: Technical Report* (United Nations Environmental Programme–World Conservation Monitoring Centre (UNEP-WCMC), Cambridge, 2011).
13. Supplementary materials are available on Science Online.
14. Department for Environment, Food, and Rural Affairs (Defra) (United Kingdom); Department of Agriculture and Rural Development (Northern Ireland); The Department for Rural Affairs and Heritage, Welsh Assembly Government; Rural and Environment Research and Analysis Directorate, The Scottish Government, *Agriculture in the United Kingdom 2011* (Office for National Statistics, Newport, UK, 2011).
15. I. J. Bateman, G. M. Mace, C. Fezzi, G. Atkinson, K. Turner, *Environ. Resour. Econ.* **48**, 177–218 (2011).
16. G. J. Jenkins *et al.*, *UK Climate Projection: Briefing Report* (Met Office Hadley Centre, Exeter, UK, 2009).
17. J. H. Lawton *et al.*, "Making space for nature: A review of England's wildlife sites and ecological network: Report to Defra" (Defra, London, 2010).
18. D. B. Lobell, W. Schlenker, J. Costa-Roberts, *Science* **333**, 616–620 (2011).
19. J. Schmidhuber, F. N. Tubiello, *Proc. Natl. Acad. Sci. U.S.A.* **104**, 19703–19708 (2007).
20. E. H. Simpson, *Nature* **163**, 688 (1949).
21. C. Fezzi, D. Rigby, I. J. Bateman, D. Hadley, P. Posen, *Agric. Econ.* **39**, 197–205 (2008).
22. I. J. Bateman, A. A. Lovett, J. S. Brainerd, *Applied Environmental Economics: A GIS Approach to Cost-Benefit Analysis* (Cambridge Univ. Press, Cambridge, 2003).
23. A. D. Barnosky *et al.*, *Nature* **486**, 52–58 (2012).
24. B. J. Cardinale *et al.*, *Nature* **486**, 59–67 (2012).
25. A. P. Kinzig *et al.*, *Science* **334**, 603–604 (2011).
26. A. Moxey, "Agriculture and water quality: Monetary costs and benefits across OECD countries" (OECD, Paris, 2012).
27. Defra, CAP payments (Defra, London, 2013); www.cap-payments.defra.gov.uk/Default.aspx.
28. U.K. Agriculture, Economic trends (Living Countryside, Peterfield, UK, 2013); www.ukagriculture.com/farming_today/economic_trends.cfm.
29. P. J. Ferraro, *Ecol. Econ.* **65**, 810–821 (2008).
30. Ordinance Survey data, Crown copyright and database right 2013.
31. Department for Environment Food and Rural Affairs, "June agricultural census" (Edina, Manchester, 2010).
32. Ordnance Survey, "Land-Form PANORAMA (Digital Elevation Model)" (OS OpenData, Southampton, 2010); www.ordnancesurvey.co.uk/oswebsite/products/os-opendata.html.
33. M. Van Liedekerke, P. Panagos, ESDbV2 Raster Archive (European Commission and the European Soil Bureau Network, Brussels, 2005).
34. C. Fezzi, I. J. Bateman, *Am. J. Agric. Econ.* **93**, 1168–1188 (2011).
35. C. Fezzi *et al.*, *Agric. Econ.* **41**, 123–134 (2010).
36. R. Lal, *Environ. Int.* **30**, 981–990 (2004).
37. A. R. Mosier *et al.*, *Clim. Change* **40**, 39–80 (1998).
38. P. Smith *et al.*, *Agric. Ecosyst. Environ.* **118**, 6–28 (2007).
39. Department of Energy and Climate Change, "Guidance on estimating carbon values beyond 2050: An interim approach" (Department of Energy and Climate Change, London, 2009).
40. Natural England, "Monitor of engagement with the natural environment" (Technical Report NECR050, Natural England, London, 2010).
41. Casweb, "UK Census" (UK Data Service Census Support, Mimas, 2001); <http://casweb.mimas.ac.uk/>.
42. K. Risely *et al.*, *The Breeding Bird Survey 2011* (BTO Research Report 624, British Trust for Ornithology, Thetford, UK, 2011).

Acknowledgments: This work was funded by The UK-NEA and its Follow-On program [which are together supported by the UK Defra; the devolved administrations of Scotland, Wales, and Northern Ireland; the Natural Environment Research Council (NERC) and the Economic and Social Research Council (ESRC)]; and the Social and Environmental Economic Research (SEER) project (ESRC Funder Ref: RES-060-25-0063). I.J.B. led the project with support from all authors; the analysis was designed by I.J.B., A.R.H., G.M.M., and R.W.; C.F., I.J.B., U.P., D.H., P.M., A.R.H., and A.S. undertook the farm land-use analysis; D.J.A., U.P., M.T., C.F., and I.J.B. undertook the GHG analysis; A.S., A.R.H., I.J.B., A.C., J.F., and P.M. undertook the recreation analysis; G.P., B.A., A.K., and I.J.B. undertook the urban green space analysis; M.H., G.S., S.D., and A.A.L. undertook the biodiversity analysis; R.H.-Y. and J.P. undertook the scenario-building exercise; A.R.H. undertook the synthesis and targeting analysis with I.J.B., G.M.M., A.B., B.H.D., and D.V.S.; I.J.B., A.R.H., and G.M.M. wrote the paper with contributions from all authors. We are grateful to P. Dasgupta and K.-G. Mäler for research advice. We declare no conflict of interest. Data are included in the supplementary materials available on Science Online.

Supplementary Materials

www.sciencemag.org/cgi/content/full/341/6141/45/DC1
Supplementary Text
Figs. S1 and S2
Tables S1 to S15
References (43–132)
Data Table S1

20 December 2012; accepted 20 May 2013
10.1126/science.1234379

REPORTS

Signatures of Cool Gas Fueling a Star-Forming Galaxy at Redshift 2.3

N. Bouché,^{1,2*} M. T. Murphy,³ G. G. Kacprzak,³ C. Péroux,⁴ T. Contini,^{1,2} C. L. Martin,⁵ M. Dessauges-Zavadsky⁶

Galaxies are thought to be fed by the continuous accretion of intergalactic gas, but direct observational evidence has been elusive. The accreted gas is expected to orbit about the galaxy's halo, delivering not just fuel for star formation but also angular momentum to the galaxy, leading to distinct kinematic signatures. We report observations showing these distinct signatures near a typical distant star-forming galaxy, where the gas is detected using a background quasar passing 26 kiloparsecs from the host. Our observations indicate that gas accretion plays a major role in galaxy growth because the estimated accretion rate is comparable to the star-formation rate.

At all epochs, galaxies have short gas depletion time scales (1, 2); to sustain the observed levels of star formation over

many billions of years, galaxies must continuously replenish their gas reservoir with fresh gas accreted from the vast amounts available in the

intergalactic medium. In numerical cosmological simulations (3–5), the accretion phenomenon is often referred to as "cold accretion" (6), and this term describes the mass regime where the accretion is most efficient (7, 8). The cold accreted gas should orbit about the halo before falling in to build the central disk, delivering fuel for star formation and also angular momentum to shape the outer parts of the galaxy (9, 10). Thus, accreting

¹CNRS/IRAP, 14 Avenue E. Belin, F-31400 Toulouse, France.

²Université de Toulouse/UPS-OMP/IRAP, F-31400 Toulouse, France. ³Swinburne University of Technology, P.O. Box 218, Hawthorn, Victoria 3122, Australia. ⁴Aix Marseille Université, CNRS, LAM (Laboratoire d'Astrophysique de Marseille) UMR 7326, 13388 Marseille, France. ⁵Department of Physics, University of California, Santa Barbara, CA 93106, USA. ⁶Observatory of Geneva, 51 Chemin des Maillettes, CH-1290 Versoix, Switzerland.

*Corresponding author. E-mail: nicolas.bouche@irap.omp.eu

material should corotate with the central disk in the form of a warped, extended cold gaseous disk, producing distinct kinematic signatures in absorption systems. In particular, the gas kinematics are expected to be offset by about 100 km s^{-1} from the galaxy's systemic velocity, and these kinematic signatures of gas accretion should be observable in suitable quasar absorption line systems (6, 11–13).

Here, we describe observations of a background quasar whose apparent location on the sky is fortuitously aligned with the galaxy's projected major axis, making it possible to test these predictions. The associated star-forming galaxy with redshift $z = 2.3285$ is located just 26 kpc from the damped Lyman absorber (DLA) seen toward the quasar HE 2243–60 (14). The galaxy was detected in our $z \approx 2$ SINFONI (15) survey, called the SINFONI Mg II Program for Line Emitters (SIMPLE) (16). Recent adaptive optics (AO)-assisted SINFONI observations (17) of this $z = 2.3285$ star-forming galaxy (Fig. 1A), obtained at the Very Large Telescope (VLT) with $\sim 1 \text{ kpc}$ (0.25 arc sec) resolution (table S1), allow

us to map the emission kinematics with precision (Fig. 1B and figs. S3 and S4). The kinematics reveal that this galaxy has physical properties (Table 1) typical for rotationally supported disks seen at that redshift (18). For instance, the galaxy has a star-formation rate (SFR) of $33^{+40}_{-11} M_{\odot} \text{ year}^{-1}$ (where M_{\odot} is the mass of the Sun), its maximum rotation velocity is $150 \pm 15 \text{ km s}^{-1}$ from 3D fitting (fig. S4 and table S3), and its metallicity is about $\frac{1}{2}$ solar ($[\text{O}/\text{H}] = -0.35 \pm 0.1 \text{ dex}$) determined from a joint fit to all the major nebular emission lines ($[\text{O II}]$, $[\text{O III}] + \text{H}\beta$, and $\text{H}\alpha/[\text{N II}]$; figs. S1 and S2).

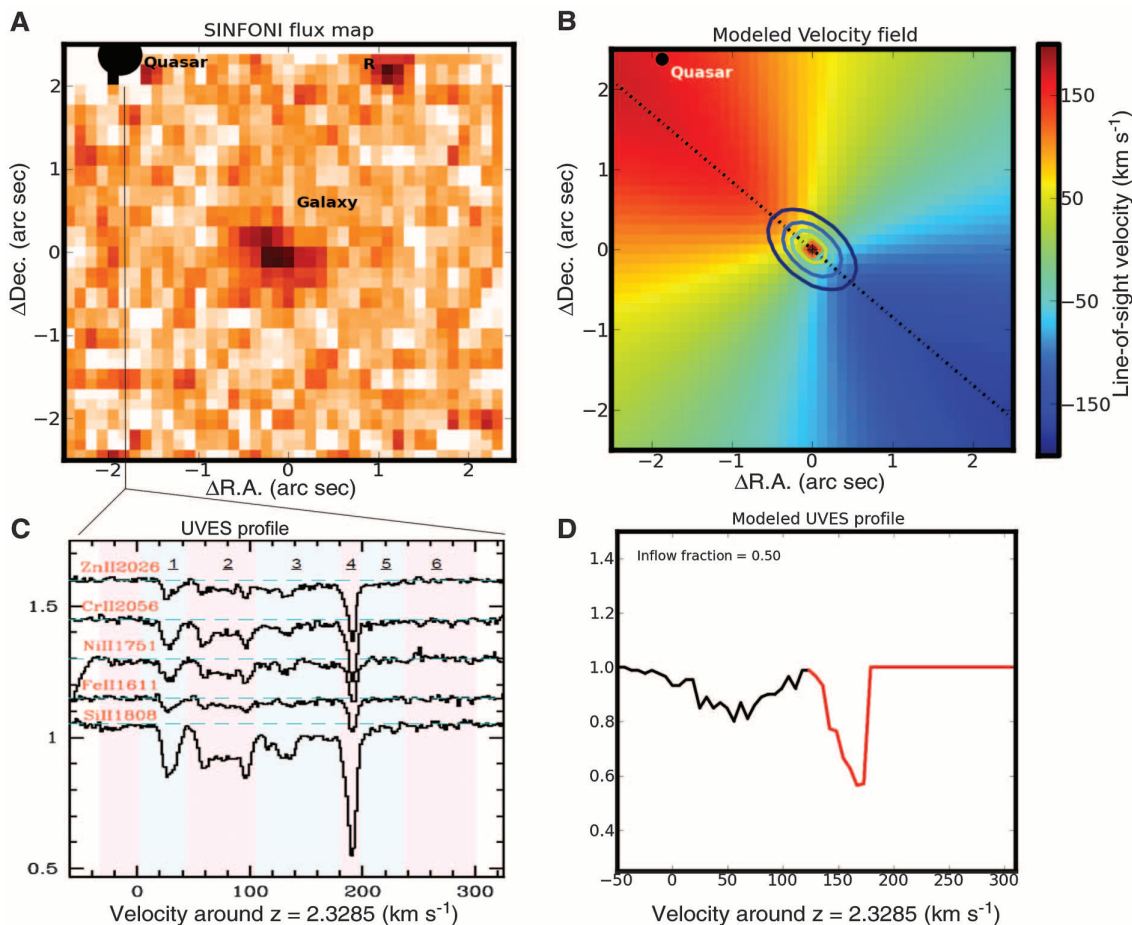
Analysis of a deep high-resolution VLT/UVES (Ultraviolet and Visual Echelle Spectrograph) spectrum of the background quasar HE 2243–60 (fig. S5) (17) shows that the gas metallicity can give us insights into the physical nature of the gas. In particular, the total H I column is $\log(N_{\text{H}}/\text{cm}^{-2}) \approx 20.6$ (i.e., almost entirely neutral) and, from the undepleted low-ionization ion Zn II , the gas metallicity ($[\text{Zn}/\text{H}] = -0.72 \pm 0.05$) (17) is much lower than that of the galaxy ($[\text{O}/\text{H}] = -0.35 \pm 0.1 \text{ dex}$). This comparison dis-

favors an outflow scenario because these tend to be metal-rich (19). Moreover, a biconical outflow should have a very wide cone opening angle ($>140^{\circ}$) in order to intercept the quasar line of sight given the galaxy inclination of 55° (fig. S6). Such a wide cone would result in a very large covering fraction, not supported by DLA host statistics, and would not be compatible with the current constraints on opening angles for outflows near star-forming galaxies at $z = 0.1$ to 1 (20–22).

The kinematics of the absorbing gas give us more clues about the nature of the gas. Thanks to our VLT/SINFONI-AO observations giving us the orientation of the galaxy with respect to the line of sight, the gas kinematics show distinct features (Fig. 1 and fig. S5), and these features can be put in the broader context of the host galaxy kinematics. For instance, the gas seen in absorption 26 kpc from the galaxy—corresponding to 7 times the half-light radius $R_{1/2} = 3.6 \text{ kpc}$, or one-third of the virial size of the halo R_{vir} —is moving in the same direction as the galaxy rotation; that is, the gas appears to be corotating. Indeed, the observed velocity field of this rotating

Fig. 1. Emission and absorption kinematics.

(A) The color scale represents a narrow-band image (rest frame $\text{H}\alpha$) with the continuum subtracted from our AO-assisted VLT/SINFONI datacube. The quasar HE2243–60 and the host $z \sim 2.328$ galaxy are marked. The residuals from the continuum subtraction are visible both near the quasar and near the position labeled R. The galaxy is detected in $\text{H}\alpha$ with a maximum SNR of ~ 5 to 8 per pixel; no continuum emission is detected. The beam has a full width at half maximum (FWHM) of $\sim 0.25 \text{ arc sec}$. **(B)** The fitted velocity field (extrapolated over the entire field) is shown along with the flux contours. The kinematic parameters were determined using our 3D analysis (17). The dotted line shows the kinematic major axis. At the quasar location (solid circle), the rotation speed is expected to be ~ 160 to 180 km s^{-1} . **(C)** The absorption profiles from the VLT/UVES spectra showing the line-of-sight velocity of the various absorption components in the low-ionization ion (Zn II , Cr II , Ni II , Fe II , and Si II) where $v = 0 \text{ km s}^{-1}$ corresponds to the galaxy redshift. The main component (component 4) contains half of the Si II column density and appears to contain more dust (17). This component has a line-of-sight velocity $v = 180 \text{ km s}^{-1}$, consistent with that of the galaxy velocity field shown in (A). **(D)** A simulated line-of-sight profile



for the geometry of this quasar-galaxy pair from a toy model that includes an inflow component (black) in addition to a component determined from the extended galaxy velocity field (red). A schematic representation of the model is shown in Fig. 2 and a more detailed representation is presented in fig. S6.

galaxy (Fig. 1B) shows redshifted velocities in the direction of the quasar location, and in the quasar spectrum, all of the low-ionization ions (Zn II, Cr II, Fe II, and Si II) tracing the cold gas also show redshifted velocities (Fig. 1C).

Thanks to the apparent quasar location on the sky being only 10° to 20° from the galaxy’s projected major axis, we can identify two distinct features in the low-ionization lines. The first feature comes from a quantitative comparison between the velocity field of the galaxy (Fig. 1B) and the low-ionization kinematics (Fig. 1C): The velocities seen in absorption for component 4 and seen in emission from the galaxy closely match one another. This would indicate that a simple rotating disk with circular orbits and a normal (flat) rotation curve can account for the bulk of the absorbing gas kinematics, but not all. Thus, components 1 to 3, which have a line-of-sight velocity less than the rotation speed, correspond to gas that is also corotating but is not rotationally supported, because these components do not have the required speed. In other words, two groups of components (1 to 3; 4 to 6) are seen, and one group is offset by about 100 km s^{−1} from the rotation pattern; hence, this group cannot be gravitationally supported and therefore should be flowing in. Each of these two groups contains about half of the total H I column log *N*_H ≈ 20.6 (fig. S5) (17).

Thus, our SINFONI and UVES data show that the absorbing components have the broad characteristics of low-metallicity, coplanar, corotating accreting material similar to the expected features from numerical simulations (9). Moreover, the dust profile (fig. S5D) determined from the data (17) indicates that components 1 to 3 are less enriched than the main components (4 and 5). Given that the amount of dust (or dust-to-gas ratio) correlates with the metallicity (23), the dust profile also supports the scenario in which the quasar line of sight probes a mix of accreting material with that of an extended gaseous disk.

To gain further insights into the accreting gas, we experimented with a simple geometrical toy model using a Monte Carlo approach to generate simulated absorption profiles (17). In the model, we distribute “particles” representing gas clouds or absorption components where the cloud kinematics reflect an inflowing gas (radial for simplicity; see Fig. 2). Because the relative galaxy orientation is well determined by the VLT/SINFONI data, the only free parameter is the inflow speed (fig. S6). The resulting absorption profile simulated at the UVES resolution (Fig. 1D) shows qualitative agreement with the data (Fig. 1C).

We do not expect such a model to be completely realistic nor to fit the data perfectly; there are many uncertainties such as the exact geometry of the accreting gas. However, the model can give us a framework to estimate the amount of accretion (17). The accreting material coming from the large-scale filamentary structure is presumed to form a roughly coplanar structure around the galaxy (9, 10). Assuming an azimuth-

al symmetry (see Fig. 2 and fig. S6), the global mass flux rate through an area of 2π*b**h_z* is thus

$$\begin{aligned} \dot{M}_{\text{in}}(b) &\propto 2\pi N_{\text{H}} b V_{\text{in}} \cos(i) \\ &= 46 \left(\frac{\mu}{1.6}\right) \left(\frac{N_{\text{H}}}{2 \times 10^{20} \text{ cm}^{-2}}\right) \left(\frac{b}{26 \text{ kpc}}\right) \\ &\quad \times \left(\frac{V_{\text{in}}}{200 \text{ km/s}}\right) \left(\frac{\cos(i)}{0.57}\right) M_{\odot} \text{ year}^{-1} \quad (1) \end{aligned}$$

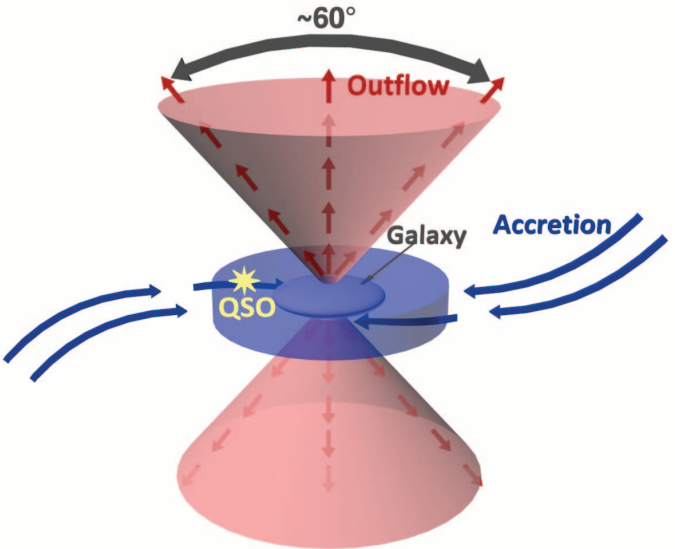
where μ is the mean molecular weight, *N*_H is the total gas column, *b* is the impact parameter, *V*_{in} is the radial velocity component, and *i* is the disk inclination. This expression holds for any thin structure of thickness *h_z* and density ρ because we used the identity *N*_H = ∫ *dz* ρ(*b*) = ρ(*b*) *h_z* / cos(*i*).

Table 1. Physical properties of the galaxy.

Galaxy properties	Measured values
Quasar impact parameter (<i>b</i>)	3.1 arc sec or 26 kpc
Major-axis position angle	62° ± 5°
Quasar position angle	42° ± 1°
Redshift <i>z</i> _{Hα}	2.3283 ± 0.0001
Half-light radius (<i>R</i> _{1/2})	3.6 ± 0.3 kpc
Maximum circular velocity (<i>V</i> _{max})	150 ± 15 km s ^{−1}
Inclination (<i>i</i>)	55° ± 1°
Dispersion velocity (σ _{<i>i</i>})	158 ± 5 km s ^{−1}
Halo mass (<i>M</i> _h)	~4 × 10 ¹¹ <i>M</i> _⊙
Virial radius (<i>R</i> _{vir})	~90 kpc
Dynamical mass (<i>M</i> _{dyn})*	2.0 × 10 ¹⁰ <i>M</i> _⊙
Interstellar gas mass (<i>M</i> _g)†	1.5 × 10 ¹⁰ <i>M</i> _⊙
Gas fraction (<i>f</i> _g)	~0.75
Metallicity (log <i>Z</i> / <i>Z</i> _⊙)	−0.35 ± 0.1
SFR _{Hα} ‡	18 ± 2 <i>M</i> _⊙ year ^{−1}
Dust-corrected SFR _{Hα}	33 ⁺⁴⁰ _{−11} <i>M</i> _⊙ year ^{−1}
Gas accretion rate (<i>Ḣ</i> _{in})	~45 <i>M</i> _⊙ year ^{−1}

*Within the half-light radius *r*_{1/2} assuming *V_c*² = *GM*/*r*_{1/2}. †Within the half-light radius *r*_{1/2} determined from the Hα surface density by inverting the star-formation law. ‡Integrated SFR (17).

Fig. 2. Schematic diagram of the simplified model. The star-forming galaxy is experiencing a supernova-driven outflow (red) and receiving gas with low angular momentum from the intergalactic medium (blue). The opening angle of the bipolar outflow is assumed to be ~60°, as found in low-redshift observations (20–22). The accreting cold gas is expected to dissipate its angular momentum and migrate toward the galaxy, delivering fuel for the galaxy and forming an extended gaseous coplanar structure. The quasar (yellow) line of sight is represented by the star and is about α = 20° from the major axis, leading to distinct kinematic features seen in the absorption spectra (Fig. 1D and fig. S6). For the observed geometric configuration, the line of sight is intercepting the accreting material but not the outflowing material.



Using the constraints on *V*_{in} and on *N*_H from our SINFONI and UVES data set, the estimated mass flux *M*_{in} in cold gas is around 30 to 60 *M*_⊙ year^{−1} given the uncertainties in the column density and inflow speed. This accretion rate could be overestimated if the flow is very asymmetric, and more realistic models with spiral orbits will lead to results that may differ by the cosine of the spiral opening angle, leading to (downward) corrections by factors of 2 to 3. Similarly, if we relax our assumption of a flat H I profile, the gas column density must be higher for components 1 to 3 to account for both the dust profile and the Si II column density, leading to an upward correction to the accretion rate.

The range of accretion rates estimated from Eq. 1, 30 to $60 M_{\odot} \text{ year}^{-1}$, is found to be close to the galaxy's SFR of $\sim 33^{+40}_{-11} M_{\odot} \text{ year}^{-1}$. This is in agreement with the simplest arguments for galaxy growth via self-regulation (24, 25) and from numerical simulations (4, 6). Furthermore, for this galaxy's halo mass, $M_h \sim 4 \times 10^{11} M_{\odot}$ (determined from its rotation curve), this value of \dot{M}_{in} corresponds to an accretion efficiency ϵ of $\sim 100\%$ [where ϵ is defined as the ratio of the observed and maximum expected baryonic accretion rates, namely $\epsilon \equiv \dot{M}_{\text{in}} / (f_B \dot{M}_h)$, where f_B is the universal baryonic fraction and \dot{M}_h is the halo growth rate (26, 27)].

Our study shows the potential of the technique of using background quasars passing near galaxies to further understand the process of gas accretion in galaxies, which is complementary to other recent studies (28–30). Our observations, which are merely consistent with cold accretion, provide key evidence important to consider against hydrodynamical simulations.

References and Notes

- E. Daddi *et al.*, *Astrophys. J.* **713**, 686 (2010).
- R. Genzel *et al.*, *Mon. Not. R. Astron. Soc.* **407**, 2091 (2010).
- D. Kereš, N. Katz, D. H. Weinberg, R. Davé, *Mon. Not. R. Astron. Soc.* **363**, 2 (2005).
- C.-A. Faucher-Giguère, D. Kereš, C.-P. Ma, *Mon. Not. R. Astron. Soc.* **417**, 2982 (2011).
- F. van de Voort *et al.*, *Mon. Not. R. Astron. Soc.* **414**, 2458 (2011).
- A. Dekel *et al.*, *Nature* **457**, 451 (2009).
- S. D. M. White, C. S. Frenk, *Astrophys. J.* **379**, 52 (1991).
- Y. Birnboim, A. Dekel, *Mon. Not. R. Astron. Soc.* **345**, 349 (2003).
- K. R. Stewart *et al.*, *Astrophys. J.* **738**, 39 (2011).
- S. Shen *et al.*, *Astrophys. J.* **765**, 89 (2013).
- K. R. Stewart *et al.*, *Astrophys. J.* **735**, L1 (2011).
- M. Fumagalli *et al.*, *Mon. Not. R. Astron. Soc.* **418**, 1796 (2011).
- T. Goerdt, A. Dekel, A. Sternberg, O. Gnat, D. Ceverino, *Mon. Not. R. Astron. Soc.* **424**, 2292 (2012).
- S. Lopez, D. Reimers, S. D'Odorico, J. X. Prochaska, *Astron. Astrophys.* **385**, 778 (2002).
- SINFONI is the near-infrared integral field spectrograph at one of the Very Large Telescopes (VLTs) of the European Southern Observatory (ESO).
- N. Bouché *et al.*, *Mon. Not. R. Astron. Soc.* **419**, 2 (2012).
- See supplementary materials on Science Online.
- N. M. Förster Schreiber *et al.*, *Astrophys. J.* **706**, 1364 (2009).
- T. M. Tripp *et al.*, *Science* **334**, 952 (2011).
- R. Bordoloi *et al.*, *Astrophys. J.* **743**, 10 (2011).
- N. Bouché *et al.*, *Mon. Not. R. Astron. Soc.* **426**, 801 (2012).
- G. Kacprzak, C. W. Churchill, N. M. Nielsen, *Astrophys. J.* **760**, L7 (2012).
- G. Vladilo *et al.*, *Astron. Astrophys.* **454**, 151 (2006).
- A. A. Dutton, F. C. van den Bosch, A. Dekel, *Mon. Not. R. Astron. Soc.* **405**, 1690 (2010).
- N. Bouché *et al.*, *Astrophys. J.* **718**, 1001 (2010).
- S. Genel *et al.*, *Astrophys. J.* **688**, 789 (2008).
- J. McBride, O. Fakhouri, C. Ma, *Mon. Not. R. Astron. Soc.* **398**, 1858 (2009).
- M. Giallisco *et al.*, *Astrophys. J.* **743**, 95 (2011).
- K. H. R. Rubin, J. X. Prochaska, D. C. Koo, A. C. Phillips, *Astrophys. J.* **747**, L26 (2012).
- J. Ribado *et al.*, *Astrophys. J.* **743**, 207 (2011).

Acknowledgments: We thank the ESO Paranal staff for their continuous support and the SINFONI instrument team for their hard work, which made SINFONI a very reliable instrument. N.B. thanks S. Lilly and R. Bordoloi for stimulating discussions and S. Genel for a careful read of the manuscript. We thank I. Schroetter for his assistance in making Fig. 2. We thank the reviewers for their thorough review, comments, and suggestions. This research was based on work supported in part by NSF grant 1066293 and the hospitality of the Aspen Center for Physics. It was partly supported by a Marie Curie International Outgoing Fellowship (PIOF-GA-2009-236012) and by a Marie Curie International Career Integration Grant (PCIG11-GA-2012-321702) within the 7th European Community Framework Program. M.T.M. thanks the Australian Research Council for a QEII Fellowship (DP0877998) and Discovery Project grant DP130100568. C.L.M. is supported by NSF grant AST-1109288. The data used in this paper are tabulated in the supplementary materials and archived at <http://archive.eso.org> under program ID 383.A-0750 and 088.B-0715. G.G.K. is an Australian Research Council Super Science Fellow.

Supplementary Materials

www.sciencemag.org/cgi/content/full/341/6141/50/DC1
Supplementary Text
Figs. S1 to S6
Tables S1 to S4
References (31–73)

18 December 2012; accepted 29 May 2013
10.1126/science.1234209

A Population of Fast Radio Bursts at Cosmological Distances

D. Thornton,^{1,2*} B. Stappers,¹ M. Bailes,^{3,4} B. Barsdell,^{3,4} S. Bates,⁵ N. D. R. Bhat,^{3,4,6} M. Burgay,⁷ S. Burke-Spolaor,⁸ D. J. Champion,⁹ P. Coster,^{2,3} N. D'Amico,^{10,7} A. Jameson,^{3,4} S. Johnston,² M. Keith,² M. Kramer,^{9,1} L. Levin,⁵ S. Milia,⁷ C. Ng,⁹ A. Possenti,⁷ W. van Straten^{3,4}

Searches for transient astrophysical sources often reveal unexpected classes of objects that are useful physical laboratories. In a recent survey for pulsars and fast transients, we have uncovered four millisecond-duration radio transients all more than 40° from the Galactic plane. The bursts' properties indicate that they are of celestial rather than terrestrial origin. Host galaxy and intergalactic medium models suggest that they have cosmological redshifts of 0.5 to 1 and distances of up to 3 gigaparsecs. No temporally coincident x- or gamma-ray signature was identified in association with the bursts. Characterization of the source population and identification of host galaxies offers an opportunity to determine the baryonic content of the universe.

The four fast radio bursts (FRBs) (Fig. 1) reported here were detected in the high Galactic latitude region of the High Time Resolution Universe (HTRU) survey (1), which was designed to detect short-time-scale radio transients and pulsars (Galactic pulsed radio sources). The survey uses the 64-m Parkes radio telescope and its 13-beam receiver to acquire data across a bandwidth of 400 MHz centered at 1.382 GHz (table S1). We measured minimum fluences for the FRBs of $F = 0.6$ to 8.0 Jy ms ($1 \text{ Jy} = 10^{-26} \text{ W m}^{-2} \text{ Hz}^{-1}$) (2). At cosmological distances, this indicates that they are more luminous than bursts from any known transient radio source (3). Follow-up observations at the original beam positions have not detected any repeat events,

indicating that the FRBs are likely cataclysmic in nature.

Candidate extragalactic bursts have previously been reported with varying degrees of plausibility (4–7), along with a suggestion that FRB 010724 (the “Lorimer burst”) is similar to other signals that may be of local origin (8, 9). To be consistent with a celestial origin, FRBs should exhibit certain pulse properties. In particular, observations of radio pulsars in the Milky Way (MW) have confirmed that radio emission is delayed by propagation through the ionized interstellar medium (ISM), which can be considered a cold plasma. This delay has a power law dependence of $\delta t \propto \text{DM} \cdot \nu^{-2}$ and a typical frequency-dependent width of $W \propto \nu^{-4}$. The dispersion

measure (DM) is related to the integrated column density of free electrons along the line of sight to the source and is a proxy for distance. The frequency-dependent pulse broadening occurs as an astrophysical pulse is scattered by an inhomogeneous turbulent medium, causing a characteristic exponential tail. Parameterizing the frequency dependence of δt and W as α and β , respectively, we measured $\alpha = -2.003 \pm 0.006$ and $\beta = -4.0 \pm 0.4$ for FRB 110220 (Table 1 and Fig. 2), as expected for propagation through a cold plasma. Although FRB 110703 shows no evidence of scattering, we determined $\alpha = -2.000 \pm 0.006$. The other FRBs do not have sufficient

¹Jodrell Bank Centre for Astrophysics, School of Physics and Astronomy, University of Manchester, Manchester M13 9PL, UK. ²Commonwealth Science and Industrial Research Organisation (CSIRO) Astronomy and Space Science, Australia Telescope National Facility, Post Office Box 76, Epping, NSW 1710, Australia. ³Centre for Astrophysics and Supercomputing, Swinburne University of Technology, Mail H30, Post Office Box 218, Hawthorn, VIC 3122, Australia. ⁴Australian Research Council Centre of Excellence for All-Sky Astrophysics (CAASTRO), Mail H30, Post Office Box 218, Hawthorn, VIC 3122, Australia. ⁵West Virginia University Center for Astrophysics, West Virginia University, Morgantown, WV 26506, USA. ⁶International Centre for Radio Astronomy Research, Department of Imaging and Applied Physics, Faculty of Science and Engineering, Curtin University, Post Office Box U1987, Perth, WA 6845, Australia. ⁷Istituto Nazionale di Astrofisica, Osservatorio Astronomico di Cagliari, Loc. Poggio dei Pini, Strada 54, 09012 Capoterra (CA), Italy. ⁸Jet Propulsion Laboratory, California Institute of Technology, 4800 Oak Grove Drive, Pasadena, CA 91104, USA. ⁹Max-Planck-Institut für Radio Astronomie, Auf dem Hügel 69, 53121 Bonn, Germany. ¹⁰Dipartimento di Fisica, Università di Cagliari, Cittadella Universitaria 09042, Monserrato (CA), Italy.

*Corresponding author. E-mail: thornton@jb.man.ac.uk

signal-to-noise ratios (SNRs) to yield astrophysically interesting constraints for either parameter and show no evidence of scattering.

Our FRBs were detected with DMs in the range from 553 to 1103 $\text{cm}^{-3} \text{ pc}$. Their high Galactic latitudes ($|b| > 41^\circ$, Table 1) correspond to lines of sight through the low column density Galactic ISM corresponding to just 3 to 6% of the DM measured (10). These small Galactic DM contributions are highly supportive of an extragalactic origin and are substantially smaller fractions than those of previously reported bursts, which were 15% of $\text{DM} = 375 \text{ cm}^{-3} \text{ pc}$ for FRB 010724 (4) and 70% of $\text{DM} = 746 \text{ cm}^{-3} \text{ pc}$ for FRB 010621 (5).

The non-Galactic DM contribution, DM_E , is the sum of two components: the intergalactic medium (IGM; DM_{IGM}) and a possible host galaxy (DM_{Host}). The intervening medium could be purely intergalactic and could also include a contribution from an intervening galaxy. Two options are considered according to the proximity of the source to the center of a host galaxy.

If located at the center of a galaxy, this may be a highly dispersive region; for example, lines of sight passing through the central regions of Milky Way-like galaxies could lead to DMs in excess of 700 $\text{cm}^{-3} \text{ pc}$ in the central $\sim 100 \text{ pc}$ (11), independent of the line-of-sight inclination. In this case, DM_E is dominated by DM_{Host} and requires FRBs to be emitted by an unknown mechanism in the central region, possibly associated with the supermassive black hole located there.

If outside a central region, then elliptical host galaxies (which are expected to have a low electron density) will not contribute to DM_E substantially, and DM_{Host} for a spiral galaxy will only contribute substantially to DM_E if viewed close to edge-on [inclination, $i > 87^\circ$ for $\text{DM} > 700 \text{ cm}^{-3} \text{ pc}$; probability($i > 87^\circ$) ≈ 0.05]. The chance of all four FRBs coming from edge-on spiral galaxies is therefore negligible (10^{-6}). Consequently, if the sources are not located in a galactic center, DM_{Host} would likely be small, and DM_{IGM} dominates. Assuming an IGM free-electron distribution, which takes into account cosmological redshift and assumes a universal ionization fraction of 1 (12, 13), the sources are inferred to be at redshifts $z = 0.45$ to 0.96, corresponding to comoving distances of 1.7 to 3.2 Gpc (Table 1).

In principle, pulse scatter-broadening measurements can constrain the location and strength of an intervening scattering screen (14). FRBs 110627, 110703, and 120127 are too weak to enable the determination of any scattering; however, FRB 110220 exhibits an exponential scattering tail (Fig. 1). There are at least two possible sources and locations for the responsible scattering screens: a host galaxy or the IGM. It is possible that both contribute to varying degrees.

For screen-source, D_{src} , and screen-observer, D_{obs} , distances, the magnitude of the pulse broadening resulting from scattering is multiplied by the factor $D_{\text{src}} D_{\text{obs}} / (D_{\text{src}} + D_{\text{obs}})^2$. For a screen and source located in a distant galaxy, this effect

probably requires the source to be in a high-scattering region, for example, a galactic center.

The second possibility is scattering because of turbulence in the ionized IGM, unassociated with any galaxy. There is a weakly constrained empirical relationship between DM and measured scattering for pulsars in the MW. If applicable to the IGM, then the observed scattering implies $\text{DM}_{\text{IGM}} > 100 \text{ cm}^{-3} \text{ pc}$ (2, 15). With use of the aforementioned model of the ionized IGM, this DM equates to $z > 0.11$ (2, 12, 13). The probability of an intervening galaxy located along the line of sight within $z \approx 1$ is ≤ 0.05 (16). Such a galaxy could be a source of scattering and dispersion, but the magnitude would be subject to the same inclination dependence as described for a source located in the disk of a spiral galaxy.

It is important to be sure that FRBs are not a terrestrial source of interference. Observations at Parkes have previously shown swept frequency pulses of terrestrial origin, dubbed “peryttons.” These are symmetric $W > 20 \text{ ms}$ pulses, which imperfectly mimic a dispersive sweep (2, 8). Although peryttons peak in apparent DM near 375 $\text{cm}^{-3} \text{ pc}$ (range from ~ 200 to $420 \text{ cm}^{-3} \text{ pc}$),

close to that of FRB 010724, the FRBs presented here have much higher and randomly distributed DMs. Three of these FRBs are factors of >3 narrower than any documented perytton. Last, the characteristic scattering shape and strong dispersion delay adherence of FRB 110220 make a case for cold plasma propagation.

The Sun is known to emit frequency-swept radio bursts at 1 to 3 GHz [type III dm (17)]. These bursts have typical widths of 0.2 to 10 s and positive frequency sweeps, entirely inconsistent with measurements of W and α for the FRBs. Whereas FRB 110220 was separated from the Sun by 5.6° , FRB 110703 was detected at night and the others so far from the Sun that any solar radiation should have appeared in multiple beams. These FRBs were only detected in a single beam; it is therefore unlikely they are of solar origin.

Uncertainty in the true position of the FRBs within the frequency-dependent gain pattern of the telescope makes inferring a spectral index, and hence flux densities outside the observing band, difficult. A likely off-axis position changes the intrinsic spectral index substantially. The spectral

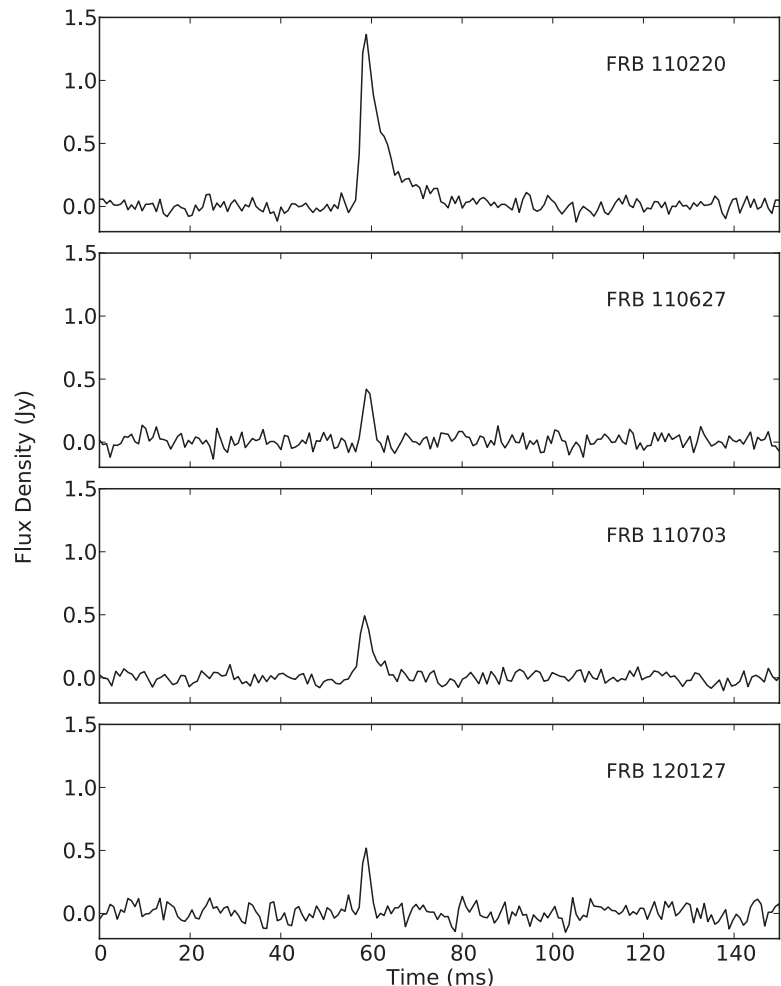
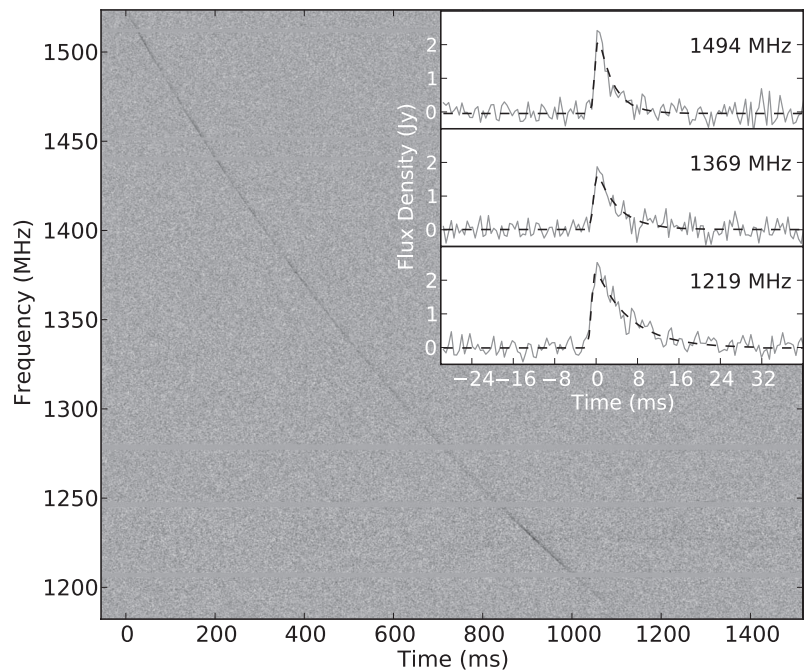


Fig. 1. The frequency-integrated flux densities for the four FRBs. The time resolutions match the level of dispersive smearing in the central frequency channel (0.8, 0.6, 0.9, and 0.5 ms, respectively).

Table 1. Parameters for the four FRBs. The position given is the center of the gain pattern of the beam in which the FRB was detected (half-power beam width ~ 14 arc min). The UTC corresponds to the arrival time at 1581.804688 MHz. The DM uncertainties depend not only on SNR but also on whether α and β are assumed ($\alpha = -2$; no scattering) or fit for; where fitted, α and β are given. The comoving distance was calculated by using $DM_{\text{Host}} = 100 \text{ cm}^{-3} \text{ pc}$ (in the rest frame of the host) and a standard, flat-universe Λ CDM cosmology, which describes the expansion of the universe with baryonic and dark matter and dark energy [$H_0 = 71 \text{ km s}^{-1} \text{ Mpc}^{-1}$, $\Omega_M = 0.27$, $\Omega_\Lambda = 0.73$; H_0 is the Hubble constant and Ω_M and Ω_Λ are fractions of the critical density of matter and dark energy, respectively (29)]. α and β are from a series of fits using intrinsic pulse widths of 0.87 to 3.5 ms; the uncertainties reflect the spread of values obtained (2). The observed widths are shown; FRBs 110627, 110703, and 120127 are limited by the temporal resolution due to dispersion smearing. The energy released is calculated for the observing band in the rest frame of the source (2).

	FRB 110220	FRB 110627	FRB 110703	FRB 120127
Beam right ascension (J2000)	22 ^h 34 ^m	21 ^h 03 ^m	23 ^h 30 ^m	23 ^h 15 ^m
Beam declination (J2000)	−12° 24′	−44° 44′	−02° 52′	−18° 25′
Galactic latitude, b (°)	−54.7	−41.7	−59.0	−66.2
Galactic longitude, l (°)	+50.8	+355.8	+81.0	+49.2
UTC (dd/mm/yyyy hh:mm:ss.sss)	20/02/2011 01:55:48.957	27/06/2011 21:33:17.474	03/07/2011 18:59:40.591	27/01/2012 08:11:21.723
DM ($\text{cm}^{-3} \text{ pc}$)	944.38 ± 0.05	723.0 ± 0.3	1103.6 ± 0.7	553.3 ± 0.3
DM_E ($\text{cm}^{-3} \text{ pc}$)	910	677	1072	521
Redshift, z ($DM_{\text{Host}} = 100 \text{ cm}^{-3} \text{ pc}$)	0.81	0.61	0.96	0.45
Co-moving distance, D (Gpc) at z	2.8	2.2	3.2	1.7
Dispersion index, α	-2.003 ± 0.006	—	-2.000 ± 0.006	—
Scattering index, β	-4.0 ± 0.4	—	—	—
Observed width at 1.3 GHz, W (ms)	5.6 ± 0.1	<1.4	<4.3	<1.1
SNR	49	11	16	11
Minimum peak flux density S_ν (Jy)	1.3	0.4	0.5	0.5
Fluence at 1.3 GHz, F (Jy ms)	8.0	0.7	1.8	0.6
$S_\nu D^2$ ($\times 10^{12} \text{ Jy kpc}^2$)	10.2	1.9	5.1	1.4
Energy released, E (J)	$\sim 10^{39}$	$\sim 10^{37}$	$\sim 10^{38}$	$\sim 10^{37}$

Fig. 2. A dynamic spectrum showing the frequency-dependent delay of FRB 110220. Time is measured relative to the time of arrival in the highest frequency channel. For clarity we have integrated 30 time samples, corresponding to the dispersion smearing in the lowest frequency channel. (Inset) The top, middle, and bottom 25-MHz-wide dedispersed subband used in the pulse-fitting analysis (2); the peaks of the pulses are aligned to time = 0. The data are shown as solid gray lines and the best-fit profiles by dashed black lines.



energy distribution across the band in FRB 110220 is characterized by bright bands ~ 100 MHz wide (Fig. 2); the SNRs are too low in the other three FRBs to quantify this behavior (2). Similar spectral characteristics are commonly observed in the emission of high- $|b|$ pulsars.

With four FRBs, it is possible to calculate an approximate event rate. The high-latitude HTRU survey region is 24% complete, resulting in 4500 square degrees observed for 270 s. This corresponds to an FRB rate of $R_{\text{FRB}}(F \sim 3 \text{ Jy ms}) = 1.0^{+0.6}_{-0.5} \times 10^4 \text{ sky}^{-1} \text{ day}^{-1}$, where the 1- σ uncertainty assumes Poissonian statistics. The MW foreground would reduce this rate, with increased sky temperature, scattering, and dispersion for surveys close to the Galactic plane. In the absence of these conditions, our rate implies that 17^{+9}_{-7} , 7^{+4}_{-3} , and 12^{+6}_{-5} FRBs should be found in the completed high- and medium-latitude parts of the HTRU (I) and Parkes multibeam pulsar (PMPS) surveys (18).

One candidate FRB with $DM > DM_{\text{MW}}$ has been detected in the PMPS [$|b| < 5^\circ$ (5, 19)]. This burst could be explained by neutron star emission, given a small scale-height error; however, observations have not detected any repetition. No excess-DM FRBs were detected in a burst search of the first 23% of the medium-latitude HTRU survey [$|b| < 15^\circ$ (20)].

The event rate originally suggested for FRB 010724, $R_{010724} = 225 \text{ sky}^{-1} \text{ day}^{-1}$ (4), is consistent with our event rate given a Euclidean universe and a population with distance-independent intrinsic luminosities (source count, $N \propto F^{-3/2}$) yielding $R_{\text{FRB}}(F \sim 3 \text{ Jy ms}) \sim 10^2 R_{\text{FRB}}(F_{010724} \sim 150 \text{ Jy ms})$.

There are no known transients detected at gamma-ray, x-ray, or optical wavelengths or gravitational wave triggers that can be temporally associated with any FRBs. In particular there is

no known gamma-ray burst (GRB) with a coincident position on a time scale commensurate with previous tentative detections of short-duration radio emission (6). GRBs have highly beamed gamma-ray emission (21), and, if FRBs are associated with them, the radio emission must be beamed differently. By using the distances in Table 1, we found that the comoving volume contains $\sim 10^9$ late-type galaxies (22), and the FRB rate is therefore $R_{\text{FRB}} \sim 10^{-3} \text{ year}^{-1}$ per galaxy. R_{FRB} is thus inconsistent with $R_{\text{GRB}} \sim 10^{-6} \text{ year}^{-1}$ per galaxy, even when beaming of emission is accounted for (21). Soft gamma-ray repeaters (SGRs) undergo giant bursts at a rate consistent with FRBs (23), and the energy within our band is well within the budget of the few known SGR giant burst cases (24).

Another postulated source class is the interaction of the magnetic fields of two coalescing neutron stars (25). However, the large implied FRB luminosities indicate that coalescing neutron stars may not be responsible for FRBs. Furthermore, R_{FRB} is substantially higher than the predicted rate for neutron star mergers. Black hole evaporation has also been postulated as a source of FRBs; however, the predicted luminosity within our observing band far exceeds the energy budget of an evaporation event (26).

The core-collapse supernova (ccSN) rate of $R_{\text{ccSN}} \sim 10^{-2} \text{ year}^{-1}$ per galaxy (27) is consistent with R_{FRB} . There is no known mechanism to generate an FRB from a lone ccSN. It may, however, be possible that a ccSN with an orbiting neutron star can produce millisecond-duration radio bursts during the interaction of the ccSN explosion and the magnetic field of the neutron star (28), although the need for an orbiting neutron star will make these rarer.

As extragalactic sources, FRBs represent a probe of the ionized IGM. Real-time detections and immediate follow-up at other wavelengths may identify a host galaxy with an independent redshift measurement, thus enabling the IGM baryon content to be determined (12). Even without host identifications, further bright FRB detections will be a unique probe of the magneto-ionic properties of the IGM.

References and Notes

- M. J. Keith *et al.*, *Mon. Not. R. Astron. Soc.* **409**, 619–627 (2010).
- Materials and methods are available as supplementary materials on Science Online.
- J. M. Cordes, *SKA Memo Ser.* **97**, 1 (2009).
- D. R. Lorimer *et al.*, *Science* **318**, 777–780 (2007); 10.1126/science.1147532.
- E. F. Keane, B. W. Stappers, M. Kramer, A. G. Lyne, *Mon. Not. R. Astron. Soc.* **425**, L71–L75 (2012).
- K. W. Bannister, T. Murphy, B. M. Gaensler, J. E. Reynolds, *Astrophys. J.* **757**, 38 (2012).
- E. Rubio-Herrera, B. W. Stappers, J. W. T. Hessels, R. Braun, *Mon. Not. R. Astron. Soc.* **428**, 2857–2873 (2013).
- S. Burke-Spolaor *et al.*, *Astrophys. J.* **727**, 18 (2011).
- The Lorimer burst is designated as FRB 010724; this date is a correction to that in the original paper.
- J. M. Cordes, T. J. W. Lazio (2002), <http://arxiv.org/abs/astro-ph/0207156>.
- J. S. Deneva, J. M. Cordes, T. J. W. Lazio, *Astrophys. J.* **702**, L177–L181 (2009).
- K. Ioka, *Astrophys. J.* **598**, L79–L82 (2003).
- S. Inoue, *Mon. Not. R. Astron. Soc.* **348**, 999–1008 (2004).
- I. P. Williamson, *Mon. Not. R. Astron. Soc.* **157**, 55 (1972).
- N. D. R. Bhat *et al.*, *Astrophys. J.* **605**, 759–783 (2004).
- R. C. Roeder, R. T. Verreault, *Astrophys. J.* **155**, 1047 (1969).
- H. Isliker, A. O. Benz, *Astron. Astrophys. Suppl. Ser.* **104**, 145 (1994).
- R. N. Manchester *et al.*, *Mon. Not. R. Astron. Soc.* **328**, 17–35 (2001).
- M. Bagchi, A. C. Nieves, M. McLaughlin, *Mon. Not. R. Astron. Soc.* **425**, 2501–2506 (2012).
- S. Burke-Spolaor *et al.*, *Mon. Not. R. Astron. Soc.* **416**, 2465–2476 (2011).
- D. A. Frail *et al.*, *Astrophys. J.* **562**, L55–L58 (2001).
- D. S. Madgwick *et al.*, *Mon. Not. R. Astron. Soc.* **333**, 133–144 (2002).
- E. O. Ofek, *Astrophys. J.* **659**, 339–346 (2007).
- K. Hurley *et al.*, *Nature* **434**, 1098–1103 (2005).
- B. M. S. Hansen, M. Lyutikov, *Mon. Not. R. Astron. Soc.* **322**, 695–701 (2001).
- M. J. Rees, *Nature* **266**, 333–334 (1977).
- R. Diehl *et al.*, *Nature* **439**, 45–47 (2006).
- A. E. Egorov, K. A. Postnov, *Astron. Lett.* **35**, 241–246 (2009).
- N. Spergel *et al.*, *Astrophys. J. Suppl. Ser.* **148**, 175–194 (2003).

Acknowledgments: This research has made use of the NASA/IPAC (Infrared Processing and Analysis Center) Extragalactic Database (NED), which is operated by the Jet Propulsion Laboratory, California Institute of Technology, under contract with NASA. This research has made use of data obtained from the High Energy Astrophysics Science Archive Research Center, provided by NASA's Goddard Space Flight Center. Part of this research was carried out at the Jet Propulsion Laboratory, California Institute of Technology, under a contract with NASA. The Parkes radio telescope is part of the Australia Telescope National Facility, which is funded by the Commonwealth of Australia for operation as a National Facility managed by CSIRO. Part of this research was conducted because of the support of CAASTRO through project number CE110001020. D.T. gratefully acknowledges the support of the Science and Technology Facilities Council and CSIRO Astronomy and Space Science in his Ph.D. studentship. N.D.R.B. is supported by a Curtin Research Fellowship (CRF12228).

Supplementary Materials

www.sciencemag.org/cgi/content/full/341/6141/53/DC1
Materials and Methods
Figs. S1 to S4
Table S1
References (30, 31)

19 February 2013; accepted 30 May 2013
10.1126/science.1236789

Ultrafast Three-Dimensional Imaging of Lattice Dynamics in Individual Gold Nanocrystals

J. N. Clark,^{1*} L. Beitra,¹ G. Xiong,¹ A. Higginbotham,² D. M. Fritz,³ H. T. Lemke,³ D. Zhu,³ M. Chollet,³ G. J. Williams,³ M. Messerschmidt,³ B. Abbey,⁴ R. J. Harder,⁵ A. M. Korsunsky,^{6,7} J. S. Wark,² I. K. Robinson^{1,7}

Key insights into the behavior of materials can be gained by observing their structure as they undergo lattice distortion. Laser pulses on the femtosecond time scale can be used to induce disorder in a “pump-probe” experiment with the ensuing transients being probed stroboscopically with femtosecond pulses of visible light, x-rays, or electrons. Here we report three-dimensional imaging of the generation and subsequent evolution of coherent acoustic phonons on the picosecond time scale within a single gold nanocrystal by means of an x-ray free-electron laser, providing insights into the physics of this phenomenon. Our results allow comparison and confirmation of predictive models based on continuum elasticity theory and molecular dynamics simulations.

Coherent lattice vibrations (phonons) in solids play an important role in many phenomena such as melting (1–5), phase transitions (6), bond softening (7) and hardening

(8), and ferroelectricity (9). Ultrashort (femtosecond) laser pulses have been used to reveal great detail about the dynamics of these phenomena; however, many of these studies have been confined

to bulk samples or ensembles of nanoparticles. With nanoparticles playing an increasingly important role in technology, from catalysis (10) and photonic devices (11) to single-particle mass spectrometry (12) and sensing, understanding the mechanical and dynamical properties of single nanoparticles becomes very important as many of the processes occur on femtosecond (fs) and picosecond (ps) time scales.

The characterization of lattice displacements in individual nanoparticles over very short time scales with atomic sensitivity has been challenging. The interrogation of individual particles is important, as ensemble heterogeneity can give the

¹London Centre for Nanotechnology, University College London, London WC1E 6BT, UK. ²Department of Physics, Clarendon Laboratory, University of Oxford, Parks Road, Oxford OX1 3PU, UK. ³Linac Coherent Light Source, SLAC National Accelerator Laboratory, 2575 Sand Hill Road, Menlo Park, CA 94025, USA.

⁴ARC Centre of Excellence for Coherent X-ray Science, Department of Physics, La Trobe University, Bundoora, Victoria 3086, Australia. ⁵Advanced Photon Source, Argonne, IL 60439, USA.

⁶Department of Engineering Science, University of Oxford, Parks Road, Oxford OX1 3PJ, UK. ⁷Research Complex at Harwell, Didcot, Oxfordshire OX11 0DE, UK.

*Corresponding author. E-mail: jesse.clark@ucl.ac.uk

impression of considerably shorter-lived dynamics than actually exist (13, 14) and may hide the presence of high-order phonon modes or anharmonicity. Optical pump-probe experiments have shown promising results, particularly for single particles (15) over very short time scales; however, because of the long wavelength of the probe, atomic-scale motions cannot be measured without relying on interpretations from continuum elasticity theory. Pump-probe experiments on nanoparticles using electrons or x-rays overcome this problem by probing the atomic-scale motions directly (16, 17). The low scattering cross sections of x-rays and the (relatively) low number of photons in the ultrashort x-ray pulses from plasma sources (required for the short pulse duration) limit the ability to study individual nanoparticles. Likewise, for electrons, the small number of electrons per ultrashort pulse has meant that probing individual nanoparticles has been difficult. The increased flux of synchrotron sources in comparison to plasma sources provides a sufficient number of x-ray photons to probe individual nanoparticles, but at the expense of time resolution. This provides a strong motivation to develop ultrafast pump-probe x-ray diffraction methods on individual nanocrystals using x-ray free-electron lasers (XFELs) (18). Using this approach, one can elucidate the elastic response of the atomic lattice to laser irradiation while simultaneously obtaining high-resolution real-space images of the deformation field inside the nanocrystal by means of Bragg coherent diffraction imaging (BCDI) (19, 20).

BCDI is sensitive to very small variations in strain within nanocrystals as it recovers the projected distortion of the electron density with picometer (pm) sensitivity. The recovered image comprises the amplitude, which is related to the

electron density, and the phase, $\phi(\mathbf{r})$, which is related to the (vector) displacement field $\mathbf{u}(\mathbf{r})$ of the atoms from the ideal lattice points and the scattering vector \mathbf{Q} via $\phi(\mathbf{r}) = \mathbf{u}(\mathbf{r}) \cdot \mathbf{Q}$ (21). Images obtained from noncoplanar Bragg peaks can be combined to recover the full displacement field (22).

Figure 1 shows a schematic of the experimental arrangement for ultrafast BCDI, which was performed at the x-ray pump probe (XPP) instrument at the Linac Coherent Light Source (LCLS). Truncated octahedra gold nanocrystals, ~300 to 400 nm in diameter (21), were placed at the center of a diffractometer. A Ti-sapphire laser with a wavelength of 800 nm and a pulse length of 50 fs [full duration at half-maximum (FDHM)] was used to generate coherent acoustic phonons in the gold nanocrystals. The incident fluence used in the experiment was 1 mJ/cm². The sample was illuminated with 80-fs (FDHM), 9.2-keV x-rays generated by LCLS operating at a repetition rate of 120 Hz. A Si (111) monochromator was used to select ~1 eV bandwidth. Beryllium lenses were used to focus the illumination to an ~30 μm by 30 μm spot. Multiple nanocrystals were illuminated simultaneously, but orientation differences between them allowed Bragg peaks from individual nanocrystals to be spatially separated on the detector. The relative timing (accurate to sub-ps) of the optical and x-ray pulse was adjusted to provide the time-resolved data with the two beams almost parallel for spatial coincidence. Both fluences were below the damage threshold to allow repeated measurements. The coherent diffraction patterns were recorded with a Cornell-SLAC pixel array detector (CS-PAD) (23) positioned 1.2 m from the sample at the gold (111) Bragg peak, a sufficient distance to oversample (19) the diffraction patterns. A helium-filled bag

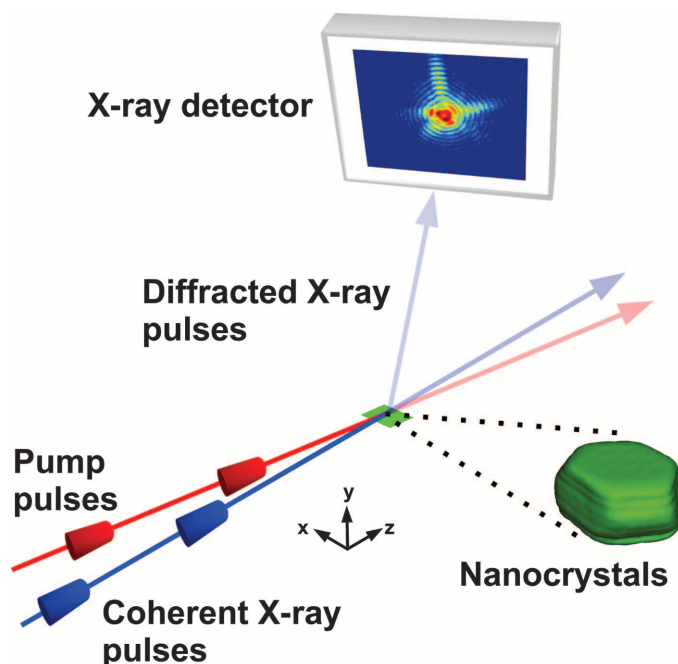
was placed between the sample and detector to reduce absorption and scattering from air.

The coherent diffraction patterns that were recorded from an individual nanocrystal (Fig. 2, A and B) show the modulated diffraction fringes, a consequence of the coherent illumination and finite nanocrystal size, which was much smaller than the x-ray beam. The fringes are most prominent in the faceted directions of the nanocrystal. The diffraction pattern collected immediately before the pump laser (Fig. 2A) shows a relatively symmetric fringe pattern, whereas the diffraction pattern collected +60 ps after (Fig. 2B) is more asymmetric, which is attributed to inhomogeneous lattice distortions i.e., an elastic strain gradient. Homogeneous contraction and expansion of the lattice (radial breathing modes) are manifested as a shift of the entire diffraction pattern (21) as the average lattice spacing changes across the nanocrystal. Shown in Fig. 2, C and D, is the angular shift of the gold (111) Bragg peak for two nanocrystals, I and II. For each time delay, the center of mass from the sum of 100 diffracted LCLS pulses was used to obtain the angular shift, with the error for each delay point given by the standard deviation. At the center of the rocking curve, ~10⁴ diffracted photons are recorded per pulse. The homogeneous lattice expansion and contraction are evident as harmonic motion of the Bragg peak angular shift. Immediately after the arrival of the optical pump laser (positive delay times), the diffraction pattern starts shifting to lower angles. Because the crystal is much bigger than the electromagnetic “skin depth,” this behavior is only consistent with an electron-mediated model, such as the “two-temperature” model (24) of heating in which electrons are excited first and subsequently transfer energy to the lattice through electron-phonon coupling. The peak shift, $S(\tau)$ as a function of delay time, τ , is fitted by

$$S(\tau) = \sum_{n=1}^N A_n \exp\left[-\frac{\tau}{\tau_{d,n}}\right] \times \cos\left[\frac{2\pi}{T_n}(\tau + \tau_{0,n})\right] + C_n \quad (1)$$

where n is the mode number, $N(=2)$ is the total number of fitted modes, A is the amplitude, τ_d is the decay time, T is the period of the oscillation, and τ_0 is the time offset. Two oscillation modes (red solid curve) are sufficient to fit the data shown in Fig. 2, C and D, within their errors with the fitted parameters summarized in table S1. The fitted values of the two periods from the data for nanocrystal I were 101 and 241 ps, and for nanocrystal II were 90 and 256 ps; the different oscillation periods between nanocrystals were a consequence of unequal sizes. These two oscillation modes are well reproduced by a molecular dynamics (MD) simulation (21) (fig. S1). Using the thermal expansion coefficient for bulk gold of $14.4(2) \times 10^{-6} \text{ K}^{-1}$ and the maximum change in the lattice constant, we estimated the

Fig. 1. Ultrafast time-resolved Bragg coherent diffraction imaging. Optical pulses (red) perturb the sample (green), generating phonons. Coherent x-ray pulses (generated from an XFEL) (blue) arrive a short time later. The diffracted pulses are recorded by an area detector, such as a CS-PAD.



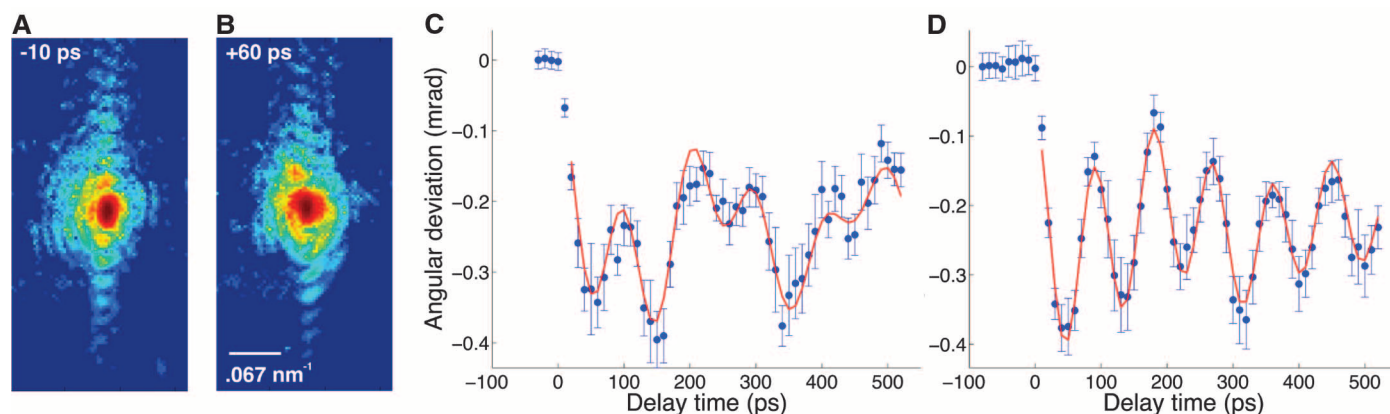
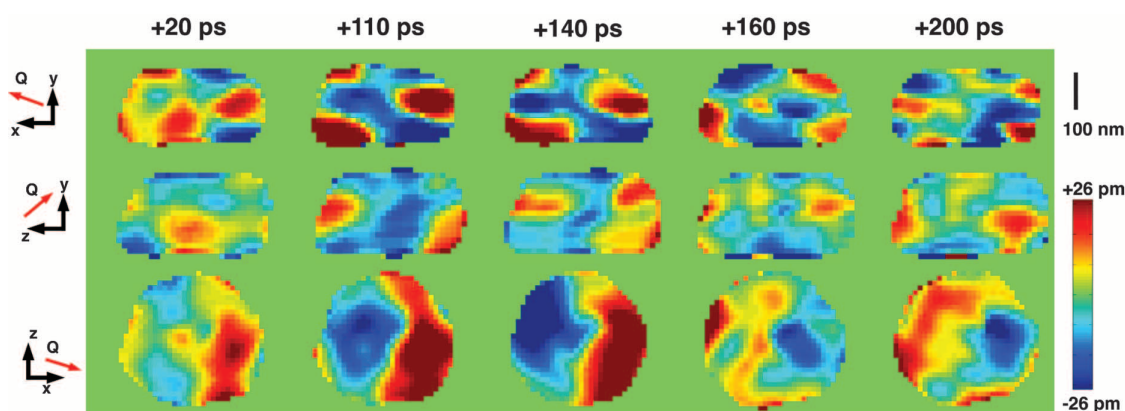


Fig. 2. Time-resolved Bragg coherent diffraction data from single nanocrystals. (A and B) Experimentally recorded coherent diffraction patterns from a single nanocrystal for delay times of -10 and $+60$ ps, respectively. The diffraction patterns are the sum of 100 shots and are scaled logarithmically.

(C and D) Gold (111) Bragg peak angular shift as a function of delay time from the same nanocrystal [(C), nanocrystal I] and a different nanocrystal [(D), nanocrystal II]. The blue dots are the experimental data and the solid red line is the modeled peak shift.

Fig. 3. Imaging of acoustic phonons in a nanocrystal.

Orthogonal cut planes through the center of nanocrystal I showing the projected displacement as a function of delay time. Three different viewing directions are shown. The direction of the displacement field is given by the \mathbf{Q} vector in red. For clarity, the range of displacement has been truncated to ± 26 pm instead of the full range of ± 53 pm.



temperature increase on each pump-probe cycle to be 44 K for each of the two nanocrystals. The fitted vibration amplitudes correspond to a maximum displacement of 600 pm at the surface of the crystal.

The peak position versus delay time shown in Fig. 2 agrees well with previous studies of gold nanoparticles (13, 25, 26) or thin films (5). The important distinction in this study is that we can monitor the behavior of individual nanocrystals using x-ray diffraction rather than the behavior of an ensemble (13, 25, 26). X-rays provide the structural sensitivity evident in Fig. 2, C and D, where both in-plane and out-of-plane cylinder oscillations are observed owing to the coupling of the \mathbf{Q} vector to both these directions. Notably, the lifetime of the oscillations is relatively long in comparison to previous studies, because there is no ensemble averaging of heterogeneous periods in our experiment (13–15, 21).

Thus far, we have identified two clear vibration modes in the expansion of the crystal. Further modes, such as shear modes, can be identified only by imaging the crystal distortions directly because these do not result in a shift of the Bragg peak position. Three-dimensional (3D) images as a function of delay time were obtained for nanocrystal I by collecting 3D coherent dif-

fraction patterns and then recovering the lost phase of the diffracted wavefield by using iterative phase retrieval (21, 27). Complete knowledge of the diffracted wavefield (both amplitude and phase) allows an image of the nanocrystal to be obtained by an inverse Fourier transform. To obtain the missing phase of the diffracted wavefield, an iterative procedure is used that enforces the a priori knowledge that the nanocrystal is isolated, as well as consistency with the measured amplitude of the diffracted wavefield (from the measured intensity). These two constraints are enforced successively until a self-consistent solution is reached.

Figure 3 shows images of the phase of nanocrystal I, displayed as orthogonal cuts through the center for selected times. This phase is the change in the displacement of the crystal, projected onto the diffraction vector \mathbf{Q} , whose direction is also shown in Fig. 3. The homogeneous (linear) lattice expansion and contraction resulting from the breathing modes of the nanocrystal have been removed (21), leaving only the inhomogeneous component that would manifest itself as a broadening or distortion of the Bragg peak rather than a peak shift. To emphasize the changes, we have subtracted the image at -40 ps from the subsequent times, which removes the contribution of small, static residual stresses in the nanocrystal.

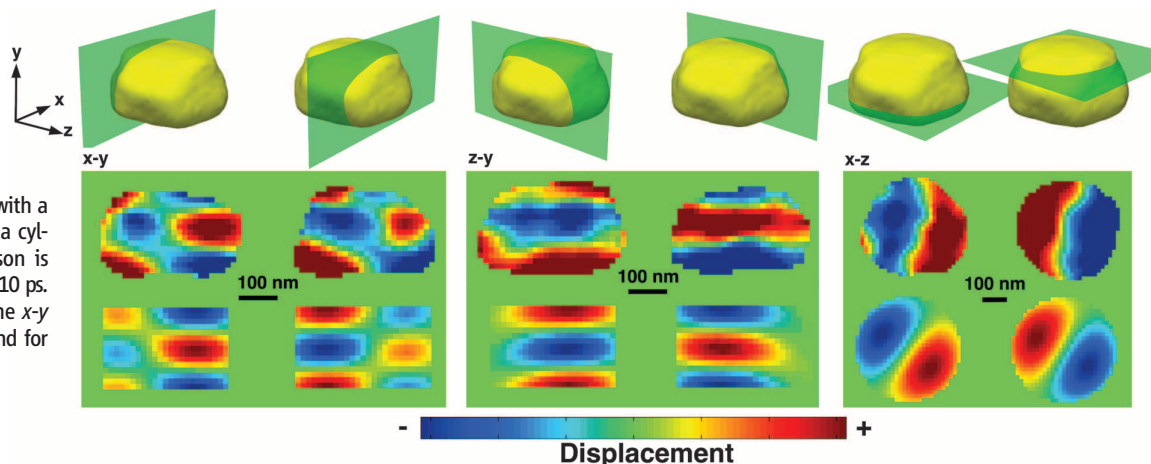
The spatial pattern of oscillating regions of expansion and contraction are well within the resolution of the image (21), estimated as 51 ± 7 , 22 ± 3 , and 55 ± 6 nm in the x , y , and z directions, respectively.

What is particularly evident in Fig. 3 is that the regions of expansion become regions of contraction and vice versa as the delay time increases (movie S1). This spatial and temporal reversal of expansion and contraction is indicative of the presence of a shear vibration mode of higher order than a simple breathing mode. Figure 4 shows the location of selected slices (top row) used to compare the experimental images (middle row) with the theoretical (1, 1) mode of a cylinder (bottom row) with a radius of 200 nm and a height of 220 nm (21). The good agreement between the data, theory, and MD simulation (fig. S2) strongly supports the presence of this otherwise invisible higher-order mode. Our observation of this 50-pm amplitude mode in the presence of a 600-pm breathing mode shows the considerable sensitivity gain by BCDI imaging.

The combination of intense, coherent, and ultrashort x-ray pulses provided by XFELs has enabled direct, unambiguous imaging of coherent acoustic phonons in gold nanocrystals in three dimensions. The technique demonstrated here can

Fig. 4. Comparison of data with theory. Or-

thogonal slices taken either side of the center (**top**) of nanocrystal I compare the projected displacement obtained from the experiment (**middle**) with a simulated (1, 1) mode for a cylinder (**bottom**). Comparison is made for a delay time of +110 ps. The separation between the x-y and y-z slices is 180 nm and for the x-z slices 120 nm.



be applied widely to investigate other materials such as semiconductors and nanostructures and, with continued improvement in experimental design, it should be possible to image particles with sizes less than 100 nm. Many other applications will become possible with the advent of coherent, ultrashort electron sources (28), which could provide atomic-scale images when used with diffractive imaging.

References and Notes

1. C. Rose-Petruck *et al.*, *Nature* **398**, 310–312 (1999).
2. C. W. Sidors *et al.*, *Science* **286**, 1340–1342 (1999).
3. B. J. Siwick, J. R. Dwyer, R. E. Jordan, R. J. D. Miller, *Science* **302**, 1382–1385 (2003).
4. K. Sokolowski-Tinten *et al.*, *Nature* **422**, 287–289 (2003).
5. J. Chen, W.-K. Chen, J. Tang, P. M. Rentzepis, *Proc. Natl. Acad. Sci. U.S.A.* **108**, 18887–18892 (2011).
6. A. M. Lindenberg *et al.*, *Phys. Rev. Lett.* **84**, 111–114 (2000).
7. D. M. Fritz *et al.*, *Science* **315**, 633–636 (2007).
8. R. Ernstorfer *et al.*, *Science* **323**, 1033–1037 (2009).
9. A. Cavalleri *et al.*, *Nature* **442**, 664–666 (2006).
10. M. Turner *et al.*, *Nature* **454**, 981–983 (2008).
11. S. A. Maier *et al.*, *Adv. Mater.* **13**, 1501–1505 (2001).
12. M. S. Hanay *et al.*, *Nat. Nanotechnol.* **7**, 602–608 (2012).
13. G. V. Hartland, *J. Chem. Phys.* **116**, 8048 (2002).
14. M. Pelton *et al.*, *Nat. Nanotechnol.* **4**, 492–495 (2009).
15. M. A. van Dijk, M. Lippitz, M. Orrit, *Phys. Rev. Lett.* **95**, 267406 (2005).
16. C.-Y. Ruan, Y. Murooka, R. K. Raman, R. A. Murrick, *Nano Lett.* **7**, 1290–1296 (2007).
17. A. Plech, V. Kotaidis, S. Grésillon, C. Dahmen, G. von Plessen, *Phys. Rev. B* **70**, 195423 (2004).
18. P. Emma *et al.*, *Nat. Photonics* **4**, 641–647 (2010).
19. J. Miao, P. Charalambous, J. Kirz, D. Sayre, *Nature* **400**, 342–344 (1999).
20. M. A. Pfeifer, G. J. Williams, I. A. Vartanyants, R. Harder, I. K. Robinson, *Nature* **442**, 63–66 (2006).
21. Materials and methods are available as supplementary materials on Science Online.
22. M. C. Newton, S. J. Leake, R. Harder, I. K. Robinson, *Nat. Mater.* **9**, 120–124 (2010).
23. P. Hart *et al.*, *Proc. SPIE* **8504**, 85040C (2012).
24. P. B. Allen, *Phys. Rev. Lett.* **59**, 1460–1463 (1987).
25. G. V. Hartland, M. Hu, J. E. Sader, *J. Phys. Chem. B* **107**, 7472–7478 (2003).
26. K. Ichinagani *et al.*, *Phys. Rev. B* **84**, 024110 (2011).
27. J. R. Fienup, *Appl. Opt.* **21**, 2758–2769 (1982).
28. A. J. McCulloch *et al.*, *Nat. Phys.* **7**, 785–788 (2011).

Acknowledgments: This work was supported by FP7 advanced grant from the European Research Council. I.K.R. is appreciative of support from the Engineering and Physical Sciences Research Council (EPSRC) under grant EP/I022562/1 and from the Biotechnology and Biological Sciences Research Council (BBSRC) under grant BB/H022597/1. A.H. was supported by Atomic Weapons Establishment. J.S.W. is grateful for support from the UK EPSRC under grant EP/H035877/1. A.M.K. is grateful for support from the EPSRC under grant EP/I020691/1. B.A. acknowledges the support of the Australian Research Council Centre of Excellence for Coherent X-ray Science. The experimental work was carried out at the Linac Coherent Light Source, a National User Facility operated by Stanford University on behalf of the U.S. Department of Energy, Office of Basic Energy Sciences. We acknowledge S. Boutet for insightful discussion.

Supplementary Materials

www.sciencemag.org/cgi/content/full/science.1236034/DC1
Materials and Methods
Figs. S1 and S2
Table S1
References (29–40)
Movie S1

4 February 2013; accepted 7 May 2013
Published online 23 May 2013;
10.1126/science.1236034

Chiral Symmetry Breaking in Superfluid $^3\text{He-A}$

H. Ikegami,^{1,2*} Y. Tsutsumi,³ K. Kono^{1,2}

Spontaneous symmetry breaking is an important concept in many branches of physics. In helium-3 (^3He), the breaking of symmetry leads to the orbital chirality in the superfluid phase known as $^3\text{He-A}$. Chirality is a fundamental property of $^3\text{He-A}$, but its direct detection has been challenging. We report direct detection of chirality by transport measurements of electrons trapped below a free surface of $^3\text{He-A}$. In particular, we observed the so-called intrinsic Magnus force experienced by a moving electron; the direction of the force directly reflected the chirality. We further showed that, at the superfluid transition, the system selected either right- or left-handed chirality. The observation of such selection directly demonstrates chiral symmetry breaking.

Spontaneous symmetry breaking plays an essential role in phase transitions. It occurs in systems that have multiple ground states of equal energy. Symmetry is broken when the system settles into a particular ground

state. This process can result in marked changes to the properties of the system. One notable consequence of symmetry breaking is the orbital chirality in the A phase of the superfluid ^3He ($^3\text{He-A}$), which emerges from the symmetric

normal ^3He (*I*, 2). In $^3\text{He-A}$, ^3He atoms form Cooper pairs of orbital angular momentum $L = 1$, and the angular momenta of all the pairs are oriented in the same direction denoted by the unit vector \hat{l} . The chirality is characterized by the orientation of \hat{l} , and its meaning becomes clear by considering the orbital motion just near a surface: Because of the boundary condition ($\hat{l} \parallel \hat{z}$, where \hat{z} is the surface normal) (3), all the Cooper pairs rotate in either a right- or left-handed direction around \hat{z} ($\hat{l} = +\hat{z}$ or $\hat{l} = -\hat{z}$, respectively). These two chiral states are a degenerate time-reversal pair, and the selection of either state amounts to spontaneous chiral symmetry breaking (4). Chirality was detected only

¹Low Temperature Physics Laboratory, RIKEN, Wako, Saitama 351-0198, Japan. ²The RIKEN Center for Emergent Matter Science, RIKEN, Wako, Saitama 351-0198, Japan. ³Condensed Matter Theory Laboratory, RIKEN, Wako, Saitama 351-0198, Japan.

*Corresponding author. E-mail: hikegami@riken.jp

recently by rotating $^3\text{He-A}$ (5), in which opposite chiralities were identified by their different responses to the rotation. In that experiment, however, the lifting of the degeneracy by the rotation was essential; hence, it did not allow the exploration of spontaneous chiral symmetry breaking.

Here we report the discovery of the intrinsic Magnus (IM) force (6, 7) experienced by a moving electron trapped below a free surface of $^3\text{He-A}$, which enabled a direct detection of chirality without lifting the degeneracy. Furthermore, this allowed us to demonstrate that $^3\text{He-A}$ selects either right- or left-handed chirality at the superfluid transition.

The IM force \vec{F}_{IM} acts on an impurity moving at velocity \vec{v} through $^3\text{He-A}$ (Fig. 1A) (6–8). It originates from the nonzero orbital angular momentum of Cooper pairs, which gives rise to an asymmetric scattering of quasiparticles by the impurity in the plane normal to \hat{l} (6, 7). This leads to an asymmetric transverse momentum transfer to the impurity, resulting in a transverse \vec{F}_{IM} of the form $\vec{F}_{\text{IM}} \propto \vec{v} \times \hat{l}$. The direction of \vec{F}_{IM} reflects the orientation of \hat{l} , and thus a moving impurity can be used as a microscopic probe for detecting chirality directly. In an ordinary fluid, a hydrodynamic, transverse Magnus force acts on a moving object if it accompanies the circulation of the surrounding fluid. By contrast, \vec{F}_{IM} does not involve the circulation of the fluid.

We studied chiral symmetry breaking at a free surface of $^3\text{He-A}$, where a spatially uniform \hat{l} anchored normal to the surface is expected (3). In this situation, the two chiral states correspond to $\hat{l} = \pm \hat{z}$, where \hat{z} is the surface normal pointing upward. The free surface has two advantages: It lacks irregularities that trap topological defects, and it is perfectly specular; i.e., the order parameter is not suppressed at the surface (3). Below the surface, we trapped electrons at a depth $d \sim 30$ nm (9) and induced their motion along the surface to experience the IM force ($\vec{v} \perp \hat{l}$). The electrons in liquid helium are in the state of an electron bubble; a state of an electron self-trapped in a spherical cavity with a radius $R = 2.0$ nm (10, 11). The electron bubbles trapped below the surface form a two-dimensional (2D) rectangular charge sheet (~ 16 mm by 16 mm) with an areal density $n \sim 10^{11} \text{ m}^{-2}$. The transport measurement of electron bubbles was carried out by a contactless capacitive coupling technique using three electrodes located above the surface (Fig. 1B) (9). An ac voltage V_{in} with frequency $f = 0.05$ to 100 Hz was applied to the input electrode, which produced an in-plane electric field and induced the motion of electron bubbles along the surface. The induced current was then recorded by the right (I_R) and left (I_L) electrodes through capacitive coupling. If electron bubbles experienced the IM force, their trajectories deflected from the direction of the electric field, generating a difference in current: $\Delta I \equiv I_R - I_L \neq 0$. To realize $^3\text{He-A}$, a magnetic field $B \sim 0.3$ T was applied normal to the surface (Fig. 1, B and C). The Lorentz force due to this

field was smaller than the IM force by a factor of 10^{-4} to 10^{-6} (9).

First, we demonstrated the IM force. Figure 2A shows the real and imaginary parts of ΔI as a function of temperature T measured at fixed V_{in} and f in $^3\text{He-A}$. We clearly observed that ΔI appears in both real and imaginary parts below the transition temperature T_c . The observed ΔI is at most 6% of $I_R + I_L$. To verify that ΔI originates from the IM force, we performed the same measurement in nonchiral $^3\text{He-B}$, where the IM force is not expected because of zero total orbital angular momentum of Cooper pairs. As shown in Fig. 2B, ΔI apparently disappears in $^3\text{He-B}$, providing unambiguous evidence of the IM force. Notably, two symmetric temperature dependences equal in magnitude but opposite in sign are observed in different runs cooled from the normal phase (runs 1 and 2 in Fig. 2A) even though they were measured under the same experimental conditions. The two behaviors correspond to monodomains with opposite chiralities, and we could assign chirality by examining the direction of \vec{F}_{IM} from the sign of ΔI : $\hat{l} = -\hat{z}$ for run 1 and $\hat{l} = +\hat{z}$ for run 2 (8). The observation of the two behaviors indicated that one of the two chiral states was adopted at the transition, directly demonstrating chiral symmetry breaking.

The temperature dependence of ΔI in Fig. 2A is understood by referring to the frequency dependence of ΔI (Fig. 3A). Broad resonance-like behaviors are found with a peak in the imaginary part of ΔI at a frequency f_0 . The resonance-like behavior is not a true resonance, but arises as a result of the effect of nonzero frequency on the Hall effect in the finite-sized 2D electron bubble system as described in (9) (in this case, the Hall effect is caused by the IM force instead of the Lorentz force). f_0 shows a rapid increase with decreasing T , and the temperature dependence of ΔI in Fig. 2A is inter-

preted as f_0 passing through the measurement frequency upon a temperature sweep.

To extract the magnitude of \vec{F}_{IM} from the resonance-like behaviors, we performed numerical simulations of ΔI by solving the equation of motion of electron bubbles, including the IM force in our experimental geometry (9). In the simulations, only the ratio $\alpha \equiv |\vec{F}_{\text{IM}}|/|\vec{F}_D|$ is a free parameter, where \vec{F}_D is the drag force deduced from the mobility of an electron bubble (9). As shown in Fig. 3A, the simulations reproduce the observed signals by assuming a chiral monodomain, and a comparison with the experimental data gives the magnitude of α . The obtained α shows a temperature dependence similar to that found in our theoretical calculation (Fig. 3B) (6, 7, 12), although the magnitude differs by a factor of ~ 2.5 . The theoretical prediction (6) suggests that α should be proportional to $\Delta_A(T)/T$ near T_c for the IM force, whereas the hydrodynamic Magnus force would have the quadratic dependence on $\Delta_A(T)/T$, where $\Delta_A(T)$ is the maximum gap of $^3\text{He-A}$. As shown in the inset of Fig. 3B, the observed α is proportional to $\Delta_A(T)/T$ near T_c , being consistent with the prediction.

In some cooling runs, we found multiple chiral domains coexisting in a sample. In these cases, ΔI showed different temperature dependences at different cooling runs because of the different configurations of domain walls (DWs). In addition, ΔI often exhibited an abrupt jump associated with the motion of DWs induced by a small mechanical shock on the cryostat (13). For a monodomain sample, by contrast, ΔI was reproducible and robust; the signal showed the same temperature dependence in different cooling runs and recovered after a shock within the time constant of our measurement system (5 to 10 min). The robustness is attributable to the topological nature of the state; a domain with the

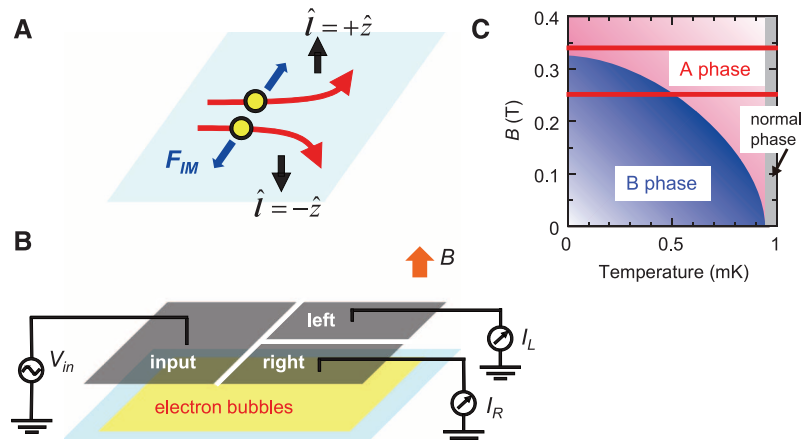


Fig. 1. Intrinsic Magnus force. (A) A moving impurity (yellow circles) experiences the IM force $\vec{F}_{\text{IM}} \propto \vec{v} \times \hat{l}$ (8). (B) Experimental setup. The motion of electron bubbles along the surface is induced by the ac voltage applied on the input electrode, and the induced current is detected by the right and left electrodes. If electron bubbles experience the IM force, $\Delta I = I_R - I_L$ is generated. (C) Phase diagram of superfluid ^3He at zero pressure in T - B space (19). Two phases appear, chiral $^3\text{He-A}$ and nonchiral $^3\text{He-B}$. The red lines indicate the fields at which data in Fig. 2 are taken.

opposite chirality cannot be created in a monodomain sample by a continuous transformation of the order parameter without destroying the $^3\text{He-A}$ phase.

That a monodomain as large as ~ 16 nm by 16 nm can be formed is attributed to the lack of pinning of DWs on the free surface: The DWs formed at the transition can escape from the surface during slow cooling. This is in sharp contrast

to the formation of many small domains reported in a slab $^3\text{He-A}$ sandwiched between two microscopically rough surfaces with strong pinning (14, 15), where the growth of domains stops when their size reaches approximately the slab thickness (\sim submillimeter).

The two symmetric behaviors in Fig. 2A are a clear demonstration of chiral symmetry breaking. If the two chiral states are degenerate—that is, if

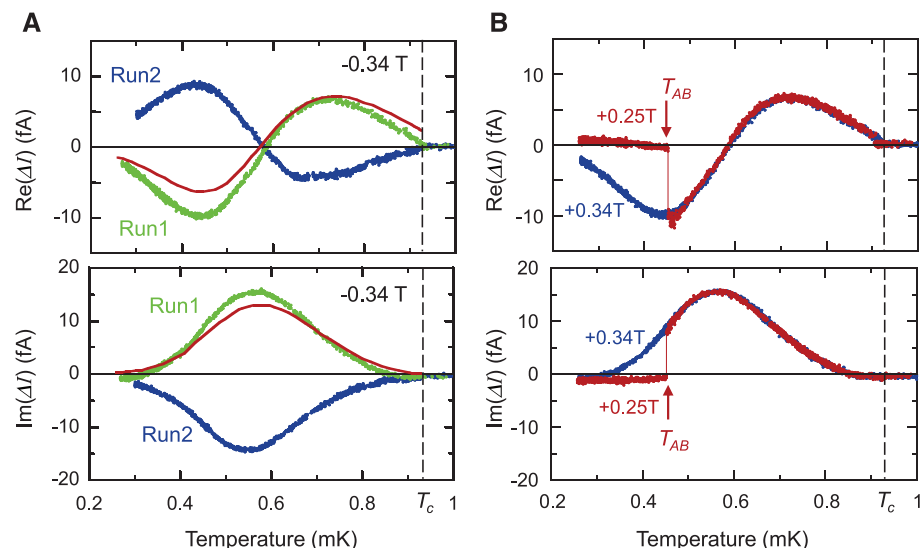


Fig. 2. Temperature dependences of real (upper panels) and imaginary (lower panels) parts of ΔI . Data are taken at $f = 0.611$ Hz and $V_{in} = 400$ mV for $n = 4.7 \times 10^{11} \text{ m}^{-2}$ trapped at $d = 35$ nm. **(A)** Data in $^3\text{He-A}$ ($B = -0.34$ T). Two sets of data for monodomain with $\hat{l} = -\hat{z}$ (run 1) and $\hat{l} = +\hat{z}$ (run 2) are shown. Solid red lines are the numerical simulations for $\hat{l} = -\hat{z}$ and $\alpha = 0.15$. **(B)** Data in $^3\text{He-B}$ obtained at $B = +0.25$ T upon cooling, along with those in $^3\text{He-A}$. ΔI disappears in $^3\text{He-B}$, which is realized below the A-B transition temperature T_{AB} . The small ΔI (~ 1 fA) seen in $^3\text{He-B}$ is caused by the slight asymmetry of the two electrodes (9).

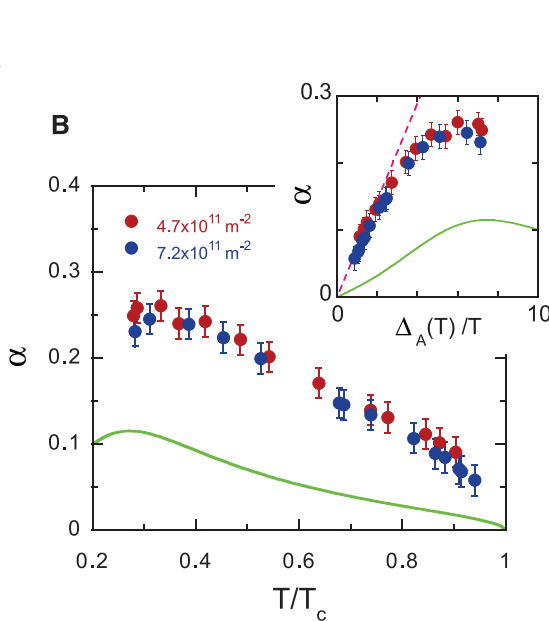
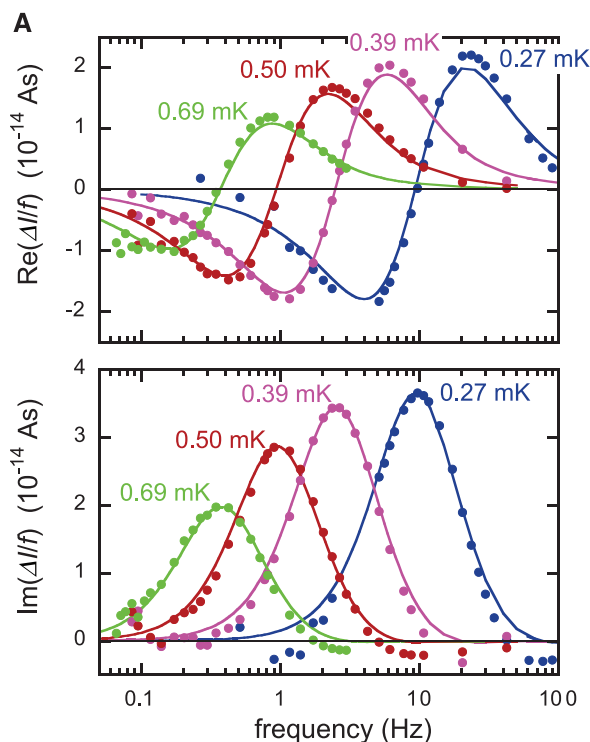


Fig. 3. Frequency and temperature dependence of the IM force. **(A)** Real (upper panel) and imaginary (lower panel) parts of ΔI for $V_{in} = 400$ mV as a function of frequency. They are measured at the same n and d as in Fig. 2. In the graphs, ΔI is divided by frequency to suppress the apparent increase in current in proportion to frequency arising from the capacitive coupling technique. Solid lines are the results of the numerical simulations for the monodomain of $\hat{l} = -\hat{z}$. **(B)** Temperature dependence of $\alpha = |\bar{F}_M|/|\bar{F}_D|$ obtained at $n = 4.7 \times 10^{11} \text{ m}^{-2}$ ($d = 35$ nm) and $n = 7.2 \times 10^{11} \text{ m}^{-2}$ ($d = 31$ nm). The solid line represents our theoretical calculation at zero pressure ($k_F R = 16$) (12), where k_F is the Fermi wave number. (Inset) α as a function of $\Delta_A(T)/T$. The dashed line indicates a linear dependence.

chiral symmetry breaking occurs “spontaneously”—the two states should appear at equal probabilities. To check this, we carried out a number of slow cooling runs and recorded the chirality detected just below T_c (Table 1). At $B = -0.34$ T (applied downward), both chiralities appear at almost equal probabilities, indicating close degeneracy. At $B = +0.34$ T, we found $\hat{l} = -\hat{z}$ in most cooling runs. This unusual observation implies a slight energy splitting between the two chiral states that is asymmetric to the direction of B . In the current understanding of $^3\text{He-A}$, however, there is no well-elucidated mechanism for lifting the degeneracy by a magnetic field for charge-neutral Cooper pairs. Furthermore, the asymmetry with respect to the direction of B prevents our straightforward understanding of its origin. We speculate that it involves more than one competing effect with an energy much smaller than Δ_A , including the nontrivial coupling of chirality to a magnetic field (16).

In solid-state materials, the direct observation of symmetry breaking at a macroscopic scale, in the absence of any external symmetry breaking field, is generally difficult because of the formation of many small domains. That we could observe chiral symmetry breaking at a large scale indicates that our system is also suitable for exploring the consequences of this symmetry breaking. Of particular interest are the static and dynamic properties of exotic topological defects specific to the chiral superfluid, including DWs and monopole-like surface defects called boojums (1, 17). In particular, investigations of their dynamics by space-resolved and temporal measurements of chirality may deepen our understanding of the creation and annihilation processes of

Table 1. Appearance ratio of chirality detected just below T_c after many slow cooling runs (≤ 50 $\mu\text{K}/\text{hour}$). Numbers in parentheses—for example, (8/24) in the column of $B = -0.34$ T and $\hat{l} = +\hat{z}$ —indicate that $\hat{l} = +\hat{z}$ is observed in 8 of the 24 cooling runs. Chirality is determined mostly at $0.8T_c < T < T_c$. Because of the rather small signals in this temperature range, we cannot exclude the possibility of the coexistence of a small opposite chiral domain.

B	$\hat{l} = +\hat{z}$ (monodomain)	$\hat{l} = -\hat{z}$ (monodomain)	Multidomain
+0.34 T (applied upward)	0% (0/18)	83% (15/18)	17% (3/18)
−0.34 T (applied downward)	33% (8/24)	42% (10/24)	25% (6/24)

topological defects, and may shed light on the roles of these processes at symmetry-breaking phase transition in condensed-matter physics and cosmology (18).

References and Notes

1. D. Vollhardt, P. Wölfle, *The Superfluid Phases of Helium 3* (Taylor & Francis, London, 1990).
2. E. R. Dobbs, *Helium Three* (Oxford Univ. Press, Oxford, 2000).
3. V. Ambegaokar, P. G. deGennes, D. Rainer, *Phys. Rev. A* **9**, 2676 (1974).
4. C. Kallin, *Rep. Prog. Phys.* **75**, 042501 (2012).
5. P. M. Walmsley, A. I. Golov, *Phys. Rev. Lett.* **109**, 215301 (2012).
6. R. H. Salmelin, M. M. Salomaa, V. P. Mineev, *Phys. Rev. Lett.* **63**, 868 (1989).

7. R. H. Salmelin, M. M. Salomaa, *Phys. Rev. B Condens. Matter* **41**, 4142 (1990).
8. The calculations by Salmelin *et al.* (6, 7) suggested that $\vec{F}_{\text{IM}} = A\vec{v} \times \hat{l}$ with $A > 0$ [see, for example, figure 11 in (7)]. However, our detailed analysis of their calculations finds that $A < 0$. In this report, we use $A < 0$.
9. See supplementary materials on Science Online.
10. A. L. Fetter, in *The Physics of Liquid and Solid Helium*, Part I, K. H. Bennemann, J. B. Ketterson, Eds. (Wiley, New York, 1976), p. 207.
11. A. I. Ahonen *et al.*, *J. Low Temp. Phys.* **30**, 205 (1978).
12. The original calculation by Salmelin *et al.* suggested a monotonic increase in α with decreasing T (6, 7). However, our calculation using the same formulation shows a nonmonotonic dependence on T , as shown in Fig. 3B. The origin of this discrepancy between our calculation and theirs is unknown, but our calculation is performed with a finer momentum grid.

13. We have had at least several small aftershocks in a day, which were associated with the 2011 Tohoku-Oki earthquake on 11 March 2011 (data presented here were taken from January to July 2012).
14. T. D. C. Bevan *et al.*, *J. Low Temp. Phys.* **109**, 423 (1997).
15. P. M. Walmsley, I. J. White, A. I. Golov, *Phys. Rev. Lett.* **93**, 195301 (2004).
16. A. J. Leggett, *Nature* **270**, 585 (1977).
17. N. D. Mermin, in *Quantum Fluids and Solids*, S. B. Trickey, E. D. Adams, J. W. Dufty, Eds. (Plenum, New York, 1977), p. 3.
18. W. H. Zurek, *Nature* **317**, 505 (1985).
19. J. M. Kyyräinen, J. P. Pekola, A. J. Manninen, K. Torizuka, *Phys. Rev. Lett.* **64**, 1027 (1990).

Acknowledgments: We thank M. Tsubota, A. I. Golov, T. Mizushima, H. Takeuchi, H. Akimoto, J. A. Sauls, M. Krusius, Y. Okuda, A. Furusaki, G. E. Volovik, and A. J. Leggett for fruitful discussions. This work was partly supported by Grants-in-Aid for Scientific Research (grants 23684030, 23103517, 24840048, and 24000007) from the Japan Society for the Promotion of Science and the Ministry of Education, Culture, Sports, Science, and Technology, Japan.

Supplementary Materials

www.sciencemag.org/cgi/content/full/341/6141/59/DC1
Materials and Methods
Supplementary Text
Figs. S1 to S4
References (20–29)

13 February 2013; accepted 30 May 2013
10.1126/science.1236509

Crystal Structure Determination of the Nonclassical 2-Norbornyl Cation

F. Scholz,¹ D. Himmel,¹ F. W. Heinemann,² P. v. R. Schleyer,^{3,4} K. Meyer,^{2*} I. Krossing^{1*}

After decades of vituperative debate over the classical or nonclassical structure of the 2-norbornyl cation, the long-sought x-ray crystallographic proof of the bridged, nonclassical geometry of this prototype carbonium ion in the solvated $[\text{C}_7\text{H}_{11}]^+[\text{Al}_2\text{Br}_7]^- \cdot \text{CH}_2\text{Br}_2$ salt has finally been realized. This achievement required exceptional treatment. Crystals obtained by reacting norbornyl bromide with aluminum tribromide in CH_2Br_2 undergo a reversible order-disorder phase transition at 86 kelvin due to internal 6,1,2-hydride shifts of the 2-norbornyl cation moiety. Cooling with careful annealing gave a suitably ordered phase. Data collection at 40 kelvin and refinement revealed similar molecular structures of three independent 2-norbornyl cations in the unit cell. All three structures agree very well with quantum chemical calculations at the MP2(FC)/def2-QZVPP level of theory.

Carbocations have been controversial throughout their 11-decade history. Editors and referees were long reluctant even to allow a positive charge to be associated with a carbon (1). The scientific “war” over “the nonclassical ion problem” [the title of H. C. Brown’s book (2)] raged among many of the leading physical organic chemists for a quarter century, from

Brown’s modest opening salvo (3) until his withdrawal from active discussion in 1986 (4). Still unconvinced by the arguments, ingenious “proofs,” and “compelling evidence” for the nonclassical structure that had been put forward, Brown called for definitive experimental evidence for the proposed symmetry of the nonclassical norbornyl cation. Indeed, the experimental authentication one would desire most—the x-ray single-crystal structure analysis—was even then (in 1986) conspicuous by its absence, 22 years after the first preparation of the 2-norbornyl cation under stable ion conditions (5, 6). Only now, after an additional 27 years, can we report the solution to this vexing x-ray diffraction analysis problem.

Although not the first among the many proposed nonclassical carbocations, the 2-norbornyl cation became the paradigm, “originally presented

to me [Brown] as the least ambiguously known case for a nonclassical ion” (4). Nonclassical ions “cannot be represented adequately by a single Lewis structure” (2) and typically were depicted as having penta- (or higher) carbon coordination. Although there were antecedents, the nonclassical structure of the 2-norbornyl cation (Fig. 1A) was first described by Winstein in 1949 in order to explain the reaction stereochemistry and enhanced reactivity of 2-exo-norbornyl cation precursors (7–10). But Brown argued, “that there was no convincing evidence for σ -bridging in these systems” since all the facts “could be accounted for without including this new feature (2).” Instead, he proposed the rapidly equilibrating pair of classical ions (Fig. 1B) and still insisted

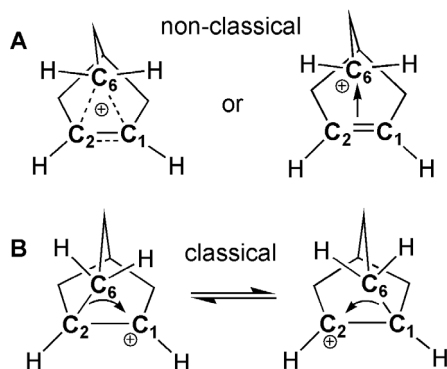


Fig. 1. Proposed 2-norbornyl cation structures. (A) Nonclassical C_2 structure of the 2-norbornyl cation, depicted in 3c-2e and π complex formulations. (B) Brown’s rapidly equilibrating C_1 classical norbornyl cation enantiomers.

¹Institut für Anorganische und Analytische Chemie, Albert-Ludwigs-Universität Freiburg, Albertstrasse 21, 79104 Freiburg, Germany.

²Department of Chemistry and Pharmacy, Inorganic Chemistry, Friedrich-Alexander-University, Erlangen-Nuremberg, Egerlandstrasse 1, 91058 Erlangen, Germany. ³Department of Chemistry, University of Georgia, Athens, GA 30602, USA.

⁴Department of Organic Chemistry, University of Erlangen-Nuremberg, Henkestraße 42, 91054 Erlangen, Germany.

*Corresponding author. E-mail: krossing@uni-freiburg.de (I.K.); karsten.meyer@chemie.uni-erlangen.de (K.M.)

that the 2-norbornyl cation “has neither the large stabilization nor the symmetry of the original proposed structure” in his last statements on the topic (4).

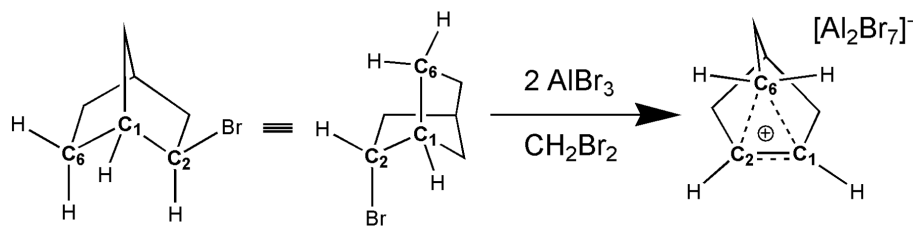
The first direct observation of the 2-norbornyl cation by nuclear magnetic resonance (NMR) as an $[\text{SbF}_6]^-$ salt was reported in 1964 (5, 6). Many routes lead to the 2-norbornyl cation, such as ionization of various norbornyl halides or the protonation of norbornene or nortricyclene (5, 6, 11–16). Because of fast degenerate 3,2- as well as 6,1,2-hydride shifts and Wagner-Meerwein-rearrangements, the room-temperature ^1H NMR spectrum of the 2-norbornyl cation had only a single peak at 3.10 parts per million in $\text{SbF}_5\text{-SO}_2$ (5). According to variable-temperature ^1H NMR experiments, the barriers for the 3,2- and the 6,1,2-hydride shifts are $45.2 \pm 2.5 \text{ kJ mol}^{-1}$ and $24.7 \pm 0.8 \text{ kJ mol}^{-1}$, respectively (14). The 3,2-hydride shift is fully frozen out in $\text{SbF}_5\text{-SO}_2\text{ClF-SO}_2\text{F}_2$ solvent at 173 K (12). The very small line-widths at 115 K imply either that the 6,1,2-hydride shifts and the Wagner-Meerwein-rearrangements are frozen, with the 2-norbornyl cation having a C_s -symmetric nonclassical structure, or that the Wagner-Meerwein-rearrangement is still fast on the NMR time scale with a very low barrier (17). Saunders’ isotopic perturbation (11, 18) and special ^{13}C NMR spectral techniques (12, 17), including magic angle spinning cross-polarization

in SbF_5 at 77 K (19) and even at 5 K (20), support the nonclassical structure. These results also are in agreement with adequately high-level quantum chemical computations (21–26) and further NMR (27), infrared (28, 29), and Raman (16, 30) measurements.

Despite numerous attempts, a single-crystal x-ray structure determination of the parent 2-norbornyl cation has remained elusive. Although crystalline 2-norbornyl salts have been obtained earlier (31), numerous attempts by various research groups to solve the x-ray structure failed (32, 33). The structural characterization of related, but metrically and electronically rather different, norbornyl cation derivatives (31–34) increases the desirability of overcoming the intransigence of the parent species. Our interest in binding challenging ions such as the $[\text{CX}_3]^+$ ($\text{X} = \text{Cl}, \text{Br}, \text{I}$) cations (35–37) to weakly coordinating anions (38, 39) led us to exploit the ability of soft bromoaluminate anions, such as $[\text{Al}_2\text{Br}_7]^-$, to stabilize, for example, the $[\text{C}(\text{CH}_3)_3]^+$ carbocation in the solid state (40). This bromoaluminate anion also led to the successful preparation and full characterization of the ordered solid-state structure of the 2-norbornyl cation salt reported here. Thus, crystals of $[\text{C}_7\text{H}_{11}]^+[\text{Al}_2\text{Br}_7]^- \cdot \text{CH}_2\text{Br}_2$ (**1**) were obtained reproducibly from the reaction of 2-*exo*-norbornyl bromide with aluminum tribromide in CH_2Br_2 at 243 K. Storage at 245 K for

several days led to the formation of large crops of slightly brownish but nearly colorless needles of **1** (Scheme 1 and supplementary materials).

Fully assigned vibrational spectra of samples from these crystals agree with prior measurements (16, 28) as well as with computations (figs. S1 to S8 and tables S1 to S4). Despite being extremely air- and temperature-sensitive above 213 K, single crystals from independent batches seemed suitable for x-ray structure determination. However, numerous full single-crystal x-ray diffraction (XRD) measurements at temperatures above 86 K always led to a phase with well-ordered anions but completely disordered cations. This observed rotational disorder is due to the near-spherical shape of the cation moieties as individual entities. Reversible ordering with phase transition takes place at 86 K and is completed upon cooling to approximately 50 K. At higher temperatures, two dynamic processes take place due to entropy: spherical movement of the cations in their positions in the crystals and concomitant intramolecular 6,1,2-hydride shifts. Rapid freezing out of the 6,1,2-hydride shift results in static norbornyl cations on the XRD time scale, but these are still orientationally disordered. Thus, both annealing and very low temperatures are needed for the 2-norbornyl cations to reach their best orientations in their true minimum positions. Consequently, a carefully controlled and monitored annealing procedure had to be developed to obtain good quality data sets of the ordered structure of **1** (see the supplementary materials for a detailed description). Several data sets that pass International Union of Crystallography (IUCr) criteria were recorded after overcoming great difficulties in the crystal mounting and annealing of different crystals at temperatures representing the lower- and the higher-temperature phases. Here we present only the converged data recorded at 120 K and at 40 K that were obtained from the same crystal [high-temperature form,



Scheme 1.

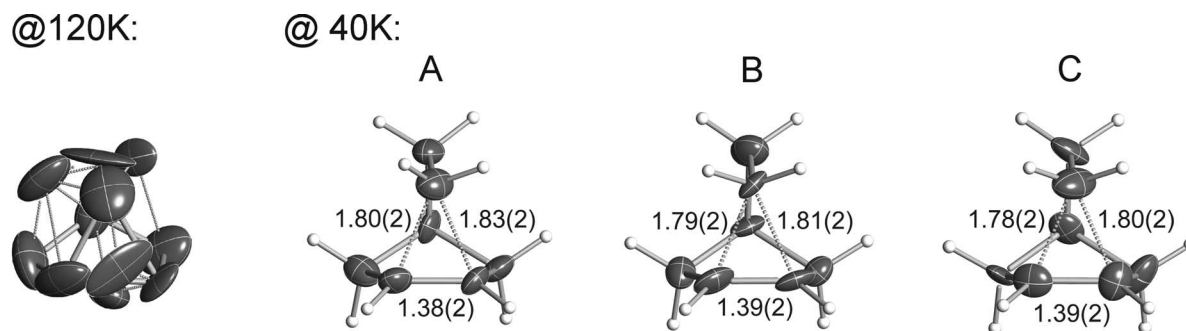


Fig. 2. Molecular structure of the 2-norbornyl cation in crystals of $[\text{C}_7\text{H}_{11}]^+[\text{Al}_2\text{Br}_7]^- \cdot \text{CH}_2\text{Br}_2$ (**1**). The topology of the electron density maxima representing the norbornyl cation moiety in the disordered 120 K form (**left**) is compared with those of the three well-resolved crystallographically independent nonclassical cation moieties **A**, **B**, and **C** at 40 K (**right**). The principal C–C bond distances of the three crystallographically independent cations **A**, **B**, and **C** in the ordered 40 K structure of the low-temperature phase of $[\text{C}_7\text{H}_{11}]^+[\text{Al}_2\text{Br}_7]^- \cdot \text{CH}_2\text{Br}_2$ (crystal no.

Mean value of all six C···C, x-ray: 1.80 Å (MP2: 1.825 Å)
Mean value of all three C=C, x-ray: 1.39 Å (MP2: 1.393 Å)

1, thermal ellipsoids at the 50% probability level, H atoms as spheres of arbitrary size, distances in angstroms, C–C bond precision ± 0.017 to 0.019 Å) all agree excellently with the MP2(FC)/def2-QZVPP-optimized data. See figs. S9 to S20 in the supplementary materials for further drawings.

$T = 120$ K: $R_1 = 0.040$, $wR_2 = 0.081$; orthorhombic $Cmc2_1$: a 12.1499(5), b 14.0677(6), c 12.8625(5) Å; low-temperature form, $T = 40$ K: $R_1 = 0.066$, $wR_2 = 0.129$; orthorhombic $Pna2_1$: a 14.040(4), b 36.042(9), c 12.851(3) Å]. The well-ordered 40 K crystal structure of **1** comprises three independent ion pairs and crystallized CH_2Br_2 solvate molecules in the unit cell tripled along the b axis (Fig. 2 and figs. S14 to S18).

No reliable geometrical information could be extracted from all the structure determinations at temperatures above 86 K, where the norbornyl moiety was completely disordered because of the superposition of different orientations. However, the annealed well-ordered form at $T < 50$ K provided consistent and unambiguous results for all three crystallographically independent cations. Thus, the three sets of bridging C–C distances were 1.80(2) and 1.83(2) Å (ion A), 1.79(2) and 1.81(2) Å (ion B), and 1.78(2) and 1.80(2) Å (ion C) in our best structure determination at 40 K. All these values far exceed the usual C–C single bond length (1.54 Å), whereas the quite uniform basal bond distances of the three independent cations A to C, 1.38(2), 1.39(2), and 1.39(2) Å, respectively, resemble the 1.39 Å benzene value and indicate partial double-bond character (Fig. 2), as does the Raman stretching vibration frequency at 1462 cm^{-1} . Our experimentally determined structure and metrical parameters agree with theoretical computations, such as the 1.825 Å and 1.393 Å distances in the C_s -symmetric 2-norbornyl cation minimum at the MP2(FC)/def2-QZVPP level. Accordingly, our XRD analysis unequivocally confirms the bridged (nonclassical) geometry of the norbornyl cation elucidated by prior indirect experimental and theoretical studies. The remaining structural parameters of the cation, as well as the $[Al_2Br_7]^-$ anions and CH_2Br_2 solvates, are typical and agree equally well with the computations (supplementary materials). The earlier difficulties in attempted crystal structure determinations encountered in several x-ray laboratories may have been due to order-disorder phase transitions like those we observed at approximately 86 K. This is supported by our measurements of crystal no. 5 at 50 K (supplementary materials): Variations in the bridging bond distances increased even at temperatures only 10 K higher than that in our best 40 K structure.

What is the origin of this phase transition, which may have prevented earlier x-ray determinations of other crystalline 2-norbornyl cation salts? Analysis of the structural changes in the disordered >86 K temperature phase upon cooling suggested that ordering takes place when the 6,1,2-hydride shift in the norbornyl cation at 86 K starts to freeze out. The onset of ordering is observed in the 1H NMR spectrum already at about 115 K. Different experimental time scales (a few milliseconds for NMR but many seconds for an XRD charge-coupled device image exposure) are responsible for such disparate ordering temperatures. A calculation employing standard Eyring theory and the reported Gibbs activation energy

of $24.7 \pm 0.8\text{ kJ mol}^{-1}$ (14) give a half-life of 48 ms for the 6,1,2-hydride shift of the 2-norbornyl cation at 115 K (supplementary materials). Hence, the 2-norbornyl cation is essentially static on the NMR time scale at this experimental temperature. Assuming that about a 1000-s lifetime (supplementary materials) is needed to trigger ordering and phase transition of the 2-norbornyl cation in the solid state, an Eyring estimation using the Gibbs activation energy of $24.7 \pm 0.8\text{ kJ mol}^{-1}$ (14) gives 88 K as the transition temperature (nearly the same as the experimental 86 K). The computed Gibbs activation energies for this 6,1,2-hydride shift, 32.5 kJ mol^{-1} in the gas phase or 23.8 kJ mol^{-1} in simulated solvent $\epsilon_r = \infty$ at 115 K [CCSD(T)/DZ→QZ//MP2(FC)/def2-QZVPP; COSMO model] agree quantitatively with experiment and corroborate our interpretation that the rapid intramolecular 6,1,2-hydride shift is responsible for the phase transition. Thus, the inherent hydride shift dynamics of the 2-norbornyl cation may well have been responsible for the disorder, which frustrated prior crystal structure determinations (32, 33).

The reaction of 2-exo-norbornyl bromide in CH_2Br_2 solution with the strong Lewis acid aluminum tribromide formed the 2-norbornyl cation as a crystalline $[Al_2Br_7]^-$ salt. However, its >86 K form suffered from strong disorder of the norbornyl cation moiety. Carefully controlled and monitored annealing via a reversible order-disorder phase transition resulted in a well-ordered low-temperature form. Only single-crystal x-ray structure determination of this form at <50 K resulted in unambiguous characterization and provided the long-sought crystallographic evidence for the nonclassical, bridged structure of the parent norbornyl cation. The propensity of bromoaluminate anions to stabilize carbocations, such as $[C(CH_3)_3]^+$ (40) and the 2-norbornyl cation, seems worthy of more general exploration.

References and Notes

- F. C. Whitmore, *J. Am. Chem. Soc.* **54**, 3274 (1932).
- H. C. Brown, *The Nonclassical Ion Problem*, with comments by P. v. R. Schleyer (Springer, New York, 1977).
- H. C. Brown, *Chem. Soc. Spec. Publ.* **16**, 140 (1962).
- H. C. Brown, *Acc. Chem. Res.* **19**, 34 (1986).
- P. v. R. Schleyer *et al.*, *J. Am. Chem. Soc.* **86**, 5679 (1964).
- M. Saunders, P. v. R. Schleyer, G. A. Olah, *J. Am. Chem. Soc.* **86**, 5680 (1964).
- S. Winstein, D. S. Trifan, *J. Am. Chem. Soc.* **71**, 2953 (1949).
- S. Winstein, D. Trifan, *J. Am. Chem. Soc.* **74**, 1147 (1952).
- S. Winstein, D. Trifan, *J. Am. Chem. Soc.* **74**, 1154 (1952).
- S. Winstein, E. Clippinger, R. Howe, E. Vogelfanger, *J. Am. Chem. Soc.* **87**, 376 (1965).
- G. A. Olah, G. K. S. Prakash, M. Saunders, *Acc. Chem. Res.* **18**, 292 (1985).
- G. A. Olah, G. K. S. Prakash, M. Arvanaghi, F. A. L. Anet, *J. Am. Chem. Soc.* **104**, 7105 (1982).
- G. A. Olah, *Acc. Chem. Res.* **9**, 41 (1976).
- G. A. Olah, A. M. White, J. R. Demember, A. Commeyras, C. Y. Lui, *J. Am. Chem. Soc.* **92**, 4627 (1970).
- G. A. Olah, A. M. White, *J. Am. Chem. Soc.* **91**, 3956 (1969).
- G. A. Olah, A. Commeyras, C. Y. Lui, *J. Am. Chem. Soc.* **90**, 3882 (1968).
- G. A. Olah, G. K. S. Prakash, Á. Molnár, J. Sommer, *Superacid Chemistry* (Wiley, Hoboken, NJ, ed. 2, 2009).
- M. Saunders, M. R. Kates, *J. Am. Chem. Soc.* **105**, 3571 (1983).
- C. S. Yannoni, V. Macho, P. C. Myhre, *J. Am. Chem. Soc.* **104**, 907 (1982).
- C. S. Yannoni, V. Macho, P. C. Myhre, *J. Am. Chem. Soc.* **104**, 7380 (1982).
- Y. J. Hong, D. J. Tantillo, *J. Org. Chem.* **72**, 8877 (2007).
- T. M. Zuo, T. Huang, *J. Theor. Comput. Chem.* **3**, 269 (2004).
- W. Koch, B. Liu, D. J. DeFrees, *J. Am. Chem. Soc.* **111**, 1527 (1989).
- M. J. S. Dewar, K. M. Merz, *J. Am. Chem. Soc.* **108**, 5634 (1986).
- K. Raghavachari, R. C. Haddon, P. v. R. Schleyer, H. F. Schaefer, *J. Am. Chem. Soc.* **105**, 5915 (1983).
- N. H. Werstik, H. M. Muchall, S. Noury, *J. Phys. Chem. A* **104**, 11601 (2000).
- S. A. Perera, R. J. Bartlett, *J. Am. Chem. Soc.* **118**, 7849 (1996).
- W. Koch *et al.*, *Angew. Chem. Int. Ed. Engl.* **29**, 183 (1990).
- H. Vancik, D. E. Sunko, *J. Am. Chem. Soc.* **111**, 3742 (1989).
- G. A. Olah, *Angew. Chem. Int. Ed. Engl.* **12**, 173 (1973).
- L. K. Montgomery, M. P. Grendze, J. C. Huffman, *J. Am. Chem. Soc.* **109**, 4749 (1987).
- T. Laube, *J. Am. Chem. Soc.* **111**, 9224 (1989).
- T. Laube, *Angew. Chem. Int. Ed. Engl.* **26**, 560 (1987).
- T. Laube, *Angew. Chem. Int. Ed. Engl.* **25**, 349 (1986).
- A. J. Lehner, N. Trapp, H. Scherer, I. Krossing, *Dalton Trans.* **40**, 1448 (2011).
- I. Raabe *et al.*, *Dalton Trans.* (7), 946 (2008).
- I. Krossing, A. Bihlmeier, I. Raabe, N. Trapp, *Angew. Chem. Int. Ed. Engl.* **42**, 1531 (2003).
- I. Krossing, A. Reisinger, *Coord. Chem. Rev.* **250**, 2721 (2006).
- I. Krossing, I. Raabe, *Angew. Chem. Int. Ed. Engl.* **43**, 2066 (2004).
- F. Scholz, D. Himmel, H. Scherer, I. Krossing, *Chemistry* **19**, 109 (2013).

Acknowledgments: This paper is dedicated to the memory of Saul Winstein and Daniel S. Trifan, who first studied the 2-norbornyl cation. This work was supported by the University of Freiburg, the Friedrich-Alexander-University of Erlangen-Nuremberg, the Freiburg Institute for Advanced Studies, the Deutsche Forschungsgemeinschaft (Normalverfahren and SFB 583), and the European Research Council in the UniChem project 291383. We also thank the Fonds der Chemischen Industrie and the U.S. NSF (grant CHE 105-7466) for support. All crystal structures have been deposited with the Cambridge crystallographic database and may be accessed by quoting the deposition numbers: CCDC 931449 (for **1** at 120 K, crystal 1), CCDC 931450 (for **1** at 40 K, crystal 1), CCDC 931451 (for **1** at 40 K, crystal 2), CCDC 895701 (for **1** at 120 K, crystal 4), and CCDC 901047 (for **1** at 50 K, crystal 5).

Supplementary Materials

www.sciencemag.org/cgi/content/full/341/6141/62/DC1
Materials and Methods
Figs. S1 to S20
Tables S1 to S5
Scheme S1
References (41–64)

8 April 2013; accepted 7 June 2013
10.1126/science.1238849

Emergence of Agriculture in the Foothills of the Zagros Mountains of Iran

Simone Riehl,^{1,2*} Mohsen Zeidi,^{2,3} Nicholas J. Conard^{2,3}

The role of Iran as a center of origin for domesticated cereals has long been debated. High stratigraphic resolution and rich archaeological remains at the aceramic Neolithic site of Chogha Golan (Ilam Province, present-day Iran) reveal a sequence ranging over 2200 years of cultivation of wild plants and the first appearance of domesticated-type species. The botanical record from Chogha Golan documents how the inhabitants of the site cultivated wild barley (*Hordeum spontaneum*) and other wild progenitor species of modern crops, such as wild lentil and pea. Wild wheat species (*Triticum* spp.) are initially present at less than 10% of total plant species but increase to more than 20% during the last 300 years of the sequence. Around 9800 calendar years before the present, domesticated-type emmer appears. The archaeobotanical remains from Chogha Golan represent the earliest record of long-term plant management in Iran.

Southwestern Asia has been viewed as a key area for the development of agriculture, and researchers have long debated whether agriculture had its origin in a single or in multiple regions of the Fertile Crescent (FC) (1–3). Although the archaeological and biomolecular evidence for the process of plant domestication suggests the presence of multiple centers and events over many hundreds of years (2, 4–6), research has been hampered by limited data and a near-absence of plant remains from the eastern part of the FC (7–10). Domesticated species evolved through management of their wild progenitors, thus identification of pre-domestication cultivation or management of phenotypically wild species is required to provide the crucial link made between gathering wild cereals and cultivating domesticated species. Knowledge of this process is essential for our understanding of how hunter-gatherers evolved into farmers. Until now, pre-domestication has been documented only for a few Pre-Pottery-Neolithic (PPN) sites in the Levant and northern Mesopotamia (11). Despite speculation, the role of the eastern FC in the domestication process has remained unclear.

Chogha Golan is situated in a semiarid region, in the foothills of the Zagros Mountains, Iran, at an elevation of 485 m (Fig. 1). Within the Tübingen-Iranian Stone Age Research Project (TISARP), archaeologists from the University of Tübingen and the Iranian Center for Archaeological Research conducted excavations at the site in 2009 and 2010. The tell, roughly 3 ha in size, preserves an 8-m sequence of exclusively aceramic deposits rich in chipped stone, architectural features, clay figurines, and a large number

of mortars and grinding tools. Excavators unearthed 11 archaeological horizons (AHs), separated by plaster floors or other clear stratigraphic features. The lithic assemblages show gradual changes in the composition of the tool types and the raw materials used. Small objects, such as clay figurines depicting animals and humans, worked bone artifacts, and stone vessels and ground stone tools document a high degree of continuity throughout the sequence. The archaeological findings suggest that comparatively

large social groups lived there under relatively stable economic conditions that allowed an extremely rich tell to form (12). Ten accelerator mass spectrometry (AMS) dates place the occupation of the site between 12,000 and 9800 calendar years before the present (cal yr B.P.) (12, 13) (Fig. 2). Initial occupation of the site started near the end of the Younger Dryas, and the stratigraphic sequence is contemporaneous with archaeological sites of the Levant and northern Mesopotamia, ranging from PPNa to middle PPNB. Chogha Golan represents the earliest aceramic Neolithic documented in Iran, with only Sheikh-e Abad providing similar ages (14).

Systematic sampling resulted in the recovery of large amounts of exceptionally well-preserved bioarchaeological remains, including wild progenitor species of modern crops, such as wild barley (*Hordeum spontaneum*), wild wheat species (*Triticum boeoticum*, *T. dicoccoides*, and Triticoid types), lentil (*Lens* spp.), and grass pea (*Lathyrus* spp.) (15). We identified more than 21,000 plant remains from 25 of the samples from 203 liters of sediment, resulting in 116 taxa (table S1). Faunal remains document the presence of caprines, wild boar, gazelles, equids, large bovids, rodents, hares, reptiles, birds, fish, mussels, and freshwater crustaceans (12).

Interpreting the evidence of domestication at aceramic sites in the Near East is not straightforward (11), but the refinement of morphological criteria throughout the past decades has

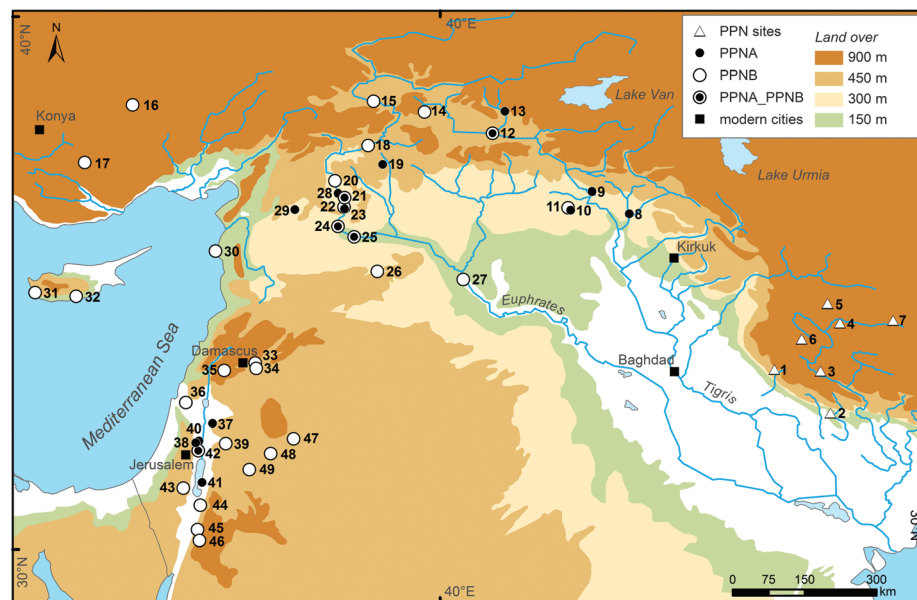


Fig. 1. Location of Chogha Golan (1) and other important PPN sites in the FC: (2) Ali Kosh, (3) Chia Sabz, (4) Ganj Dareh Tepe, (5) Sheikh-e Abad, (6) Jani, (7) Tepe Abdul Hosein, (8) M'lefaat, (9) Nemrik, (10) Qermez Dere, (11) Magzalia, (12) Körtik Tepe, (13) Hallan Cemi, (14) Cayonu, (15) Cafer Hoyuk, (16) Asikli Hoyuk, (17) Can Hasan III, (18) Nevali Cori, (19) Göbekli Tepe, (20) Akarçay Tepe, (21) Djade, (22) Halula, (23) Jerf el Ahmar, (24) Mureybet, (25) Abu Hureyra, (26) El Kowm I and II, (27) Bouqras, (28) Abr, (29) Qaramel, (30) Tell Ras Shamra, (31) Kissonerga, (32) Parekklisha-Shillourokambos, (33) Tell Ghoraifé, (34) Tell Aswad, (35) Tell Ramad, (36) Yiftah'el, (37) Iraq ed Dubb, (38) Gilgal, (39) 'Ain Ghazal, (40) Netiv Hagdud, (41) Dhra, (42) Jericho, (43) Nahal Hemar, (44) Wadi Fidan, (45) Beidha, (46) Basta, (47) Dhuweila, (48) Azraq 31, (49) Wadi Jilat 7. PPN is applied to Iranian sites, because PPNa and PPNB have additional cultural connotations that apply only to sites in the western and northern part of the FC.

¹Institute for Archaeological Sciences, University of Tübingen, Rümelinstraße 23, 72070 Tübingen, Germany. ²Tübingen Senckenberg Center for Human Evolution and Palaeoecology, Rümelinstraße 23, 72070 Tübingen, Germany. ³Abteilung für Ältere Urgeschichte und Quartärökologie, Institut für Ur- und Frühgeschichte und Archäologie des Mittelalters, Universität Tübingen, Schloss Hohentübingen, 72070 Tübingen, Germany.

*Corresponding author. E-mail: simone.riehl@uni-tuebingen.de

demonstrated that domesticated cereals appear in the early to middle PPNB at several key sites (9, 16–18). Because the transition from pre-domestication of wild taxa to domestication is a gradual process and most sites have yielded only limited evidence, the record of the domestication process is still incomplete (6, 9). The high density of botanical remains at Chogha Golan in comparison to other PPN sites, along with high stratigraphic resolution, allows us to document a nearly continuous record of early plant management, including pre-domestication cultivation and the initial use of domesticated-type emmer.

With the end of the Younger Dryas and throughout the first three archaeological horizons (AH XI to IX), the proportions of wild barley (*H. spontaneum*) increase, whereas *Triticum*-type taxa appear in low counts (Fig. 2) (15). Numerous chaff remains and increased amounts of arable weeds in AH IX indicate probable cultivation of wild progenitor species of modern crops, including pulses such as lentil (fig. S1). In AH VIII around 10,700 cal yr B.P., the percentages of wild barley and possible arable weeds decrease (Fig. 2). Shortly before 10,000 cal yr B.P. (AH

V and IV), the percentages of all taxa decline except that of the small-seeded grasses, which we tentatively interpret as a shift in the subsistence economy, only on the basis of the plant remains (fig. S1). After 9800 cal yr B.P. (AH II), spikelets of domesticated-type emmer appear in increased amounts and subsequently outnumber those of other large-seeded grasses. These developments are accompanied by an increase in the proportions of arable weed taxa (Fig. 2).

Our interpretation of the management of phenotypically wild species, in other words pre-domestication cultivation, is consistent with a number of criteria (11, 15, 19–21). First, the high proportions (up to 40%) of wild progenitor species of barley, wheat, lentil, and other large-seeded pulses outline a plant diet focusing on large-seeded species, which are the ancestors of modern crops (fig. S1). Second, the number of possible arable weeds at Chogha Golan is already high in AH XI and correlates with the percentages of wild progenitors of modern crops. The general presence and abundance of arable weeds are in good agreement with those from sites along the Euphrates in the northern FC (10). Third, in AH II the abundance

of arable weeds increases and correlates with a strong increase in *Triticum*-type taxa (Fig. 2).

The presence of bases of domesticated-type emmer wheat spikelets (*T. dicoccum*) from AH II onward marks the beginning of management of domesticated species (Fig. 3). Within the large-seeded grasses group from AH II, about 21% of specimens preserve the domesticated-type spikelet bases of emmer (*T. dicoccum*; table S1). This percentage is above the values observed in wild populations and suggests that the chaff remains recorded at Chogha Golan indicate genotypic changes toward domesticated emmer. Domesticated-type rachis internodes of barley occur in only low proportions from the beginning of the occupation of the site, increasing to 2.5% in AH IV, which is consistent with observed values in wild populations (20).

A Triticoid type with no modern counterpart appears in all AHs at Chogha Golan, but mainly in horizons XI and IV, and documents the already-high diversity in wild *Triticum*-type cereals at the onset of the stratigraphic sequence of Chogha Golan (15). The observation of Triticoid-type species, large-seeded barley grains, and high proportions of arable weeds already in AH XI also

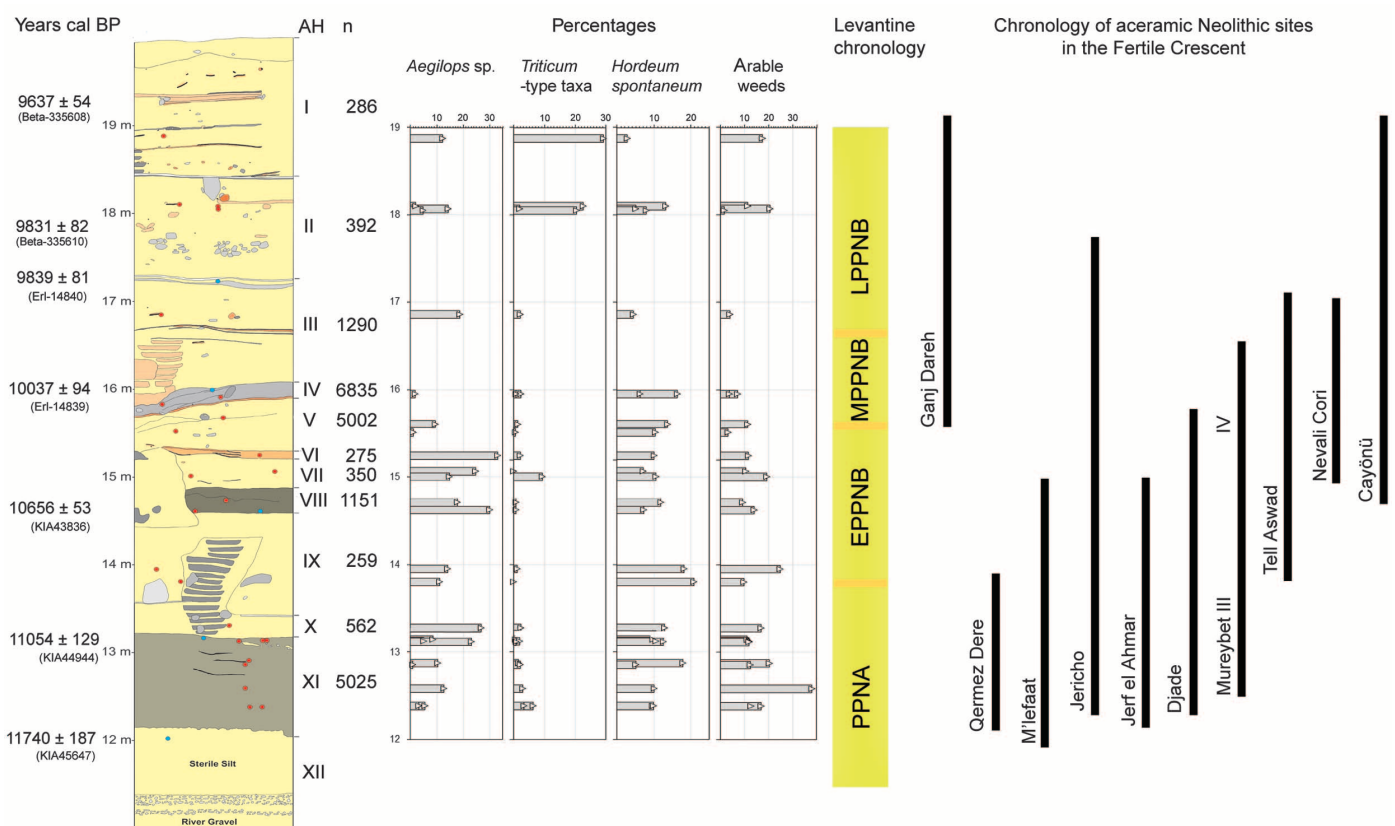


Fig. 2. Stratigraphic profile from Chogha Golan (left) with AMS dates in cal yr B.P. (locations of dated samples are indicated with blue circles in the profile) and AHs in Roman numbers. Percentages of taxa and groups of taxa relevant for the development of cultivation and domestication in each sample are based on the total of all identifications from each AH (locations of samples are indicated with red circles in the profile): *Aegilops* sp. (goat-grass); *Triticum*-type taxa: agglomeration of

different *Triticum* taxa (see text for description); *H. spontaneum* (wild barley); and arable weeds (for further explanation see the supplementary text). n, number of seed and chaff records identified in each horizon. The yellow bar indicates the equivalent Levantine chronology. The black lines on the right depict the cultural-chronological placement of well-known aceramic Neolithic sites in the FC. EPPN, early PPN; MPPN, middle PPN; LPPN, late PPN.

suggests that the starting point of cultivation in the foothills of the Zagros may extend further back into the Epipaleolithic.

The archaeobotanical data from Chogha Golan are consistent with the local evolution of agricultural economies, but interregional exchanges of ideas and cultigens may well have accompanied this process. Our results are in agreement with biomolecular research suggesting multiple domestications for barley (22) and goats (8) and in pointing to a large region for the emergence of agriculture that includes the Zagros Mountains.

The results presented here refute models arguing against the eastern FC being one of multiple key regions where domestication evolved (3, 23). The rich record from Chogha Golan, when taken together with other results, points to largely simultaneous processes in the management of wild plants and the beginnings of cereal domestication over much of the FC. These data demonstrate that the eastern region of the FC made important contributions to the development of Neolithic lifeways that formed the economic basis for the rise of urban centers and early states in the subsequent millennia.

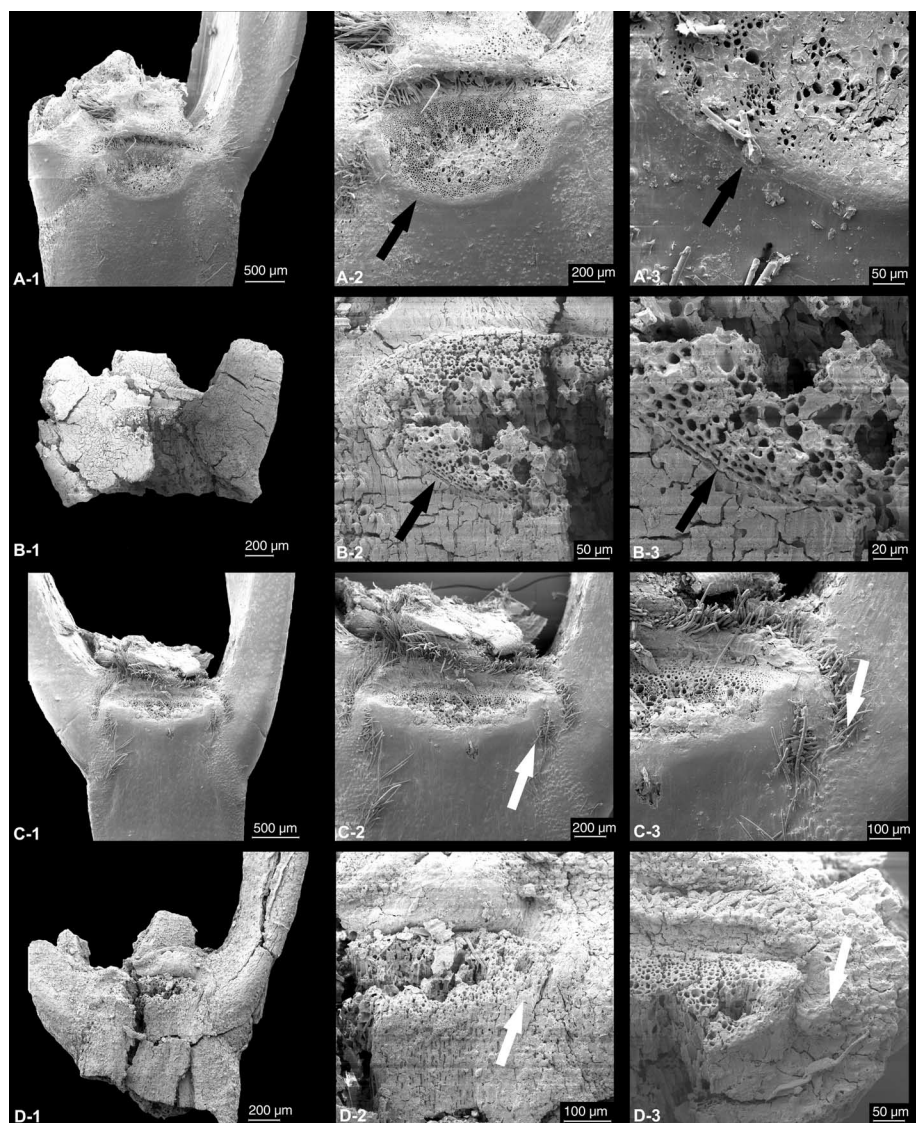


Fig. 3. Emmer spikelets illustrating criteria for identification of (A) modern wild emmer (*T. dicoccoides*), (B) wild emmer from Chogha Golan AH II, (C) modern domesticated emmer (*T. dicoccum*), and (D) phenotypic domesticated-type emmer from Chogha Golan AH II. The principal identification criteria used were according to Tanno and Willcox (11); note the wide, concave attachment scar of the next upper rachis internode, with a smooth lower rim in wild emmer; the angle between the attachment scar and upgoing glumes is between 140° and 180° [(A) and (B)], in contrast to the narrow, rough incision scar with a projecting lower part in domesticated emmer; the angle is between 90° and 140° [(C) and (D)]. Additional criteria used are marked by arrows. Black arrows indicate the lower attachment scar area in wild emmer (A-2 and -3, B-2 and -3), which represents a genetically inherent line of breakage. White arrows indicate the vertically downward-extended upper attachment area, bordering the central stem of the rachis internode (C-2 and -3, D-2 and -3).

References and Notes

1. R. J. Braidwood, *Sci. Am.* **203**, 131 (1960).
2. D. Fuller, G. Willcox, R. G. Allaby, *World Archaeol.* **43**, 628 (2011).
3. F. Hole, in *The Origins and Spread of Agriculture and Pastoralism in Eurasia*, D. Harris, Ed. (Smithsonian Institution Press, Washington, DC, 1996), pp. 263–281.
4. H. G. Gebel, *Neolithics* **1**, 28 (2004).
5. F. Salamini, H. Özkan, A. Brandolini, R. Schäfer-Pregl, W. Martin, *Nat. Rev. Genet.* **3**, 429 (2002).
6. K. Tanno, G. Willcox, *Science* **311**, 1886 (2006).
7. P. L. Morrell, M. T. Clegg, *Proc. Natl. Acad. Sci. U.S.A.* **104**, 3289 (2007).
8. S. Naderi *et al.*, *Proc. Natl. Acad. Sci. U.S.A.* **105**, 17659 (2008).
9. M. Nesbitt, in *The Dawn of Farming in the Near East*, R. T. J. Cappers, S. Bottema, Eds. (ex oriente, Berlin, 2002), pp. 113–132.
10. G. Willcox, S. Fornite, L. Herveux, *Veg. Hist. Archaeobot.* **17**, 313 (2008).
11. K.-i. Tanno, G. Willcox, *Veg. Hist. Archaeobot.* **21**, 107 (2012).
12. M. Zeidi, S. Riehl, H. Napierala, N. Conard, in *Proceedings of the 7th International Congress on the Archaeology of the Ancient Near East*, R. Matthews, J. Curtis, Eds. (Harrassowitz Verlag, Wiesbaden, Germany, 2012), pp. 259–275.
13. S. Riehl *et al.*, *Veg. Hist. Archaeobot.* **21**, 95 (2012).
14. R. Matthews, Y. Mohammadifar, W. Matthews, A. Motarjem, *Antiquity Project Gallery* (2010); <http://antiquity.ac.uk/projgall/matthews323/>.
15. See supplementary materials on Science Online.
16. G. C. Hillman, R. E. M. Hedges, A. Moore, S. Colledge, P. Pettitt, *Holocene* **11**, 383 (2001).
17. M. Nesbitt, D. Samuel, *Science* **279**, 1431e (1998).
18. G. Willcox, S. Fornite, *Veg. Hist. Archaeobot.* **8**, 21 (1999).
19. D. Q. Fuller, *Ann. Bot.* **100**, 903 (2007).
20. M. E. Kislev, in *People and Culture in Change*, I. Hershkovitz, Ed. (British Archaeological Reports, International Series, Oxford, 1989), vol. 508, pp. 147–151.
21. G. Willcox, *Veg. Hist. Archaeobot.* **21**, 163 (2012).
22. P. L. Morrell, M. T. Clegg, in *Wild Crop Relatives: Genomic and Breeding Resources - Cereals*, C. Kole, Ed. (Springer, Berlin, 2011), pp. 309–319.
23. O. Bar-Yosef, *Evol. Anthropol.* **6**, 159 (1998).

Acknowledgments: We thank the Tübingen-Iranian Stone Age Research Project team and S. Hamzavi, representative of the Iranian students, for their support during fieldwork. A. Khoshnevis, the former director of the Research Center of the Iran Cultural Heritage and Tourism Organization, provided permission for the fieldwork. We are grateful to M. Mortezaei and A. Lashkari, directors of the Iranian Center for Archaeological Research and L. Niyakan for granting our permits. Additional support was bestowed by M. Skandari, Director of the Cultural Heritage Office of Ilam Province, and by D. Chamanara, prefect of Salehabad. We thank A. Orendi and D. Karakaya for their contributions to the archaeobotanical study and K. Pustovoytov for technical support with geographic information systems. The Eberhard-Karls-Universität Tübingen, the Heidelberg Academy of Sciences, the Tübingen Senckenberg Center for Human Evolution and Palaeoecology, and the German Research Foundation (DFG) funded this research. The University of Hohenheim provided scanning electron microscopy facilities. The archaeobotanical samples are currently archived at the University of Tübingen. The raw data are presented in the supplementary materials.

Supplementary Materials

www.sciencemag.org/cgi/content/full/341/6141/65/DC1

Materials and Methods

Supplementary Text

Fig. S1

Table S1

References (24–27)

19 February 2013; accepted 10 May 2013

10.1126/science.1236743

Space Partitioning Without Territoriality in Gannets

Ewan D. Wakefield,^{1*†} Thomas W. Bodey,^{2*†} Stuart Bearhop,^{2*} Jez Blackburn,³ Kendrew Colhoun,⁴ Rachel Davies,¹ Ross G. Dwyer,² Jonathan A. Green,⁵ David Grémillet,^{6,7} Andrew L. Jackson,⁸ Mark J. Jessopp,⁹ Adam Kane,⁸ Rowena H. W. Langston,¹⁰ Amélie Lescroël,^{6,11} Stuart Murray,¹² Mélanie Le Nuz,¹³ Samantha C. Patrick,^{14‡} Clara Péron,⁶ Louise M. Soanes,⁵ Sarah Wanless,¹⁵ Stephen C. Votier,^{16*} Keith C. Hamer^{1*}

Colonial breeding is widespread among animals. Some, such as eusocial insects, may use agonistic behavior to partition available foraging habitat into mutually exclusive territories; others, such as breeding seabirds, do not. We found that northern gannets, satellite-tracked from 12 neighboring colonies, nonetheless forage in largely mutually exclusive areas and that these colony-specific home ranges are determined by density-dependent competition. This segregation may be enhanced by individual-level public information transfer, leading to cultural evolution and divergence among colonies.

Colonial animals are constrained by their colony locations, which are ultimately limited by resource availability (1). However, within species, potential colony home ranges often overlap, implying that competition among colonies may also be limiting (2). In eusocial central-place foragers, the spatial effects of direct competition among colonies are well understood (2). By contrast, the spatial influences of indirect competition and information transfer on nonterritorial species (e.g., seals, swallows, and seabirds), where levels of relatedness are much lower, remain conjectural. For example, the hinterland model (3) predicts that breeding seabirds segregate along colonial lines, because of inequalities in travel costs from each colony. Predicted home ranges therefore comprise Voronoi

polygons (Fig. 1A), as seen in some territorial animals (2). Food availability is assumed to be proportional to polygon area, limiting colony size. An alternative model proposes that density-dependent competition among colony members is limiting (4). As colonies grow, local prey depletion or disturbance requires birds to travel further to provision their young. However, this model (“Ashmole’s halo”) does not consider interactions among colonies and tacitly assumes that adjacent colonies’ home ranges overlap (5).

Indirect evidence exists to support both models (3, 6, 7), and recent tracking studies suggest that seabirds and pinnipeds segregate along colonial lines (8–12). However, these studies proved inconclusive on the causes and ubiquity of segregation, largely because few colonies were sampled or tracking resolution was low. Here we used high-resolution satellite tracks of the foraging movements of 184 chick-rearing northern gannets, *Morus bassanus* (hereafter gannets), from 12 of the 26 colonies fringing the British Isles (median 17 birds/colony), representing ~80% of the area’s breeding population (Fig. 1A and table S1), to test whether among-colony segregation occurs in a model colonial nonterritorial central-place forager. We then used population- and individual-level models to explore potential mechanisms underlying spatial segregation.

Gannets are wide-ranging (maximum foraging range ~700 km) pelagic seabirds that forage in patches of enhanced production, primarily on shoaling, mesotrophic fish and to a lesser extent, fisheries discards (13–15). In almost all cases, we tracked birds from adjacent colonies simultaneously (16). Individual gannet tracks (Fig. 1B and fig. S1) and percentage utilization distributions (UDs) (Fig. 2A and fig. S2) showed a distinctive pattern of between-colony variation and spatial segregation, within and across years (fig. S3). The size of 95% foraging UD was strongly dependent ($F_{1,8} = 149.7$, $P < 0.001$, $R^2 = 0.94$; fig. S4) on square-root colony size (N). Likewise, maximum foraging range and trip duration were dependent on $N^{0.5}$ [linear mixed-effects (LME)

models, $P = 0.002$ and < 0.001 ; tables S2 and S3]. Birds from colonies of all sizes divided their time equally between foraging and chick attendance (LME, $P = 0.191$; table S4), and the number of foraging trips per day was negatively dependent on $N^{0.5}$ (LME, $P = 0.024$; table S5). Prey delivery rate, for which we assume trips per day is a proxy, is therefore negatively dependent on $N^{0.5}$, supporting the prediction that colony size is limited by density-dependent competition (4, 6). Contrary to the hinterland model (3), we found no relationship between colony Voronoi polygon area and colony size ($F_{1,35} < 0.01$, $P = 0.699$, $R^2 < 0.01$; fig. S5).

Using empirical relationships between colony size and foraging area, we devised a population-level null model of the distribution of foraging gannets, assuming negligible competition between birds from neighboring colonies (16). This successfully explains among-colony segregation when colonies are far apart but predicts extensive overlap between several study colonies, particularly in the Celtic Sea (Fig. 2A). However, observed UD were largely mutually exclusive (fig. S2), overlapping markedly less than predicted (fig. S6). For example, the null population overlap index (POI) [the number of potential pairwise interactions between birds from adjacent colonies (16)] for Little Skellig and Bull Rock (populations ~29,700 and 3700 pairs; separation distance 27 km) was 105,000, whereas the empirical estimate was 6000, largely because foraging trips were directed away from closely neighboring colonies (Fig. 1B). This pattern differs from the hinterland model in two key respects: Segregation was not absolute, and divisions between the UD of unequally sized colonies were not equidistant between the two (Fig. 1B and fig. S2) but typically occurred closer to the smaller colony, a phenomenon also observed in penguins (9). Hence, the predictive performance of the hinterland model (log-likelihood, $L = -0.54$, AIC 3691; table S6) was poor in comparison to that of the null model [$L = -0.30$, Akaike information criterion (AIC) = 2231].

Given the inability of existing models to explain gannet distribution when colonies are close together, we propose a multicolony extension of Ashmole’s halo (4), which we term the density-dependent hinterland (DDH) model. As adjacent colonies grow, foraging ranges increase as a result of prey depletion or disturbance (6) until their home ranges overlap. At low densities, birds from different colonies may forage together, but as prey availability decreases, populations respond by spreading down conspecific density gradients to the nearest areas subject to a lower rate of exploitation (6). As a first approximation, we assume a simple inverse relationship between the exploitation by conspecifics from adjacent colonies and the likelihood of new birds foraging in an area (16). However, the trade-off between transport and competition costs means that birds favor areas close to their own colonies, so density declines with colony distance d (10). Hence,

¹School of Biology, University of Leeds, Leeds LS2 9JT, UK. ²Centre for Ecology and Conservation, University of Exeter, Penryn, Cornwall TR10 9EZ, UK. ³British Trust for Ornithology, The Nunnery, Thetford IP24 2PU, UK. ⁴The Royal Society for the Protection of Birds, Northern Ireland Headquarters, Belvoir Park Forest, Belfast BT8 4QT, UK. ⁵School of Environmental Sciences, University of Liverpool, Environmental Sciences, Liverpool L69 3GP, UK. ⁶CEFE-CNRS, 1919 Route de Mende, F-34293 Montpellier Cedex 5, France. ⁷FitzPatrick Institute, Department of Science and Technology–National Research Foundation Centre of Excellence, University of Cape Town, Rondebosch 7701, South Africa. ⁸Department of Zoology, School of Natural Sciences, Trinity College Dublin, Dublin 2, Ireland. ⁹Coastal and Marine Research Centre, University College Cork, Cork, Ireland. ¹⁰The Royal Society for the Protection of Birds, Sandy, Bedfordshire SG19 2DL, UK. ¹¹Biodiversité et gestion des territoires, Université de Rennes 1–UMR 7204, Muséum National d’Histoire Naturelle, 35042 Rennes Cedex, France. ¹²Easter Craigie Dhu, Dunkeld, Perthshire PH8 0EY, UK. ¹³Réserve naturelle des Sept-Îles, Ligue pour la Protection des Oiseaux, F-22560 Pleumeur Bodou, France. ¹⁴Marine Biology and Ecology Research Centre, Plymouth University, Plymouth PL4 8AA, UK. ¹⁵Centre for Ecology and Hydrology, Penicuik EH26 0QB, UK. ¹⁶Environment and Sustainability Institute, University of Exeter, Penryn, Cornwall TR10 9EZ, UK.

*Corresponding author. E-mail: e.d.wakefield@leeds.ac.uk (E.D.W.); t.w.bodey@exeter.ac.uk (T.W.B.); s.bearhop@exeter.ac.uk (S.B.); stephen.votier@plymouth.ac.uk (S.C.V.); k.c.hamer@leeds.ac.uk (K.C.H.)

†These authors contributed equally to this work.

‡Present address: Centre d’Etudes Biologiques de Chizé, CNRS-UPR1934, Villiers en Bois, France.

when colonies are large or close together, segregation between home ranges may become absolute. Using these assumptions, we modeled the development of spatial segregation as colonies grow (16). We aim to replicate colony growth at the onset of the breeding season (9) but note that historical colony growth patterns may also influence spatial segregation (6) and that colony sizes are unlikely to be in equilibrium (6, 14). Initial comparisons with our tracking data showed that weighting the relative rate of exploitation by $d^{-0.5}$ improved this model, implying a decline in competitive fitness with distance. The DDH model

proved a better fit to the tracking data ($L = -0.58$, $AIC = 25440$) than the null ($L = -0.61$, $AIC = 27015$; table S7; compare Fig. 2, A and B). Furthermore, unlike the null, the DDH model successfully predicted the POI (fig. S6) and the angular displacement of the center of gravity of the 75% UD from their colonies (circular correlation, observed versus predicted directions, null model, $r = 0.214$, $P = 0.463$, $n = 12$; DDH model, $r = 0.761$, $P = 0.020$, $n = 12$). The shapes of the UD predicted by the DDH model were closer to those observed (Dice's similarity coefficient $s = 0.57$, table S8) than the null model's predictions ($s =$

0.45) (16). The DDH model's greater predictive strength was most marked for colonies with close neighbors (Fig. 2 and table S8). Notably, the DDH model predicts greater foraging ranges than the null model (paired t test, square-root mean distance $t_{24} = 4.542$, $P < 0.001$), which implies that indirect competition from neighboring colonies diminishes chick provisioning rates, limiting colony size (5).

Like Ashmole's halo and the hinterland model, the DDH model assumes that gannets are ideal free foragers. However, seabird prey occurs in widely dispersed, partially predictable

Fig. 1. Gannet colony foraging ranges. (A) Gannets tracked from colonies around the British Isles forage in largely mutually exclusive areas, despite their potential home ranges overlapping (red, study colonies; yellow, others). Home ranges predicted by the hinterland model (3) form Voronoi polygons, bounded by lines of equidistance between colonies (black lines). (B) Satellite tracks from 184 individuals show that foraging birds direct their movements away from neighboring colonies (colors correspond to different colonies). Data were collected in 2011, except for St Kilda (SK), which were collected in 2010. Gray lines, 200- and 1000-m isobaths; LS, Little Skellig; TB, Bull Rock (mentioned in the text; see table S1 for colony details).

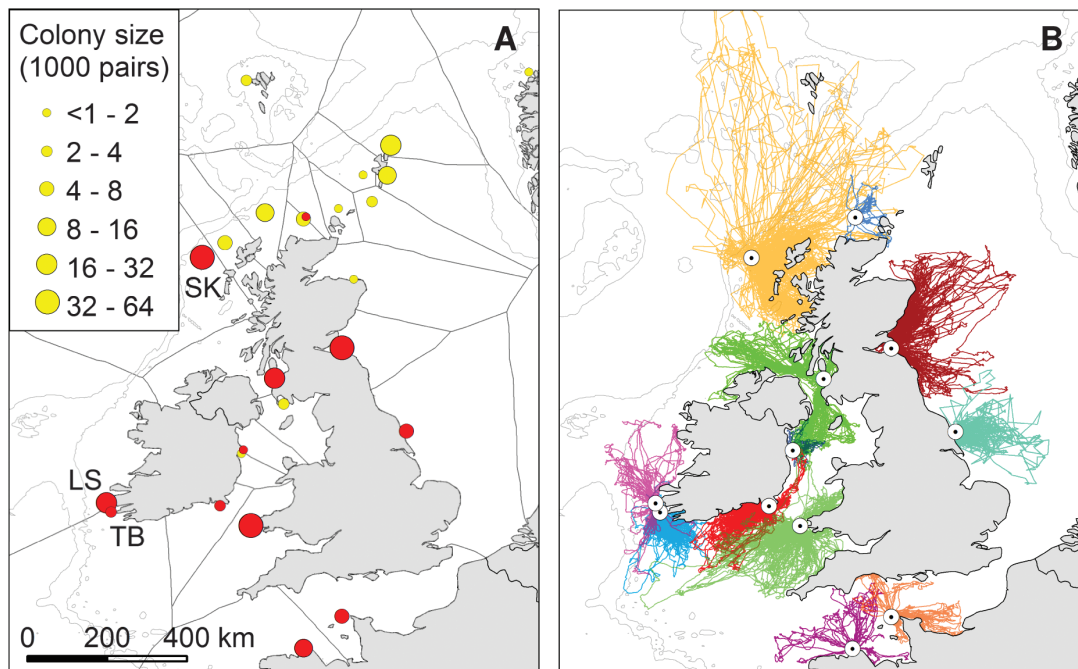
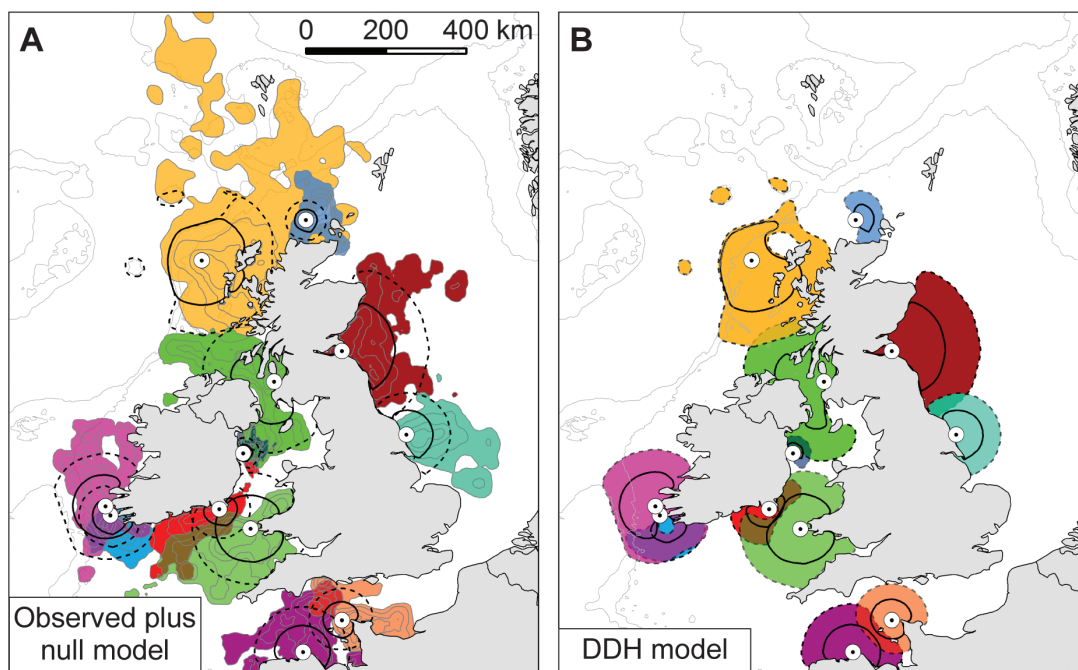


Fig. 2. Density-dependent competition and colony segregation. Density-dependent competition within and between colonies explains large-scale among-colony segregation. (A) Observed colony utilization distributions (colored polygons plus 95, 75, 50, and 25% UD contours) are largely mutually exclusive. This is at odds with the null model (predicted 75 and 95% UDs, solid and dashed lines), which assumes density-dependent competition only within colonies, predicting broad overlap between some UDs. (B) The density-dependent hinterland (DDH) model additionally assumes competition between colonies, providing a better fit to the tracking data.



patches (17). Thus, seabirds may not base foraging decisions on personal information (memory) alone but may also exploit public information (8, 18), gained by observing conspecifics at the colony (19–21) or at sea (22, 23), although empirical evidence remains limited (24). To examine these hypotheses, we developed a range of two-dimensional individual-based models of gannets foraging from two colonies (30 and 300 individuals), constrained by energy reserves (Table 1), to determine whether segregation emerges through information sharing (16). Only one model, incorporating memory and public information transfer at sea and at the colony, produced a significant reduction in overlap between colony UD_s (Fig. 3 and fig. S7). Between-colony segregation rapidly became established and then persisted (fig. S8), a pattern consistent at multiple food patch densities and most marked when colonies were close (figs. S9 and S10).

Public information is probably transmitted unintentionally, as in other colonial species (18, 21, 23, 25, 26). Several traits make this likely: Specifically, on arrival and departure from the nest, gannets signal visually and audibly. Before beginning foraging trips they land on the sea, near the colony, frequently departing in groups (14). These behaviors may allow conspecifics to

follow or copy successful birds (20, 21), channeling information from the population to the individual, thereby allowing birds to efficiently select foraging locations where they are competitively advantaged over conspecifics from other colonies. Although these mechanisms are likely to operate over temporal scales of minutes to weeks, gannets have overlapping generations and a long prebreeding period (≥ 4 years), during which they attend colonies with increasing regularity (14, 27). This is thought to allow young birds to learn about prey distribution. If this involves public information acquisition, the preconditions exist for cultural evolution of foraging behavior over much longer time scales (8, 28).

Our results suggest that density-dependent competition, rather than territoriality, causes spatial segregation in a model colonial central-place forager. Although the mechanisms remain unclear, there is increasing recognition that nonterritorial colonial central-place foragers utilize public information to inform decisions (18, 21, 23, 25, 26, 28). Contrary to the prevailing view, we predict that between-colony segregation is the norm when aggregations of animals such as bats, seals, bumblebees, and birds occur at high densities (i.e., when colonies are clustered or large), forcing a

reexamination of our understating of their foraging ecology.

References and Notes

1. J. F. Wittenberger, G. L. J. Hunt Jr., in *Avian Biology*, D. S. Farner, J. R. King, K. C. Parkes, Eds. (Academic Press, New York, 1985), vol. 8, pp. 1–78.

2. E. S. Adams, *Annu. Rev. Ecol. Syst.* **32**, 277–303 (2001).

3. D. K. Cairns, *Am. Nat.* **134**, 141 (1989).

4. N. P. Ashmole, *Ibis* **103b**, 458–473 (1963).

5. R. W. Furness, T. R. Birkhead, *Nature* **311**, 655–656 (1984).

6. S. Lewis, T. N. Sherratt, K. C. Hamer, S. Wanless, *Nature* **412**, 816–819 (2001).

7. K. H. Elliott et al., *Auk* **126**, 613–625 (2009).

8. D. Grémillat et al., *Mar. Ecol. Prog. Ser.* **268**, 265–279 (2004).

9. D. G. Ainley et al., *Ecol. Monogr.* **74**, 159–178 (2004).

10. E. D. Wakefield et al., *Ecol. Monogr.* **81**, 141–167 (2011).

11. S. Wanless, M. P. Harris, *Colon. Waterbirds* **16**, 176 (1993).

12. A. M. M. Baylis, B. Page, S. D. Goldsworthy, *Mar. Ecol. Prog. Ser.* **361**, 279–290 (2008).

13. K. C. Hamer et al., *Mar. Ecol. Prog. Ser.* **338**, 295–305 (2007).

14. B. Nelson, *The Atlantic Gannet* (Fenix Books, Great Yarmouth, UK, ed. 2, 2001).

15. S. C. Votier et al., *J. Appl. Ecol.* **47**, 487–497 (2010).

16. Information on materials and methods is available on Science Online.

17. P. Fauchald, *Mar. Ecol. Prog. Ser.* **391**, 139–151 (2009).

18. T. J. Valone, *Behav. Ecol. Sociobiol.* **62**, 1–14 (2007).

19. P. Ward, A. Zahavi, *Ibis* **115**, 517–534 (1973).

20. A. E. Burger, *Colon. Waterbirds* **20**, 55 (1997).

21. H. Weimerskirch, S. Bertrand, J. Silva, J. C. Marques, E. Goya, *PLoS ONE* **5**, e9928 (2010).

22. N. J. Buckley, *Am. Nat.* **149**, 1091–1112 (1997).

23. E. D. Silverman, R. R. Veit, G. A. Nevitt, *Mar. Ecol. Prog. Ser.* **277**, 25–36 (2004).

24. H. Richner, P. Heeb, *Adv. Stud. Behav.* **24**, 1–45 (1995).

25. M. Baude, E. Danchin, M. Mugabo, I. Dajoz, *Proc. Biol. Sci.* **278**, 2806–2813 (2011).

26. D. K. N. Dechmann et al., *Proc. Biol. Sci.* **276**, 2721–2728 (2009).

27. S. C. Votier, W. J. Grecian, S. Patrick, J. Newton, *Mar. Biol.* **158**, 355–362 (2011).

28. E. Danchin, L. A. Giraldeau, T. J. Valone, R. H. Wagner, *Science* **305**, 487–491 (2004).

Table 1. Rules governing information use in individual-based models of foraging gannets (see table S10 for details).

Foraging rules	Description
Null	Birds forage randomly during each trip
Memory (ME)	Birds return to previously successful locations (private information)
Local enhancement (ME + LE)	ME + uninformed birds may follow informed birds at sea (private and public information)
Information centre (ME + IC)	ME + uninformed birds may follow informed birds from their colony (private and public information)
All sources combined (ME + LE + IC)	ME + uninformed birds may follow informed birds from the colony and at sea (public and private information)

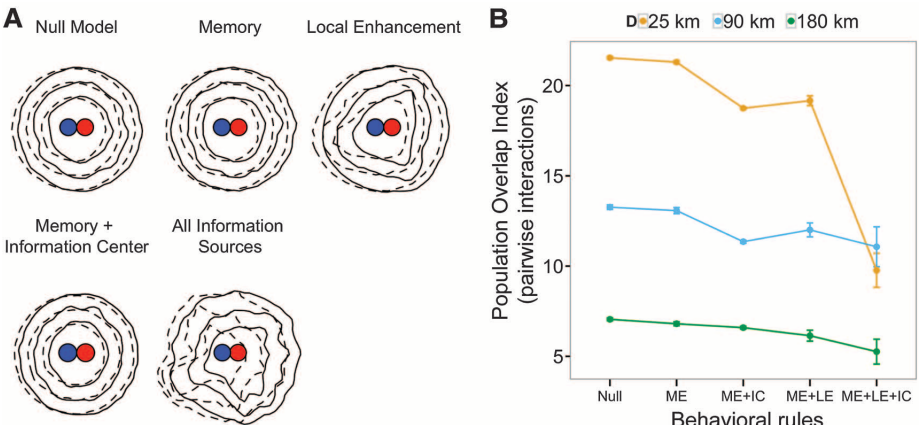


Fig. 3. Utilization distribution overlaps. Individual-based simulations show that overlap between the utilization distributions (UD_s) of two hypothetical colonies (A) (solid lines/blue circle, large colony; dashed lines/red circle, small colony) reduces (B) only when birds use private information and gain public information before departure and during foraging trips (see Table 1 for model rules). Isopeleths: 50, 75, and 95% UD_s. Results shown for 25 prey patches. Error bars show 95% confidence intervals.

Acknowledgments: Funding was provided by the Natural Environment Research Council (Standard Grant NE/H007466/1 to K.C.H., S.B., and S.C.V.), the UK Department of Energy and Climate Change, the Centre for Ecology and Hydrology, the Centre National de la Recherche Scientifique, the Ligue pour la Protection des Oiseaux, the Alderney Commission for Renewable Energy, the Beaufort Marine Research Award, and the European Union INTERREG projects CHARM III and FAME. We acknowledge use of www.seaturtle.org and their analysis tools. Data reported in this paper are tabulated in the supplementary materials and archived by BirdLife International (www.seabirdtracking.org).

Supplementary Materials
www.sciencemag.org/cgi/content/full/science.1236077/DC1
Materials and Methods
Supplementary Text
Figs. S1 to S13
Tables S1 to S10
R model algorithm and supporting data
References (29–50)

4 February 2013; accepted 10 May 2013
Published online 6 June 2013;
10.1126/science.1236077

MiR-200b and miR-429 Function in Mouse Ovulation and Are Essential for Female Fertility

Hidetoshi Hasuwa, Jun Ueda, Masahito Ikawa, Masaru Okabe*

Ovulation in the mouse and other mammals is controlled by hormones secreted by the hypothalamo-pituitary-ovarian axis. We describe anovulation and infertility in female mice lacking the microRNAs miR-200b and miR-429. Both miRNAs are strongly expressed in the pituitary gland, where they suppress expression of the transcriptional repressor ZEB1. Eliminating these miRNAs, in turn, inhibits luteinizing hormone (LH) synthesis by repressing transcription of its β -subunit gene, which leads to lowered serum LH concentration, an impaired LH surge, and failure to ovulate. Our results reveal roles for miR-200b and miR-429, and their target the *Zeb1* gene, in the regulation of mammalian reproduction. Thus, the hypothalamo-pituitary-ovarian axis was shown to require miR-200b and miR-429 to support ovulation.

MicroRNAs (miRNAs) are 21- to 22-nucleotide-long RNAs that silence gene expression posttranscriptionally by binding to and/or cleaving the 3'-untranslated regions (UTRs) of target mRNAs (1–3). They function in various biological processes, including development and tumorigenesis (4–6). To investigate the roles of miRNAs in reproduction, we produced

miRNA-disrupted gene knockout (KO) mouse lines, choosing miR-200b as a candidate because it was initially detected in the mouse testis (7). The expression of miR-200b in the testis reached its peak at 2 weeks of age and persisted into adulthood (fig. S1A) but was also detected in other organs, including the kidney, lung, and thymus (fig. S1B). We produced a double-knockout mouse line for miR-200b and miR-429 (miR-DKO), which has the same seed sequence and resides in the genomic vicinity of miR-200b (figs. S2 and S3).

We did not detect abnormalities in the testis, nor did we observe fertility defects in the miR-DKO male mice (fig. S4). However, miR-DKO female mice displayed greatly reduced fertility. When the miR-DKO females were mated with heterozygous males, they seldom became pregnant—despite successful coitus demonstrated by vaginal plug formation. The pregnancy rate of the 8-week-old miR-DKO females was at most 9% after coitus (versus 85% in wild-type and heterozygous females) with an average litter size of 6.29 ± 0.57 ($n = 7$) versus 7.48 ± 0.45 ($n = 26$) in heterozygous mice. However, these miR-DKO mice did not become pregnant again even after another 3 months of pairing with males, including the postpartum estrus period (Fig. 1A). When estrous cyclicity was examined by taking daily vaginal smears, estrus was found to be prolonged in miR-DKO mice compared with wild-type females, but the cyclicity itself was maintained (fig. S5). To eliminate the possibility that the infertile phenotype in miR-DKO female mice was caused by unknown side effects reported in some gene KO experiments (8, 9), we produced miR-200b- and miR-429-expressing transgenic mouse lines using the H1 promoter (fig. S6) and crossed them with the miR-DKO mouse line (fig. S7). As shown in Fig. 1A, miR-DKO females regained their fecundity from the transgenically expressed miR-200b and/or miR-429. These results indicate that the sterility observed in miR-DKO females was caused directly by the lack of miR-200b and/or miR-429.

Research Institute for Microbial Diseases, Osaka University, Yamadaoka 3-1, Suita, Osaka 565-0871, Japan.

*Corresponding author. E-mail: okabe@biken.osaka-u.ac.jp

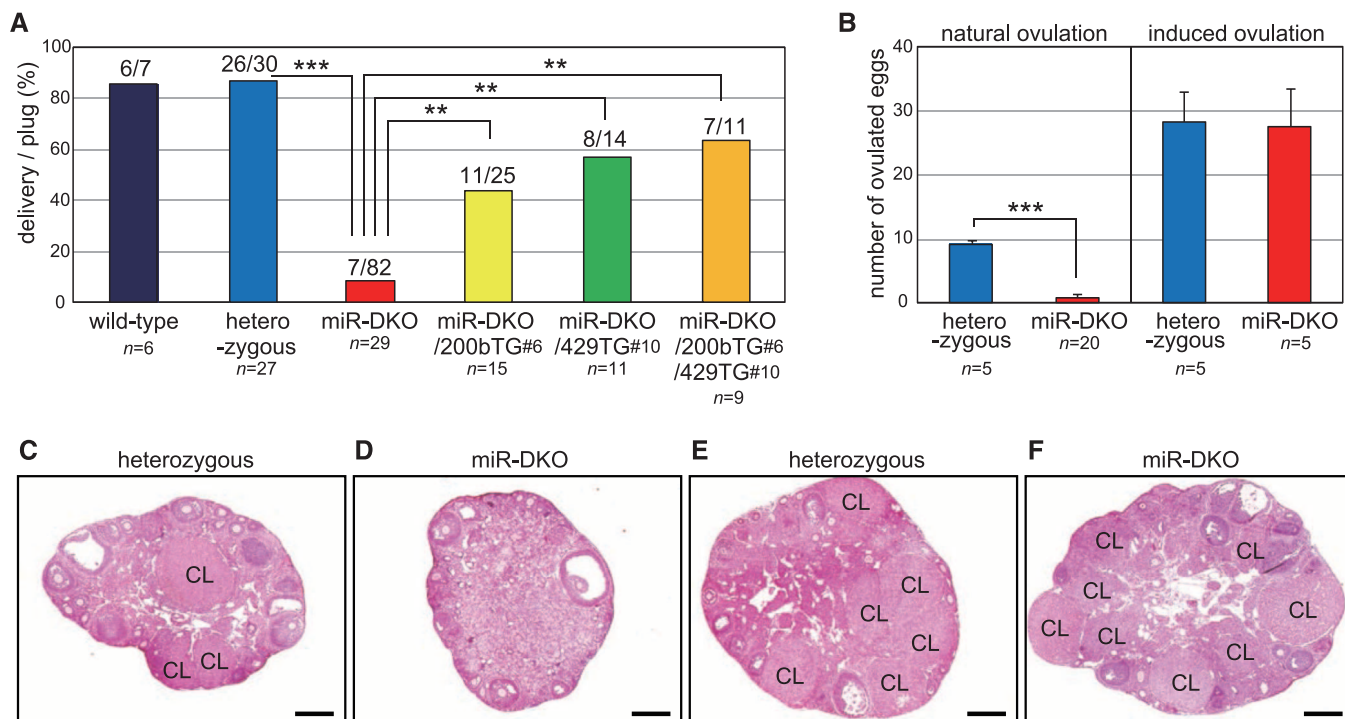


Fig. 1. Infertility phenotype of miR-DKO mice. (A) Fecundity of female mice was analyzed by natural mating; n indicates the number of female mice used in each genotype. The numbers on the bar indicate pregnancy per vaginal plug formation. (** $P < 0.01$, *** $P < 0.001$ by Fisher's exact test) (200bTG#6: miR-200b transgenic mouse line no. 6 and 429TG#10: miR-429 transgenic mouse line no. 10). (B) Number of ovulated oocytes from mated females. Superovulation was

induced with 5 IU (international units) each of PMSG and hCG at 48-hour intervals; n shows the number of females analyzed, and error bars indicate \pm SEM; *** $P < 0.001$. (C and D) Hematoxylin and eosin (HE)-stained ovarian sections of mated heterozygous and miR-DKO mice, respectively. No corpora lutea (CL) were found in miR-DKO ovaries. (E and F) Sections of ovaries from mated mice following superovulation. Many CL were observed in the miR-DKO mice. Scale bars, 0.4 mm.

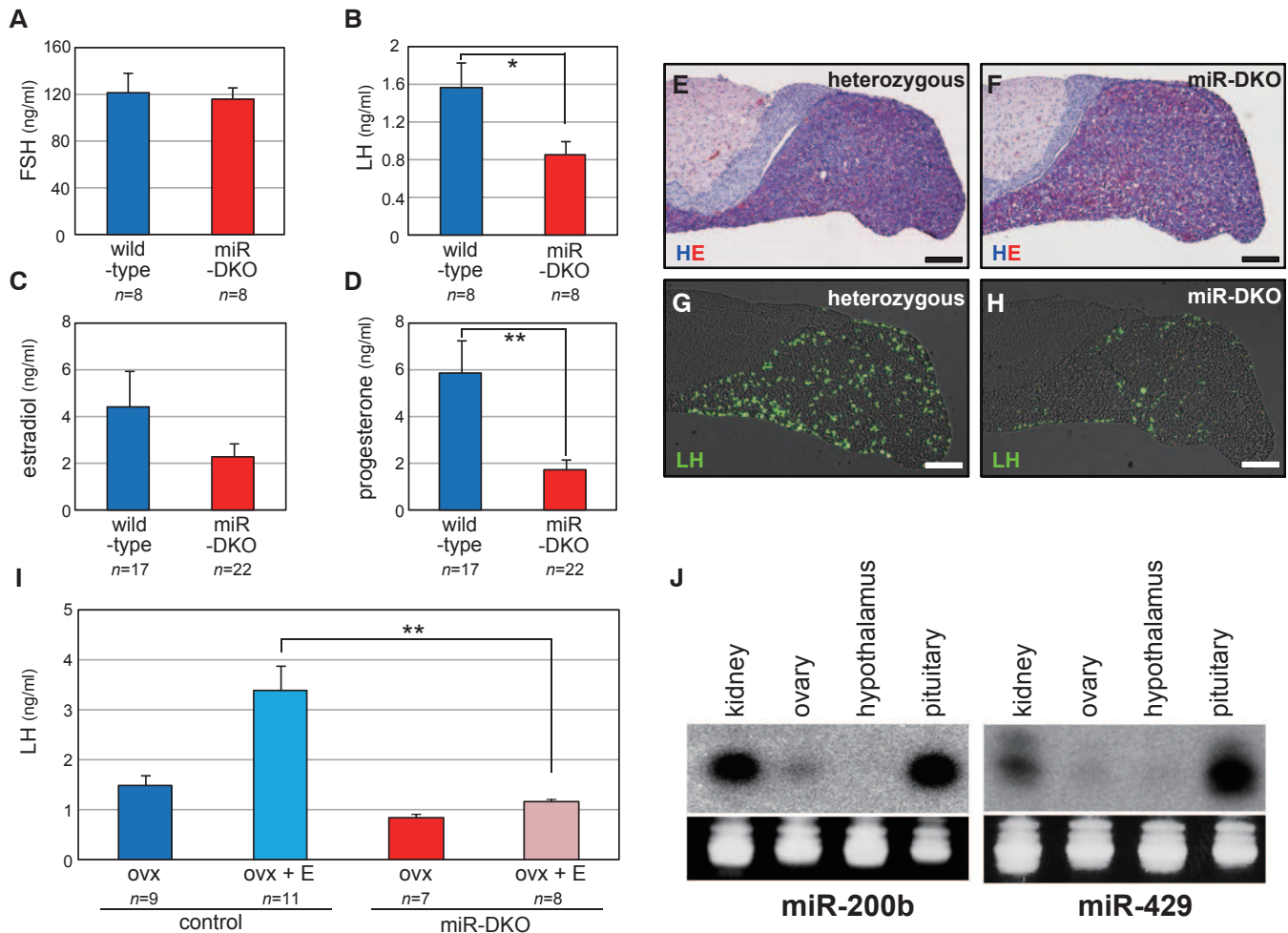


Fig. 2. Pituitary defects in miR-DKO female mice. (A to D) The FSH (A) and LH (B) serum concentrations were measured by radioimmunoassay (RIA), and estradiol (C) and progesterone (D) levels were measured by liquid chromatography–tandem mass spectrometry (LC-MS/MS). (E to H) Histology of pituitaries from 12-week-old mice heterozygous (E and G) and miR-DKO mice (F and H). (E and F) Paraffin wax sections of pituitaries were stained with HE. (G and H) Paraffin wax sections of pituitaries were stained with a rabbit antibody against LH (Biogenesis) and an Alexa 488–conjugated secondary antibody

(Invitrogen). Scale bars, 0.2 mm. (I) Induction of LH surges by estradiol injection in miR-DKO mice. Bars indicate serum LH concentrations with or without estradiol injection in ovariectomized (OVX) control mice (wild-type or heterozygous) and OVX miR-DKO mice (error bars indicate \pm SEM; * $P < 0.05$, ** $P < 0.01$). (J) Expression levels of miR-200b and miR-429 in the kidney, ovary, hypothalamus, and pituitary were analyzed by Northern blotting (top) using 4- μ g aliquots of total RNA from wild-type female mice. Ethidium bromide–stained tRNAs were used as loading controls (bottom).

To examine whether the miR-DKO mice could ovulate, we tried to collect oocytes from the oviducts in the morning of the day that the vaginal plug was found. Oocytes were recovered in only 2 out of 20 females (Fig. 1B). To examine the ovulation of miR-DKO mice more precisely, we prepared histology sections of miR-DKO mouse ovaries on the day that the plug was formed after natural mating (Fig. 1, C and D). When sections from heterozygous mice were examined, we found many early corpora lutea, as shown in Fig. 1C, which indicated successful ovulation. In contrast, they were basically not found in miR-DKO mice, except in $\sim 10\%$ of the miR-DKO females, which ovulated (Fig. 1B) and formed corpora lutea. However, when we superovulated the mice by injecting pregnant mare serum gonadotropin (PMSG) and human chorionic gonadotropin (hCG), the miR-DKO females ovulated about 27.6 ± 6.0 (mean \pm SEM) oocytes per fe-

male, similar to heterozygous females (Fig. 1B). When the oocytes from superovulated miR-DKO females were subjected to in vitro fertilization, the oocytes were fertilized at a normal rate and produced phenotypically normal pups after the resulting embryos were transplanted into the oviducts of pseudopregnant female wild-type foster mothers (fig. S8). The ovaries from prepubertal 3-week-old miR-DKO mice showed normal morphology (fig. S9), and normal corpora lutea were formed in the superovulated mature miR-DKO ovaries (Fig. 1, E and F). This indicates that the miR-DKO females can undergo normal oogenesis and ovulate when hormones are supplemented exogenously, which suggests that impaired hormonal regulation prevents these mice from ovulating naturally.

We examined the hormone levels in the sera of wild-type and miR-DKO female mice. Although decreases in follicle-stimulating hormone

(FSH) and estradiol were not apparent, a statistically significant decrease in serum LH, together with a decrease in serum progesterone, was observed in the female miR-DKO mice (Fig. 2, A to D). The serum LH levels in male miR-DKO mice were unaffected and were similar to that of heterozygous mice (fig. S10). Thus, the miR-DKO male mice were fertile, whereas females were infertile. We do not know the reason for this sex-dependent phenotype. Female-specific infertility caused by a decrease in LH secretion was reported for *Ptprn* and *Ptprn2* (dense-core vesicle proteins, which relate to LH secretion) DKO mice (10) and *Lhb*-regulating transcription factor *Egr1* KO mice (11). A decrease in LH protein content in the pituitary of miR-DKO female mice was also demonstrated by immunostaining, whereas tissue sections appeared histologically normal (Fig. 2, E to H, and fig. S11). To examine the integrity of pituitary function in miR-DKO mice,

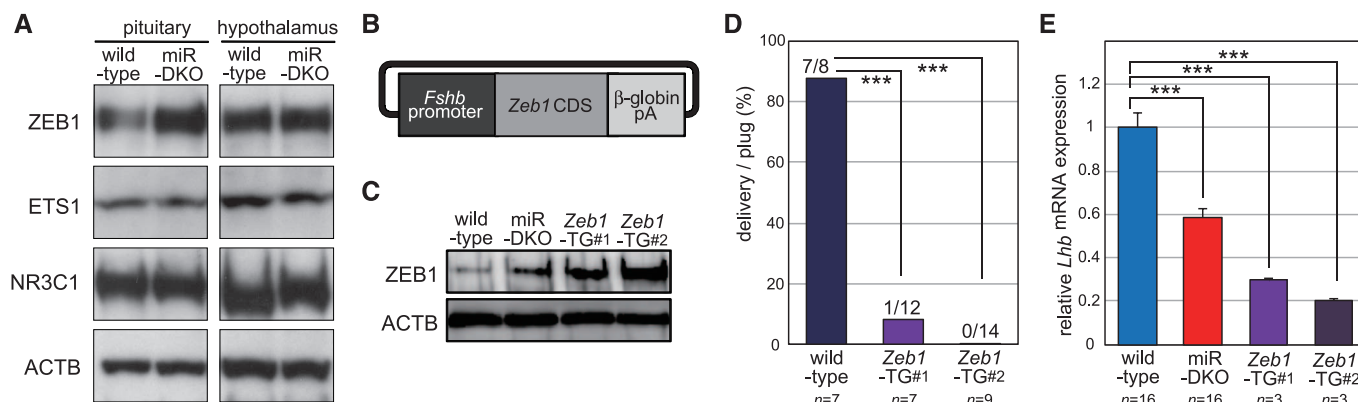


Fig. 3. *Lhb* expression is regulated by ZEB1 as a potential target of miR-200b and miR-429. (A) Total lysates (20 μ g) of pituitary and hypothalamic tissues from wild-type and miR-DKO mice were subjected to Western blotting. Hypothalamic tissue with little miR-200b or miR-429 expression was used as a control. **(B)** The *Zeb1* transgene was constructed with an *Fshb* promoter, *Zeb1* CDS and rabbit β -globin poly(A)⁺ sequence. **(C)** Expression of *Zeb1* in transgenic mouse lines. Western blotting was performed with total lysates (20 μ g)

of pituitaries from each mouse line (*Zeb1*-TG#1 and #2). **(D)** Fecundity of *Zeb1* transgenic females was analyzed by natural mating; *n* indicates the number of female mice used for each genotype. The numbers on the bars indicate litter deliveries per vaginal plug formation. (****P* < 0.001 by Fisher's exact test) **(E)** Expression of *Lhb* in the pituitaries of wild-type, miR-DKO, and *Zeb1*-TG#1 and #2 were analyzed by quantitative reverse transcription polymerase chain reaction (normalized to *Actb*; error bars indicate \pm SEM; ****P* < 0.001).

we analyzed the LH surge induced by an exogenous estradiol administration after ovariectomy (mouse LH surge protocol) (12). Both the basal and estradiol-induced LH release levels were significantly impaired in ovariectomized miR-DKO compared with control mice (Fig. 2I).

We examined the expression of miR-200b and miR-429 in the ovary, hypothalamus, and pituitary (Fig. 2J) by Northern blotting and found a high expression of miRNAs solely in the pituitary. (Kidney was also examined as a high-expression control.) The expression level changed significantly during the estrous cycle, but the absolute values remained within a narrow range (fig. S12). Working on the hypothesis that these miRNAs might act in regulating pituitary function, we searched for their target mRNAs in public databases using a computer algorithm named miGTS (miRNA Global Target Search; developed by Kyowa Hakko Kirin Co., Ltd., Tokyo, Japan). Among the putative target mRNAs listed, the 3'-UTRs of both mouse and human *Zeb1* and *Zeb2* have the highest number of loci that were complementary to the "seed sequence" of miR-200b and miR-429 (table S1).

An in vitro reporter assay allowed us to focus on *Zeb1* as a potential target for miR-200b and miR-429 (fig. S13). Consistent with the in vitro experiments, the amount of ZEB1 in the pituitary increased in miR-DKO females, whereas ZEB1 remained unaffected in the hypothalamus, where the miR-200b and miR-429 expression levels were low (Figs. 2J and 3A). Given that the *Zeb1* mRNA level in the pituitary was not altered by deficiencies in these miRNAs, the amount of ZEB1 must be regulated by a posttranscriptional mechanism (fig. S14). Moreover, the increased level of ZEB1 in miR-DKO mice was decreased to near the wild-type level in the miR-200b and miR-429 transgenic mouse lines (fig. S15). The transcriptional repressor ZEB1 has CACCT-binding ability

(13), and the *Lhb* 5' upstream region has multiple CACCT sites. Therefore, we performed an electrophoretic mobility shift assay (EMSA) and found that ZEB1 bound to at least three sites upstream of *Lhb* (fig. S16). The influence of *Zeb1* on *Lhb* was also confirmed in a clonal gonadotroph L β T2 cell line (14). When *Zeb1* was knocked down by small interfering RNA in L β T2 cells, the *Lhb* mRNA level increased about 80% (fig. S17). The same line of evidence was obtained in vivo. To test the hypothesis that increased ZEB1 expression in the pituitaries of miR-DKO mice might cause LH suppression, we produced transgenic mice overexpressing *Zeb1* under the control of the *Fshb* promoter (Fig. 3, B and C). In transgenic females, the *Lhb* expression was decreased, and the mice were anovulatory as in miR-DKO mice (Fig. 3, D and E, and fig. S18). One possible explanation for the infertility could be the aberrant expression of *Egr1*, but we found no difference in *Egr1* expression between wild-type and miR-DKO pituitaries (fig. S19). Combining these results, it appears that the loss of miR-200b and miR-429 led to an increase in the expression of ZEB1 in the pituitary, resulting in a decrease in *Lhb* expression (fig. S20).

There are reports that miR-200b and miR-429 affect the malignancy of tumors by regulating E-cadherin expression (15, 16). Although susceptibility to oncogenesis was not examined here, the homozygous mutant mice did not show any overt abnormality in organs such as the lung, thymus, or kidney (where miR-200b and miR-429 are highly expressed), and the mice appeared normal during more than a year of observation. Because the miR-200b cluster is also present in humans and the upstream regions of human *LHB* also contain ZEB1-binding sites, the roles of these miRNAs in maintaining normal ovulation in the mouse could also be applicable to human reproductive physiology.

References and Notes

1. D. P. Bartel, *Cell* **116**, 281–297 (2004).
2. A. Grimson *et al.*, *Mol. Cell* **27**, 91–105 (2007).
3. S. Yekta, I. H. Shih, D. P. Bartel, *Science* **304**, 594–596 (2004).
4. W. P. Kloosterman, R. H. Plasterk, *Dev. Cell* **11**, 441–450 (2006).
5. C. Y. Park, Y. S. Choi, M. T. McManus, *Hum. Mol. Genet.* **19**, R169–R175 (2010).
6. M. S. Nicoloso, R. Spizzo, M. Shimizu, S. Rossi, G. A. Calin, *Nat. Rev. Cancer* **9**, 293–302 (2009).
7. M. Lagos-Quintana, R. Rauhut, J. Meyer, A. Borkhardt, T. Tuschl, *RNA* **9**, 175–179 (2003).
8. E. N. Olson, H. H. Arnold, P. W. Rigby, B. J. Wold, *Cell* **85**, 1–4 (1996).
9. D. Rossi *et al.*, *EMBO J.* **20**, 694–702 (2001).
10. A. Kubosaki, S. Nakamura, A. Clark, J. F. Morris, A. L. Notkins, *Endocrinology* **147**, 811–815 (2006).
11. S. L. Lee *et al.*, *Science* **273**, 1219–1221 (1996).
12. C. A. Christian, J. L. Mobley, S. M. Moenter, *Proc. Natl. Acad. Sci. U.S.A.* **102**, 15682–15687 (2005).
13. R. Sekido *et al.*, *Mol. Cell. Biol.* **14**, 5692–5700 (1994).
14. E. T. Alarid, J. J. Windle, D. B. Whyte, P. L. Mellon, *Development* **122**, 3319–3329 (1996).
15. P. A. Gregory *et al.*, *Nat. Cell Biol.* **10**, 593–601 (2008).
16. S. M. Park, A. B. Gaur, E. Lengyel, M. E. Peter, *Genes Dev.* **22**, 894–907 (2008).

Acknowledgments: We thank the late N. B. Hecht for critical reading of the manuscript and Y. Esaki and Y. Maruyama for preparing the KO and TG mice. We also thank T. Miyazawa and T. Yoshida of Kyowa Hakko Kirin Co., Ltd. for analyzing the miRNA target predictions. This work was supported by Ministry of Education, Culture, Sports, Science and Technology of Japan and the Japan Society for the Promotion of Science KAKENHI; grant numbers 20062008, 20700364, 18700397, and 24115710. The miR-DKO mice (RBRC05917) are available from RIKEN BioResource Center with a materials transfer agreement.

Supplementary Materials

www.sciencemag.org/cgi/content/full/science.1237999/DC1
Materials and Methods
Figs. S1 to S21
Tables S1 and S2
References (17–20)

19 March 2013; accepted 23 May 2013
Published online 13 June 2013;
10.1126/science.1237999

A Secreted Disulfide Catalyst Controls Extracellular Matrix Composition and Function

Tal Ilani,^{1*} Assaf Alon,¹ Iris Grossman,¹ Ben Horowitz,¹ Elena Kartvelishvili,² Sidney R. Cohen,³ Deborah Fass^{1*}

Disulfide bond formation in secretory proteins occurs primarily in the endoplasmic reticulum (ER), where multiple enzyme families catalyze cysteine cross-linking. Quiescin sulfhydryl oxidase 1 (QSOX1) is an atypical disulfide catalyst, localized to the Golgi apparatus or secreted from cells. We examined the physiological function for extracellular catalysis of de novo disulfide bond formation by QSOX1. QSOX1 activity was required for incorporation of laminin into the extracellular matrix (ECM) synthesized by fibroblasts, and ECM produced without QSOX1 was defective in supporting cell-matrix adhesion. We developed an inhibitory monoclonal antibody against QSOX1 that could modulate ECM properties and undermine cell migration.

Oxidation of cysteine side chains to form disulfide bonds is a fundamental event during protein folding in the endoplasmic reticulum (ER) (1). However, an additional disulfide catalyst, quiescin sulfhydryl oxidase 1 (QSOX1), is found downstream of the ER in the secretory pathway. QSOX1 is present in glandular secretions (2–4) and induced in (5) and secreted from (6) quiescent cultured fibroblasts. Despite detailed enzymological characterization (7–9) and tissue localization (10–12), the physiological role of QSOX1 remains to be determined (1). More generally, no biological process requiring a catalyst of de novo disulfide formation in the Golgi or extracellular environment is known.

Endogenous QSOX1 was Golgi-localized in various cell types (Fig. 1A and fig. S1A), as ex-

pected (12, 13). QSOX1 secretion, however, was observed only for confluent fibroblasts (Fig. 1B and figs. S1B and S2). Sulfhydryl oxidase activity in fibroblast culture media correlated with QSOX1 transcript and protein levels (Fig. 1C), was not due to the paralogous QSOX2 (Fig. 1D), and reached maximal values comparable to 40 to 50 nM recombinant QSOX1 (rQSOX1) (Fig. 1E) (14).

To address the extracellular biological functions of QSOX1, we depleted the enzyme from WI-38 embryonic lung fibroblasts using small interfering RNA (siRNA) (fig. S3). The most evident outcome was a relative decrease in cell numbers in QSOX1-depleted fibroblast monolayers by day 4 after knockdown (Fig. 2A). While ruling out other causes (fig. S4), we noted the appearance of detached cells in the culture media after day 2 (Fig. 2A). Addition of 50 nM rQSOX1 to the culture media after knockdown both restored cell numbers and prevented cell detachment, but rQSOX1-AA, a catalytically inactive mutant (Fig. 2B and fig. S5), had no effect. By addition of catalase, we ruled out peroxide, the by-product of QSOX1-mediated disulfide formation (Fig. 2B), as the factor required for cell adherence (fig. S6).

Detached QSOX1-depleted cells were viable and readily reattached to control fibroblast monolayers (Fig. 2C), indicating that they retained functional cell adhesion components and pointing to a defective extracellular adhesion platform in QSOX1-knockdown cultures. Indeed, epithelial cells adhered poorly to QSOX1-depleted fibroblast cultures (Fig. 2D). Higher thiol content (i.e., less disulfide formation) was seen in extracellular material of QSOX1-knockdown compared with control cultures (fig. S7). Thus, QSOX1 extracellular disulfide catalysis is involved in a non-cell-autonomous adhesion mechanism.

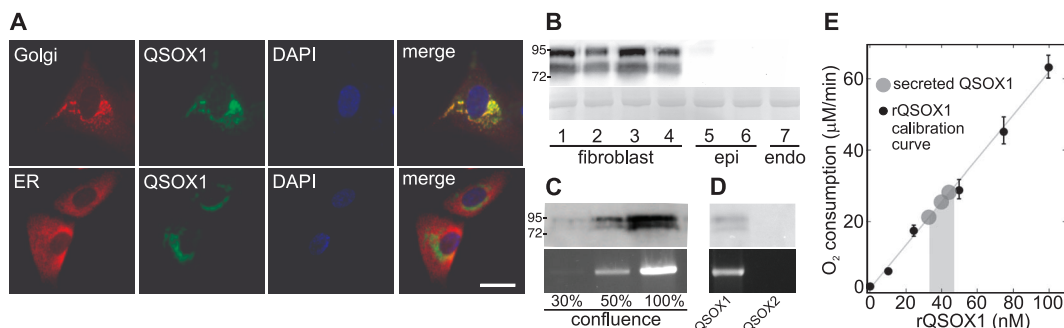
Because quiescent fibroblasts produce copious extracellular matrix (ECM) (15), we examined the dependence of various ECM proteins on QSOX1 for proper assembly. Collagen IV, a major component of WI-38 ECM, appeared normal in quantity and morphology upon QSOX1 knockdown (fig. S8). The fibronectin matrix and a number of other prominent ECM proteins were also unaffected (fig. S8). In contrast, severe defects in ECM incorporation of the key basement membrane component laminin were observed. Specifically, soluble laminin appeared in culture media upon QSOX1 depletion (Fig. 3A), accompanied by a large decrease in laminin within the ECM (Fig. 3B and figs. S9 and S10). Addition of 50 nM rQSOX1, but not rQSOX1-AA, completely reversed the laminin-incorporation defect, demonstrating that sulfhydryl oxidase activity is required for laminin incorporation into the ECM. To locate sites of QSOX1 activity that may contribute to laminin incorporation, extracellular unpaired thiols in QSOX1-depleted cultures were labeled with maleimide-functionalized gold particles and visualized using scanning electron microscopy (SEM). Cultures lacking QSOX1 activity showed heavy gold labeling of defined ECM meshworks, whereas gold was nearly undetected in ECM of control cell cultures (Fig. 3C and fig. S11). Therefore, QSOX1 target cysteines are located in the ECM itself rather than on putative laminin scaffolding sites on the cell membrane.

¹Department of Structural Biology, Weizmann Institute of Science, Rehovot 76100, Israel. ²The Irving and Cherna Moskowitz Center for Nano and Bio-Nano Imaging, Weizmann Institute of Science, Rehovot 76100, Israel. ³Department of Chemical Research Support, Weizmann Institute of Science, Rehovot 76100, Israel.

*Corresponding author. E-mail: tal.ilani@weizmann.ac.il (T.I.); deborah.fass@weizmann.ac.il (D.F.)

Fig. 1. Localization and secretion of QSOX1.

(A) Subconfluent WI-38 fibroblasts immunostained with Golgi-specific (p115) or ER-specific (calnexin) antibody (red) and QSOX1 antibody (green). DAPI (4',6-diamidino-2-phenylindole) staining (blue) indicates nuclei. Scale bar, 20 μ m. (B) (Top) QSOX1 immunoblot of supernatants from confluent fibroblast, epithelial (epi), and endothelial (endo) cell cultures. 1, WI-38; 2, human foreskin fibro-



blasts; 3, pancreatic cancer-associated fibroblasts; 4, hTERT-immortalized WI-38 fibroblasts; 5, primary human mammary epithelial cells; 6, H460 large-cell lung carcinoma; 7, primary human umbilical vein endothelial cells. Molecular weight indicated in kD. (Bottom) Coomassie-stained load control. (C) QSOX1 immunoblot of WI-38 culture supernatants (top) and QSOX1 polymerase chain reaction (PCR) product from WI-38 total RNA

(bottom) as a function of confluence. (D) Immunoblot of confluent WI-38 cell extracts (top) and PCR (bottom) demonstrate expression of QSOX1 but not QSOX2. (E) Sulfhydryl oxidase activity in culture supernatants measured by oxygen consumption. The calibration curve (black circles) was obtained using the indicated rQSOX1 concentrations. Gray circles are rates for three supernatant samples from confluent WI-38 cultures.

Laminin is secreted as a cross-shaped heterotrimer. Each laminin subunit, known as α , β , and γ , has multiple isoforms (16), combinations of

which produce trimers with different assembly properties and perhaps functions (17). A significant fraction of unincorporated laminin from

QSOX1-knockdown cultures was found in a trimeric complex (Fig. 3D), suggesting that QSOX1 is required not for forming laminin heterotrimers

Fig. 2. Active QSOX1 is required for cell adherence to a monolayer. (A) (Top) DAPI staining of WI-38 cells after transfection with control (siCONTROL) or QSOX1-specific (siQSOX1) siRNA. Where indicated, siQSOX1 cultures were supplemented with 50 nM rQSOX1 or inactive mutant rQSOX1-AA. Scale bar, 20 μ m. (Bottom left) Average cell numbers from 30 fields. (Bottom center and right) Total adherent and detached cells per well counted by flow cytometry. (B) Diagram of QSOX1 domain structure. Paired yellow balls represent redox-active disulfides. FAD, flavin adenine dinucleotide cofactor. Alternative splicing (jagged vertical line) generates either soluble or membrane-anchored (TM, transmembrane) QSOX1. H_2O_2 is a by-product of the disulfide formation mechanism. (C) Detached, red fluorescently labeled QSOX1-depleted fibroblasts readhered to control WI-38 monolayers. QSOX1 in the recipient monolayer is immunostained in green. Left panels highlight a readhered, QSOX1-depleted cell (arrows). Right panel demonstrates the general lack of QSOX1 in readhered cells, with exceptions indicated (arrowheads). Scale bars in left and right panels are 20 and 50 μ m, respectively. (D) Fluorescently labeled HEK293 epithelial cells

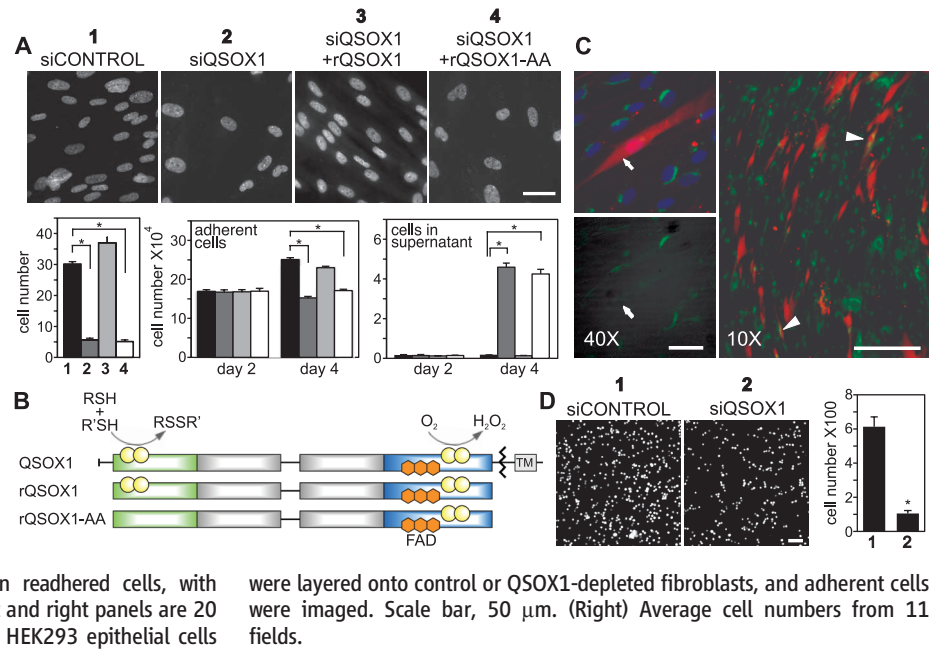
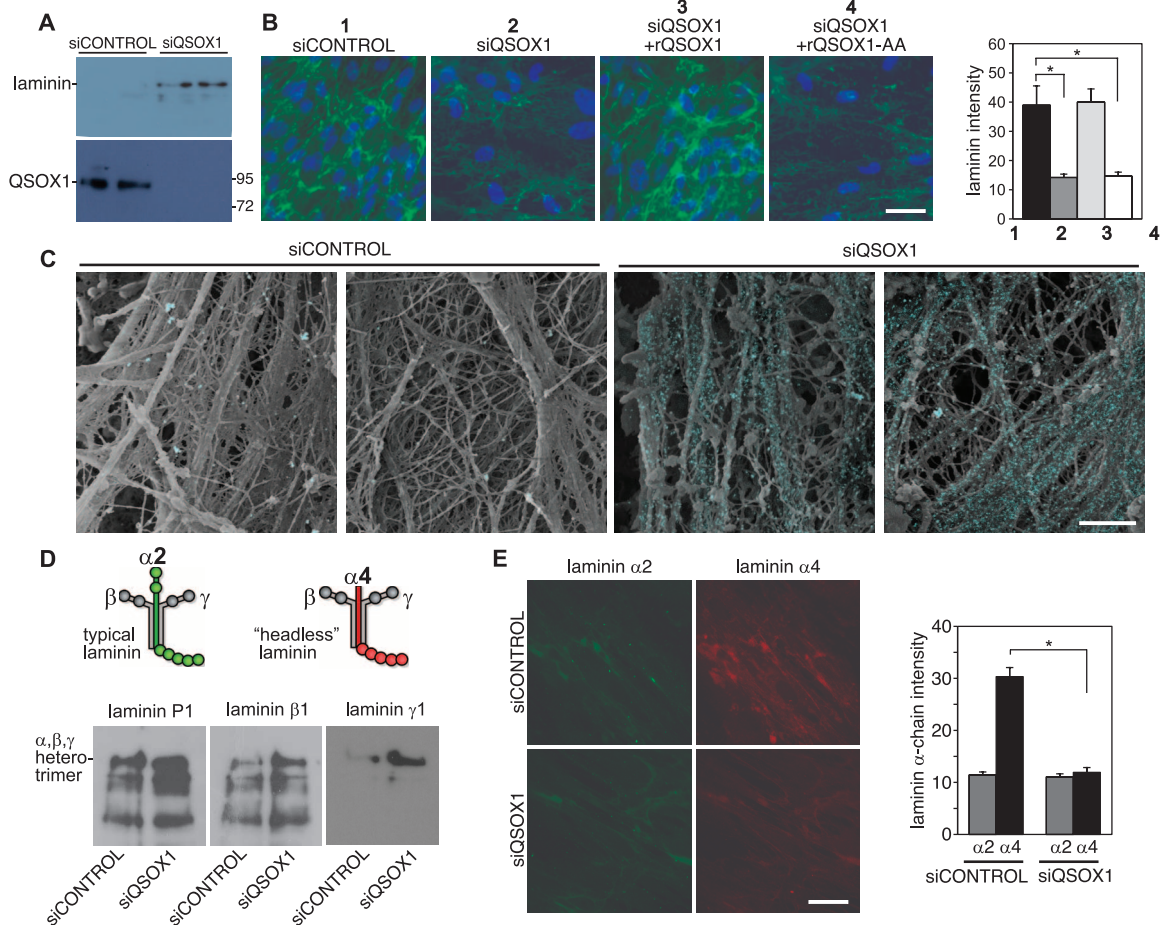
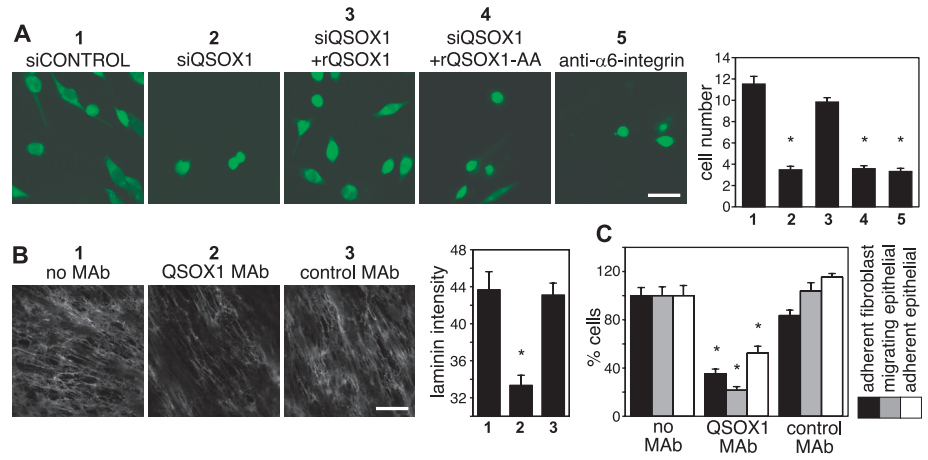


Fig. 3. QSOX1 is required for laminin incorporation into ECM. (A) Immunoblot of laminin (top) and QSOX1 (bottom) in WI-38 culture supernatants. Molecular weight is indicated in kD. (B) Immunostaining using P1 polyclonal antibody revealed a more substantial laminin matrix (green) in siCONTROL compared with siQSOX1 WI-38 cultures. Supplementation with rQSOX1, but not the rQSOX1-AA mutant, restored the thick laminin matrix. DAPI staining (blue) indicates nuclei. Scale bar, 20 μ m. Right, quantification of laminin intensity. (C) SEM images of ECM in fibroblast monolayers labeled with maleimide-functionalized gold. Back-scattering from gold (false colored in cyan) is superposed. Scale bar, 500 nm. (D) (Top) Illustration of laminin trimers containing $\alpha 2$ and $\alpha 4$ chains. (Bottom) Immunoblots of laminin in culture supernatants using P1 antibody or antibodies specific for laminin subunits $\beta 1$ or $\gamma 1$. (E) Immunostaining of siCONTROL and siQSOX1 WI-38 fibroblast cultures with laminin subunit-specific ($\alpha 2$ or $\alpha 4$) antibodies. Scale bar, 20 μ m. (Right) Quantification of laminin chain intensity.



(E) Immunostaining of siCONTROL and siQSOX1 WI-38 fibroblast cultures with laminin subunit-specific ($\alpha 2$ or $\alpha 4$) antibodies. Scale bar, 20 μ m. (Right) Quantification of laminin chain intensity.

Fig. 4. QSOX1 inhibition blocks tumor cell migration. (A) (Left) Fluorescently labeled H460 lung cancer cells that crossed a preformed stromal layer of WI-38 fibroblasts subjected to the indicated treatments. Recombinant enzymes (rQSOX1 and rQSOX1-AA) were added after transfection of fibroblasts. As a positive control, H460 cells were treated with antibody that blocks activity of $\alpha 6$ integrin, a laminin receptor, before layering onto control fibroblasts. Scale bar, 20 μ m. (Right) Quantification of migratory cells. (B) Immunostaining of laminin in untreated WI-38 fibroblasts or fibroblasts treated with QSOX1 inhibitory or control monoclonal antibody. Scale bar, 20 μ m. (Right) Quantification of laminin intensity from 15 fields. (C) WI-38 fibroblasts in monolayer (black), epithelial cells that migrated through a preformed stromal layer of WI-38 fibroblasts (gray), and epithelial cells remaining adherent to a fibroblast layer after subsection to force (white) after pretreatment of fibroblasts with QSOX1 inhibitory or control antibody, as a percentage of control (no monoclonal antibody) values.



but for integration of assembled trimers into the ECM. Isotype-specific antibodies were selected based on the major laminin transcripts produced by WI-38 fibroblasts (table S1), and QSOX1 depletion was shown to result in disappearance of a meshwork containing $\alpha 4$ laminin, whereas $\alpha 2$ levels in the ECM were unchanged (Fig. 3E). Thus, multiple laminin matrices coexist within fibroblast ECM (figs. S12 and S13), differing in their requirement of QSOX1 for assembly.

The contribution of laminin to tumor progression (18), coupled with up-regulation of both the QSOX1 and LAMA4 (encoding laminin $\alpha 4$) transcripts in stromal cells surrounding invasive breast carcinomas (19), prompted us to investigate whether QSOX1 activity in ECM assembly contributes to tumor cell migration. We found that lung cancer cell migration across a preformed layer of WI-38 fibroblasts and their associated ECM (fig. S14A) was severely attenuated when QSOX1 was depleted during formation of the fibroblast layer (Fig. 4A). Subsequent tumor cell migration was re-established when QSOX1-depleted fibroblasts were supplemented with 50 nM rQSOX1, but not rQSOX1-AA, during ECM deposition. Similar results were obtained using paired pancreatic fibroblasts and epithelial cells (fig. S14B), indicating the generality of QSOX1 catalytic activity in construction of promigratory ECM. Although QSOX1-depleted fibroblast monolayers were more elastic than controls (fig. S15), suggesting greater penetrability, their failure to support migration is consistent with the known role of laminin in integrin-mediated adhesion, a prerequisite for tumor metastasis (18, 20).

QSOX1 inhibition may therefore be a strategy to control ECM functionality. We developed an inhibitory monoclonal antibody against QSOX1 (fig. S16), designated MAb492.1. When MAb492.1 was supplied to WI-38 fibroblasts, less laminin was found in ECM produced by these cells (Fig. 4B), and fewer fibroblasts were present in the culture monolayer (Fig. 4C). Finally, a major drop in cell adhesion to and migration through

the fibroblast layer were observed when the QSOX1 inhibitory antibody was added to the growing fibroblasts (Fig. 4C). Thus, blocking extracellular QSOX1 activity can modulate the architecture and properties of the ECM (fig. S17). Notably, peptides derived from QSOX1 are over-represented in the serum of pancreatic cancer patients (21), suggesting an increase in extracellular QSOX1 in this disease state.

Here, we addressed the physiological function of QSOX1, a disulfide catalyst isolated more than three decades ago (4) and recently linked to human disease (21–23). Both QSOX1 and fundamental components of basement membrane ECM such as laminin arose near the base of the metazoan branch of the evolutionary tree (24, 25). A role for secreted QSOX1 in laminin assembly suggests that QSOX enzymes may have contributed to the initial organization of multicellular organisms and may have acquired important functions during development in complex animals. In normal development, laminin guides cell migration (26), and under pathological conditions it lines metastatic niches and contributes to adhesive interactions required for tumor cell invasion (20, 27). QSOX1 enzymatic activity potentially provides a handle with which to modulate ECM assembly and function in this context.

References and Notes

- N. J. Bulleid, L. Ellgaard, *Trends Biochem. Sci.* **36**, 485 (2011).
- V. G. Janolino, H. E. Swaisgood, *J. Biol. Chem.* **250**, 2532 (1975).
- M. C. Ostrowski, W. S. Kistler, *Biochemistry* **19**, 2639 (1980).
- M. C. Ostrowski, W. S. Kistler, H. G. Williams-Ashman, *Biochem. Biophys. Res. Commun.* **87**, 171 (1979).
- D. L. Coppock, C. Kopman, S. Scandalis, S. Gilleran, *Cell Growth Differ.* **4**, 483 (1993).
- D. Coppock, C. Kopman, J. Gudas, D. A. Cina-Poppe, *Biochem. Biophys. Res. Commun.* **269**, 604 (2000).
- K. L. Hooper, B. Jones, H. B. White 3rd, C. Thorpe, *J. Biol. Chem.* **271**, 30510 (1996).
- E. J. Heckler, A. Alon, D. Fass, C. Thorpe, *Biochemistry* **47**, 4955 (2008).
- A. Alon et al., *Nature* **488**, 414 (2012).

- K. F. Portes et al., *J. Mol. Histol.* **39**, 217 (2008).
- A. Tury et al., *Cell Tissue Res.* **323**, 91 (2006).
- G. Mairet-Coello, A. Tury, D. Fellmann, P. Y. Risold, B. Griffond, *J. Comp. Neurol.* **484**, 403 (2005).
- S. Chakravarthi, C. E. Jessop, M. Willer, C. J. Stirling, N. J. Bulleid, *Biochem. J.* **404**, 403 (2007).
- Materials and methods are available as supplementary materials on Science Online.
- J. M. S. Lemons et al., *PLoS Biol.* **8**, e1000514 (2010).
- K. J. Hamill, K. Kligis, S. B. Hopkinson, J. C. Jones, *J. Cell Sci.* **122**, 4409 (2009).
- P. D. Yurchenco, *Cold Spring Harb. Perspect. Biol.* **3**, a004911 (2011).
- V. Givant-Horwitz, B. Davidson, R. Reich, *Cancer Lett.* **223**, 1 (2005).
- G. Finak et al., *Nat. Med.* **14**, 518 (2008).
- M. Patarroyo, K. Tryggvason, I. Virtanen, *Semin. Cancer Biol.* **12**, 197 (2002).
- K. Antwi et al., *J. Proteome Res.* **8**, 4722 (2009).
- B. A. Katchman et al., *Mol. Cancer Res.* **9**, 1621 (2011).
- M. Soloviev, M. P. Esteves, F. Amiri, M. R. Crompton, C. C. Rider, *PLoS ONE* **8**, e57327 (2013).
- K. Limor-Waisberg, S. Ben-Dor, D. Fass, *BMC Evol. Biol.* **13**, 70 (2013).
- R. O. Hynes, *J. Cell Biol.* **196**, 671 (2012).
- A. Domogatskaya, S. Rodin, K. Tryggvason, *Annu. Rev. Cell Dev. Biol.* **28**, 523 (2012).
- N. E. Reticker-Flynn et al., *Nat. Commun.* **3**, 1122 (2012).

Acknowledgments: Y. Yarden provided valued advice and guidance throughout this project. We also thank V. Rotter, S. Feigelson, R. Alon, G. Shakhbar, N. Friedman, M. Oren, and B. Geiger for reagents and advice. O. Leitner, Z. Landau, and H. Hamawi from the Weizmann Institute Antibody Unit performed technical aspects of antibody production. T. Mehlman provided mass spectrometry service. K. Shakhbar provided statistics support. This work was supported by the Israel Science Foundation, Israel Cancer Association, Abisch-Frenkel Foundation, Kimmelman Center for Macromolecular Assemblies, and European Research Council under the European Union's Seventh Framework Programme (ERC grant agreement 310649). T.I., A.A., I.G., and D.F. have applied for a patent concerning the QSOX1 inhibitory antibody and its use in modulating assembly of laminin in the basement membrane.

Supplementary Materials

www.sciencemag.org/cgi/content/full/science.1238279/DC1
Materials and Methods
Figs. S1 to S17
Table S1
References (28–35)

25 March 2013; accepted 10 May 2013
Published online 23 May 2013;
10.1126/science.1238279

Structure of the Repulsive Guidance Molecule (RGM)–Neogenin Signaling Hub

Christian H. Bell,^{1*} Eleanor Healey,^{1†} Susan van Erp,^{2†} Benjamin Bishop,¹ Chenxiang Tang,^{1‡} Robert J.C. Gilbert,¹ A. Radu Aricescu,¹ R. Jeroen Pasterkamp,² Christian Siebold^{1§}

Repulsive guidance molecule family members (RGMs) control fundamental and diverse cellular processes, including motility and adhesion, immune cell regulation, and systemic iron metabolism. However, it is not known how RGMs initiate signaling through their common cell-surface receptor, neogenin (NEO1). Here, we present crystal structures of the NEO1 RGM-binding region and its complex with human RGMB (also called dragon). The RGMB structure reveals a previously unknown protein fold and a functionally important autocatalytic cleavage mechanism and provides a framework to explain numerous disease-linked mutations in RGMs. In the complex, two RGMB ectodomains conformationally stabilize the juxtamembrane regions of two NEO1 receptors in a pH-dependent manner. We demonstrate that all RGM-NEO1 complexes share this architecture, which therefore represents the core of multiple signaling pathways.

The repulsive guidance molecule (RGM) family has three major, membrane-attached members: RGMA, RGMB (dragon), and RGMC (hemojuvelin, HFE2). Their functions span biological phenomena ranging from cell

motility and adhesion (e.g., axon guidance, neural tube closure, and leucocyte chemotaxis) to immune cell regulation and systemic iron metabolism (1–5). Abnormal RGM expression or function has been linked to regenerative failure;

inflammation (3); and diseases such as multiple sclerosis (6), cancer (7), and juvenile hemochromatosis (JHH) (5). All RGMs bind directly to the cell surface receptor neogenin (NEO1) (8), triggering structural rearrangements of the actin cytoskeleton through the Rho family of small guanosine-5'-triphosphate (GTP)-hydrolyzing GTPases that mediate cell repulsion (1, 9, 10). RGM binding to NEO1 activates the bone morphogenetic protein (BMP)-regulated signaling involved in morphogenesis and iron homeostasis (11–14).

Human RGMs contain an Arg-Gly-Asp (RGD) motif (conserved in RGMA and RGMC), which is important for integrin-mediated adhesive function (15), and a region homologous to the von

¹Division of Structural Biology, Wellcome Trust Centre for Human Genetics, University of Oxford, Roosevelt Drive, Oxford OX3 7BN, UK. ²Department of Neuroscience and Pharmacology, Rudolf Magnus Institute of Neuroscience, University Medical Center Utrecht, CG Utrecht 3584, Netherlands.

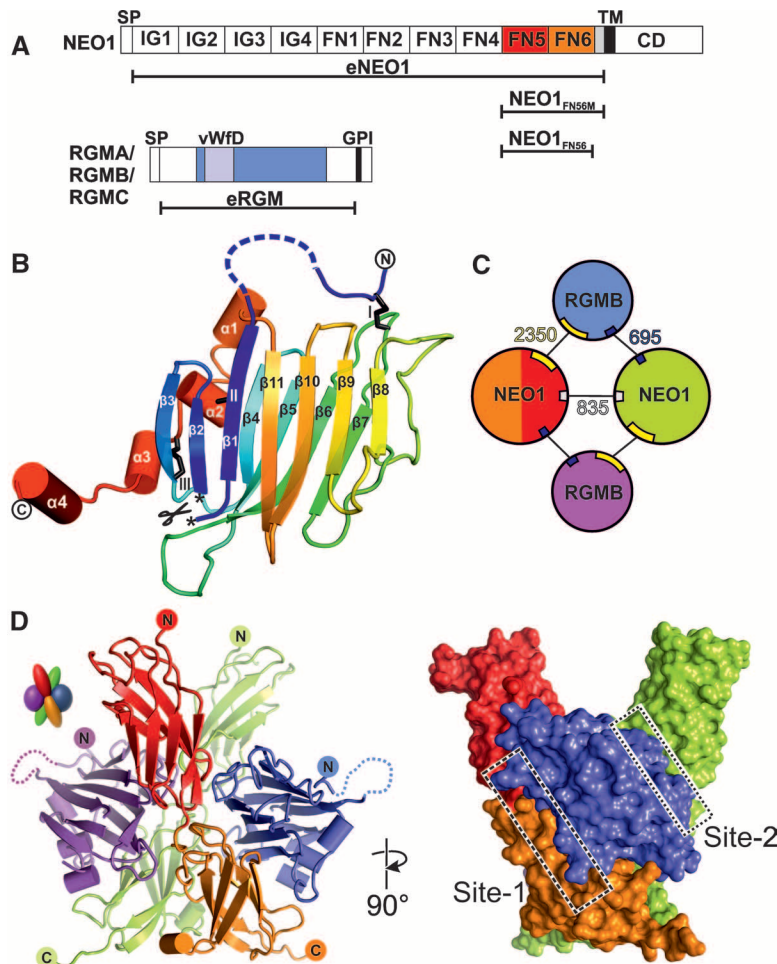
*Present address: Roche Diagnostics GmbH, Nonnenwald 2, 82377 Penzberg, Germany.

†These authors contributed equally to this work.

‡Present address: Molecular Biophysics and Biochemistry Department, Yale University, 260 Whitney Avenue, New Haven, CT 06520-8114, USA.

§Corresponding author. E-mail: christian@strubi.ox.ac.uk

Fig. 1. Structure of the RGMB-NEO1 complex. (A) Schematic of NEO1 and RGMs. SP indicates signal peptide; IG, Ig-like C2-type 1; TM, transmembrane; CD, C-terminal domain; GPI, glycosylphosphatidylinositol anchor; and vWFD, von Willebrand factor D domain-like. (B) eRGMB ribbon diagram in rainbow coloring (blue, N terminus, red, C terminus). Disulfides (black sticks) are depicted with roman numerals. The autocatalytic cleavage site is marked with asterisks. (C) Schematics of the 2:2 RGMB-NEO1 complex. RGMB is blue and violet; NEO1 is red (FN5), orange (FN6), and green. Interface-buried surface areas (\AA^2) are shown. (D) Ribbon (left) and surface representation of the 2:2 eRGMB-NEO1_{FN56} complex. Site-1 and site-2 interfaces are highlighted with boxes. Color coding is as in (C). Right image is 90° rotated around the y axis compared with the left representation.



Willebrand factor type D (vWfD) domain, which contains an autocatalytic Gly-Asp-Pro-His cleavage site (1, 16) (Fig. 1A). NEO1 is a type-I transmembrane protein of the immunoglobulin (Ig) receptor superfamily related to the netrin-1 receptor DCC (deleted in colorectal cancer) (17, 18). Its extracellular region consists of four Ig domains followed by six fibronectin type III (FN) domains and 50 juxtamembrane residues that are predicted to be unstructured. The cytoplasmic region comprises three conserved motifs (P1, P2, and P3) containing several phosphorylation sites and is required for receptor oligomerization of DCC (18, 19). FN domains five and six contain the binding site for RGMs (20). However, the molecular mechanisms underlying extracellular RGM reception by NEO1 and the mode of signal transduction across the membrane are not known.

We solved a series of crystal structures of the fifth and sixth FN domains of NEO1 (NEO1_{FN56}) in complex with the ectodomain of RGMB (eRGMB) (Fig. 1A, fig. S1, and table S1). In all of the NEO1-RGMB complexes, only the middle domain of RGMB (residues 134 to 338) could be resolved unequivocally. This domain represents a previously unknown protein fold consisting of a tightly packed β sandwich (Fig. 1B and fig. S2) extended by four short helices at the C terminus. The N and C termini, linked to the β sandwich by three disulfide bonds (fig. S3), point in opposite directions and into the solvent channels of the crystal, suggesting that the N- and C-terminal regions, which were disordered in the crystal, are flexible and do not associate with the middle domain. The autocatalytic cleavage site between Asp¹⁶⁸-Pro¹⁶⁹ is located in the loop connecting β sheets 1 and 2 (Fig. 1B and figs. S3A and S4) and is conserved in all RGM family members (fig. S3A). Asp-Pro bonds are hydrolyzed in low pH environments, for example, in the Golgi and secretory vesicles (21). This autocatalytic cleavage allows Pro¹⁶⁹ to be deeply buried in the protein core (fig. S4A). Seven out of the 14 RGMC disease mutations leading to JHH (5, 22, 23), a severe iron-overload condition, cluster at the cleavage site (fig. S5). Ten of these map onto the β sandwich (fig. S5A) and abolish protein secretion in mammalian cells (fig. S5B). These include Asp to Glu at position 172 (Asp172Glu^{RGMC}) from the cleavage site itself (figs. S4 and S5), highlighting the importance of autocatalytic cleavage for the structural integrity of the middle domain and indeed the entire protein.

The eRGMB-NEO1_{FN56} complex structure determined at neutral pH [(24), fig. S6, and table S1] has a 2:2 stoichiometry and exhibits twofold symmetry with both NEO1 C-termini oriented in the same direction (Fig. 1, C and D), as observed in two independent crystal forms (fig. S6). Each RGMB molecule acts as a staple, bringing two NEO1 receptors together with one major interaction site (site 1) and a minor site (site 2) (Fig. 1, C and D), positioning the NEO1 C-termini in close proximity to each other (Fig. 1C). Whereas

the two NEO1 molecules in the complex contact each other, the two RGMB molecules do not. Most of the site-1 contacts are formed between RGMB and the FN6 domain of NEO1, with the remainder of the interface made by the L3 loop of NEO1-FN5 (Fig. 2, A to C). The JHH-linked RGMC mutation Gly320Val^{RGMC}, which cannot interact with NEO1 anymore (25), is located close to the site-1 interface (fig. S5D), thereby confirming the importance of the RGMB-NEO1 site-1 interface. We also solved three independent crystal structures of NEO1_{FN56} alone (table S1). Together with a previously reported NEO1 structure (26), these reveal flexibility or disorder of the L3 loop as well as variation in the relative orientation of the FN5 and FN6 domains, in contrast to the rigidity of the NEO1 molecules in the RGMB complex structures (fig. S7). The site-2 interaction between RGMB and the neighboring NEO1 molecule (Fig. 2D and fig. S8) has a buried surface area one-fourth the size of site 1 (Fig. 1C). Therefore, the site-1 interaction is likely to be the driving force for the RGM-NEO1 complex formation, whereas site 2 has a supporting role because of its shallow geometry and predominantly hydrophobic nature.

Surface plasmon resonance (SPR) measurements revealed nanomolar equilibrium dissociation constants between the full-length ectodomains of NEO1 (eNEO1) and RGMA, RGMB, and RGMC, respectively (Fig. 3A and fig. S8). Furthermore, the truncated NEO1_{FN56} and NEO1_{FN56M} constructs (Fig. 1A) were necessary and sufficient for the RGM interaction [Fig. 3B, fig. S9, and (20)]. Site-directed mutagenesis of site-1 interface residues abolished or severely impaired the NEO1-RGM interaction, validating the observed binding mode (Fig. 3C and figs. S9 and S10). Mutations in the L3 loop of NEO1-FN5 and the corresponding RGMB surface did not abolish binding, consistent with NEO1-FN5 being important but not essential for interaction with RGMs. Unlike the majority of site-1 residues, the L3 loop residues are not conserved between NEO1 and DCC, possibly explaining why no binding between RGMs and DCC was observed in immunoprecipitation experiments (8, 25). Indeed, the interaction between RGMA, RGMB, or RGMC and the full-length DCC ectodomain was one-thousandth that observed for the equivalent NEO1 construct (fig. S11).

To test whether the RGMB-NEO1 complex observed in the crystal structures exists in

Fig. 2. Detailed interactions of the RGMB-NEO1 complex. Color coding is as Fig. 1D. (A) Ribbon representation of the RGMB-NEO1 site-1 complex. The L3 loop of NEO1 is marked. (B and C) Open-book view showing the solvent-accessible surface of the site-1 interface (formed by 17 hydrogen bonds and 147 nonbonded contacts). (B) Interface residues (I, Ile; L, Leu; Q, Gln; T, Thr). Cyan, hydrophilic interactions; yellow, nonbonded contacts. Residues tested by site-directed mutagenesis and functional experiments are labeled. (C) Residue conservation (from nonconserved, white, to conserved, black) based on sequence alignments from vertebrate NEO1 and RGM family members. (D) Ribbon representation of the RGMB-NEO1 site-2 complex. The site-2 interaction uses the RGMB β 5- β 6 and β 10- β 11 loop regions contacting the NEO1 FN5 and FN6 domains. K, Lys; V, Val.

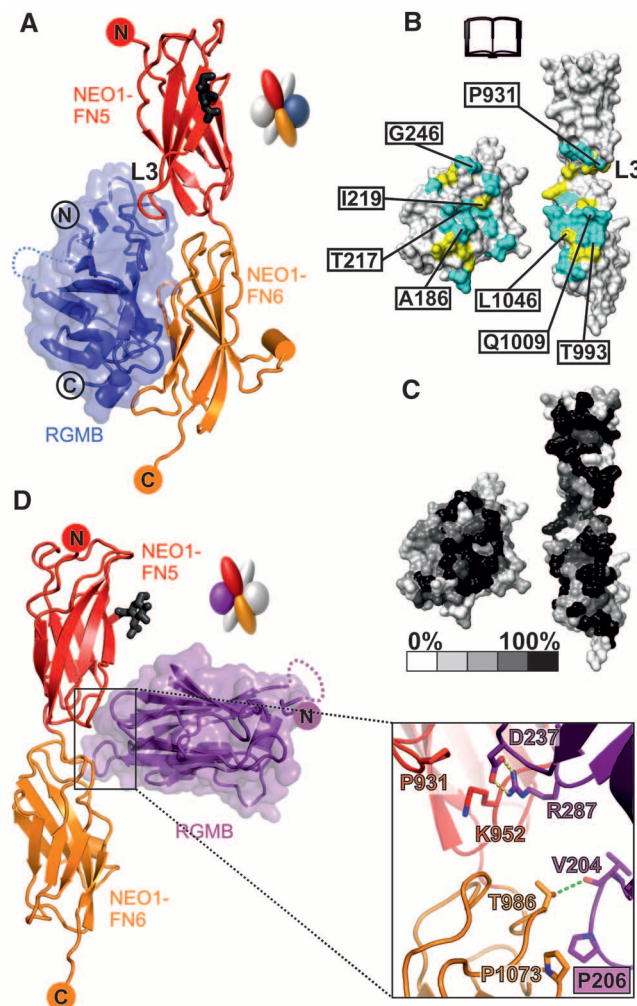
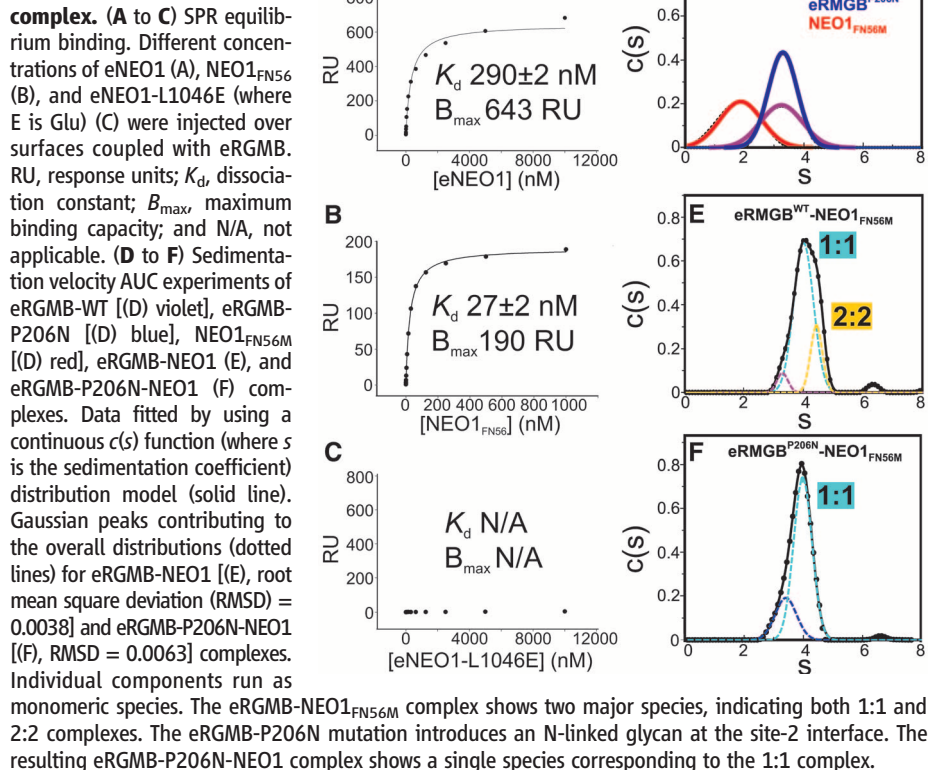


Fig. 3. Biophysical characterization of the RGMB-NEO1 complex.



Data fitted by using a continuous $c(s)$ function (where s is the sedimentation coefficient) distribution model (solid line). Gaussian peaks contributing to the overall distributions (dotted lines) for eRGMB-NEO1 [(E), RMSD = 0.0038] and eRGMB-P206N-NEO1 [(F), RMSD = 0.0063] complexes. Individual components run as monomeric species. The eRGMB-NEO1_{FN56M} complex shows two major species, indicating both 1:1 and 2:2 complexes. The eRGMB-P206N mutation introduces an N-linked glycan at the site-2 interface. The resulting eRGMB-P206N-NEO1 complex shows a single species corresponding to the 1:1 complex.

solution, we performed multiangle light scattering (MALS) measurements of purified proteins. At concentrations up to 3 μ M, we observed a 1:1 RGMB-NEO1 complex (fig. S12A). Sedimentation velocity analytical ultracentrifugation (AUC), allowing exploration of higher concentrations of eRGMB and NEO1_{FN56M} (up to 90 μ M), revealed that the individual components were monomeric (Fig. 3D), and the RGMB-NEO1 mixture showed both a major species, corresponding to the 1:1 stoichiometry, and a higher-order oligomer, likely the 2:2 complex (Fig. 3E). A mutation of RGMB-Pro²⁰⁶ to asparagine in the site-2 interface (Fig. 2D), introducing an N-linked glycan, abolished the larger oligomer (Fig. 3F). The same AUC experiment performed with wild-type proteins at pH = 4.5 revealed only the 1:1 complex (fig. S12, B and C), suggesting that the site-2 interface is pH sensitive. This is in agreement with our structural data, because in a crystal form grown at pH = 4.5 to 5.0 (fig. S6C) the site-2 interface is absent, whereas site-1 is essentially identical to the neutral pH crystal form (fig. S7).

To explore the physiological relevance of the 2:2 oligomeric arrangement, we assessed the effect of RGMB mutants in neuronal explant cultures. Binding of RGMBs to NEO1 inhibits neurite outgrowth from cerebellar granule neurons (CGNs) (27). To assess the functional consequences of site-1 and site-2 RGMB mutants, we cultured postnatal mouse CGN explants on substrates of control, RGMB-A186R (site-1 mutant with Ala changed to Arg at position 186), RGMB-P206N (site-2 mutant with Pro changed to Asn at position 206), and RGMB-WT (wild-type) proteins. As previously shown, neurite outgrowth was reduced on coverslips coated with RGMB-WT compared with control substrate (Fig. 4, A and B, and fig. S13). This inhibitory effect was not observed in neurons grown on RGMB-A186R and was reduced but not abolished by RGMB-P206N (Fig. 4 and fig. S13). These results support a functional role for RGMB-NEO1 interactions mediated through site-1 and to a lesser extent through site-2.

To investigate the RGMB-NEO1 complex stoichiometry within a cellular context, we coexpressed full-length NEO1 tagged with either a His⁶ or 1D4 tag in human embryonic kidney 293T cells. We found that a specific antibody against NEO1-1D4 was able to coimmunoprecipitate NEO1-His⁶, indicating the presence of high-affinity NEO1 oligomers in the cellular lysate (fig. S14). This result suggests that NEO1 molecules may also be present in an RGM-independent, preclustered form at the cell surface.

The 2:2 stoichiometry of the RGM-NEO1 ectodomains may facilitate a common mechanism based on ligand-dependent receptor stabilization of NEO1 dimers within supramolecular signaling clusters (Fig. 4, C and D). Activation of the small GTPase RhoA and its downstream effectors Rho kinase and protein kinase C is a direct consequence of RGM-NEO1 interaction (9, 28). NEO1 can also interact with netrin-1 (NET1) (8), which

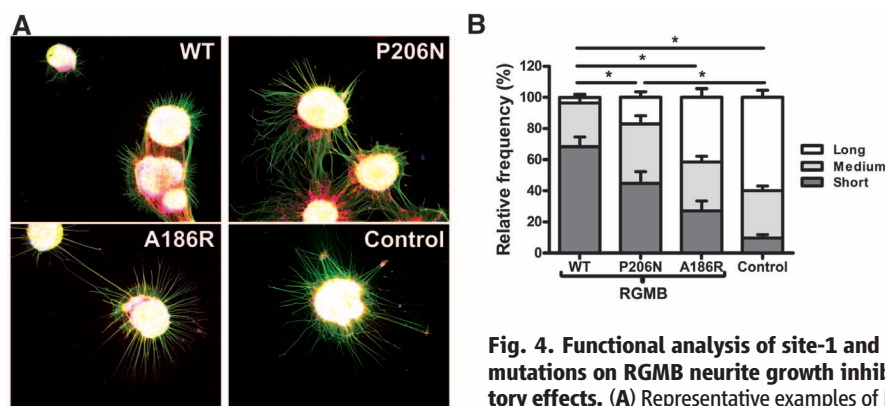


Fig. 4. Functional analysis of site-1 and -2 mutations on RGMB neurite growth inhibitory effects. (A) Representative examples of P9 mouse CGN explants on coverslips coated with RGMB-WT (top left), site-2 mutant RGMB-P206N (top right), site-1 mutant RGMB-A186R (bottom left), or control (bottom right) proteins. Green, β -tubulin; red, F-actin; blue, nuclei. (B) Quantification of CGN neurite outgrowth. Distribution of neurite length (short, medium, and long) relative to the control is displayed (total number of explants analyzed for WT, $n = 27$; P206N, $n = 24$; A186R, $n = 26$; control $n = 23$; error bars are SEM, and $*P < 0.01$). (C) Model of trans RGMB-NEO1 signaling. RGM ectodomains can be shed by proteolytic or phospholipase activity (open triangle). RGM-binding to preclustered NEO1 results in formation of NEO1 dimers with

a defined, signaling-compatible orientation that may be part of a supramolecular clustered state. This arrangement leads to activation of downstream signaling via RhoA (9) (gray lightning bolt). NET1 can inhibit RGM signaling by either simultaneous NEO1 binding or competing with the RGM-NEO1 interaction. The gray box highlights the RGM-NEO1 signaling hub observed in the crystal structure.

functionally competes with RGMA, suppressing growth cone collapse in dorsal root ganglion axons (9). The NET1 binding site on the NEO1-related receptor DCC minimally involves the interface between its FN domains 4 and 5, including loop 5 of FN5 (29) occupied by a sucrose octasulphate (SOS) molecule in our apo-NEO1 structure (fig. S7B). This region, which borders the RGM interaction interface, is strictly conserved in NEO1 and DCC (fig. S3B), so NET1 might occupy the same position in NEO1, impairing the formation of an active 2:2 RGM-NEO1 complex and thus explaining the ability of NET1 to reduce RGM-induced growth cone collapse (Fig. 4C). An additional level of signaling control may be related to the subcellular localization of the RGM-NEO1 complex. The neutral pH at the cell surface allows an active 2:2 stoichiometry, whereas internalization and gradual acidification of the milieu promotes dissociation of the complex and signal termination. Such a signaling mechanism might prevent premature activation and allow dissociation upon internalization when RGM, NEO1, and associated proteins are expressed on the same cell.

Although diversity in the signaling triggered at downstream levels in a cell- and tissue-specific manner can be expected, our experimental evidence coupled with sequence conservation suggests that all RGM family members engage NEO1 in a similar way. Molecular details of the direct cross-talk between different receptors in signaling “supercomplexes,” such as RGM-NEO1-BMP ligand-BMP receptors (12–14), remain to be determined. However, we predict that the RGM-stapled NEO1 dimer provides a mode of pH-

dependent organization, which forms the signaling hub common to multiple extracellular guidance cues and morphogens.

References and Notes

- P. P. Monnier *et al.*, *Nature* **419**, 392–395 (2002).
- V. Niederkofler, R. Salie, M. Sigrist, S. Arber, *J. Neurosci.* **24**, 808–818 (2004).
- V. Mirakaj *et al.*, *Proc. Natl. Acad. Sci. U.S.A.* **108**, 6555–6560 (2011).
- Y. Xia *et al.*, *J. Immunol.* **186**, 1369–1376 (2011).
- G. Papanikolaou *et al.*, *Nat. Genet.* **36**, 77–82 (2004).
- R. Muramatsu *et al.*, *Nat. Med.* **17**, 488–494 (2011).
- V. S. Li *et al.*, *Gastroenterology* **137**, 176–187 (2009).
- S. Rajagopalan *et al.*, *Nat. Cell Biol.* **6**, 756–762 (2004).
- S. Conrad, H. Genth, F. Hofmann, I. Just, T. Skutella, *J. Biol. Chem.* **282**, 16423–16433 (2007).
- K. Hata *et al.*, *J. Cell Biol.* **173**, 47–58 (2006).
- J. L. Babitt *et al.*, *Nat. Genet.* **38**, 531–539 (2006).
- Z. Zhou *et al.*, *Dev. Cell* **19**, 90–102 (2010).
- D. H. Lee *et al.*, *Blood* **115**, 3136–3145 (2010).
- A. S. Zhang *et al.*, *J. Biol. Chem.* **282**, 12547–12556 (2007).
- J. P. Xiong *et al.*, *Science* **296**, 151–155 (2002); 10.1126/science.1069040.
- M. E. Lidell, M. E. Johansson, G. C. Hansson, *J. Biol. Chem.* **278**, 13944–13951 (2003).
- N. H. Wilson, B. Key, *Int. J. Biochem. Cell Biol.* **39**, 874–878 (2007).
- K. Lai Wing Sun, J. P. Correia, T. E. Kennedy, *Development* **138**, 2153–2169 (2011).
- E. Stein, Y. Zou, M. Poo, M. Tessier-Lavigne, *Science* **291**, 1976–1982 (2001).
- F. Yang, A. P. West Jr., G. P. Allendorph, S. Choe, P. J. Bjorkman, *Biochemistry* **47**, 4237–4245 (2008).
- X. Landon, *Methods Enzymol.* **47**, 145–149 (1977).
- C. Lanzara *et al.*, *Blood* **103**, 4317–4321 (2004).

- P. L. Lee, E. Beutler, S. V. Rao, J. C. Barton, *Blood* **103**, 4669–4671 (2004).
- Materials and methods are available as supplementary materials on Science Online.
- A. S. Zhang, A. P. West Jr., A. E. Wyman, P. J. Bjorkman, C. A. Enns, *J. Biol. Chem.* **280**, 33885–33894 (2005).
- F. Yang, A. P. West Jr., P. J. Bjorkman, *J. Struct. Biol.* **174**, 239–244 (2011).
- X. Liu *et al.*, *Biochem. Biophys. Res. Commun.* **382**, 795–800 (2009).
- K. Hata, K. Kaibuchi, S. Inagaki, T. Yamashita, *J. Cell Biol.* **184**, 737–750 (2009).
- B. V. Geisbrecht, K. A. Dowd, R. W. Barfield, P. A. Longo, D. J. Leahy, *J. Biol. Chem.* **278**, 32561–32568 (2003).

Acknowledgments: We thank Diamond and European Synchrotron Radiation Facility beamline staff for assistance; T. Walter, K. Harlos, and G. Sutton for technical support; and M. Zebisch, E. Y. Jones, and D. I. Stuart for discussions. Work was funded by the Wellcome Trust (C.S.) and Human Frontier Science Program and the Netherlands Organization for Health Research and Development (R.J.P.). The Division of Structural Biology is supported by a Wellcome Trust Core Grant. R.J.C.G. was a Royal Society University Research Fellow. A.R.A. was a Medical Research Council Career Development Award Fellow. C.S. is a Cancer Research UK Senior Research Fellow. Structure coordinates of eRGM-NEO1_{FN56}-Form 1, eRGM-NEO1_{FN56}-Form 2, eRGM-NEO1_{FN56}-Form 3, NEO1_{FN56}-Form 1, NEO1_{FN56}-Form 2, and NEO1_{FN56}-SOS are deposited in the Protein Data Bank (identification codes 4BQ6, 4BQ7, 4BQ8, 4BQ9, 4BQB, and 4BQC, respectively).

Supplementary Materials

www.sciencemag.org/cgi/content/full/science.1232322/DC1
Materials and Methods
Figs. S1 to S14
Table S1
References (30–59)

2 November 2012; accepted 23 May 2013
Published online 6 June 2013;
10.1126/science.1232322

Inhibition of RNA Helicase Brr2 by the C-Terminal Tail of the Spliceosomal Protein Prp8

Sina Mozaffari-Jovin,^{1*} Traudt Wandersleben,^{2*} Karine F. Santos,^{2*} Cindy L. Will,¹ Reinhard Lührmann,^{1†} Markus C. Wahl^{2†}

The Ski2-like RNA helicase Brr2 is a core component of the spliceosome that must be tightly regulated to ensure correct timing of spliceosome activation. Little is known about mechanisms of regulation of Ski2-like helicases by protein cofactors. Here we show by crystal structure and biochemical analyses that the Prp8 protein, a major regulator of the spliceosome, can insert its C-terminal tail into Brr2’s RNA-binding tunnel, thereby intermittently blocking Brr2’s RNA-binding, adenosine triphosphatase, and U4/U6 unwinding activities. Inefficient Brr2 repression is the only recognizable phenotype associated with certain retinitis pigmentosa-linked Prp8 mutations that map to its C-terminal tail. Our data show how a Ski2-like RNA helicase can be reversibly inhibited by a protein cofactor that directly competes with RNA substrate binding.

For each round of pre-mRNA splicing, a spliceosome is assembled, catalytically activated, and, after splicing catalysis, disassembled (1). During spliceosome activation, the U5 small nuclear ribonucleoprotein (snRNP) protein, Brr2, unwinds U4/U6 di-snRNAs, allowing

U6 to base-pair with U2 and the 5’ splice site and a catalytically important U6 internal stem-loop to form (2–4). Additional requirements for Brr2 during splicing catalysis (5) and spliceosome disassembly (6) are independent of its adenosine triphosphatase (ATPase) and helicase activities (5, 7), suggesting

that after spliceosome activation, Brr2 must be repressed. Brr2 must also be silenced in the U4/U6-U5 tri-snRNP, where it encounters its U4/U6 substrate before association with the spliceosome. The U5 snRNP proteins Prp8 and Snl14 interact with Brr2 and modulate its activity (6, 8, 9). A C-terminal Jab1/MPN (Jab1) domain of Prp8 interacts directly with Brr2 (10–13), and many mutations leading to a severe form of retinitis pigmentosa (RP13) in humans (14, 15) cluster in the C terminus of this domain (16, 17).

We determined the crystal structure of a fragment of human (h) Brr2 comprising its helicase region (Brr2^{HR}) with tandem helicase cassettes (18) in complex with hPrp8^{Jab1} at 3.6 Å resolution (fig. S1 and table S1) (19). hPrp8^{Jab1} directly interacts with all six domains of the N-terminal hBrr2 cassette but does not contact the C-terminal cassette (Fig. 1A and fig. S2). One flank of

¹Department of Cellular Biochemistry, Max Planck Institute for Biophysical Chemistry, Am Fassberg 11, D-37077 Göttingen, Germany. ²Laboratory of Structural Biochemistry, Freie Universität Berlin, Takustrasse 6, D-14195 Berlin, Germany.

*These authors contributed equally to this work.

†Corresponding author. E-mail: reinhard.luehrmann@mpi-bpc.mpg.de (R.L.); mwahl@zedat.fu-berlin.de (M.C.W.)

hPrp8^{Jab1} rests on the exposed β -sheet surface of the N-terminal immunoglobulin-like (IG) domain of hBrr2^{HR}, and an N-terminal helix of hPrp8^{Jab1} runs along one edge of the N-terminal hBrr2^{HR} helical bundle (HB) domain (Fig. 1A). The proximal part of an hPrp8^{Jab1} C-terminal tail (residues 2310 to 2320) binds along a cleft between the N-terminal helix-loop-helix (HLH) and HB domains of hBrr2^{HR} (Fig. 1B) and then turns toward the interior of the N-terminal cassette. There, the distal part of the tail (residues 2321 to 2335) runs between the RecA-2 and HB domains, continues

along a surface of the RecA-1 domain, and ultimately interacts via its C terminus with the RecA-1, winged helix (WH), and HB domains (Fig. 1C). Both proteins undergo conformational changes upon complex formation (fig. S3).

Because the C-terminal tail of hPrp8^{Jab1} is positioned in hBrr2's RNA-binding tunnel, we monitored the association of yeast (y) Brr2, which is highly homologous to hBrr2, with U4/U6 di-snRNA by histidine (His) pull-downs (Fig. 1D). Efficient pull-down of U4/U6 di-snRNA was observed with yBrr2 alone but not in the presence

of yPrp8^{Jab1}, irrespective of added ATP γ S (Fig. 1D, lower panel). A truncation mutant of yPrp8^{Jab1} lacking the last 16 amino acids (yPrp8^{Jab1- Δ C16}) still bound to yBrr2, but in its presence U4/U6 di-snRNA was efficiently coprecipitated (Fig. 1D). Likewise, yBrr2's affinity for a 24-nt RNA was reduced by yPrp8^{Jab1} but enhanced if the C-terminal tail was truncated (fig. S4A). Because Prp8^{Jab1} alone does not bind RNA (13), these results indicate that the insertion of the C-terminal tail of Prp8^{Jab1} into Brr2's RNA-binding tunnel obstructs RNA binding by Brr2.

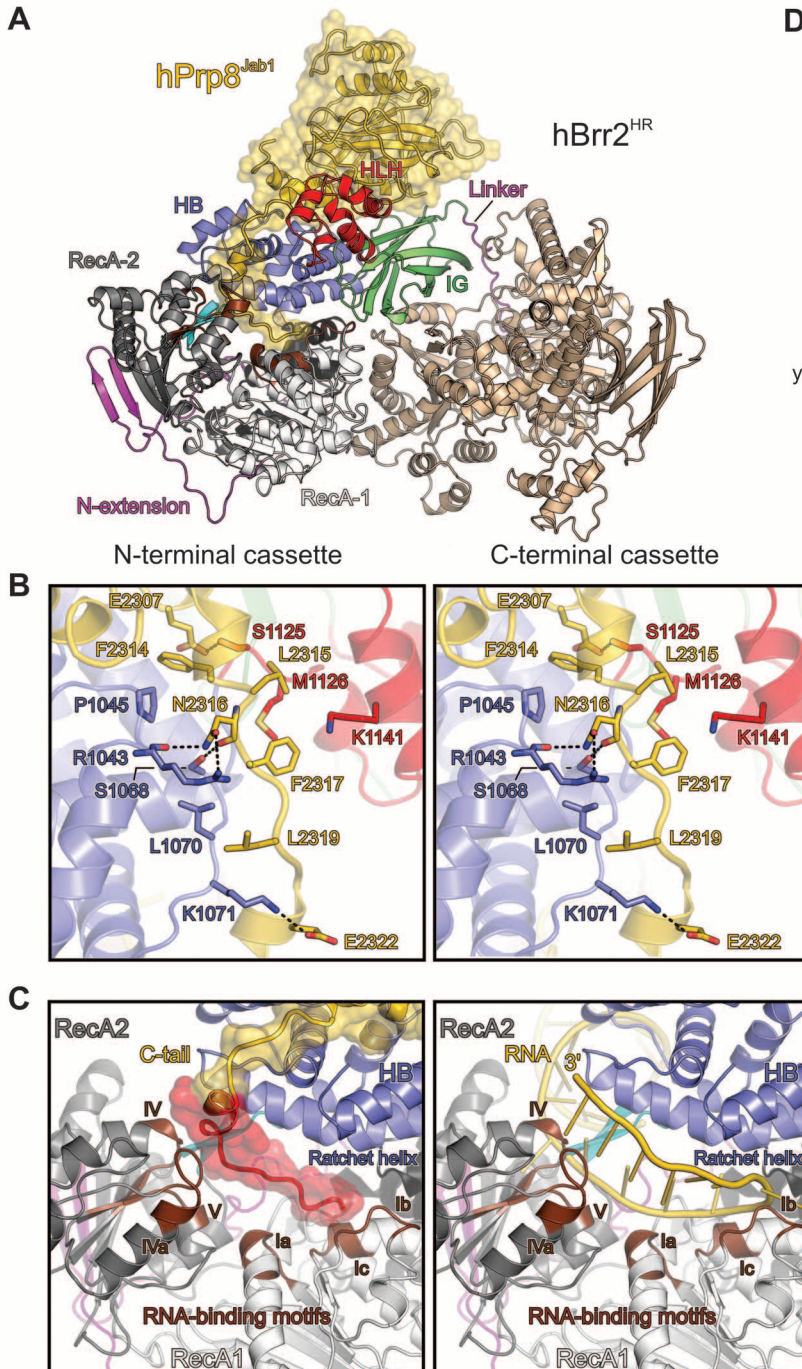
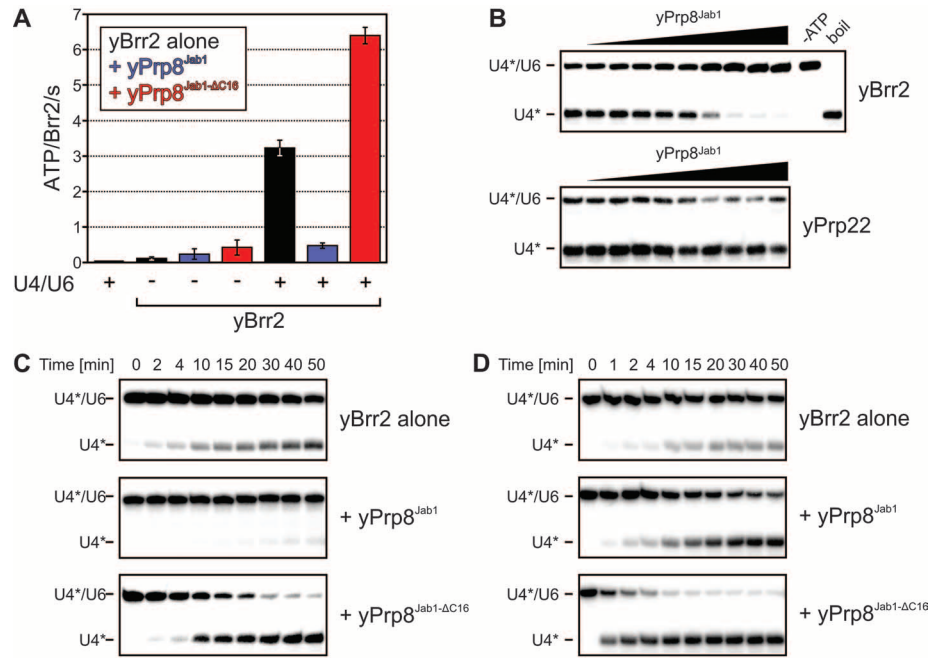


Fig. 1. Structure of a hBrr2^{HR}-hPrp8^{Jab1} complex and inhibition of Brr2 interaction with U4/U6 di-snRNA. (A) Structural overview of a hBrr2^{HR}-Prp8^{Jab1} complex. N-terminal hBrr2 cassette, colored by domain; separator loop, cyan; RecA RNA-binding motifs, brown; C-terminal cassette, beige; hPrp8^{Jab1}, gold. (B) Stereoview of the proximal hPrp8^{Jab1} tail bridging the hBrr2^{HR} HB and HLH domains. Interacting residues are colored by atom type: carbon, as the respective domain; nitrogen, blue; oxygen, red; sulfur, yellow. Dashed lines indicate hydrogen bonds or salt bridges. The view is rotated 80° clockwise about the vertical axis and 50° about the horizontal axis (top to front) as compared to (A). (C) Left: hPrp8^{Jab1} C-terminal tail running across all canonical RNA-binding motifs of the N-terminal RecA-1 (motifs Ia, Ib, and Ic) and RecA-2 (motifs IV, IVa and V) domains. Right: Model of an RNA bound in the central tunnel (18). Orientations are as in (A). (D) His-yBrr2 pull-down assays in the presence of U4/U6 snRNA and the indicated proteins. Lane 7, 50% input of all proteins. Lane 8, 10% of input RNA.

Fig. 2. Effects of yPrp8^{Jab1} or yPrp8^{Jab1-ΔC16} on yBrr2's ATPase and U4/U6 unwinding activities. (A) Intrinsic (–U4/U6 di-snRNA) and RNA-stimulated (+U4/U6 di-snRNA) steady-state ATPase activity of yBrr2 alone (black bars) or in the presence of yPrp8^{Jab1} (blue bars) or yPrp8^{Jab1-ΔC16} (red bars). Error bars represent SEMs of at least two independent experiments. U4/U6-stimulated ATPase rates (k_{ATPase} in ATP/Brr2/s) are as follows: $k_{\text{ATPase}}(\text{yBrr2}) = 3.2 \pm 0.2 \text{ s}^{-1}$; $k_{\text{ATPase}}(\text{yBrr2-yPrp8}^{\text{Jab1}}) = 0.4 \pm 0.1 \text{ s}^{-1}$; $k_{\text{ATPase}}(\text{yBrr2-yPrp8}^{\text{Jab1-}\Delta\text{C16}}) = 6.3 \pm 0.2 \text{ s}^{-1}$. (B) Inhibition of yBrr2-mediated U4/U6 unwinding (upper panel) but not of yPrp22-mediated U4/U6 unwinding (lower panel) by increasing amounts of yPrp8^{Jab1}. (C) Time course of U4/U6 duplex unwinding (0.5 nM U4/U6, 20°C) under multiple turnover conditions by yBrr2 in the absence (upper panel) or presence (middle panel) of yPrp8^{Jab1} or yPrp8^{Jab1-ΔC16}. (D) Same as in (C) except with 50 nM U4/U6, 30°C.



Although the addition of U4/U6 di-snRNA strongly increased the rate of ATP hydrolysis by yBrr2 alone or in the presence of yPrp8^{Jab1-ΔC16}, yPrp8^{Jab1} reduced this rate ~eightfold (Fig. 2A), which is consistent with the Prp8^{Jab1} tail disrupting the interaction of RNA with the conserved helicase motifs inside the Brr2 central tunnel. When yBrr2 (200 nM) was used in large excess over U4/U6 di-snRNA (0.5 nM), yPrp8^{Jab1} also reduced the amount of U4/U6 unwound at a given time, whereas it had essentially no effect on yPrp22 unwinding activity (Fig. 2B). yPrp8^{Jab1} decreased the rate and extent of yBrr2-mediated U4/U6 unwinding ~five- and ~twofold, respectively, whereas yPrp8^{Jab1-ΔC16} increased the rate and extent of unwinding ~2.5- and 1.5-fold, respectively (Fig. 2C and fig. S5A). Thus, under these conditions, the distal tail of Prp8^{Jab1} leads to a more than 10-fold reduction in the U4/U6 unwinding rate constant. At a higher U4/U6 (50 nM)–to–Brr2 (200 nM) ratio, yPrp8^{Jab1} no longer reduced the rate of U4/U6 unwinding and instead increased the extent of unwinding ~twofold (Fig. 2D and fig. S5B), similar to results obtained with a C-terminal fragment (CTF) of yPrp8 (10, 20). However, yPrp8^{Jab1-ΔC16} enhanced the rate and extent of unwinding even further (~8-fold and ~2.5-fold, respectively; Fig. 2D and fig. S5B), showing that under these conditions, the distal Prp8^{Jab1} tail has an inhibitory effect that is hidden by the stimulatory effect of the globular part and proximal tail of Prp8^{Jab1}. The reduction of yBrr2 ATPase activity at high RNA concentrations in the presence of yPrp8^{Jab1} (but not yPrp8^{Jab1-ΔC16}, Fig. 2A) suggests increased coupling of yBrr2 ATPase and helicase activity by yPrp8^{Jab1}, as previously proposed for yPrp8^{CTF} (10). hPrp8^{Jab1} and hPrp8^{Jab1-ΔC15} had little effect on the unwinding activity of hBrr2 containing only the

N-terminal cassette (fig. S6); thus, regulation requires the presence of the catalytically inactive C-terminal cassette.

All known Prp8 mutations linked to RP13 map to the Jab1 domain (Fig. 3A). We can divide the affected residues into three groups (Fig. 3, B to E). Group I residues in the globular Jab1 region (S2118, P2301, F2304, or H2309) contribute to its fold stability (Fig. 3C), group II residues in the proximal part of the C-terminal tail (R2310 and F2314) interact with Brr2 between the HLH and HB domains (Fig. 3D), and group III residues (Q2321stop, Y2334, and frameshift mutations) lie in the distal tail that can bind Brr2's RNA-binding tunnel (Fig. 3E). All RP13-linked hPrp8 mutations led to inhibition of yeast growth and in vivo splicing (fig. S7) (10, 21). However, only group I (S2197F, P2379T, and H2387P in yeast) and II mutations (R2388K and F2392L in yeast) inhibited U4/U6-U5 tri-snRNP formation (fig. S8, A to C) (10, 21), which correlated with reduced solubility (group I) or reduced affinity for yBrr2 (group II) of the corresponding yPrp8^{Jab1} variants (fig. S8D) (10, 21). In contrast, the only known group III point mutation (F2412N in yeast) did not interfere with U4/U6-U5 tri-snRNP formation (fig. S8, A to C) and also had no apparent effect on yPrp8^{Jab1} solubility or interaction with yBrr2 (fig. S8D). yPrp8^{Jab1-F2412N} enhanced yBrr2's RNA affinity (fig. S4B), repressed yBrr2's RNA-stimulated ATPase activity less efficiently than wild-type yPrp8^{Jab1} (Fig. 3G), and de-repressed yBrr2's helicase activity similar to yPrp8^{Jab1-ΔA2399stop} or yPrp8^{Jab1-ΔC16} (Fig. 3H). In the crystal structure, the equivalent residue in hPrp8^{Jab1} (Y2334) is inserted into the N-terminal cassette's tunnel where it interacts with both motif Ic of the RecA-1 domain and with residues from the WH and HB domains (Fig. 3E). Therefore, this RP13

mutation substantially alleviates the negative effect of the Prp8^{Jab1} C-terminal tail on Brr2 unwinding activity, presumably by destabilizing the tail's interaction with the RNA-binding tunnel of Brr2. To further test this notion, we mutated the conserved residues E2407 and D2410 (human D2329 and D2332), which contact Brr2's RNA-binding motifs (Fig. 3F), to lysines. yPrp8^{E2407K/D2410K} (yPrp8^{ED/KK}) led to yeast growth and in vivo splicing defects (fig. S7). yPrp8^{Jab1-ED/KK} no longer inhibited yBrr2 RNA binding (fig. S4B) or RNA-stimulated ATPase activity (Fig. 3G), and yBrr2-mediated U4/U6 unwinding was de-repressed as with yPrp8^{Jab1-F2412N} or variants lacking a tail (Fig. 3H).

Our work reveals a regulatory mechanism of the Ski2-like helicase Brr2, in which the Prp8 C-terminal tail intermittently occludes the enzyme's RNA-binding tunnel and thereby blocks its ATP-dependent helicase activity (fig. S9). Although some RP13-linked mutations lead to U4/U6-U5 tri-snRNP assembly defects and thus may exert their effects via reduced amounts of the splicing machinery, the lack of Brr2 inhibition is the only recognizable phenotype of group III RP13 mutations. Thus, a complete intermittent block in Brr2 activity is required for splicing, presumably to avoid premature U4/U6 unwinding, and its disruption can lead to RP13 in humans. An RNase H-like domain of Prp8 additionally contributes to this block before catalytic activation by competing with Brr2 loading onto U4/U6 (13). In subsequent steps, both blocks must be relieved by presently unknown triggers (such as posttranslational modifications; fig. S10), so that Brr2 can bind and unwind its substrate. The Prp8^{Jab1} tail would be well suited to switch Brr2 off again after spliceosome activation (fig. S9).

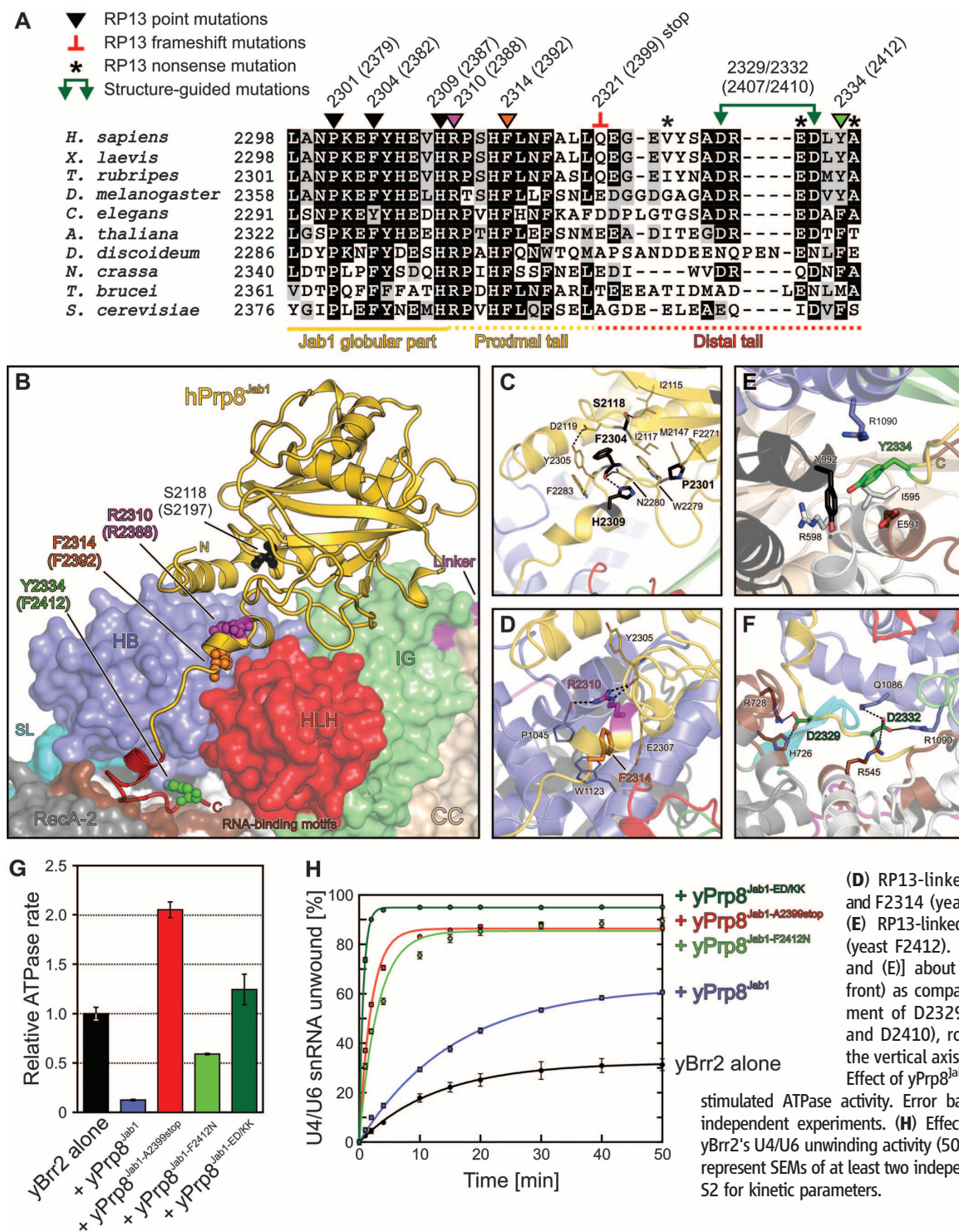


Fig. 3. Structural basis for the phenotypes of Prp8^{Jab1} mutants. (A) Multiple sequence alignment of the C-terminal region of Prp8^{Jab1}. Triangles, T-bar, and asterisks indicate the positions of the RP13 point, nonsense, frameshift mutations, respectively. The dark green double arrows indicate conserved acidic residues mutated additionally in this work. Numbers indicate human (yeast) residues. (B) Location of investigated RP13-linked residues in hPrp8^{Jab1} bound to hBrr2^{HR}; S2118 (2197), black; R2310 (2388), magenta; F2314 (2392), orange; Y2334 (2412), green. Human (yeast) numbering is shown. The distal C-terminal tail, removed by the Q2321stop (A2399stop) RP13 mutation, is shown in red, rotated 30° about the horizontal axis (top to front) as compared to Fig. 1A. (C) RP13-linked group I (globular core) residues S2118, P2301, F2304, and H2309 (yeast S2197, P2379, F2382, and H2387), (D) RP13-linked group II residues R2310 and F2314 (yeast R2388 and F2392), and (E) RP13-linked group III residue Y2334 (yeast F2412). Rotated 40° (C) or 60° [(D) and (E)] about the horizontal axis (top to front) as compared to Fig. 1A. (F) Environment of D2329 and D2332 (yeast E2407 and D2410), rotated 30° to the left about the vertical axis as compared to Fig. 1A. (G) Effect of yPrp8^{Jab1} mutations on yBrr2's RNA-stimulated ATPase activity. Error bars represent SEMs of three independent experiments. (H) Effect of yPrp8^{Jab1} mutations on yBrr2's U4/U6 unwinding activity (50 nM U4/U6, 30°C). Error bars represent SEMs of at least two independent experiments. See table S2 for kinetic parameters.

References and Notes

- M. C. Wahl, C. L. Will, R. Lührmann, *Cell* **136**, 701 (2009).
- B. Lagerbauer, T. Achsel, R. Lührmann, *Proc. Natl. Acad. Sci. U.S.A.* **95**, 4188 (1998).
- P. L. Raghunathan, C. Guthrie, *Curr. Biol.* **8**, 847 (1998).
- D. H. Kim, J. J. Rossi, *RNA* **5**, 959 (1999).
- D. Hahn, G. Kudla, D. Tollervy, J. D. Beggs, *Genes Dev.* **26**, 2408 (2012).
- E. C. Small, S. R. Leggett, A. A. Winans, J. P. Staley, *Mol. Cell* **23**, 389 (2006).
- J. B. Fourmann *et al.*, *Genes Dev.* **27**, 413 (2013).
- A. N. Kuhn, E. M. Reichl, D. A. Brow, *Proc. Natl. Acad. Sci. U.S.A.* **99**, 9145 (2002).
- A. N. Kuhn, D. A. Brow, *Genetics* **155**, 1667 (2000).
- C. Maeder, A. K. Kutach, C. Guthrie, *Nat. Struct. Mol. Biol.* **16**, 42 (2009).
- L. Zhang *et al.*, *Nat. Struct. Mol. Biol.* **16**, 731 (2009).
- G. Weber *et al.*, *Genes Dev.* **25**, 1601 (2011).
- S. Mozaffari-Jovin *et al.*, *Genes Dev.* **26**, 2422 (2012).
- D. Mordes *et al.*, *Mol. Vis.* **12**, 1259 (2006).
- K. V. Towns *et al.*, *Hum. Mutat.* **31**, E1361 (2010).
- V. Pena, S. Liu, J. M. Bujnicki, R. Lührmann, M. C. Wahl, *Mol. Cell* **25**, 615 (2007).
- L. Zhang *et al.*, *Protein Sci.* **16**, 1024 (2007).
- K. F. Santos *et al.*, *Proc. Natl. Acad. Sci. U.S.A.* **109**, 17418 (2012).
- Materials and methods are available as supplementary materials on Science Online.
- V. Pena *et al.*, *Mol. Cell* **35**, 454 (2009).
- K. L. Boon *et al.*, *Nat. Struct. Mol. Biol.* **14**, 1077 (2007).

Acknowledgments: We thank G. Heyne for excellent technical assistance, P. Fabrizio for help with yeast genetics, G. Weber and B. Loll for crystallographic support, J. D. Beggs for

providing the antibody to yPrp8, and K.-L. Boon for helpful discussions. We acknowledge access to beamlines of the BESSY II storage ring (Berlin, Germany) via the Joint Berlin MX-Laboratory sponsored by the Helmholtz Zentrum Berlin für Materialien und Energie, the Freie Universität Berlin, the Humboldt-Universität zu Berlin, the Max-Delbrück-Centrum, and the Leibniz-Institut für Molekulare Pharmakologie. This work was supported by the Deutsche Forschungsgemeinschaft (grants SFB 860 to R.L. and SFB 740/2 to M.C.W.). S.M.J.

was supported by a scholarship from the International Max Planck Research School Program for Molecular Biology. Coordinates and structure factors have been deposited in the Research Collaboratory for Structural Bioinformatics Protein Data Bank (www.pdb.org) with accession code 4KIT.

Supplementary Materials

www.sciencemag.org/cgi/content/full/science.1237515/DC1
Materials and Methods

Figs. S1 to S10
Tables S1 and S2
References (22–31)

7 March 2013; accepted 9 May 2013
Published online 23 May 2013;
10.1126/science.1237515

Monitoring Drug Target Engagement in Cells and Tissues Using the Cellular Thermal Shift Assay

Daniel Martinez Molina,^{1*} Rozbeh Jafari,^{1*} Marina Ignatushchenko,^{1*} Takahiro Seki,² E. Andreas Larsson,³ Chen Dan,³ Lekshmy Sreekumar,³ Yihai Cao,^{2,4} Pär Nordlund^{1,3,†}

The efficacy of therapeutics is dependent on a drug binding to its cognate target. Optimization of target engagement by drugs in cells is often challenging, because drug binding cannot be monitored inside cells. We have developed a method for evaluating drug binding to target proteins in cells and tissue samples. This cellular thermal shift assay (CETSA) is based on the biophysical principle of ligand-induced thermal stabilization of target proteins. Using this assay, we validated drug binding for a set of important clinical targets and monitored processes of drug transport and activation, off-target effects and drug resistance in cancer cell lines, as well as drug distribution in tissues. CETSA is likely to become a valuable tool for the validation and optimization of drug target engagement.

Drug development faces multiple challenges that lead to high costs and long development cycles for new therapeutics (1–3); meanwhile, insights into molecular, cellular and physiological processes have identified a large number of proteins as potential drug targets

(4). Therefore, methods that promote accelerated drug development are urgently needed.

The therapeutic effect of most clinically available drugs is achieved through direct binding of the drug to one or a few target proteins. This binding typically occurs at a functional site of

the protein and has either an activating or inhibitory effect. The resulting modulation of protein activity in the context of cells and tissues leads to the desired molecular, cellular, and physiological responses. The efficacy of a drug is critically dependent on the extent of its target engagement, and adverse effects are often due to excessive binding of the drug in toxicity-prone cells or its off-target binding to other proteins.

Target engagement by a drug in cells or tissues is determined by its local concentration and binding affinity. The effective drug concentration at the target depends on properties collectively referred to as ADME (absorption, distribution, metabolism and excretion), which dictate the pharmacokinetics and pharmacodynamics.

¹Department of Medical Biochemistry and Biophysics, Karolinska Institute, Scheeles väg 2, SE-17177 Stockholm, Sweden. ²Department of Microbiology, Tumor and Cell Biology, Karolinska Institute, Nobels väg 16, SE-17177 Stockholm, Sweden. ³School of Biological Sciences, Nanyang Technological University, 61 Nanyang Drive, Singapore 639798, Singapore. ⁴Department of Medicine and Health Sciences, Linköping University, 581 83 Linköping, Sweden.

*These authors contributed equally to this work.

†Corresponding author. E-mail: par.nordlund@ki.se

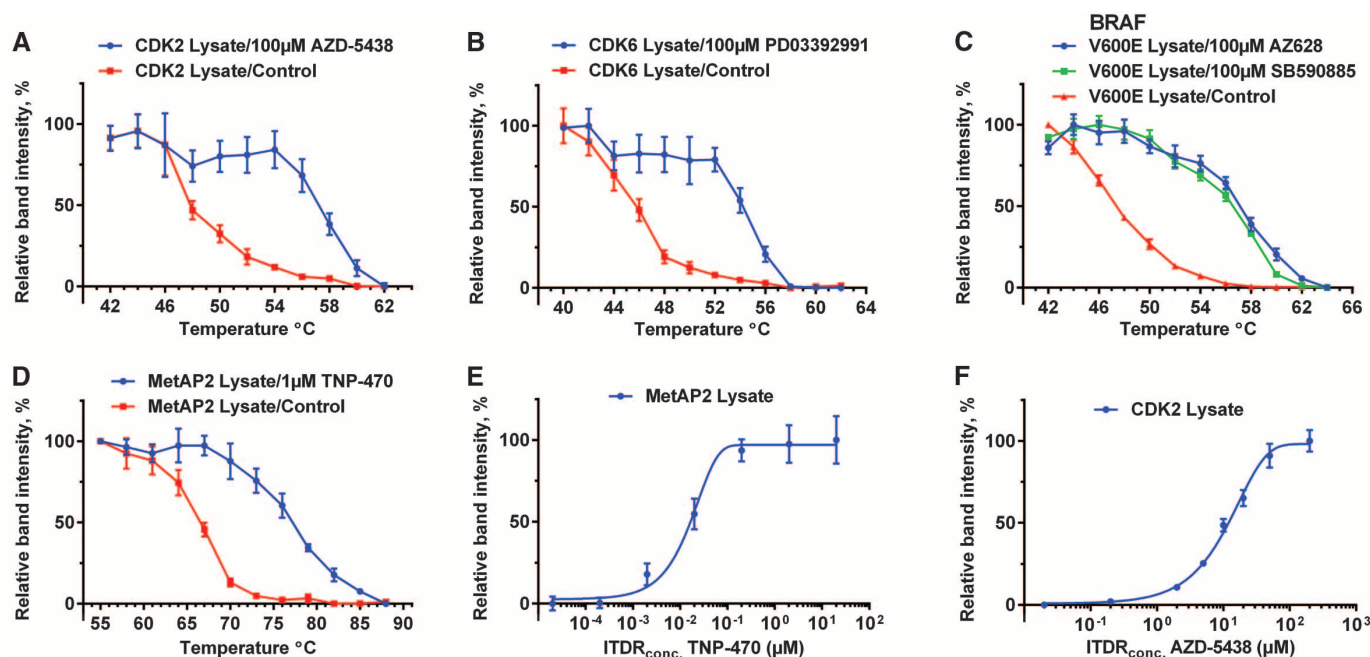


Fig. 1. CETSA melt curves and ITRF_{CETSA} in lysate. CETSA curves for four therapeutic targets, with their corresponding inhibitors measured in cell lysates; CDK2 (A) and CDK6 (B); v-Raf murine sarcoma viral oncogene homolog B1 (BRAF)

(C); and MetAP2 (D). Examples of ITRF_{CETSA} in lysates for MetAP2 with TNP-470 (E) and CDK2 with AZD-5438 (F) at fixed temperatures (72° and 52°C, respectively) are shown. Data are presented as means ± SEM, $n \geq 3$ independent experiments.

dynamics of the drug (5). Furthermore, the affinity of a ligand for the drug target can be modulated by changing the activation state of the target protein; for example, by phosphorylation or binding of regulatory proteins or allosteric effector ligands. Consistent with the complexity of protein regulation and ADME processes, residual target engagement can vary significantly during therapy and in individual patients, leading to inherent and acquired drug resistance (6, 7).

A problem in monitoring drug efficacy is that drug binding cannot be directly measured in cells and tissues; instead it is monitored indirectly by studying downstream cellular responses. Consequently, several drugs have failed in advanced clinical trials and later been shown to not act on the predicted drug target within cells (8–10). We have developed a method to directly monitor target engagement inside cells, based on ligand-induced stabilization of the target protein.

Protein thermal melting curves can be generated for purified proteins, in which the extent

of unfolding is measured using different techniques (11, 12); this is exploited in thermal shift assays (TSAs). Thermal shifts at high compound concentrations have been shown to correlate with median inhibitory concentration (IC_{50}) values and affinities measured by other methods (13, 14) and are widely used for characterization of ligand binding in structural biology and drug screening in a broad range of affinities. However, these methods have been applied only to purified proteins. We have developed a process in which multiple aliquots of cell lysate were heated to different temperatures. After cooling, the samples were centrifuged to separate soluble fractions from precipitated proteins. We then quantified the presence of the target protein in the soluble fraction by Western blotting (fig. S1).

Surprisingly, when we evaluated the thermal melt curve of four different clinical drug targets in lysates from cultured mammalian cells, all target proteins showed distinct melting curves. When drugs known to bind to these proteins were added to the cell lysates, obvious shifts in the melting

curves were detected (Fig. 1, A to D). Because this method has conceptual similarities to the TSAs used for purified proteins, we named it the cellular thermal shift assay (CETSA). Further characterization of basic aspects of the method is found in the supplementary materials (figs. S2 and S3).

To investigate drug concentration effects, we established an isothermal dose-response procedure in which lysate aliquots were exposed to different concentrations of drug while time of heating and temperature were kept constant. Unlike traditional dose-response experiments in which half-saturation points are related to affinities, the response here is typically reached at higher drug concentrations (see discussion in the supplementary materials). Nevertheless, this procedure yields a characteristic fingerprint of the target engagement along the drug concentration axis (Fig. 1, E and F). This isothermal dose-response fingerprint (ITDRF_{CETSA}) was used to estimate relative differences in drug concentration required to establish a similar extent of target engagement.

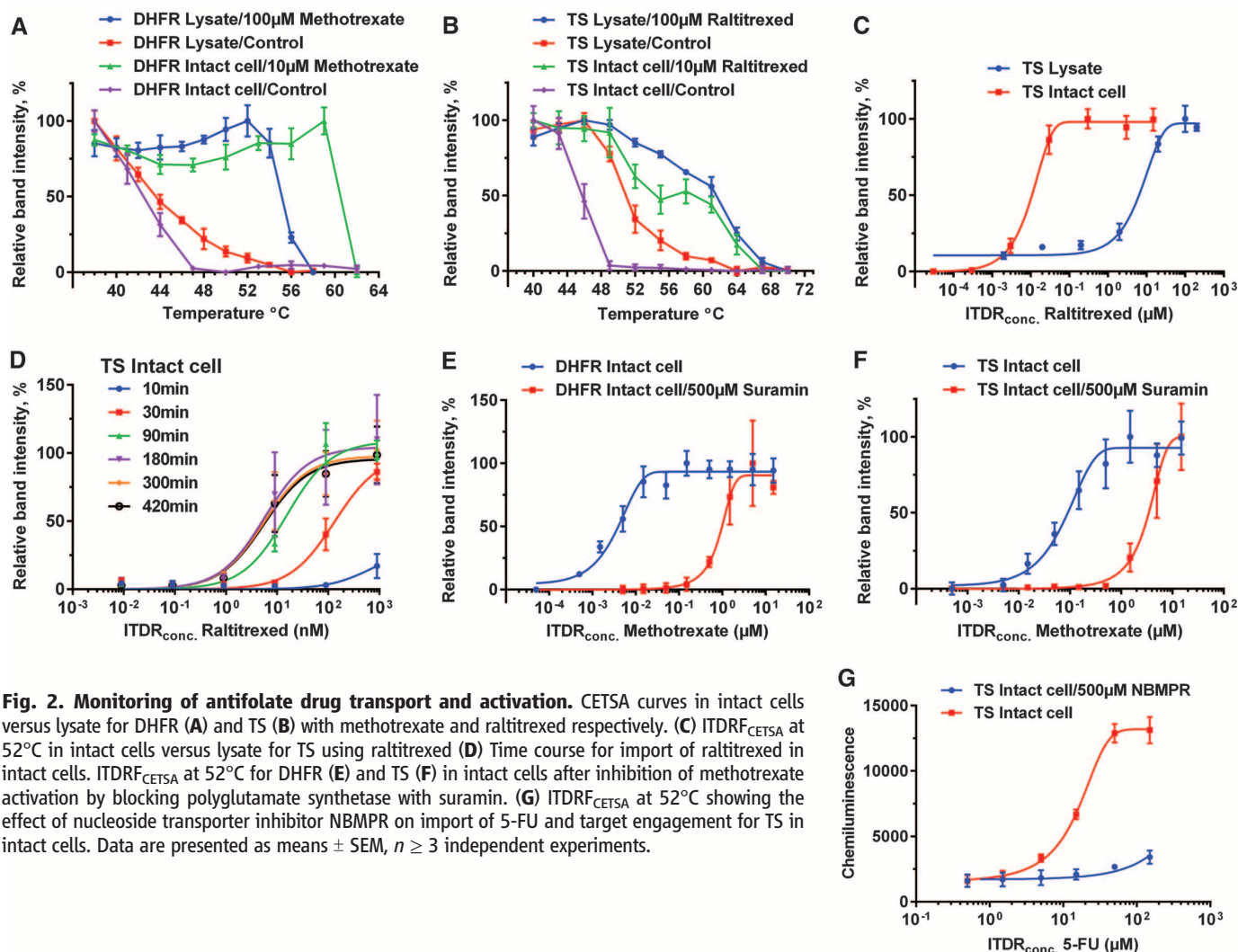


Fig. 2. Monitoring of antifolate drug transport and activation. CETSA curves in intact cells versus lysate for DHFR (A) and TS (B) with methotrexate and raltitrexed respectively. (C) ITDRF_{CETSA} at 52 $^{\circ}$ C in intact cells versus lysate for TS using raltitrexed (D) Time course for import of raltitrexed in intact cells. ITDRF_{CETSA} at 52 $^{\circ}$ C for DHFR (E) and TS (F) in intact cells after inhibition of methotrexate activation by blocking polyglutamate synthetase with suramin. (G) ITDRF_{CETSA} at 52 $^{\circ}$ C showing the effect of nucleoside transporter inhibitor NBMPR on import of 5-FU and target engagement for TS in intact cells. Data are presented as means \pm SEM, $n \geq 3$ independent experiments.

Cancer cells actively import metabolites such as folates, nucleosides, and nucleobases that are critical for DNA synthesis (15). Folate and nucleoside analogs hitchhike on these import systems and accumulate in cancer cells (16). Dihydrofolate reductase (DHFR) and thymidylate synthase (TS) are targets for the antifolate cancer drugs methotrexate and raltitrexed (17, 18). DHFR and TS were used to determine whether CETSA could be used in intact cells as well as in lysates. Cells were exposed to either methotrexate or raltitrexed, washed, heated to different temperatures, cooled, and lysed. The cell lysates were cleared by centrifugation, and the levels of soluble target protein were measured, revealing large thermal shifts for DHFR and TS

in treated cells as compared to controls (Fig. 2, A and B). To assess the relative binding in cells and lysates, an ITDRF_{CETSA} experiment with TS was conducted, demonstrating that after 3 hours of exposure to the drug, the ITDRF_{CETSA} of raltitrexed in lysate gave an at least three orders of magnitude higher value than in intact cells, suggesting a highly active transport of the drug into the cell (Fig. 2C). This transport results in dramatic accumulation of the drug in proliferating cells, which is clearly a key factor in the therapeutic efficacy. A similar shift of ITDRF_{CETSA} was obtained for DHFR with methotrexate (fig. S4A). A time-course experiment with raltitrexed indicated that after 2 to 3 hours, the ITDRF_{CETSA} of TS was saturated (Fig. 2D);

this saturation was not due to depletion of the drug in the medium (fig. S4B). In contrast, a similar experiment using starved cells resulted in a limited accumulation of the drug (fig. S4C). In addition to providing information about the transport of this folate analog, these experiments prove that CETSA monitors target engagement in intact cells. This is further supported by dye exclusion experiments supporting the notion that the cell membranes remain intact during these experiments (fig. S2).

Because resistance to folate and nucleoside analogs often occurs through changes in transport or activation events, we investigated the effect of inhibitors of such pathways. Folate analogs are activated through polyglutamation by polyglutamate synthetase; this helps to retain these compounds in the cell by minimizing their export (19). Monitoring the TS and DHFR ITDRF_{CETSA} for methotrexate in the presence of suramin, an inhibitor of polyglutamate synthetase, demonstrated that this value differs >30-fold between treated and untreated cells for both TS and DHFR. This implies that the activation of methotrexate is severely compromised by suramin (Fig. 2, E and F). Nitrobenzylmercaptapurine riboside (NBMPR) is an inhibitor of the import of fluorouracil (5-FU), which in its activated form, FUMP, is a potent inhibitor of TS (19). The ITDRF_{CETSA} shift for TS in cells treated with 5-FU suggests that its import is inhibited by the addition of NBMPR (Fig. 2G). Thus, CETSA can monitor complex processes known to be involved in drug resistance.

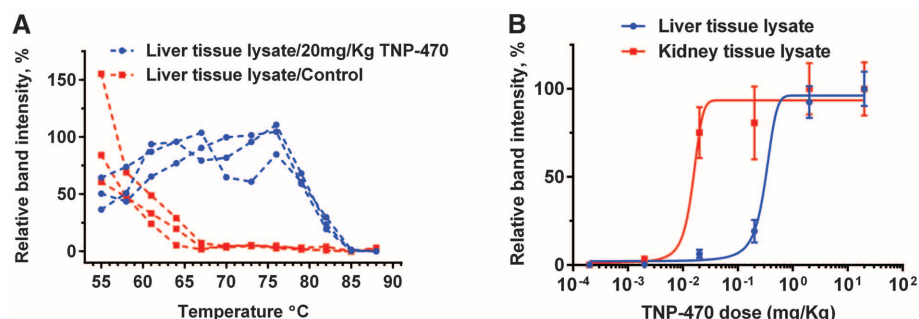


Fig. 3. Monitoring of TNP-470 target engagement in tissue samples from mice. (A) CETSA curves of MetAP2 in mouse liver lysates from untreated mice and mice treated with TNP-470 at 20 mg per kilogram of body weight. (B) ITDRF_{CETSA} at 72°C of MetAP2 in liver and kidney at six different TNP-470 dosage levels. Data in (B) are presented as means \pm SEM, $n = 3$ mice per data point.

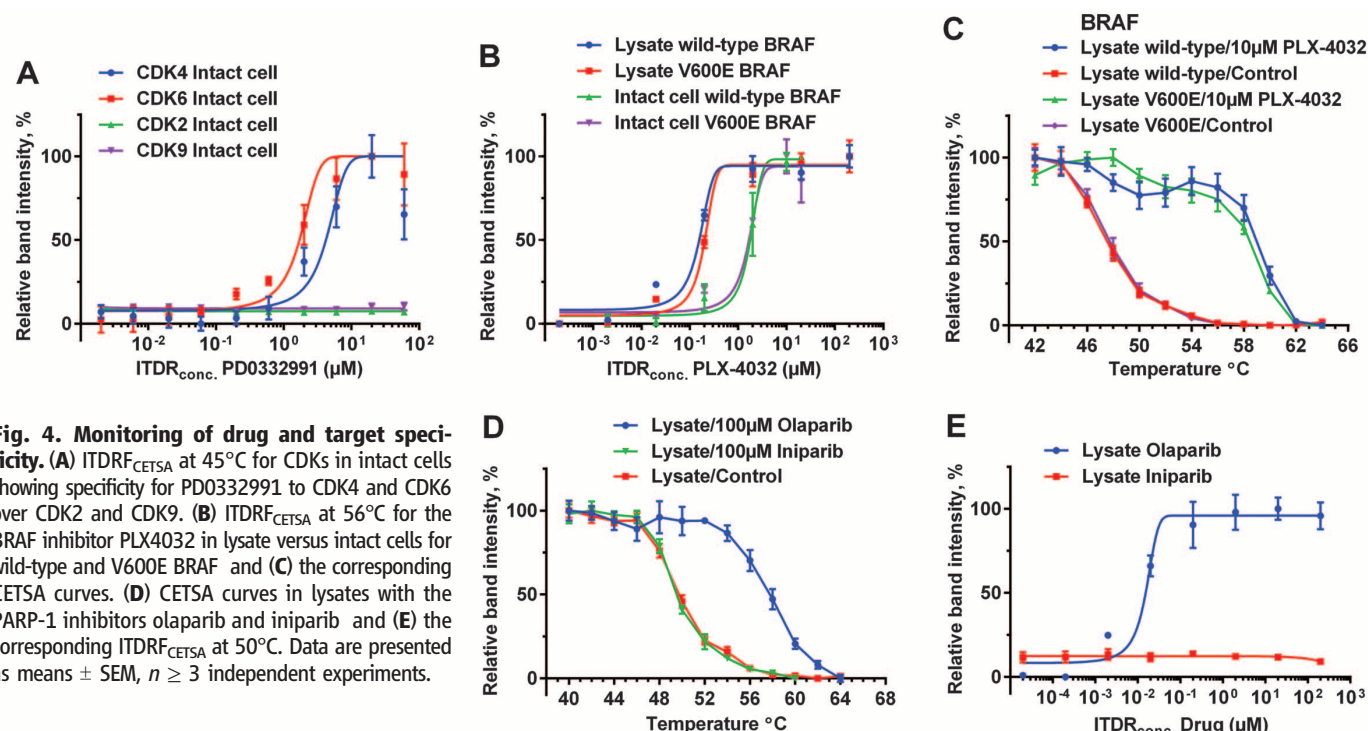


Fig. 4. Monitoring of drug and target specificity. (A) ITDRF_{CETSA} at 45°C for CDKs in intact cells showing specificity for PD0332991 to CDK4 and CDK6 over CDK2 and CDK9. (B) ITDRF_{CETSA} at 56°C for the BRAF inhibitor PLX4032 in lysate versus intact cells for wild-type and V600E BRAF and (C) the corresponding CETSA curves. (D) CETSA curves in lysates with the PARP-1 inhibitors olaparib and iniparib and (E) the corresponding ITDRF_{CETSA} at 50°C. Data are presented as means \pm SEM, $n \geq 3$ independent experiments.

To determine whether CETSA could yield information on target engagement in animals, we used the methionine aminopeptidase-2 (MetAP2) inhibitor TNP-470, an antiangiogenic compound currently in clinical development for use in treatment of solid tumors (20). In a double-blind study, mice were systemically treated with TNP-470 and compared to mice in a control group. To ensure reproducibility and facilitate sample handling in the subsequent experiments, the harvested organs were frozen and lysates were prepared before heating. Because the compound TNP-470 is a covalent inhibitor, this is likely to reflect target engagement in the cell. The corresponding thermal melt curves of MetAP2 from mouse liver samples clearly distinguished the treated mice from the nontreated mice (Fig. 3A).

To investigate dose dependence, we administered six different doses of TNP-470 to mice. Comparison of in situ CETSA response curves for MetAP2 in mice liver and kidney lysates demonstrated a 50-fold difference in ITDRF_{CETSA} (Fig. 3B). The lower effective concentration of TNP-470 in the liver than in the kidneys could be explained by the large amount of catabolic enzymes present in this organ as well as renal excretion of active metabolites (21).

Target specificity is important for optimizing drug efficacy and minimizing their adverse effects (22). Cyclin-dependent kinases (CDKs) are major regulators of cell division and differentiation, and inhibitors of these are developed for cancer and inflammation therapy (23, 24). PD0332991, currently in clinical development for cancer treatment, was used to investigate target specificity in cells using CETSA. The ITDRF_{CETSA} values show that it is selective for CDK4 and CDK6; no significant target engagement is seen for either CDK2 or CDK9, even at very high concentrations of the inhibitor in intact cells (Fig. 4A). This confirms results from activity assays, which have shown the selectivity of PD0332991 for CDK4 and CDK6 over CDK2 (25).

Cells expressing mutated forms of oncogenic proteins may (or may not) display altered drug susceptibility. BRAF is a member of the MAPK/ERK pathway that controls proliferation and apoptosis; it is mutated in 7% of human cancers; for example, in more than 50% of melanomas (26). Vemurafenib (PLX4032) is highly effective against melanomas harboring the frequent BRAF V600E mutation (27). Studies with purified BRAF kinase domains show a modest increase in the PLX4032 IC₅₀ for V600E BRAF as compared to the wild type (27, 28). When comparing target engagement of PLX4032 in intact cells with the V600E substitution and wild-type BRAF, the ITDRF_{CETSA} values demonstrate similar target engagement levels for the two protein variants (Fig. 4B), and their corresponding CETSA curves show comparable stabilization at high compound concentration (Fig. 4C).

CETSA may help to validate clinical drug candidates before significant investments in clinical

trials are made. For example, the proposed PARP-1 inhibitor iniparib reached phase III clinical trials (10), where it showed no efficacy, and was subsequently shown to lack activity against PARP-1 in living cells (10, 29). We used CETSA to compare the target engagement of PARP-1 for iniparib and olaparib, a well-established PARP-1 inhibitor in clinical development (30). Although binding of olaparib induced a large thermal shift of PARP-1, iniparib failed to induce a shift (Fig. 4D). This is also apparent when studying the ITDRF_{CETSA} results for both compounds (Fig. 4E). Apparently, the mechanism of action of iniparib is not via physical binding to PARP-1; instead, iniparib may kill cancer cells by unspecific modification of cysteine residues (29).

In this work we have shown that CETSA can be used to monitor target specificity, drug transport and activation, as well as dose-dependent target engagement in animals. The relative ease of establishing CETSA for the targets used in this study suggests that this method could be applicable for a wide range of soluble intracellular and extracellular drug targets. However, the method is not likely to work for highly inhomogeneous proteins or for proteins in which unfolding of the ligand-binding domain does not promote aggregation.

There are no direct methods for monitoring the physical binding of a drug to its target in intact cells (31–33). For cell lysates, physical target engagement can be assessed using drug-induced proteolysis protection (34) or protection of oxidation of specific amino acids (35). Apart from identifying drug targets of orphan ligands in cell lysates (31), the applicability of these methods for monitoring dynamic events in intact cells remains to be proven. When a selective and high-affinity ligand is available, in situ competition experiments can be performed for extracellularly accessible proteins or receptors to monitor target engagement (36).

In addition to the applications in preclinical drug development discussed above, CETSA has potential for monitoring drug efficacy at the target level in patients. For example, CETSA could assist in determining appropriate drug usage and dosage, as well as monitor when acquired drug resistance at the target engagement level has developed; for example, during cancer therapy. The versatility of CETSA is likely to make it a valuable tool for drug research and development.

References and Notes

- K. I. Kaitin, *Clin. Pharmacol. Ther.* **87**, 356 (2010).
- J. Orloff et al., *Nat. Rev. Drug Discov.* **8**, 949 (2009).
- T. A. Yap, S. K. Sandhu, P. Workman, J. S. de Bono, *Nat. Rev. Cancer* **10**, 514 (2010).
- M. Rask-Andersen, M. S. Almén, H. B. Schiöth, *Nat. Rev. Drug Discov.* **10**, 579 (2011).
- A. Ruiz-Garcia, M. Bermejo, A. Moss, V. G. Casabo, *J. Pharm. Sci.* **97**, 654 (2008).
- J. P. Gillet, M. M. Gottesman, *Methods Mol. Biol.* **596**, 47 (2010).
- R. Barouch-Bentov, K. Sauer, *Expert Opin. Investig. Drugs* **20**, 153 (2011).

- D. S. Auld, N. Thorne, W. F. Maguire, J. Inglese, *Proc. Natl. Acad. Sci. U.S.A.* **106**, 3585 (2009).
- C. Schmidt, *Nat. Biotechnol.* **28**, 185 (2010).
- M. Guha, *Nat. Biotechnol.* **29**, 373 (2011).
- B. I. Kurganov, *Biochemistry (Mosc.)* **67**, 409 (2002).
- M. Vedadi et al., *Proc. Natl. Acad. Sci. U.S.A.* **103**, 15835 (2006).
- E. Wahlberg et al., *Nat. Biotechnol.* **30**, 283 (2012).
- O. Fedorov et al., *Proc. Natl. Acad. Sci. U.S.A.* **104**, 20523 (2007).
- S. Marsh, *Invest. New Drugs* **23**, 533 (2005).
- Y. G. Assaraf, *Cancer Metastasis Rev.* **26**, 153 (2007).
- M. Visentin, R. Zhao, I. D. Goldman, *Hematol. Oncol. Clin. North Am.* **26**, 629, ix (2012).
- N. Hagner, M. Joerger, *Cancer Manag. Res.* **2**, 293 (2010).
- M. Huang, Y. Wang, S. B. Cogut, B. S. Mitchell, L. M. Graves, *J. Pharmacol. Exp. Ther.* **304**, 753 (2003).
- S. Q. Yin, J. J. Wang, C. M. Zhang, Z. P. Liu, *Curr. Med. Chem.* **19**, 1021 (2012).
- J. D. Moore et al., *Cancer Chemother. Pharmacol.* **46**, 173 (2000).
- E. Loukine et al., *Nature* **486**, 361 (2012).
- J. Cícenás, M. Valius, *J. Cancer Res. Clin. Oncol.* **137**, 1409 (2011).
- M. Malumbres, M. Barbacid, *Nat. Rev. Cancer* **9**, 153 (2009).
- D. W. Fry et al., *Mol. Cancer Ther.* **3**, 1427 (2004).
- H. Davies et al., *Nature* **417**, 949 (2002).
- J. T. Lee et al., *Pigment Cell Melanoma Res.* **23**, 820 (2010).
- G. Bollag et al., *Nature* **467**, 596 (2010).
- X. Liu et al., *Clin. Cancer Res.* **18**, 510 (2012).
- E. Dean et al., *Br. J. Cancer* **106**, 468 (2012).
- B. Lomenick, R. W. Olsen, J. Huang, *ACS Chem. Biol.* **6**, 34 (2011).
- J. Luo, N. L. Solimini, S. J. Elledge, *Cell* **136**, 823 (2009).
- G. P. Hussmann, K. J. Kellar, *J. Pharmacol. Exp. Ther.* **343**, 434 (2012).
- B. Lomenick et al., *Proc. Natl. Acad. Sci. U.S.A.* **106**, 21984 (2009).
- G. M. West, L. Tang, M. C. Fitzgerald, *Anal. Chem.* **80**, 4175 (2008).
- P. M. Matthews, E. A. Rabiner, J. Passchier, R. N. Gunn, *Br. J. Clin. Pharmacol.* **73**, 175 (2012).

Acknowledgments: We thank K. Johansson [Karolinska Institute (KI), Department of Medical Biochemistry and Biophysics (MBB)] for assistance with cell culturing, H. Schüller KI/MBB for PARP-1 constructs, and T. Lundbäck KI/Chemical Biology Consortium Sweden for valuable discussions. This work was supported by grants from the KI (Distinguished Professor Award), the Swedish Research Council (Vetenskapsrådet), and the Swedish Cancer Society (Cancerfonden) to P.N. and Y.C., as well as a Strategic Centre grant from Nanyang Technological University (Singapore) to P.N. and grants from the Karolinska Institute Foundation, the Torsten Söderbergs Foundation, and the European Research Council advanced grant ANGIOFAT (project no. 250021) to Y.H. P.N. is the inventor on a pending patent application covering aspects of the CETSA method, to be assigned to Pelago Bioscience AB. P.N. and D.M.M. are cofounders of Pelago Bioscience AB, which will develop CETSA for commercial applications.

Supplementary Materials

www.sciencemag.org/cgi/content/full/341/6141/84/DC1
Materials and Methods
Supplementary Text
Figs. S1 to S4
Table S1
References (37–42)

4 December 2012; accepted 9 May 2013
10.1126/science.1233606

Engineered SIRPα Variants as Immunotherapeutic Adjuvants to Anticancer Antibodies

Kipp Weiskopf,^{1,2,3*} Aaron M. Ring,^{1,2,3,4,5*} Chia Chi M. Ho,^{1,2,3,4,5} Jens-Peter Volkmer,^{1,2,3} Aron M. Levin,^{4,5} Anne Kathrin Volkmer,^{1,2,3,6} Engin Özkan,^{4,5} Nathaniel B. Fernhoff,^{1,2,3} Matt van de Rijn,⁷ Irving L. Weissman,^{1,2,3,7*} K. Christopher Garcia^{2,4,5*†}

CD47 is an antiphagocytic signal that cancer cells employ to inhibit macrophage-mediated destruction. Here, we modified the binding domain of human SIRPα, the receptor for CD47, for use as a CD47 antagonist. We engineered high-affinity SIRPα variants with about a 50,000-fold increased affinity for human CD47 relative to wild-type SIRPα. As high-affinity SIRPα monomers, they potently antagonized CD47 on cancer cells but did not induce macrophage phagocytosis on their own. Instead, they exhibited remarkable synergy with all tumor-specific monoclonal antibodies tested by increasing phagocytosis in vitro and enhancing antitumor responses in vivo. This “one-two punch” directs immune responses against tumor cells while lowering the threshold for macrophage activation, thereby providing a universal method for augmenting the efficacy of therapeutic anticancer antibodies.

Immune evasion is an emerging hallmark of cancer (1), and therapies that direct immune responses against cancer show promise in experimental and clinical settings (2, 3). Macrophages commonly infiltrate tumors, and their tumoricidal potential can be harnessed to benefit patients (4). CD47 is an antiphagocytic “don’t eat me” signal that distinguishes live cells from dying or aged cells, inhibits Fc receptor–mediated functions by myeloid cells, and is highly expressed by many cancers to avoid detection by macrophages (5–13). Antibodies that block binding of CD47 to SIRPα, an inhibitory receptor on macrophages, greatly increase phagocytosis of cancer cells (9, 10, 12, 13). However, antibodies have limited tissue distribution and can exert off-target effects (14, 15).

To improve CD47-targeted therapies, we used the single 14-kD binding domain of human SIRPα as a competitive antagonist to human CD47 (fig. S1A). Due to the weak ~1 μM affinity of the native SIRPα-CD47 interaction (16–18), however, we found that wild-type SIRPα was a poor antagonist. To improve the affinity of human SIRPα for human CD47, we created mutant libraries of the N-terminal V-set immunoglobulin (Ig) domain of SIRPα (residues 1 to 118) conjugated to Aga2p for yeast surface display (fig. S1B). Using the CD47 Ig superfamily (IgSF)

domain as a selection reagent, we conducted two “generations” of in vitro evolution using yeast surface display (figs. S1 and S2 and Fig. 1A). We

obtained variants that bound CD47 with dissociation constants (K_d) as low as 34.0 pM and dissociation half-lives ($t_{1/2}$) as long as 44 min compared with 0.3 to 0.5 μM K_d and 1.8 s $t_{1/2}$ for wild-type SIRPα (Fig. 1A). The sequences of the high-affinity SIRPα variants converged on a consensus set of mutations. When we grafted these nine conservative substitutions onto the predominant wild-type human SIRPα allele (19) (allele 2), the resulting variant (termed CV1, consensus variant 1) bound human CD47 with an affinity of 11.1 pM (Fig. 1A).

We determined the crystal structure of the high-affinity variant FD6 bound to the human CD47 IgSF domain (Fig. 1B, fig. S3, and table S1). The FD6:CD47 complex superimposed with the wild-type SIRPα:CD47 complex (17) with a root mean square deviation of only 0.61 Å, indicating a high degree of structural similarity and validating our efforts to preserve the geometry of the wild-type interaction (Fig. 1C). The overlapping binding modes of FD6 and wild-type SIRPα indicate that they would compete for the same CD47 epitope, providing maximal antagonism. As notable differences, the FD6 binding interface

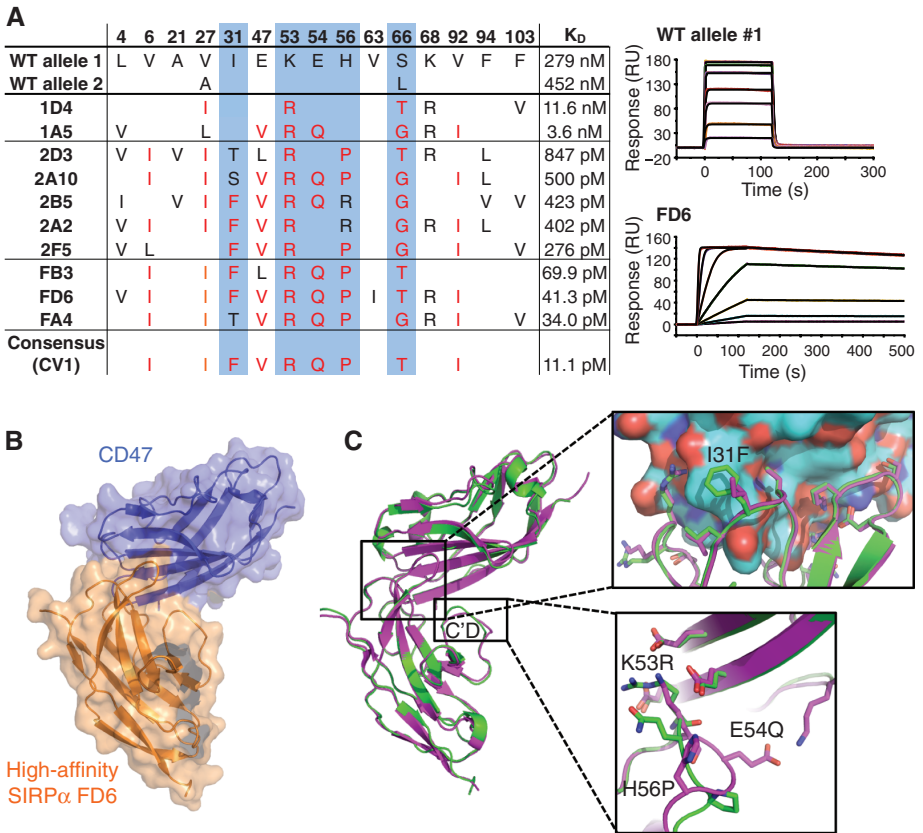


Fig. 1. Directed evolution of high-affinity SIRPα variants. (A) Summary of sequences and surface plasmon resonance (SPR) affinity measurements of engineered SIRPα variants. The position of the mutated residues and their corresponding sequence in wild-type allele 1 is denoted at the top of the table. Red text color indicates the consensus mutations, and blue shading indicates contact residues in the consensus. Representative SPR sensorgrams of wild-type SIRPα and high-affinity variant FD6 binding immobilized CD47 are shown to the right. RU, response units. (B) The crystal structure of the FD6:CD47 complex depicted as transparent surfaces containing ribbon representations of FD6 (orange) and CD47 (blue). (C) Superimposition of the wild-type (magenta) and high-affinity (green) SIRPα:CD47 complexes. (Insets) Mutated contact residues in the SIRPα C'D loop (sticks) and the binding interface of CD47 (top, surface; bottom, sticks).

¹Institute for Stem Cell Biology and Regenerative Medicine, Stanford University School of Medicine, Stanford, CA 94305, USA. ²Ludwig Center for Cancer Stem Cell Research and Medicine, Stanford University School of Medicine, Stanford, CA 94305, USA. ³Stanford Cancer Institute, Stanford University School of Medicine, Stanford, CA 94305, USA. ⁴Department of Molecular and Cellular Physiology, and Department of Structural Biology, Stanford University School of Medicine, Stanford, CA 94305, USA. ⁵Howard Hughes Medical Institute, Stanford University School of Medicine, Stanford, CA 94305, USA. ⁶Department of Obstetrics and Gynaecology, University of Dusseldorf, Germany. ⁷Department of Pathology, Stanford University Medical Center, Stanford, CA 94305, USA.

*These authors contributed equally to this work.
†Corresponding author. E-mail: kcgarcia@stanford.edu

appears stabilized by three mutations in the C'D loop (Fig. 1C, lower inset) and the Ile31Phe mutation (Fig. 1C, upper inset). These structural studies imply that the high-affinity SIRP α variants could serve as efficacious CD47 antagonists.

When we assessed their ability to antagonize CD47 on the surface of human cancer cells, we found that SIRP α variants with increased CD47 affinity exhibited greater potency in binding (fig. S4, A and C) and blocking cell-surface CD47 (Fig. 2A and fig. S4B). As single-domain monomers (fig. S5A), both FD6 and CV1 exhibited potent antagonism relative to wild-type SIRP α .

Subsequently, we evaluated the ability of high-affinity SIRP α variants to increase phagocytosis in vitro by coculturing macrophages and tumor cells in the presence of CD47-blocking agents. As fusion proteins to the Fc fragment of human IgG4 (hIgG4) (fig. S5, A and B), the high-affinity SIRP α variants led to increased phagocytosis of cancer cells as measured by microscopy and flow cytometry (Fig. 2B, fig. S6, and movies S1 and S2). No substantial phagocytosis was observed upon treatment with high-affinity SIRP α monomers, with dimers lacking Fc chains, or with B6H12 Fab fragments at concentrations that maximally

antagonize CD47 (Fig. 2, B to D, fig. S5, C and D, and fig. S7). Thus, phagocytosis was only observed when CD47 was blocked in the presence of antibody Fc chains, which contribute a necessary prophagocytic stimulus.

Consequently, we hypothesized that treatment with high-affinity SIRP α monomers would enhance phagocytosis in the presence of tumor-specific monoclonal antibodies. Thus, we performed phagocytosis assays using antibodies targeting DLD-1 colon cancer cells. Indeed, high-affinity SIRP α monomers significantly augmented phagocytosis when combined with a nonblocking antibody to

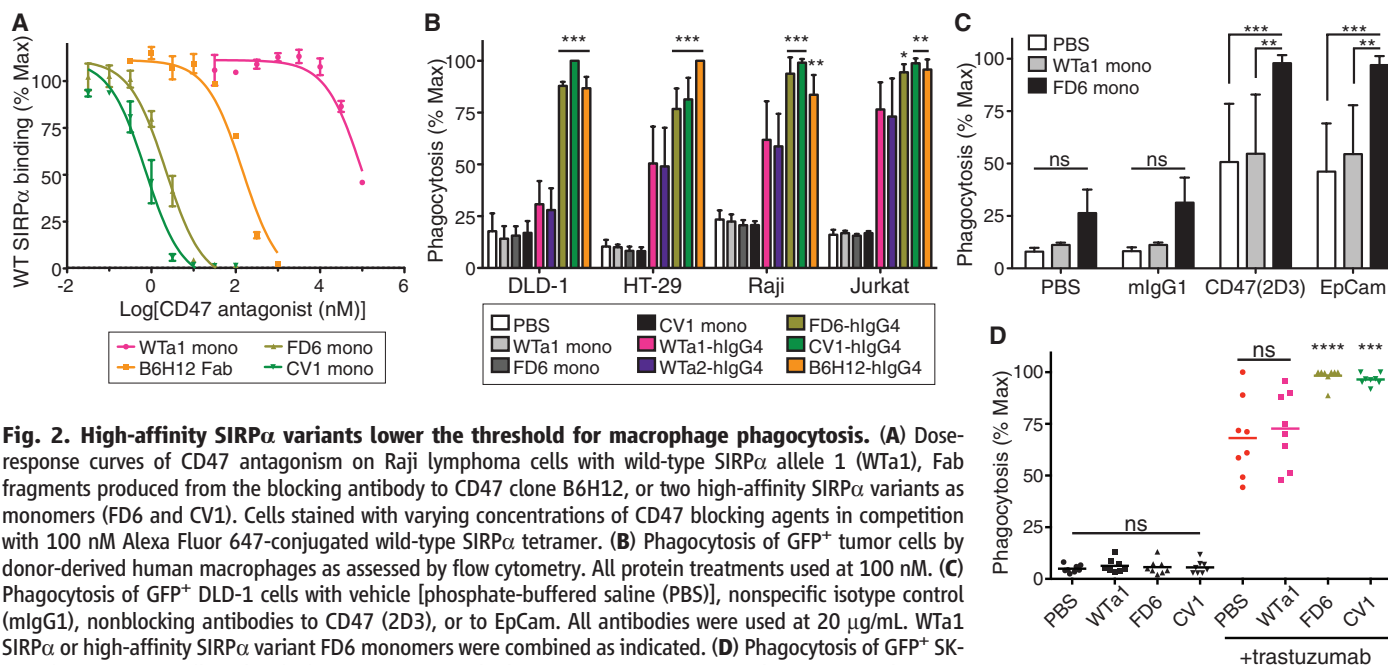


Fig. 2. High-affinity SIRP α variants lower the threshold for macrophage phagocytosis. (A) Dose-response curves of CD47 antagonism on Raji lymphoma cells with wild-type SIRP α allele 1 (WT α 1), Fab fragments produced from the blocking antibody to CD47 clone B6H12, or two high-affinity SIRP α variants as monomers (FD6 and CV1). Cells stained with varying concentrations of CD47 blocking agents in competition with 100 nM Alexa Fluor 647-conjugated wild-type SIRP α tetramer. (B) Phagocytosis of GFP $^{+}$ tumor cells by donor-derived human macrophages as assessed by flow cytometry. All protein treatments used at 100 nM. (C) Phagocytosis of GFP $^{+}$ DLD-1 cells with vehicle [phosphate-buffered saline (PBS)], nonspecific isotype control (mIgG1), nonblocking antibodies to CD47 (2D3), or to EpCam. All antibodies were used at 20 μ g/mL. WT α 1 SIRP α or high-affinity SIRP α variant FD6 monomers were combined as indicated. (D) Phagocytosis of GFP $^{+}$ SK-BR-3 breast cancer cells with vehicle, WT α 1 SIRP α , or high-affinity SIRP α monomers alone or in combination with 1 μ g/mL trastuzumab. (A to D) Phagocytosis assays were performed with macrophages derived from a minimum of three independent blood donors. The percentage of GFP $^{+}$ macrophages was normalized to the maximal response by each donor for each cell line. Data are mean \pm SD. (C and D) All SIRP α variants were used at 1 μ M. ns, not significant; * P < 0.05; ** P < 0.01; *** P < 0.001 versus wild-type SIRP α variants, or as indicated otherwise, by two-way [(B) and (C)] or one-way (D) analysis of variance with Bonferroni correction.

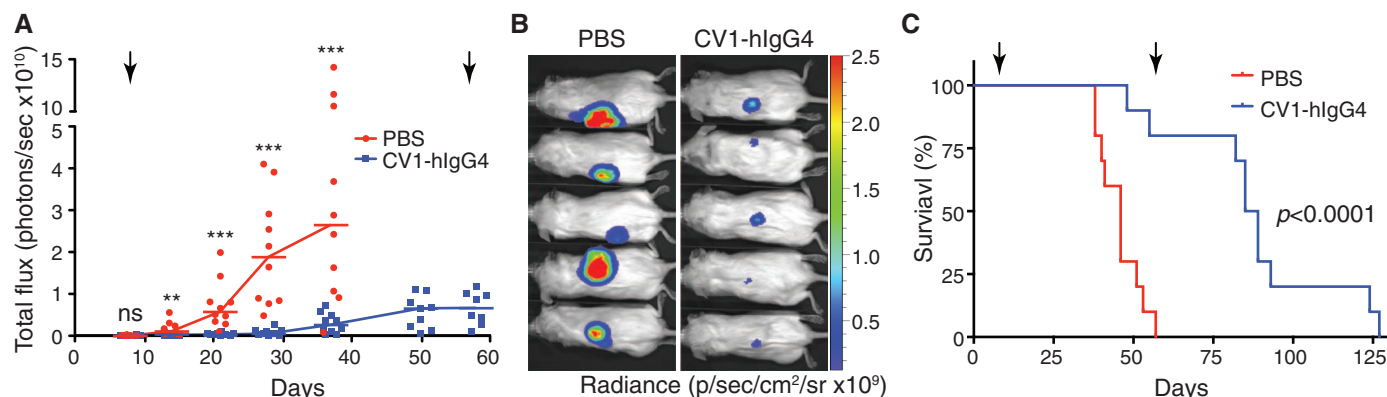


Fig. 3. High-affinity SIRP α -Fc fusion proteins are effective as single agents for cancer. (A) Growth of GFP-luciferase $^{+}$ 639-V bladder cancer cells in the dorsal subcutaneous tissue of NSG mice upon daily treatment with vehicle control (PBS) or 200 μ g high-affinity SIRP α -Fc (CV1-hlgG4) as evaluated by bioluminescence imaging. Ten mice per group were treated and analyzed, and each data point represents a measurement from an independent mouse. Bars

indicate median values for each treatment group. Black arrows depict start and stop of treatment. ns, not significant; ** P < 0.01; *** P < 0.001 by Mann-Whitney test. (B) Representative bioluminescence images of 639-V-engrafted mice from each treatment group on day 37 after engraftment. (C) Survival of mice engrafted with GFP-luciferase $^{+}$ 639-V cells. Black arrows indicate the start and stop of treatment. Statistical analysis performed by Mantel-Cox test.

CD47 (20) or to EpCam, but not an isotype control (Fig. 2C).

To demonstrate the clinical implications of this principle, we examined the ability of high-affinity SIRP α monomers to enhance the efficacy of established antibodies currently used as cancer therapies. Phagocytosis assays were performed using Her2/neu⁺ SK-BR-3 breast cancer cells (21). Baseline phagocytosis was observed with SIRP α monomers alone, whereas treatment with the therapeutic antibody to Her2/neu, trastuzumab, alone or with wild-type SIRP α monomer led to moderate increases in phagocytosis (Fig. 2D). However, the combination of trastuzumab with high-affinity SIRP α monomers FD6 or CV1 resulted in maximal levels of phagocytosis that were higher than the additive effect of either agent administered alone. Similar effects were observed with the antibody to EGFR, cetuximab, using DLD-1 cells and with Raji lymphoma cells treated with varying concentrations of rituximab, an anti-

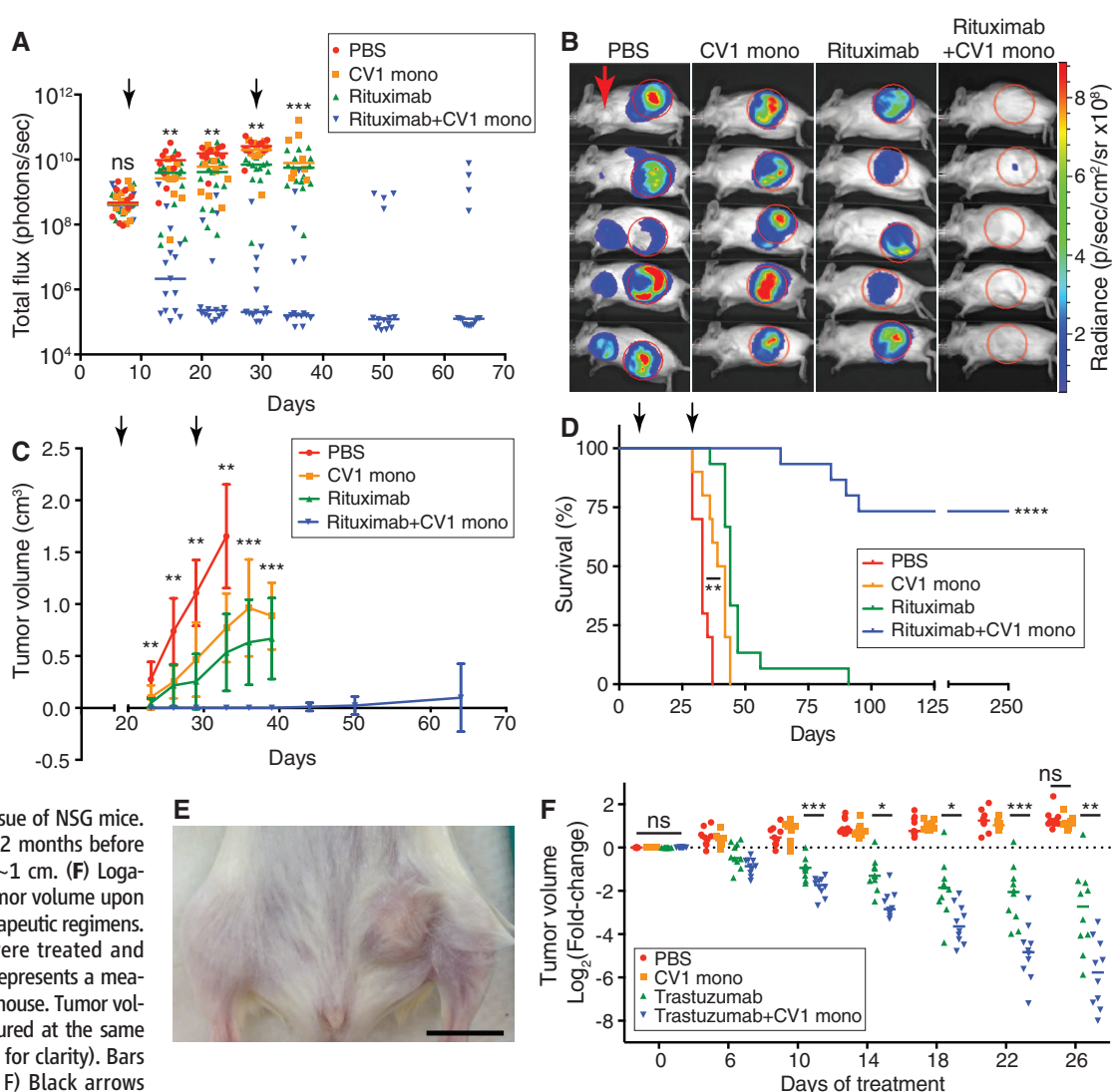
body to CD20 (fig. S7, A and B). Using a panel of recombinant antibodies to CD20 that contain the rituximab variable region and differing heavy-chain isotypes, we found that CV1 monomer was able to augment phagocytosis in response to all human IgG subclasses (fig. S7C). Therefore, the high-affinity SIRP α monomers could act as universal adjuvants to tumor-specific antibodies.

We next evaluated these principles in vivo by investigating the activity of the high-affinity SIRP α variants in mouse tumor models. We engrafted human tumors into NSG (NOD scid gamma) mice, which lack functional T, B, and natural killer (NK) cells but retain functional macrophages (10, 12, 22). NSG mice express a SIRP α allele that binds human CD47 and inhibits macrophage activity, thereby enabling in vivo evaluation of human CD47 blockade (10, 12, 19, 23–25). We tested CV1-hIgG4 in a model of human bladder cancer to determine whether a single molecule combining a high-affinity SIRP α do-

main with a prophagocytic signal could act as a single agent for cancer. Green fluorescent protein (GFP)–luciferase⁺ 639-V bladder cancer cells were subcutaneously engrafted into NSG mice. Treatment with CV1-hIgG4 inhibited tumor growth (Fig. 3, A and B) and produced a significant benefit in survival even after discontinuing treatment (Fig. 3C). In CV1-hIgG4-treated mice, palpable stromal tissue developed around the sites of tumor engraftment that contained small tumor nodules embedded in an inflammatory infiltrate containing macrophages with evidence of phagocytosis (fig. S8).

Although wild-type human SIRP α does not bind mouse CD47, the high-affinity SIRP α variants acquired cross-reactivity with mouse CD47 (fig. S10). Thus, our in vivo models allow for evaluation of efficacy in the presence of a large “antigen sink” and toxicity due to CD47 expression on normal mouse cells. Examination of the blood of treated mice revealed that CV1-hIgG4

Fig. 4. High-affinity SIRP α monomers enhance the efficacy of therapeutic antibodies in vivo. (A) Growth of GFP-luciferase⁺ Raji lymphoma tumors upon daily treatment with PBS, 200 μ g CV1 monomer, 200 μ g rituximab, or rituximab plus CV1 monomer (200 μ g each), as evaluated by bioluminescence imaging. Ten to 15 mice per group were treated and analyzed, and each data point represents a measurement from an independent mouse. Bars indicate median values. (B) Representative bioluminescence images of mice on last day of treatment (day 29 after engraftment). Red circles indicate sites of primary tumors; red arrow indicates site of metastases to axillary lymph nodes. (C) Tumor volume measurements of treated mice. Data are mean \pm SD. (D) Survival of treated mice over time. (E) Representative pre-treatment image of Her2/neu⁺ BT474M1 human breast tumors engrafted into the mammary tissue of NSG mice. Tumors were allowed to grow ~2 months before initiating treatment. Scale bar, ~1 cm. (F) Logarithmic fold-change in breast tumor volume upon treatment with the indicated therapeutic regimens. Eight to 10 mice per group were treated and analyzed, and each data point represents a measurement from an independent mouse. Tumor volumes for all cohorts were measured at the same time points (data are staggered for clarity). Bars indicate median values. (A to F) Black arrows indicate the start and stop of the treatment period. ns, not significant; * P < 0.05; ** P < 0.01; *** P < 0.001; **** P < 0.0001 for antibody alone versus combination therapy, or as indicated otherwise, by Kruskal-Wallis with Dunn's correction [(A) and (C)] or Mann-Whitney test with Bonferroni correction for the indicated comparisons (F).



coated all mouse blood cells (fig. S9A) and resulted in the development of chronic anemia as a side effect of therapy (fig. S9, B and C). No toxicity to other blood lineages was observed (fig. S9C). Red blood cell loss has also been observed with antibodies to mouse CD47 (12), consistent with these findings.

We further examined the safety of the high-affinity SIRP α variants in a toxicity study with cynomolgus macaques, which express a CD47 ortholog that is nearly identical to human CD47 (fig. S11, A and B). A single low-dose [1.5 mg per kg of weight (mg/kg)] injection of high-affinity SIRP α -Fc into two monkeys produced a substantial drop in red blood cells (fig. S11, C and D), similar to our findings in mice. By contrast, no hematologic toxicity was observed in a monkey treated with a dose escalation of high-affinity SIRP α monomer from 0.3 mg/kg to 10 mg/kg. No toxicity to other blood lineages or organ systems was detected in any of the monkeys, nor did we detect evidence of anaphylaxis (fig. S11, D and E). These findings further demonstrate that a single molecule that blocks CD47 and contains a phagocytic stimulus, such as antibody Fc chains, produces toxicity. We therefore surmised that the high-affinity SIRP α monomers, along with use of an independent antibody, may offer an alternative and improved strategy for targeting CD47.

To explore the *in vivo* potential of the high-affinity SIRP α monomers, combination with rituximab was evaluated in a localized model of Raji cell lymphoma. Beginning 8 days after engraftment (fig. S12A), mice received a 3-week course of daily treatment with either vehicle, CV1 monomer alone, rituximab alone, or a combination of rituximab plus CV1 monomer. Treatment with CV1 monomer or rituximab alone only slowed tumor growth, whereas the combination therapy completely eliminated tumors in the majority of mice, and the effects persisted after treatment was stopped (Fig. 4, A to D, and fig. S12B). During the course of treatment, no toxicity to red blood cells or other hematologic lineages was observed (fig. S13). The effects of each therapy translated to respective trends in survival (Fig. 4D). The combination therapy remained effective against large Raji tumors (fig. S14, A and B). Additionally, we administered the high-affinity SIRP α monomers in combination with alemtuzumab (antibody to CD52), a second therapeutic antibody targeting Raji lymphoma cells (26). Combination therapy significantly inhibited tumor growth and increased survival (fig. S15). Together, these findings validate our strategy as a safe and effective approach to antagonizing CD47 and provide a proof-of-concept demonstration that the high-affinity SIRP α monomers can augment the efficacy of therapeutic antibodies *in vivo*.

We performed immunohistochemical staining of the large Raji tumors after treatment to ex-

amine macrophage infiltration. Compared with rituximab alone, tumors receiving combination treatment showed extensive macrophage infiltration (fig. S14, C and D). The extent of macrophage infiltration and therapeutic efficacy *in vivo* paralleled the degree of phagocytosis *in vitro* by NSG mouse macrophages (fig. S14E). Together, these findings indicate that macrophages are effector cells for the CV1 monomer/rituximab therapy, as has previously been confirmed for rituximab and antibodies to CD47 (9, 10).

In a third model, Her2/neu⁺ BT474M1 breast cancer cells were engrafted into the mammary tissue of female NSG mice, and tumors were allowed to grow to ~1 cm in diameter (~200 mm³) (Fig. 4E). Treatment with CV1 monomer alone had no effect on tumor growth, whereas trastuzumab alone was able to reduce tumor volume over time (Fig. 4F). The addition of CV1 monomer to the antibody regimen enhanced tumor regression (Fig. 4F), consistent with the results observed with rituximab and alemtuzumab.

Our findings support a new model for the action of CD47-targeting agents (fig. S16). As observed with high-affinity SIRP α monomers, blockade of CD47 alone does not induce macrophage activation but instead lowers the threshold for phagocytosis. The combination of high-affinity SIRP α monomers with an independent, tumor-specific antibody directs macrophage attack against cancer cells without toxicity to normal cells expressing CD47. These findings are consistent with previous studies showing that disruption of the CD47/SIRP α axis potentiates responses to therapeutic antibodies (6, 10, 11). Due to their immense potential as targeted therapies, over 100 antibodies are under clinical investigation (27). Although antibodies have demonstrated considerable clinical success thus far, they often elicit limited responses, and relapse is common after treatment (28–30). We have developed reagents that broadly enhance the efficacy of tumor-specific antibodies and, thus, could act as universal adjuvants to antibody therapies. Overall, this study deepens our knowledge of macrophage responses to malignant cells and supports further evaluation of the high-affinity SIRP α reagents as immunotherapies for cancer.

References and Notes

1. D. Hanahan, R. A. Weinberg, *Cell* **144**, 646–674 (2011).
2. D. R. Leach, M. F. Krummel, J. P. Allison, *Science* **271**, 1734–1736 (1996).
3. A. J. Korman, K. S. Peggs, J. P. Allison, *Adv. Immunol.* **90**, 297–339 (2006).
4. G. L. Beatty *et al.*, *Science* **331**, 1612–1616 (2011).
5. P. A. Oldenborg *et al.*, *Science* **288**, 2051–2054 (2000).
6. P. A. Oldenborg, H. D. Gresham, F. P. Lindberg, *J. Exp. Med.* **193**, 855–862 (2001).
7. S. J. Gardai *et al.*, *Cell* **123**, 321–334 (2005).
8. S. Jaiswal *et al.*, *Cell* **138**, 271–285 (2009).
9. R. Majeti *et al.*, *Cell* **138**, 286–299 (2009).
10. M. P. Chao *et al.*, *Cell* **142**, 699–713 (2010).

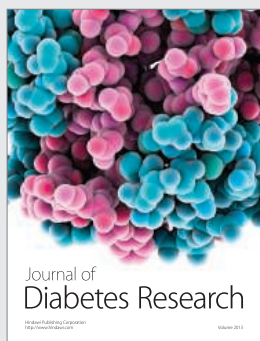
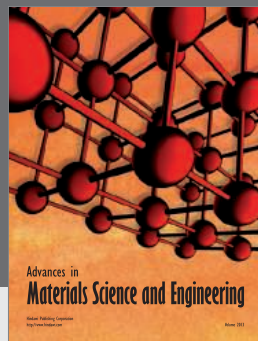
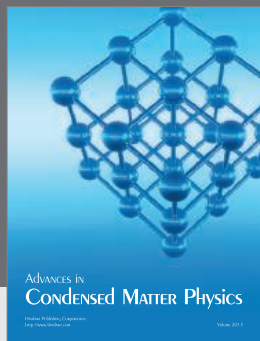
11. X. W. Zhao *et al.*, *Proc. Natl. Acad. Sci. U.S.A.* **108**, 18342–18347 (2011).
12. S. B. Willingham *et al.*, *Proc. Natl. Acad. Sci. U.S.A.* **109**, 6662–6667 (2012).
13. B. Edris *et al.*, *Proc. Natl. Acad. Sci. U.S.A.* **109**, 6656–6661 (2012).
14. R. A. Beckman, L. M. Weiner, H. M. Davis, *Cancer* **109**, 170–179 (2007).
15. M. A. Tabrizi, L. K. Roskos, *Drug Discov. Today* **12**, 540–547 (2007).
16. G. Brooke, J. D. Holbrook, M. H. Brown, A. N. Barclay, *J. Immunol.* **173**, 2562–2570 (2004).
17. D. Hatherley *et al.*, *Mol. Cell* **31**, 266–277 (2008).
18. D. Hatherley, K. Harlos, D. C. Dunlop, D. I. Stuart, A. N. Barclay, *J. Biol. Chem.* **282**, 14567–14575 (2007).
19. K. Takenaka *et al.*, *Nat. Immunol.* **8**, 1313–1323 (2007).
20. M. Seiffert *et al.*, *Blood* **94**, 3633–3643 (1999).
21. I. Stancovski *et al.*, *Proc. Natl. Acad. Sci. U.S.A.* **88**, 8691–8695 (1991).
22. L. D. Shultz *et al.*, *J. Immunol.* **174**, 6477–6489 (2005).
23. A. P. Theodorides *et al.*, *J. Exp. Med.* **209**, 1883–1899 (2012).
24. T. Yamauchi *et al.*, *Blood* **121**, 1316–1325 (2013).
25. P. L. Rodriguez *et al.*, *Science* **339**, 971–975 (2013).
26. R. Lapalombella *et al.*, *Clin. Cancer Res.* **14**, 569–578 (2008).
27. J. M. Reichert, E. Dhimolea, *Drug Discov. Today* **17**, 954–963 (2012).
28. D. G. Maloney *et al.*, *Blood* **90**, 2188–2195 (1997).
29. C. L. Vogel *et al.*, *J. Clin. Oncol.* **20**, 719–726 (2002).
30. E. Van Cutsem *et al.*, *N. Engl. J. Med.* **360**, 1408–1417 (2009).

Acknowledgments: The authors wish to thank members of the Weissman and Garcia laboratories for helpful advice and discussions. The authors thank R. Majeti, J. Liu, and the CD47 Disease Team for discussions and for providing antibodies to CD47. The authors thank T. Storm, L. Jerabek, H. Contreras-Trujillo, A. McCarty, S. Jaiswal, B. di Robilant, S. Varma, T. Naik, S. Willingham, H. Kohrt, N. Goriatcheva, D. Waghray, and S. Fischer for technical assistance, discussions, and reagents. The data presented in this paper are tabulated in the main paper and the supplementary materials. Atomic coordinates and structure factors of the FD6:CD47 complex (PDB code 4KJY) have been deposited in the Protein Data Bank. Research reported in this publication was supported by the National Cancer Institute (F30CA168059 to K.W. and CA139490 to I.L.W.), the National Institute of Diabetes and Digestive and Kidney Diseases (F30DK094541 to A.M.R.), the Stanford Medical Scientist Training Program (NIH-GM07365 to K.W. and A.M.R.), the Stanford University SPARK Program (to K.W. and A.M.R.), the Deutsche Forschungsgemeinschaft (VO 1976/1 to A.K.V.), the Joseph and Laurie Jacob Gynecologic/Ovarian Cancer Fund (to I.L.W.), the Virginia and D. K. Ludwig Fund for Cancer Research (to I.L.W.), and the Howard Hughes Medical Institute (to K.C.G.). The content of this manuscript is solely the responsibility of the authors. K.W., A.M.R., A.M.L., I.L.W., and K.C.G. have filed a patent describing the high-affinity SIRP α reagents.

Supplementary Materials

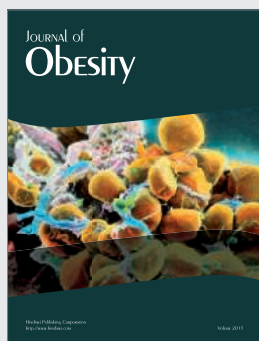
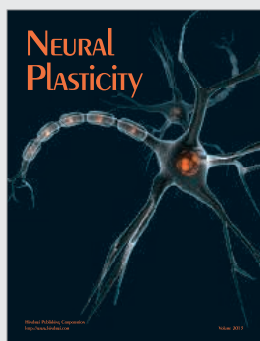
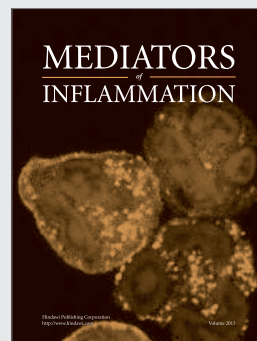
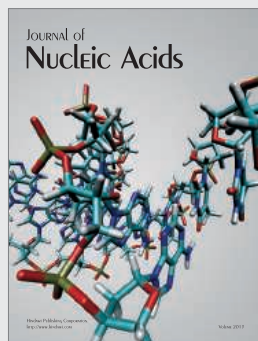
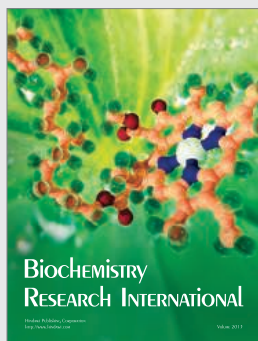
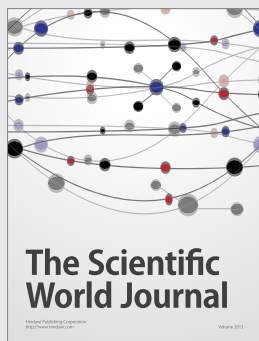
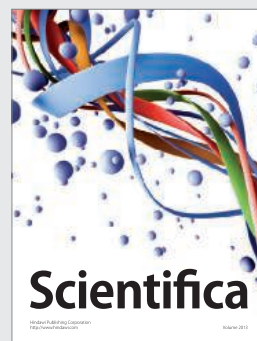
www.sciencemag.org/cgi/content/full/science.1238856/DC1
Materials and Methods
Supplementary Text
Figs. S1 to S16
Tables S1
Movies S1 and S2
References (31–38)

8 April 2013; accepted 10 May 2013
Published online 30 May 2013;
10.1126/science.1238856




Hindawi

Submit your manuscripts at
<http://www.hindawi.com>



What can RabMAbs[®] do for you?

abcam[®]
discover more

Rabbit Monoclonal Antibodies
( **RabMAbs**) offer multiple advantages to bring you the highest quality antibody possible.



#6

Novel Epitopes

#7


Multiple Applications

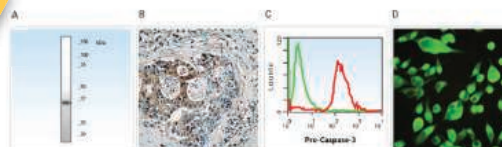
#8

Ideal for use on mouse model

#1

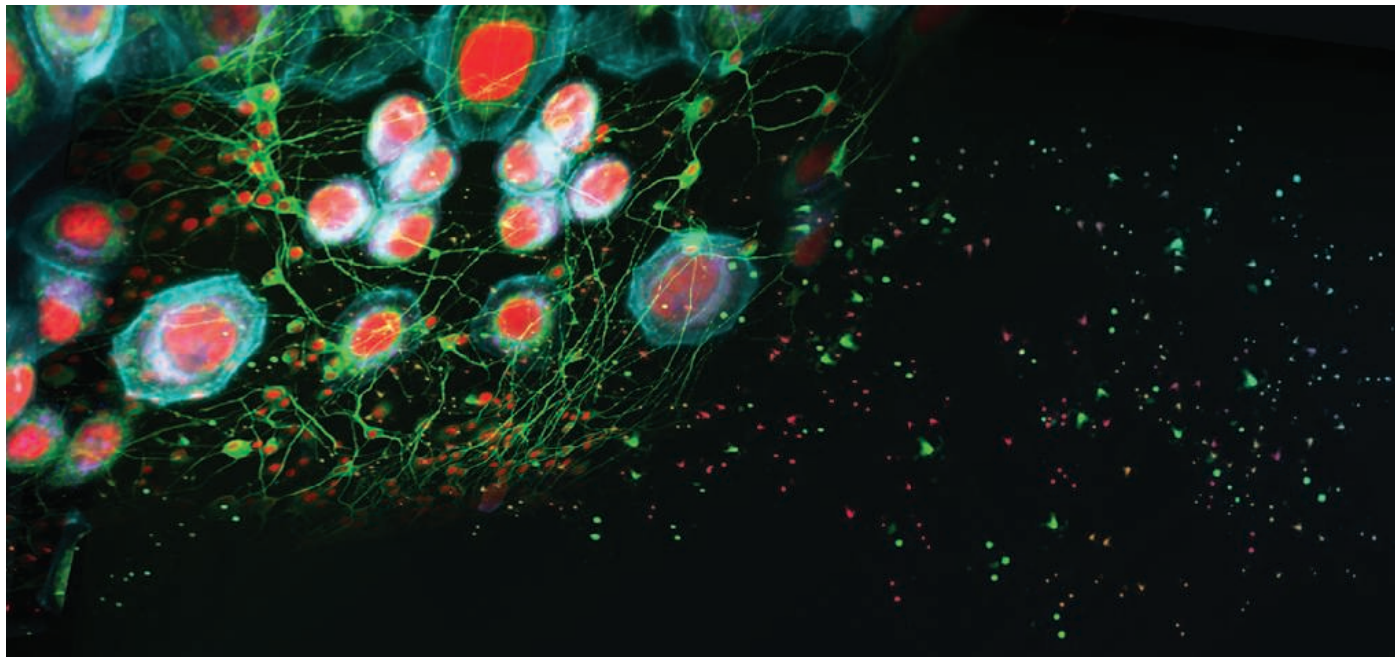
Low Background

 **RabMAbs[®]** are tested in multiple applications (WB, IHC, ICC/IF, IP and FACS) and multiple species (Human, Mouse and Rat) before release.



Validation data for Caspase-3 (Pro) RabMAb (ab32150) in A) WB on HeLa cell lysate, B) IHC on FFPE cervical carcinoma tissue, C) FACS on Jurkat cells and D) ICC on HeLa cells.

Try a RabMAb and discover more at **abcam.com/rabmabs**



Explore the universe of the cell

Cell imaging and analysis technologies from GE Healthcare Life Sciences

From high-content assays with extensive data analysis, to high- and super-resolution cellular imaging, our cutting-edge technologies give you amazing depth and breadth of investigation, allowing you to analyze interactions as they happen and gain deeper insights into complex cellular mechanisms.

See more. Understand more. Discover more.

www.gelifesciences.com/cellimaging

New
IN Cell Analyzer 2200



IN Cell Analyzer 6000



DeltaVision™



DeltaVision OMX™



imagination at work

AAAS|2014 ANNUAL MEETING

13-17 FEBRUARY • CHICAGO

MEETING GLOBAL CHALLENGES:
DISCOVERY AND INNOVATION

President's Invitation

Dear Colleagues:

On behalf of the AAAS Board of Directors, it is my honor to invite you to join us in Chicago for the 2014 AAAS Annual Meeting, 13-17 February.

This year's theme — Meeting Global Challenges: Discovery and Innovation — will focus on finding sustainable solutions through inclusive, international, and interdisciplinary efforts that are most useful to society and enhance economic growth.

Attendees will have the opportunity to choose among a broad range of activities, including plenary and topical lectures by some of the world's leading scientists and engineers, multidisciplinary symposia, cutting-edge seminars, career development workshops, and an international exhibition. You and your family can also enjoy Family Science Days, a free event open to the public.

We look forward to seeing you in Chicago. Registration and housing open in early August.



Phillip A. Sharp



Philip A. Sharp
AAAS President and
Program Chair

Institute Professor,
Koch Institute
for Integrative
Cancer Research,
Massachusetts Institute
of Technology

www.aaas.org/meetings



Want to win a rather special prize in Stockholm, Sweden this December?



Winner's paper published in the journal *Science*

\$25,000 dollars grand prize

Awards held in Stockholm in December



Henrik Rygg / Image bank, Sweden

This December a rather special prize will be awarded in Stockholm, Sweden. The journal *Science* and SciLifeLab have come together to recognize and celebrate excellence in PhD research. The *Science* and SciLifeLab Prize has been established to support young scientists at the start of their career.

“Science has never been more exciting and, as leaders in science, we need to support and encourage young researchers today and tomorrow. This prize is a way of doing just that.”

Professor Mathias Uhlen, Director SciLifeLab

The grand prize winner of this major global award will have their paper published in the journal *Science* and receive \$25,000. Three runners up will receive a combined total of an additional \$10,000 in prize money.

The prizes will be presented in Stockholm, Sweden in the middle of December 2013.

To enter

You must be a recent Ph.D. graduate (awarded between January 1, 2011 and December 31, 2012).

Submissions must be in the form of a 1000 word essay, in English, on your thesis, highlighting the significance of its contribution and overall implications in the field. The four submission areas for this prize are:

- (1) Genomics / Proteomics / Systems Biology
- (2) Developmental Biology
- (3) Molecular and Cellular Biology
- (4) Environmental Life Science.

The deadline for submissions is August 15, 2013. The overall winning essay will be published in *Science*.

For further details and to enter, please go to: www.sciencemag.org/scilifelabprize

For over 130 years the journal Science has been the world's leading journal of original scientific research, global news and commentary.

SciLifeLab is a collaboration between four universities in Stockholm and Uppsala, Sweden, and is a pioneering center for large-scale biosciences with a focus on health and environmental research.

With the kind support of the Knut and Alice Wallenberg Foundation.

*Knut och Alice
Wallenbergs
Stiftelse*



SciLifeLab

BD Accuri™ C6 Systems

Choose a configuration precisely for gene expression studies



Plum new choices for
gene expression research.

Now there is a BD Accuri™ C6 to fit your precise application needs. The BD special order program offers the widest range of choice and flexibility to researchers, including BD Accuri C6 systems preconfigured for specific application requirements such as those in gene expression studies.

Choose from 1- or 2-laser custom systems designed with a selection of laser wavelengths, and light scatter and fluorescence detectors best suited for your desired application.

The preconfigured BD Accuri C6 systems for gene expression enable research using the fruit series of fluorescent proteins (such as Living Colors® mCherry,



Helping all people
live healthy lives

mPlum, and DsRed dyes) as well as Green and Yellow Fluorescent Proteins. Other preconfigured BD Accuri C6 systems for DNA/cell cycle assays include a near ultraviolet (375-nm) laser to excite DAPI, Hoechst, and propidium iodide (PI) dyes.

The BD special order program vigorously pursues new technologies and incorporates them into BD platforms to produce advanced and flexible products available for multicolor research.

To find out more about your choices by application or to discuss a custom configuration for your lab, visit bdbiosciences.com/go/screen

BD flow cytometers are Class 1 Laser Products.
For Research Use Only. Not for use in diagnostic or therapeutic procedures.
Living Colors® is a registered trademark of Clontech, Inc.
BD, BD Logo and all other trademarks are property of Becton, Dickinson and Company. © 2013 BD
23-14908-00

BD Biosciences
2350 Qume Drive
San Jose, CA 95131
bdbiosciences.com

Eppendorf Consumables—
it's Your sample



Future included

50 years of experience in highest quality

Eppendorf consumables are the result of 50 years constant improvement and development. With the new Eppendorf Tubes® 5.0 mL a new tube format in the medium volume range will complete the legendary Eppendorf Tubes family.

Laboratory processes will become easier and more convenient.

Purest assay results are no coincidence:

- > Unique features to make every day routines faster and easier
- > Minimized risk of chemical leaching from consumables
- > Purity grades tailored to even the highest requirements

www.eppendorf.com/consumables

Eppendorf®, the Eppendorf logo and Eppendorf Tubes® are registered Trademarks of Eppendorf AG, Germany. All rights reserved, including graphics and images. Copyright © 2013 by Eppendorf AG.



CELL CULTURE CHAMBERS

The x-well cell culture system consists of slide-based vessels in a range of materials and chamber formats with excellent microscopic properties and chemical resistance. Slides are available in PCA plastic, glass, and 170 µm coverglass fitted with a polystyrene flask or one-, two-, four-, and eight-well chambers. All slide surfaces are treated for the cultivation of adherent cells. The chamber of PCA plastic slides can be easily removed without tools after cultivation, leaving no adhesive residues on the slide. All x-well products are conveniently and economically sold per sterile tray of six.

Sarstedt

For info: 800-257-5101 | www.sarstedt.com

CELL CULTURE MEDIA

Achieving desirable cell densities can present a challenge when culturing certain cell types. To address this problem, SensiCell has been developed as a first-in-class media for the enhanced growth of cells that are difficult to culture, such as the NK-92 human natural killer, BeWo human placental choriocarcinoma, and CaCo-2 human colorectal adenocarcinoma cell lines. SensiCell media are available in four types: RPMI, DMEM, DMEM/F12, and MEM. Each formulation includes GlutaMAX as a stable source of glutamine as well as a proprietary mixture of vitamins, amino acids, and other nutrients to enhance cell growth beyond limits typically achieved in traditional basal media. SensiCell is designed to be used with standard supplementation of 10% fetal bovine serum. With these proven benefits, SensiCell media offer researchers a new alternative for obtaining consistently healthy cultures of cells that are difficult to grow.

Life Technologies

For info: 800-955-6288 | www.lifetechnologies.com/sensicell

MICROPLATE READERS

The Biochrom EZ Read range of microplate readers has been developed to meet the specific application needs of scientists. Biochrom has created the EZ Read microplate reader range by matching its expertise in absorbance measurement with requests from scientists and technicians to make their experimental workflow easier and more effective. Biochrom offers a comprehensive solution for scientists running ELISA assays using Galapagos software's intuitive 'click and drag' approach for setup and analysis as well as offering a shaker/incubator and a microplate washer to complete the ELISA workflow. Biochrom's EZ Read range offers the broadest range of ELISA microplate readers so that scientists can choose the right instrument for their unique laboratory environment. The extensive EZ Read instrumentation range enables scientists to measure all their absorbance assays such as ELISA, total protein and cell viability assays, without the need to buy and install extra filters.

Biochrom

For info: +44-(0)-1223-423723 | www.biochrom.co.uk

DIFFERENTIATION MEDIUM

The OsteoMAX-XF is the first fully defined, xeno-free human mesenchymal stem cell differentiation medium for the differentiation of mesenchymal stem cells into osteocytes. Mineralization can be detected in less than one week, whereas competing products that contain serum require approximately 21 days to produce similar levels of bone formation. The formulation, licensed from Plasticell, produces more consistent and potent osteogenic differentiation than currently available formulations, enabling a more reproducible, efficient method for creating bone tissue and advancing research in bone disease and healing. Researchers will now be able to derive bone tissue from MSCs in a more rapid and consistent manner. The optimized, single application osteogenic medium was developed using Plasticell's combinatorial screening system that performed a rapid screen of 3,375 combinations of fully defined cell culture media, equivalent to hundreds of thousands of combinations of media components.

EMD Millipore

For info: 800-645-5476 | www.millipore.com/stemcell

AUTOMATED COLONY COUNTER

The new, cost-effective colony counting system, aCOLyte 3, is ideal for microbiologists who need to significantly increase their throughput and improve count accuracy. The automated colony counter is designed for a rapid count of pour, spread, and spiral plates. The system can read plates of up to 90 mm in seconds, generating precise plate count results up to 10 times faster than manual counts. The numerical count data and plate images can be directly transferred to Excel or OpenOffice to avoid errors in data transfer, ensuring accurate GLP compliant result reporting and archiving every time. The aCOLyte 3 provides full color image display and comes complete with software based on Synbiosis' powerful ProtoCOL 3 software. The aCOLyte 3 is lit by white LEDs mounted above and below the plate, enabling accurate detection of colonies as small as 0.3 mm, with the option to have a detachable screen fitted to prevent any reflection or glare affecting the count.

Synbiosis

For info: +44-(0)-1223-727125 | www.synbiosis.com/aCOLyte-3

Electronically submit your new product description or product literature information! Go to www.sciencemag.org/products/newproducts.dtl for more information.

Newly offered instrumentation, apparatus, and laboratory materials of interest to researchers in all disciplines in academic, industrial, and governmental organizations are featured in this space. Emphasis is given to purpose, chief characteristics, and availability of products and materials. Endorsement by Science or AAAS of any products or materials mentioned is not implied. Additional information may be obtained from the manufacturer or supplier.

Call for Papers

Science Translational Medicine

Integrating Medicine and Science

The peer-reviewed research journal publishes papers that identify and fill the scientific knowledge gaps at the junction of basic research and medical application in order to accelerate the translation of scientific knowledge into new ways of preventing, diagnosing, and treating human disease.

Our broad scope includes:

- Cardiovascular Disease
- Neuroscience/
Neurology/Psychiatry
- Infectious Diseases
- Cancer
- Health Policy
- Bioengineering
- Chemical Genomics/
Drug Discovery
- Phase I/II Clinical Trials
- Applied Physical Sciences
- Drug Delivery
- Gene Therapy/
Regenerative Medicine
- Cell Culture, Animal,
and Human Studies
- Other Interdisciplinary
Approaches to Medicine

Chief Scientific Advisor

Elazer Edelman, M.D., Ph.D.

Chief Scientific Advisor

Garret A. FitzGerald, M.D.

Editor

Katrina L. Kelner, Ph.D.

Managing Editor

Orla M. Smith, Ph.D.

Senior Editor

Kelly LaMarco, Ph.D.

Submit your research at
www.submit2scitranslmed.org

Subscribing to **Science Translational Medicine** ensures that you and your colleagues have access to the latest studies and breakthroughs in the field of translational medicine.

To recommend a subscription, visit
ScienceOnline.org/recommend



For more information, contact
scitranslmededitors@aaas.org



ScienceTranslationalMedicine.org

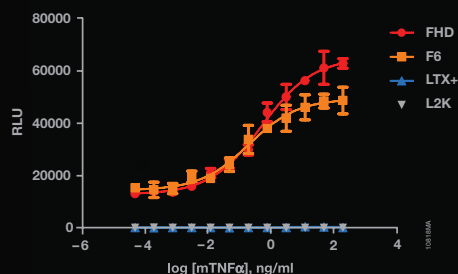
FuGENE[®] HD

Illuminate Real Biology

Don't let old toxic transfection technology get in the way of your science. FuGENE[®] HD provides the power to transfect virtually any cell type while maintaining biologically relevant cell signaling responses.

Key applications:

- Cancer Biology
- Stem Cell Research
- Developmental Biology
- Neurobiology
- Immunobiology
- Lentivirus Production
- CHO Cell Protein Production



In this BaF3 cell model of NF-κB luciferase induction, only FuGENE[®] HD and FuGENE[®] 6 are able to create a usable assay.

To discover the power of FuGENE[®] HD for your biology, request a free sample at www.promega.com/pathwaybiology

Professor of Systems Neuroscience Professor of Neurogenetics

The Department of Health Sciences and Technology (www.hest.ethz.ch) at ETH Zurich invites applications for the above-mentioned positions.

Professor of Systems Neuroscience: The Department is looking for an outstanding neurobiologist to establish a strong and dynamic research program in the field of systems neuroscience. The research is expected to focus on the molecular and cellular mechanisms of complex functions of the nervous system, both in health and disease. The successful candidate should have an outstanding international reputation and visibility, and a strong track record. He or she is expected to develop an original, interdisciplinary and exciting research program. Solid expertise in molecular and cellular biology at the level of entire organisms, in combination with developmental biology, neurophysiology, neuroimaging and/or behavioral science is expected. **Professor of Neurogenetics:** Candidates are expected to build a solid and independent research program that studies the relationship between the genome and/or epigenome, and functions of the nervous system, neurodevelopmental processes or behavior, and the underlying molecular and cellular mechanisms, both in health and disease. Strong expertise in genetics and/or epigenetics at the level of whole organisms, a solid background in molecular biology, physiology, behavioral and cognitive neurosciences is required. The successful candidate should have an excellent track record in the field of neurogenetics. Translation to humans and/or clinical applications is a plus.

For both positions, expertise in the design and use of animal and cellular models, and of state-of-the-art in vitro and in vivo methods of analyses are highly desired. Both candidates shall undertake leadership functions in research, including the mentoring of junior group leaders, and participate in teaching at undergraduate and postgraduate level in the fields of neurobiology, cell biology, and biomedical sciences. They are also expected to establish links with the clinic, and contribute to translational research and the transfer of knowledge and technology to the medical field. The successful candidates will teach at the undergraduate (German or English) and graduate (English) level.

The new professors will be member of the Department of Health Sciences and Technology and will strengthen neurosciences in this Department. They are also expected to reinforce cooperation with other strategic research areas in the Department that include medical engineering, movement sciences and sport, as well as food and nutrition. Together with the Neuroscience Centre Zurich and Life Science Zurich, two research and teaching platforms, the Department offers outstanding opportunities to build an interdisciplinary research program and provides multiple technology platforms including genomics, epigenomics and proteomics facilities, animal and human imaging centers, advanced microscopy platforms and animal facilities. Besides direct contact with other groups in the Department, multiple opportunities for interaction with researchers in the Department of Biology, and clinical research at the Medical Faculty of the University of Zurich and at local hospitals are provided through an active and lively academic community, and research consortia such as SystemsX.ch and National Centers of Competence in Research (NCCRs).

Please apply online at www.facultyaffairs.ethz.ch

Applications should include a curriculum vitae, a list of publications, and a statement of future research and teaching interest. The letter of application should be addressed to **the President of ETH Zurich, Prof. Dr. Ralph Eichler. The closing date for applications is 31 October 2013.** ETH Zurich is an equal opportunity and family friendly employer and is further responsive to the needs of dual career couples. In order to increase the number of women in leading academic positions, we specifically encourage women to apply.

There's only one

Science



Science Careers Advertising

For full advertising details, go to ScienceCareers.org and click For Employers, or call one of our representatives.

Tracy Holmes
Worldwide Associate Director
Science Careers
Phone: +44 (0) 1223 326525

THE AMERICAS

E-mail: advertise@sciencecareers.org
Fax: 202-289-6742

Tina Burks
East Coast/West Coast/South America
Phone: 202-326-6577

Marci Gallun
Midwest/Canada
Phone: 202-326-6582

Candice Nulsen
Corporate
Phone: 202-256-1528

Online Job Posting Questions
Phone: 202-312-6375

EUROPE/INDIA/AUSTRALIA/ NEW ZEALAND/REST OF WORLD

E-mail: ads@science-int.co.uk
Fax: +44 (0) 1223 326532

Axel Gesatzki
Phone: +44 (0)1223 326529

Kelly Grace
Phone: +44 (0) 1223 326528

JAPAN

Yuri Kobayashi
Phone: +81-(0)90-9110-1719
E-mail: ykobayas@aaas.org

CHINA/KOREA/SINGAPORE/ TAIWAN/THAILAND

Ruolei Wu
Phone: +86-1367-1015-294
E-mail: rwu@aaas.org

All ads submitted for publication must comply with applicable U.S. and non-U.S. laws. *Science* reserves the right to refuse any advertisement at its sole discretion for any reason, including without limitation for offensive language or inappropriate content, and all advertising is subject to publisher approval. *Science* encourages our readers to alert us to any ads that they feel may be discriminatory or offensive.

Science Careers

From the journal *Science*



ScienceCareers.org

GPCR NMR Faculty Position at the iHuman Institute, ShanghaiTech University (上海科技大学)

The iHuman Institute is established to encourage interdisciplinary research combining chemistry, biology, imaging, and structural biology of the cellular components involved in human cell signaling, with a special focus on G-protein-coupled receptors and their intracellular signaling partners. Academic basic science and applied industry research will be integrated, providing researchers with unique career opportunities. The Institute is recruiting 20 regular tenured and tenure-track faculty to generate an intellectually stimulating environment.

NMR Faculty Position and Qualifications:

The iHuman Institute at ShanghaiTech University is hiring a Professor specializing in the area of solution NMR spectroscopy focused specifically around human G-protein-coupled receptors (GPCRs). The position can be filled either at the level of a tenured senior faculty or a tenure-track junior faculty. The successful applicant will be part of an interdisciplinary research team including mentoring and guidance from Professors Raymond Stevens (GPCR expertise) and Kurt Wüthrich (NMR expertise). The goal is to apply cutting-edge NMR technology towards understanding GPCR structure and function, and to provide new foundations for GPCR-targeted drug discovery. Final decisions on the configuration of the new high-field NMR facility will be made in contact with the successful applicant for the NMR faculty position.

Senior position applicants are expected to be leading scientists in their research area. Junior level position applicants should have a Ph.D. degree in physical or life sciences as well as postdoctoral experience. The successful applicant will be expected to establish an independent, internationally recognized research program and to hire and supervise postgraduate, graduate and undergraduate students.

Computational Biology Faculty Position and Qualifications:

The iHuman Institute at ShanghaiTech University is hiring a Professor specializing in the area of Computational Biology. Researchers interested in the area of computational GPCR biology or GPCR chemistry are encouraged to apply. The iHuman Institute is incredibly strong in the area of x-ray crystallography and NMR of GPCRs, including structure based drug discovery. Computational biologists and chemists interested in understanding cell biology, molecular recognition, and drug discovery should apply.

Senior position applicants are expected to be leading scientists in their research area. Junior level position applicants should have a Ph.D. degree and at least 5 years of experience in the area of computational methods. The successful applicant will be expected to establish an independent, internationally recognized research program and to supervise graduate and undergraduate students.

Initial Research Support Package: The Institute will provide internationally competitive start-up funds plus support of Research Associates and Post-Doctoral Fellows. Research laboratory and office space will be provided to match the research needs. Our faculty will also have access to the research facilities and resources of the Chinese Academy of Science.

Compensation and Benefits: Starting salary will be competitive at the international level and commensurate with qualifications and experience. We offer a comprehensive benefits package including health and retirement benefits as well as on campus housing renting at a reduced rate. The ShanghaiTech University will also sponsor applications of national and local Talent Programs based on individuals' qualification and experience. The iHuman Institute is located in Shanghai, China, which is an exciting and rapidly growing global center of excellence for scientific research.

Application Procedure:

Submit a cover letter, a 2-3 page statement of research interests, a CV and the names and addresses of three individuals who can serve as references to the mail addresses given below:

The iHuman Institute
ShanghaiTech University, Building 8, 319 Yueyang Road, Shanghai 200031, China

Email: iHuman@shanghaitech.edu.cn

Review of applications will start immediately and will continue until positions are filled.

For more information, please visit our website: www.shanghaitech.edu.cn



SCIENTIFIC DIRECTOR, BAR HARBOR CAMPUS

The Jackson Laboratory (JAX) is seeking applications and nominations for the position of Scientific Director of the Bar Harbor campus. The Scientific Director reports to the President and Chief Executive Officer and is a member of the senior leadership team.

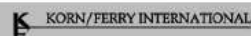
The Jackson Laboratory is an independent, non-profit biomedical research institution and NCI-designated Cancer Center with locations in Bar Harbor, Maine (established 1929); Sacramento, California (established 2001); and Farmington (established 2011). To face the emerging challenges generated by the revolution in genomics technologies, JAX has recruited Dr. Edison Liu as President and CEO and is creating a new position, Scientific Director of our Bar Harbor campus. The Bar Harbor campus remains the primary site for, and an international leader in, the study of mammalian genetics using the mouse model, while the Farmington campus is devoted to clinical genomics.

This position offers a unique and exciting opportunity to develop and implement the overall scientific vision for JAX Bar Harbor and to plan and oversee basic fundamental and applied research programs. The Scientific Director will play a key role in creating and maintaining a nurturing research environment that encourages creativity, collaboration among scientists from different disciplines, effective mentoring of faculty, and efficient utilization of resources.

Candidates will have a Ph.D., an M.D., or both, with progressive administrative experience, preferably in a research intensive institute or academic setting. He/she will be able to plan and meet budgets, measure and improve productivity and outcomes, recruit and mentor faculty, and take appropriate business risks to achieve goals. A well respected scientist and successful leader of a basic science program from an interdisciplinary institute or academic entity of at least comparable size and scope is preferred.

Korn/Ferry International is assisting The Jackson Laboratory with this important search. Please forward, as soon as possible, nominations of appropriate candidates to: **Warren E. Ross, M.D., c/o Betsy Messina** (betsy.messina@kornferry.com), Korn/Ferry International, 1835 Market Street, Suite 2000, Philadelphia, PA 19103.

The Jackson Laboratory is an Equal Opportunity/Affirmative Action Employer and Educator.



COLLEGE OF VETERINARY MEDICINE
AND BIOMEDICAL SCIENCES

Assistant or Associate Professor - Computational Biologist

The Department of Microbiology, Immunology and Pathology, College of Veterinary Medicine and Biomedical Sciences, Colorado State University, invites applications and nominations for a tenure-track faculty appointment (Assistant or Associate Professor) in computational biology, emphasizing the fundamental interactions that occur at the host-pathogen interface. This position offers an exciting opportunity for an individual to interact with faculty in a dynamic and highly successful department. The successful candidate will have a PhD and/or DVM or MD degree (or equivalents), demonstrated excellence in scholarly activity and research in computational biology, with an emphasis on host-pathogen systems, which could include pathogen genomics, computational immunology, host responses to pathogen infection and systems biology. It is expected that the successful candidate will have an established record demonstrating expertise in computational biology and analysis of data derived from post-genomic technologies and platforms including microarrays, next generation sequencing or mass spectrometry; evidence of the ability to establish an extramurally funded research program; and experience in teaching and mentoring students and fellows. Computational biology experience across several species is desired. The candidate will be expected to develop new courses in his/her area of expertise and participate in the teaching of existing courses. The full position description is available at <http://csu-cvmb.colostate.edu/documents/mip-open-position-computational-biologist.pdf>.

Applications will be accepted until the position is filled. However, for full consideration, apply by **September 1, 2013**. Applicants should send electronically a letter expressing their interest and qualifications for the position, a current curriculum vita, and the names, addresses, and telephone numbers of three references to: **Andrea Franson, Computational Biologist Search Committee, Department of Microbiology, Immunology and Pathology, College of Veterinary Medicine and Biomedical Sciences, 1619 Campus Delivery, Colorado State University, Fort Collins, CO 80523; Email: andrea.franson@colostate.edu. Request additional information by: Phone: 970-491-7861; E-Mail: andrea.franson@colostate.edu; Fax: 970-491-0603**

Colorado State University conducts background checks on all final candidates. CSU is an EO/EA/AA Employer.



Hiring Vice President at South University of Science and Technology (SUSTC) Shenzhen, China

The South University of Science and Technology, China (SUSTC) invites applications and nominations for Vice President (Academic Affairs) and Vice President (Education). SUSTC is committed to **excellence in teaching and research**; therefore, it offers internationally competitive salaries, fringe benefits, retirement and housing subsidy to the Vice Presidents. The modern campus also offers pleasant working conditions.

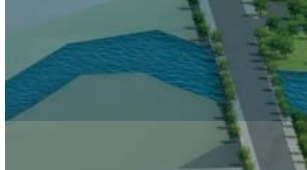
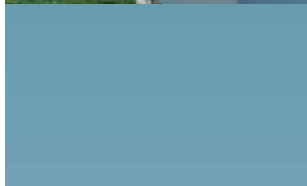
About SUSTC

SUSTC is a public institution funded by the municipal of Shenzhen, a special economic zone city in southern China. The University receives full financial support from the municipal. Set on five hundred acres of wooded landscape in the picturesque Nanshan (South Mountain) area, the campus offers an idyllic environment suitable for learning and scholarship. SUSTC engages in basic and problem-solving research of lasting impact to benefit society and mankind. Key research areas of the university include but not limited to: *Neural and Cognitive Sciences, Biology and Gene Engineering, Modern Physics, Control and Modification of Materials, Nanoscience and Nanotechnology, Mathematics and Applied Mathematics, Molecular Chemistry and Catalysis, Large-Scale Computational Research, Robotics and Artificial Intelligence, Information Systems and Electronic Engineering, Modern Cities and future developments, Energy Sciences and technology, Environmental Sciences, Financial Mathematics and Engineering.*

The Vice President (Academic Affairs, VPAA) and Vice President (Education, VPE) report directly to the president. The **VPAA** provides strategic leadership in the development and implementation of academic and research programs. The **VPE** provides strategic leadership in student education and whole person development. Successful candidates are expected to be internationally renowned scholars with administrative experience and good communication skills. Excellent leadership and organizational skills are also important.

The teaching language at SUSTC is English or Putonghua. As we expect an international faculty, the majority of teaching materials and reference books will be in English and many classes will be conducted in English. With a very high faculty-to-student ratio, SUSTC is committed to delivering a student-centered education. Students at junior and senior years are expected to participate in research in Research Centers.

Send nominations, inquiries or applications to: hiring@sustc.edu.cn. All applications should include a detailed CV and a list of publications. Additional information on SUSTC is available on the University homepage <http://www.sustc.edu.cn>



Science Careers is the forum that answers questions.



Science Careers is dedicated to opening new doors and answering questions on career topics that matter to you. With timely feedback and a community atmosphere, our careers forum allows you to connect with colleagues and experts to get the advice and guidance you seek as you pursue your career goals.

Science Careers Forum:

- » Relevant Career Topics
- » Timely Advice and Answers
- » Community, Connections, and More!

Visit the forum and join the conversation today!



Your Future Awaits.



ScienceCareers.org



Yanshan University 2013 Worldwide Recruitment Plan

Yanshan University (YSU) is located in the historic coastal city of Qinhuangdao in Hebei and was accredited as one of the eighty-eight national key institutions of higher learning in China. YSU has 11 postdoctoral research stations, 11 disciplines conferring doctoral degrees, 5 national key disciplines and 4 key disciplines in national defense and 13 provincial key disciplines. It also has State Key Laboratory of Metastable Materials Science and Technology, National Engineering Research Center for Equipment and Technology of Cold Strip Rolling, Advanced Manufacture Technology and Equipment Research Center, and State Key Laboratory of Fundamental Science of Mechanical Structure and Material Science under Extreme Conditions for National Defense. YSU is recruiting for outstanding investigators to occupy the following honorable positions. These positions will not be closed for next several years.

1. **National Thousand Talents Program:** Long-term and short-term programs of "National Thousand Foreign Talents Program" and "National Thousand Young Talents Program."
2. **Chang Jiang Scholar:** Doctoral degree, full-time, under 45 for natural science and under 50 for liberal arts.
3. **Hundred Experts Program of Hebei Province:** Ph.D. from overseas university and associate professors in overseas institutions, 3 years of work continuously in YSU and no less than 9 months per year after employment.
4. **Yanshan Scholar:** Full time, under 50, assistant professor or equivalent for overseas applicant and professor with doctoral degree for domestic applicants.
5. **Excellent Doctors and Post-doctors:** Under 35, with academic excellence and research potential. 2013 recruitment website: <http://www.ysu.edu.cn/xqzl/zpjh.htm>

Salary, Start-up Package and Benefits: According to the policy recently issued by Yanshan University, "High-level Talents Training and Introduction Enforcement Measures", the recruited faculty at different academic levels will be supported with competitive salary, the start up package (competitive start-up funds and newly renovated office/lab), housing allowance and other possible benefits. All of the above offers are negotiable.

Contact us: The interesting candidates submit curriculum vitae in both of English and Chinese, PDFs of their publications and a detailed statement of research interests to Mr. Gaoyi Zhou, Mr. Linbao Pei, Mrs. Jie Ma, and/or Mrs. Qun Mei, Personnel Division of Yanshan University, 438 Hebei Avenue, Qinhuangdao, Hebei 066004, China; Tel: 0086-335-8071323, 0086-335-8074531; Fax: 0086-335-8047376; Email: rsczp@ysu.edu.cn. You will be contacted once we receive and finish the evaluation of your application for the position. Welcome to YSU and make your contribution to the future of our university!



UNIVERSITY of MARYLAND
SCHOOL OF MEDICINE

HEMATOLOGY/ONCOLOGY

The University of Maryland Greenebaum Cancer Center (UMGCC) is recruiting for senior hematology/oncology faculty interested in developing or furthering clinical research careers in Bone Marrow Transplant Cancer. The UMGCC has a long standing clinical and laboratory research program in all aspects of cancer. Its programs in many areas of oncology are expanding rapidly. We are looking for individuals interested in clinical and translational investigations and new drug development for malignancies. Academic rank, tenure status, and salary commensurate with experience. Candidates should be board certified in internal medicine and hematology/medical oncology. The University of Maryland, Baltimore encourages women and minorities to apply and is an AA/EEO/ADA Employer. Interested applicants should submit their CV to **Stephen W. Long, Associate Director for Administration, c/o Rhonda Reed** (rreed1@medicine.umaryland.edu).

The University of Maryland, Baltimore is an Equal Opportunity, Affirmative Action employer. Minorities, women, veterans and individuals with disabilities are encouraged to apply.

Please cite Position #03-309-740 when submitting your application.

Exciting developments in Materials Chemistry: are you ready to take the lead?

The Department of Chemical Engineering & Chemistry at Eindhoven University of Technology (TU/e) invites applications and nominations for

Three Professor Positions in Materials Chemistry



To further develop our research in the field of Materials Chemistry, we are looking for three inspiring leaders in this scientific domain. Will your research proposals lead to new breakthroughs and insights in Materials Chemistry? Are you attracted by the idea of a high tech working environment with close links to industry? And are you an inspiring role model for our researchers and students? If so, we would very much like to meet you.

Applicants from all areas in the field of Materials Chemistry will be considered, but those having expertise in polymer chemistry, physical chemistry or inorganic chemistry that interfaces with or complements existing research activities in the department will receive special consideration.

Polymer chemistry

The department has a strong tradition in supramolecular and polymer chemistry. Its well-known chain-of-knowledge approach has proved to be a key success factor in bringing fundamental insights in macromolecular synthesis and polymerization mechanisms to innovative polymer materials applications in areas as functional polymer systems, biorelated polymer systems, performance coatings and plastics. Excellent candidates are invited to present new, challenging and innovative proposals to further add to this chain-of-knowledge approach, leading to basic understanding of novel polymerization mechanisms, advanced molecular applications and innovative polymer material systems with superb properties and performance characteristics.

Physical chemistry

The department plans to install a new Chair position to focus on the physical chemistry of nano- and mesoscopic structures of soft condensed matter. Proposals from excellent candidates wanting to take the lead in this important field are welcomed. New developments and material applications are expected to follow from a basic understanding of the underlying physical chemistry of dynamical phenomena that take place at the dimensions and length scales where macromolecules, supramolecular structures and bulk (polymer) materials meet. State-of-the art characterisation of mesoscopic structures using scattering techniques, combined with fundamental understanding of the underlying kinetics and thermodynamics of the interactions at the relevant molecular and material dimensions, are key factors in any research program in this field.

Inorganic chemistry

The department invites applications of excellent candidates for the newly created Chair position focusing on the chemistry, synthesis and development of functional inorganic materials. Fundamental knowledge of the crystal structure, anisotropy, defects and stoichiometry of inorganic materials is key to the understanding and development of their advanced electric, optical, magnetic or other functional properties. Exciting developments are expected, for example in the synthesis of functional inorganic coatings for applications in electronic devices, as well as the synthesis and use of quantum structures with special optical, electric, catalytic or sensoric properties.

Requirements

Successful applicants will have an outstanding, internationally recognized record of research in their specific fields, together with a strong commitment to teaching, a proven record in research funding acquisition, active collaboration with academic research groups and industry, excellent communication skills and proven leadership qualities to manage a scientific group.

Information

Enquiries about these positions may be made to the Dean of the Department, Prof.dr.ir. J.C. Schouten, j.c.schouten@tue.nl. For information concerning conditions of employment, please contact Ms. Arianne Boekema, HR advisor a.d.boekema@tue.nl, tel. +31 40 2474960.

How to apply

For a detailed job description and to apply please visit our website: www.tue.nl/jobs. Application review will begin on 1 November 2013.

www.tue.nl/jobs

TU/e

Technische Universiteit
Eindhoven
University of Technology

Where innovation starts



Nontraditional Careers: Opportunities Away From the Bench Webinar

Want to learn more about exciting and rewarding careers outside of academic/industrial research? View a roundtable discussion that looks at the various career options open to scientists and strategies you can use to pursue a nonresearch career.

Now Available On Demand
www.sciencecareers.org/webinar

Produced by the
 Science/AAAS Business Office.

Science Careers
 From the journal *Science* AAAS

POSITIONS OPEN



POSTDOCTORAL POSITIONS in Glycoscience

Several Postdoctoral Fellowships are available at the Complex Carbohydrate Research Center (CCRC) of the University of Georgia (UGA) to work on an NIH supported Program Project Grant dealing with Chemistry and Biology of Glycosyltransferases. For more Information, visit [website: http://www.ccrc.uga.edu/employment/index.php](http://www.ccrc.uga.edu/employment/index.php). Participating investigators of this multidisciplinary research projects include **Drs. Geert-Jan Boons, Kelley Moremen, James Prestegard, Richard Steet and Lance Wells**. Interested candidates must hold a Ph.D., be highly motivated and have a strong background in one of the following fields of research: (1) mammalian glycosylation enzymes, protein expression/purification, and structural biology; (2) protein NMR spectroscopy; (3) chemoenzymatic synthesis of complex oligosaccharides; (4) cell biology to study altered trafficking of glycoconjugates in the context of human disease; or (5) glycomic, proteomic, and glycoproteomic analyses by mass spectrometry. Interested individuals should send their curriculum vitae, and the contact information of three references to: **Dr. Geert-Jan Boons, Complex Carbohydrate Research Center, University of Georgia, 315 Riverbend Road, Athens, GA 30602. Affirmative Action/Equal Employment Opportunity.**

ASSISTANT PROFESSOR of Pollinator Health & Sustainability University of Maryland, College Park

The Department of Entomology seeks an Assistant Professor to develop an integrated Extension/Research/Teaching portfolio (40/40/20 split) that addresses the effects of environmental change on pollinators at multiple scales. The appointee will be expected to build a nationally prominent, robustly funded research/extension program that addresses some broad aspect of pollinator health and sustainability. In addition, he/she will work with university, government, and private sector/NGO partners to find novel ways of incorporating pollinators into multidisciplinary efforts that advance priorities of Maryland Extension, including, among others, agricultural sustainability, profitability, and literacy; environmental sustainability; local food production; and community resilience.

The appointee will also deliver innovative extension support and training in apiculture to diverse stakeholders in our state and region, train graduate students, and contribute to the department's teaching program. Applicants must have a Ph.D. in Entomology or a related field, demonstrated excellence in both scientific publication and ability to obtain external funding, and evidence of experience with Extension. Research specialties can include any aspect of pollinator biology that bears on pollinator health and sustainability. Preference will be given to candidates with postdoctoral experience, proficiency with Extension or outreach, and innovative approaches to translational science.

Electronic submission of application through the University online system ([website: http://www.ejobs.umd.edu](http://www.ejobs.umd.edu)) is required. Candidates should submit a cover letter describing qualifications, curriculum vitae, a summary of research and extension experience and future plans (three to four pages), a statement of educational interests, and contact information for three persons from whom letters of recommendation can be requested. When preparing the electronic submission, submit the statement of research and extension in the Research field, and the statement of educational interests in the Supplemental Documents field. The position remains open until filled. Best consideration will be given to applications received by August 1, 2013.

The University of Maryland is an Equal Opportunity/Affirmative Action Employer.

POSITIONS OPEN



STREAM ECOLOGIST Department of Biology

The Department of Biology ([website: http://www.bio.txstate.edu](http://www.bio.txstate.edu)) at Texas State University ([website: http://www.txstate.edu](http://www.txstate.edu)) invites applications for a stream ecologist. The position is tenure-track at the rank of **ASSISTANT PROFESSOR**. The individual selected for the position will be expected to teach both graduate and undergraduate courses in the Department of Biology and develop an externally funded research program involving students. Required qualifications are a Ph.D. in the life sciences, postdoctoral experience, and a publication record in stream ecology. Preferred qualifications are a record of extramural funding to support research, a record of collaboration with other aquatic scientists, and experience in applied research related to stream macroinvertebrates and trophic-level interactions. Salary and startup package are negotiable. A letter of application, curriculum vitae, and the names and contact information of five people willing to serve as references should be sent as a single PDF to [e-mail: streamecology@txstate.edu](mailto:streamecology@txstate.edu). Inquiries may be directed to **Dr. Weston Nowlin** ([e-mail: wn11@txstate.edu](mailto:wn11@txstate.edu)). Review of applications will begin on October 1, 2013 and continue until the position is filled.

Texas State University will not discriminate against any person (or exclude any person from participating in or receiving the benefits of any of its activities or programs) on any basis prohibited by law, including race, color, age, national origin, religion, sex, or disability, or on the basis of sexual orientation.

FACULTY POSITION

The Department of Molecular and Cell Biology at the Boston University Henry M. Goldman School of Dental Medicine has an opening at the **ASSISTANT, ASSOCIATE, OR FULL PROFESSOR** level. For this position, we seek qualified candidates with research interests in areas relevant to craniofacial or oral biology. Individuals with an outstanding publication record and an ongoing NIH R01-funded research program are encouraged to apply. Excellent laboratory facilities and startup funds are available as well as joint appointments with appropriate departments at the School of Medicine and participation in the Bioinformatics Program at the School of Engineering. Qualified applicants should submit curriculum vitae, a brief summary of research accomplishments, a description of plans for future work, and names of three to five references, by August 31, 2013. Electronically send all materials to **Dr. P. C. Trackman, Search Committee Chair** at [e-mail: mcdept@bu.edu](mailto:mcdept@bu.edu).

Please visit [website: http://dentalschool.bu.edu/research/molecular/index.html](http://dentalschool.bu.edu/research/molecular/index.html).

Boston University is an Affirmative Action and Equal Opportunity Employer.

MARKETPLACE

ProMab Biotechnologies, Inc.
Custom Monoclonal Antibody \$3,900
 > 3,000 CLONES WILL BE SCREENED
 1-866-339-0871
www.ProMab.com | info@promab.com

Widely Recognized Original & Guaranteed
KlenTaq1™ 8¢/u Truncated Taq DNA Polymerase Withstand 99°C
[e-mail: order@JEMBIO.com](mailto:order@JEMBIO.com) www.JEMBIO.com
 Call: JEM BIO Home of KlenTaq-5
 Ph: 1-866-493-3464 Fax: 636-465-3979